Study of the Three Dimensional Random Field Ising Model: Magnetic X-ray and Neutron Scattering, Magnetization, and Heat Capacity

by

Qiang Feng

B.A., Lake Forest College
(1991)

Submitted to the Department of Physics
in partial fulfillment of the requirements for the degree of

Doctor of Philosophy

at the

MASSACHUSETTS INSTITUTE OF TECHNOLOGY

September 1996

Author ....
artment of Physics
July 9th, 1996

Certified by... .....
Robert J. Birgeneau
Dean of Science and Cecil and Ida Green Professor of Physics
Thesis Supervisor

Accepted by ....
George F. Koster
Chairman, Departmental Committee on Graduate Students

Study of the Three Dimensional Random Field Ising Model: Magnetic X-ray and Neutron Scattering, Magnetization, and Heat Capacity

by

Qiang Feng

Submitted to the Department of Physics
on July 9th, 1996, in partial fulfillment of the
requirements for the degree of
Doctor of Philosophy

Abstract

An experimental study utilizing scattering and bulk thermodynamic techniques on the 3d random field Ising model, realized in diluted antiferromagnets, is presented. The work addresses the issues of the nature of the random field transition, both during zero field cooling and field cooling, and anomalous metastable behavior unique to systems with random disorder. A consistent phenomenological description for the zero field cooling transition is obtained by a comprehensive study of the non-divergent pseudo critical behavior in the order parameter, correlation length, direct and indirect heat capacity, all controlled by the random field dynamics. A reconciliation is accomplished for the long standing discrepancy between the indirect heat capacity measurements and the scattering results by attributing the hysteresis in the indirect measurements to the underlying difference in the spin configurations. On field cooling, direct and indirect evidences of an equilibrium random field transition are observed by magnetic neutron and x-ray scattering measurements. From diffuse scattering above the metastability temperature, we are able to extract exponents for the correlation length and susceptibilities, and estimate the random field Néel temperature. X-ray scattering profiles in the field cooled state at low fields displays an unusual long range order that coexists with short range order. This long range order diminishes with increasing field, and its temperature scaling differs from that of the zero field cooled or field heated order parameter. Combining magnetometry and neutron scattering, logarithmic time dependence of the size of quenched domains is observed for fields above 3T except at low temperatures where domain movements are frozen.

Thesis Supervisor: Robert J. Birgeneau
Title: Dean of Science and Cecil and Ida Green Professor of Physics

Acknowledgments

I came to graduate school not as much for an advanced degree as for the pursuit of an ideal. Like others who are enticed by the beauty of nature and drawn to physics, I hoped to search for the principles of the universe and eventually to benefit mankind. It remains a dream at the end of this five-years-long journey. The research and the learning have equipped me with an invaluable vision of the physical world. Yet, being a bigoted perfectionist, I also sense an unmistakable tinge of dissatisfaction. Even after expending a great deal of time and labor toward a research goal, physicists may still find it necessary once in a while either to compromise their standards for elegance or to concede the limit of their capabilities. Nevertheless, the successes that we achieve during this pursuit, however limited they may seem at the time being, will undoubtedly lead to the ultimate truth and redeem all our efforts. Therefore, no matter where this journey leads me, I shall always look upon my days at MIT with gratification as they have witnessed me pursue a pure goal with little disturbance from the outside world - which in itself is a dream fulfilled. This experience has been enhanced and sustained by the many people I have crossed paths with, and I find it particularly fitting to express my gratitude at the completion of this thesis.

I thank the guidance and support of my research advisor, Bob Birgeneau. I have been very fortunate to be a member of Bob's vigorous research team and to work on some of the fundamentally important physics problems that are at once challenging and rewarding. Bob's unparalleled ability of gaining quick insights into problems, formulating ingenious solutions and articulating them in a truly effective way is a quality I will always attempt to emulate. I have also benefited from the freedom and responsibilities he bestows upon his students in exploring research directions independently.

It is an honor to have professor Mehran Kardar and professor Thomas Greytak as the readers of my thesis. They are among the best physics teachers I have ever had. I am grateful to professor Kardar for suggesting many useful corrections in the draft, and to professor Greytak for agreeing to be on the committee with only less

than three weeks to the defense date.

The most wonderful aspect of graduate school is to be in the company of a diverse group of talented fellow students and scientists. Thanks are due to the current and former members whom I have met in the Birgeneau group, John Hill, Do Young Noh, Bernhard Keimer, Bill Nuttall, Kenny Blum, Kevin Fahey, Yongmei Shao, Monte Ramstad, Michael Young, Barry Wells, Martin Greven, Joan Harris, Young Sang Lee, Young-June Kim, Patrick Mang, Rebecca Christianson, Yujie Wang, Sungil Park, and Michelle Girvan. I owe much of what I know about x-ray scattering and the random field problem to John, who patiently guided me through my first experiments at MIT and at Brookhaven National Lab, and continues to be a willing source of advice. Joan has given me invaluable help on each of my many Brookhaven trips, often at great personal inconvenience. Her optimism, tenacity and patience helped us overcome many daunting difficulties at the beamlines. I also thank Yongmei and Young-June for selflessly coming to Brookhaven when help was most needed. I am very grateful to Mike, our Unix guru, for his friendship and his numerous rescues. How Mike learned all the secret key stroke combinations that enable him to work with dozens of windows without ever touching the mouse will always be a mystery to me. Special thanks are due to Barry, Young and Young-June for the many get-togethers, squash and tennis games, hiking trips and, most of all, for magnetizing the current group into a cohesive fraternity. I learned much about American football and college basketball from them. And then I paid for it in the Superbowl and March Madness pools. I thank Martin and Karen for their friendship. It was a pleasure to welcome Rebecca, Yujie, Sungil and Michelle as they joined the group in the past year. I hope they will find this group as enjoyable as I did. I will surely miss all the folks here, with their fascinating lunchtime stories, and I wish all of them well in their future endeavors.

I thank Dr. Art Ramirez and his wife Ruth for their hospitality during my visits to Bell Labs. I have learned a lot from Art whose ability in juggling several experiments simultaneously is most impressive. This thesis would not have been complete without the heat capacity work on which I received enormous help from him. I will always feel guilty for calling him with bad news in the lab while he was on vacation.

The success of the experiments at Brookhaven would not have been possible without the constant help from René Holaday and Jean Jordan-Sweet. Bean bag and nutdriver juggling, which I learned from René, ranks among the more important skills that I acquired in graduate school. It is a pleasure to acknowledge Janet Salstrom, Ann-Marie LeBlanc, Karen Fosher and Ronald Hasseltine at MIT for their help in handling scores if not hundreds of travel vouchers and purchases. Thanks are also due to Peggy Berkovitz for her kindness from which I have benefited greatly at every step towards the completion of my degree, and to Debra Martin for her help in preparing the manuscripts for publication.

I will certainly be homesick for Boston, a city that offers so many wonders. The time I spent here has been blessed with the friendship of many. It has enriched my life and helped me maintain a balanced perspective. Heartfelt thanks go to Dave Chen, Eva Jin, James Chen, Wen Hu, Yuting Kuo, Bill Kaliardos, and Michael Lo among many others. I thank Andrea Banaski for the joy she brought me through her many letters. I would also like to thank Judy Manning, Don Lundy and Peter Manning for their care throughout these years.

My foremost gratitude goes to Sherry Wang for her love and encouragement. I have learned a great deal from her extraordinary talent in art and her exuberant *joie de vivre.* It is a miraculous fortune to find someone who can share so much, including quite unexpectedly, an interest in *trompe l'oeil* phenomena. She made my final year at MIT the best I have ever lived. I earnestly hope that her love and faith in me will be rewarded by immense happiness.

This moment of remembrance brings back fond memories of the Lake Forest days. I am grateful to Professor Tung H. Jeong for his guidance and his family for their tremendous hospitality. Professor Michael Kash was both a mentor and a friend to me. I have never met a physicist who is as meticulous and as thorough in the knowledge of quantum mechanics as he is. He encouraged me to attend MIT and would undoubtedly take pride in seeing me graduate on time. I would also like to thank Virginia Crist, Rosemary Cowler, Bailey Donnally, Heidi Ford, Forest Hansen, Louise Mason, Vanaja Menon, George Speros and Gordon White for making the

College a home for me.

I am deeply grateful to Ann Hentz, who made it possible for me to come and explore this new world and cared for me as her own son. It divines one's life to be imbued in kindness and love as extraordinary and holy as hers. I thank wholeheartedly my parents, whom I always hold in the greatest esteem, and my sister for their unfailing love and support over the years. To make them proud has motivated me and will always motivate me to accomplish more.

Added without proof: To those of you who have always wondered why I have spent five years on the random field Ising problem (and end up earning a free Ph.D. from it), and were never satisfied with my far-fetched utilitarian explanations such as its possible relevance for impurities in magnetic data storage devices, I supply the following thought-provoking analogy and urge you to contemplate its ramifications. It dawned on me as I was glancing at a map of the world one day that the random field problem, at the stretch of one's imagination, could be applied to the arena of world politics and geography. Allow me to elaborate: the interface tension due to the competition between the disrupting random fields and the unifying exchange forces drives the motion of the metastable domain walls much the same way the borders between nations are shaped and re-shaped over time. The notions of fractality or self-affinity are commonly used to describe both domain surfaces and boundaries separating countries. Flipped blocks of spins in a magnetic system find their counterpart in conquered or seceded regions such as the Golan Heights or Kashmire. The logarithmic growth of domains, by way of the large expanding at the expense of the small, mimics the historical evolution of nations during which the weak are swallowed by the strong, though the two mechanisms obviously operate on quite different time scales. The strength of this analogy is utterly compelling. A fundamental conclusion on the random field Ising model, one of a precious few that we adamantly believe in, is that in weak random fields and at low temperatures, its equilibrium ground state has long range magnetic order in three dimensions. It prophesies, in my expert interpretation, that as long as deadly forces such as nuclear weapons are not in individuals' hands and people are able to maintain sensible minds, world peace can eventually be achieved.

Contents

List of Figures

List of Tables

Chapter 1

Introduction

1.1 Phase Transitions and Disorders in Condensed Matter

The step from understanding the properties of an independent entity to determining those of a collection of interdependent entities often proves enormous, if not altogether insurmountable, in nature. Centuries have passed since the inception of classical mechanics, yet the basic three-body problem remains unsolved. Not surprisingly, physicists are faced with tremendous difficulties on the subject of collective phenomena in macroscopic condensed matter, which involves up to 10^{23} interacting atoms, and breakthroughs in a comprehensive understanding beyond pure phenomenology have only occurred at the advent of modern statistical physics.

Although we are not able to predict analytically the exact motion of each of the objects in the three-body problem, much can be learned about this simple system through two different approaches. In the first approach, one combines analytical and numerical methods. Given the interaction among the objects, the boundary conditions, the external perturbations and the initial state of the system at time zero, one can calculate directly the position and velocity of each body at the next moment using simple laws of kinematics. This step can be repeated indefinitely and one is thus able to forecast approximately the state of the system at any time in the

future. The accuracy of this method can be maintained by making each time interval infinitesimally small. An alternative approach exploits the symmetries present in the problem. From the general temporal, translational and rotational symmetries (or invariances), one deduces the conservation of energy, linear momentum and angular momentum respectively . The constants of motion can be obtained and the overall behavior of the system is thus well understood.

Collective phenomena in condensed matter can be approached in analogous ways. A problem, once defined, may be attempted directly by calculating the physical quantities analytically or numerically. Onsager's solution of the two dimensional Ising model is an exact solution, while the Landau-Ginzburg mean field technique is an example of approximate methods. However, direct methods with even minimal sophistication often turn out to be overwhelmingly complicated. It is therefore of immense value to utilize symmetries and dimensionalities. A surprising amount can be learned about phase transitions this way. The revolutionary technique of renormalization group, which comprises a sequence of symmetry transformations that traces the behavior of a system at successively longer length scales, has proven to be a powerful tool for studying critical phenomena. Near a phase transition, physical quantities such as the order parameter, correlation length, susceptibility and heat capacity generally exhibit power law singularities that are characterized by a small set of interrelated critical exponents. While the mean field theory yields exact values for these exponents above the upper critical dimension, d_u, the renormalization group method enables one to calculate critical exponents for dimensions $d < d_u$. It is found that the same set of critical exponents often describe many disparate physical systems regardless of the detailed interactions, and their values are dependent only upon a few fundamental attributes of the system, such as the dimensionality of space and the relevant order parameter. This extraordinary property, that the behavior of a macroscopic system at large length scales is independent of microscopic details, is called universality. We owe much of our knowledge about critical phenomena today to renormalization group theory and the concepts of scaling and universality.

From the phenomenological study of liquid-vapor transitions over a century ago

to the more recent investigations on magnetic order-disorder transitions, the study of phase transitions, and condensed matter physics in general, has largely been preoccupied with studying pure systems. Quenched random disorder and impurities were generally excluded from the statements of problems or treated as weak perturbations and expected not to affect the outcome of the calculations significantly. However, disorder is ubiquitous and generally affect all experimental systems to a certain degree. As we undertake the studies of new physical systems, such as mesoscopic structures in which a minimal amount of impurities would introduce considerable deviation in the transport properties, or porous sediments and neural networks that have intrinsic disorder and exhibit unusual behavior, the importance of disorder can no longer be overlooked. With the maturity of advanced experimental techniques, including neutron and x-ray scattering and various bulk thermodynamic methods, the understanding of systems with competing interactions and random disorder has become a focal point in condensed matter research and provided some of the most exciting development in physics.

There are generally two types of disorders that are frequently encountered in physical systems. One is *annealed* disorder in which the disorder or impurities are free to move around to maintain thermal equilibrium with the host medium. The isotopic ^{3}He in the ^{4}He superfluid transition is an example of annealed disorder. The other type is *quenched* disorder, in which the disorder is structurally frozen in rather than being in thermal equilibrium with the state of the host material. Examples include effects of crystal imperfections on resistivity and immobile impurities absorbed on substrates. The work presented in this thesis deals with the impact of quenched disorder on phase transitions and critical phenomena.

Much of our knowledge of collective phenomena has come from the study of magnetic systems. This is not only because there exists an enormous variety of magnetic materials, simple and complex, that are accessible to experiments, but also because the theoretical models based on these systems, despite their simplicity, are able to capture the essential physics in complicated problems. In the case of studying quenched disorder, magnetic systems have the additional advantage of providing samples with

exceedingly homogeneous randomness. Further, for the study of the random field Ising model, a magnetic realization is particularly useful because it makes the strength of disorder continuously adjustable. Therefore, it is not surprising that random magnets have often been used as prototypes in experimental studies on phase transitions in disordered systems.

In the context of disordered magnets, there are three basic classes: random exchange, random field and spin glass, each associated with a different type of disorder. The subject of this thesis is the effect of random fields on an Ising model in three dimensions (3d RFIM). The experiments are carried out on several diluted antiferromagnets that, in zero applied field, are special cases of the three dimensional random exchange Ising model (REIM). In the remainder of Chapter 1, I review the theoretical background of the 3d RFIM, both equilibrium and nonequilibrium, and previous experimental results. Chapter 2 describes the samples used in the current study and the experimental techniques applied. Some data are presented to illustrate the process of analysis for each technique. In Chapter 3, a phenomenological description of the zero field cooling transition and the anomalous critical phenomena of the 3d RFIM is presented, along with a re-interpretation of the hysteresis observed in bulk thermodynamic measurements. Chapter 4 details a magnetic neutron and x-ray scattering study of the ordering process during field cooling, in which we attempt to identify the equilibrium random field transition, extract new critical exponents, and describe an unusual long range magnetic order observed so far only by x-ray scattering. Chapter 5 reports the time dependence of metastable magnetic domains measured directly by neutron scattering and indirectly by uniform magnetization. The thesis is concluded in chapter 6, with suggestions for future directions of research.

1.2 A Brief History of the RFIM

1.2.1 Hamiltonian

The random field Ising model is defined by the following Hamiltonian [1]

$$\mathcal{H} = J \sum_{<ij>} S_i^z S_j^z - \sum_i h_i S_i^z. \tag{1.1}$$

In its magnetic embodiment, this Hamiltonian depicts a collection of spins S_i located at position i on a lattice with J being the exchange interaction between nearest neighbors. h_i is a *quenched* site-random field that couples to the one dimensional order parameter S. Therefore, the constraint on h_i is that it has zero average, $\overline{h_i} = 0$, and there is no correlation between h_i at different lattice locations, $\overline{h_i h_j} = \delta_{ij} h_{RF}^2$, where h_{RF} becomes a measure of the strength of the random fields. The model does not specify the statistical distribution of the random fields. The most frequently studied cases in RFIM theory are the binary distribution and the Gaussian distribution. Unlike the pure Ising model which has spin-flip symmetry, the random field Ising model is spin-flip symmetric only in a statistical sense [2].

More generally, the simple Hamiltonian in equation 1.1 describes virtually any solid state system that has a transition with two degenerate ordered states, and contains frozen impurities that locally break the symmetry between these two states.

1.2.2 Theoretical Study of the RFIM

Despite the enormous efforts expended on the RFIM problem, its phase transition and equilibrium critical behavior are still not completely understood. This is due to the complexities that arise from the unusual nature of the random field problem, particularly its free energy distribution. In this section, we review several important theoretical topics.

The Lower Critical Dimension

For a pure magnetic system, the ordering of spins results from a competition between the energy and the entropy. In one dimension, the entropy dominates over the energy except at absolute zero temperature and therefore spins are disordered at any finite temperature [3]. For dimensions of two and above, for pure Ising systems there exists a critical temperature T_C below which energy dominates over entropy and a state of long range magnetic order can be established. In general, thermal fluctuations destroy spin ordering more easily in lower dimensions. This leads to the notion of the lower critical dimension, d_l, defined as the dimension above which an ordered phase is stable at finite temperature. Clearly, $d_l = 1$ for the pure Ising model.

Naturally, the immediate questions concerning the RFIM are its phases and its d_l. The main competition at low temperatures is now between the exchange energy, which favors long range order, and the random field energy, which tends to destroy such order. The thermal fluctuation plays a secondary role and the critical behavior at the phase transition, if there exists one, is controlled by the fixed point at zero temperature. For the case of strong random fields, $h_{RF} > J$, the random field energy is the dominant term in equation 1.1. Intuitively, the spins will largely follow their local fields h_i and are therefore uncorrelated, regardless of dimension. This has been confirmed by a rigorous treatment [4]. The situation in which $h_{RF} < J$ is much less clear. For very weak random fields, one is tempted to expect that long range order can be established at low temperature for dimensions above a certain lower critical dimension. It comes as a surprise that this deceptively simple issue has been a long standing controversy in the history of the RFIM. In the following, we briefly outline the various arguments for d_l(RFIM).

In their ground-breaking work on the RFIM, Imry and Ma presented a heuristic argument for d_l(RFIM)=2 based on the standard method of assessing the stability of long range order with respect to the formation of domains [1]. Consider a ferromagnetically ordered Ising system with quenched random fields in d dimension. Due to unsatisfied bonds, overturning any block of spins of linear size R introduces an

energy cost that is proportional to the domain surface area and the exchange energy, $\sim JR^{d-1}$. However, because of the fluctuations in the random field distribution, it is always possible to find a volume of linear size R in which there is an imbalance between up-oriented and down-oriented fields so that reversing the spins in this volume gains random field energy. Statistically, this lowers the energy by $h_{RF}R^{d/2}$. Therefore the total energy associated with creating this domain in a uniformly ordered state is

$$E(R) = JR^{d-1} - h_{RF}R^{d/2}. \tag{1.2}$$

Since $h_{RF} < J$, it is easy to see that $E(R)$ is positive for $d > 2$, but negative for $d < 2$ for sufficiently large R. This means domain formation is favorable only for $d < 2$ and long range order is stable for $d > 2$. This simple domain argument therefore predicts that $d_l = 2$ for the RFIM. The marginal dimension $d = 2$ requires more sophisticated treatment and has been shown to be unstable against domain formation. For a spin system with continuous symmetry, the exchange energy cost is $\sim JR^{d-2}$ and the same argument yields $d_l = 4$.

Despite its success in reaching an important conclusion through a remarkably simple approach, the Imry-Ma argument ignored relevant spin configurations such as domains within domains and assumed compact domain structures. It is also a zero temperature argument since entropy was not taken into account. Therefore, this heuristic method effectively placed a lower bound on d_l and did not rule out the possibility that more rigorous treatment might produce stronger instabilities. Soon afterwards, more sophisticated theoretical studies using perturbative renormalization group were performed and the results supported a "dimensional reduction" argument instead. It was concluded in these studies that the critical exponents of the d dimensional RFIM were equal to those of a $(d-2)$ dimensional pure Ising model. This was found by Aharony *et al.* [5] for $4 < d < 6$ to all orders of ϵ expansions, and by Pytte, Mukamel *et al.* [6, 7, 8] for $d > 3$ to first order in ϵ. Since d_l of the pure Ising model is 1, this led to the prediction that d_l(RFIM)=3.

However, it is now known that the perturbative renormalization group technique

has been unable to account for the anomalously slow dynamics and the hysteretic effects in random systems, and therefore its prediction for d_l(RFIM) is incorrect. Further, the possible causes of stronger instabilities not considered by the Imry-Ma reasoning have been more carefully analyzed. Specifically, the problems of random field-roughened domain interfaces [9, 10], the possible entropy effects [11, 12] and the situation of domains within domains [13, 14] were shown to introduce only small corrections and do not affect the ground state in dimensions above 2. Imbrie demonstrated rigorously that the 3d RFIM is ordered for T=0 and $h_{RF} \ll J$ [13]. Since thermal fluctuations are not strong enough to break up long range order that is present at T=0 for $d > 1$, Imbrie effectively completed the proof that d_l(RFIM)=2. The same prediction is supported by low temperature scaling arguments [15] and numerical calculations [16].

Although d_l=2 is now widely accepted as the equilibrium lower critical dimension, experiments were unable to settle the issue unambiguously for a long time due to unforeseen nonequilibrium effects inherent to the RFIM problem. We discuss these experimental results in detail in a later section.

Nonequilibrium Behavior

Theory of critical phenomena has commonly focused on equilibrium properties. However, an actual physical system does not regain equilibrium instantaneously following a change in external parameters such as temperature or magnetic field. Therefore the accuracy to which the theoretical predictions describe the experimental measurements depends on the equilibration rate of the physical system. This may cause concern in the vicinity of a phase transition where the correlation length ξ diverges. Since ξ can not approach infinity on finite time scales that experiments are constrained to, all macroscopic experimental systems will drop out of equilibrium near the critical point. As ξ grows, the equilibration (or relaxation) time τ grows accordingly and eventually diverges at the transition. This is the so called "critical slowing down". For pure systems, the relaxation time τ for a coherent volume of linear size L is $\tau \sim \tau_0 L^z$. Lifshitz argued that z=2 based on simple kinetics argument for second

order transitions [17]. τ_0 is a microscopic time that is system dependent and is generally $\sim 10^{-11}$s. One can therefore estimate that, over one second, the system is able to relax over a distance of $\sim 10^6$Å. The validity of this power-law description has been established by numerical calculations [18] and time-resolved studies on binary alloys [19, 20, 21]. For most experiments in which measurements are made over periods of seconds or longer, critical slowing down clearly does not obscure the transition and true equilibrium critical behavior is commonly observed.

As mentioned above, the failure of the dimensional reduction idea in describing the RFIM stems from the presence of many local minima in the free energy landscape that prohibits a straightforward perturbative treatment. A slower growth rate of the correlation length is expected because of the pinning effects and substantial energy barriers due to the random fields (and random bonds as well in most experimental systems). A more consistent theory of the phase transition arose from the scaling arguments for the RFIM [22, 23, 24]. An important observation is that, unlike conventional systems where the free energy variation is simply set by thermal fluctuations and the hyperscaling assumption leads to the scaling relation $2-\alpha = d\nu$, the RFIM is dominated by static fluctuations introduce by random fields both at zero temperature and in the transition region [1, 25]. Since the correlation length ξ is the only relevant length near an equilibrium transition, one may assume that the free energy variation scales as ξ^θ instead of kT. This leads to a modified hyperscaling

$$2 - \alpha = (d - \theta)\nu. \tag{1.3}$$

It also follows that the equilibration time diverges exponentially with the correlation length,

$$\tau \sim \tau_0 exp(\xi^\theta / T) \tag{1.4}$$

[23]. This means that the relaxation time τ diverges much faster than that in a conventional system and, when cooled from a disordered state, the random field system may drop out of equilibrium substantially above the equilibrium critical temperature. The correlation length ξ should grow extremely slowly with time and remain

finite at the transition. This extraordinary result essentially rules out the possibility of probing the true equilibrium critical behavior of any random field Ising magnet on experimentally accessible time scales. As we will see below, this droplet picture provides a realistic depiction of the unusual dynamic behavior at the RFIM phase transition.

A similar situation exists below the transition. Spurred by the experimental discovery of a short range ordered domain state when a random field system is cooled through the transition, theoretical ideas were developed to describe a metastable state at low temperatures. This was first considered by Villain [9] and Grinstein and Fernandez [26]. As is well known, in a pure magnet, domains with smooth surfaces may form if the system is cooled very rapidly through the transition. The growth of the domain size, R, is driven by surface tension and follows the simple power law $R(t) \sim t^{1/2}$ [27]. The growth process is quite different in the presence of random fields. The walls separating oppositely oriented domains are distorted, or roughened, according to the local distribution of random fields to minimize the energy. However, for each section of a roughened domain interface, there exist many nearby meandering paths for the domain walls to pass through that correspond to different minima in energy. As the system searches for the ground state in this complicated distribution of free energy minima, it needs to overcome energy barriers as the domain wall shifts position. The height of an energy barrier ΔE corresponding to a wall movement on the length scale L is typically $\Delta E \sim L^{\psi}$. The exponent ψ depends on the dimension d and the type of disorder. It follows from Arrhenius law that the equilibration time of domain surfaces on length scale L at temperature T is $\tau(L) \sim \tau_0 \exp(L^{\psi}/T)$. Conversely, the maximum correlation length after cooling a RFIM system to a low temperature T grows logarithmically with time $\sim (\ln\frac{t}{\tau_0})^{1/\psi}$. Similar argument leads to the time dependence for the average domain size $R(t)$. Villain [9] and Grinstein and Fernandez [26] showed that

$$R(t) \sim \frac{1}{h_{RF}^{\nu_H}} \ln(\frac{t}{\tau_0}) \tag{1.5}$$

where ν_H=2 describes the scaling of domain size with the random field strength. For an experimental system that also involves random bonds, a power $\frac{1}{\psi}$ applies to the logarithm [18], though ψ is close to 1 in 3d. The study was furthered by Nattermann and Vilfan [28] who stressed the role of anisotropies in the relaxation of domains in experimental systems. They found that in systems with weak uniaxial anisotropy the domain walls are broadened, the bond randomness becomes irrelevant and the shifting of domain walls does not produce observable increase in domain sizes. On the other hand, in strongly anisotropic systems the walls are pinned by random bonds and random fields are responsible for local readjustment on the interface. Though their arguments dealt with cases of extreme anisotropies, they provided a framework for understanding the various degrees of experimentally observed relaxations in different random field magnets and related directly to alternative means of measuring domain size, such as uniform magnetization. Note that the logarithmic increase of domain size is extremely slow at the relatively long times accessible to experiments (usually minutes to hours) and several orders of magnitude of increase in time needs to be covered in order to observe the subtle change in domain radii.

Order of the Transition

An equally important issue, in addition to the lower critical dimension, is the order of the RFIM transition. This has been another controversy that has been equally intensely debated and remains far from being resolved.

The droplet theories, the one devised by Fisher for example [23], rely upon the assumption of a second-order phase transition. However, theoretical results are divided over the order of the transition, and the majority of the results appears to support a first order transition. Early mean field approximation by Aharony showed that for binary distribution of random fields, the transition turns first order at high values of h_{RF}, via a tricritical point [29]. This result was confirmed for general distributions of random fields by high temperature series expansion of Khurana and Houghton *et al.* [30, 31]. Monte Carlo results by Young and Nauenberg [32] and Rieger and Young [33] indicated a first order transition. However, simulations by Ogielski [34] and Ogielski

and Huse [35] supported a continuous second order transition. More recently, Monte Carlo results by Rieger [36] revealed a rather unusual first order transition. It was found that the order parameter behaves discontinuously at the transition, i.e. $\beta = 0$. But, contrary to a usual first order transition where there is a discontinuity in the internal energy at the critical point [37], neither a latent heat nor a divergence in the heat capacity was detected. Further, the probability distribution of the order parameter did not show a multi-peak structure that characterizes the phase coexistence at first order transitions. This unconventional first order transition has been termed a hybrid-order transition [38]. More recently, a possible intermediate spin-glass phase that lies between the ordered phase and the paramagnetic phase has been suggested [39, 40]. If confirmed, this will lead to nontrivial effects on the transition discussed here.

It is expected that experiments and simulations would be made difficult because of the random field activated dynamics. The experiments have generally observed a continuous transition, though a smeared transition with a discontinuity in the order parameter cannot be ruled out. All things considered, there still lacks a decisive proof for the transition being either first or second order[2]. In table 1.1, we compare the known exponents for the 3d Ising model [41] and the 3d random exchange Ising model [42, 43, 44] with the theoretical and simulation estimates for the 3d random field Ising model [36, 33, 45, 46, 2, 43, 42]. Recently, for the random field connected and disconnected susceptibility exponents γ and $\bar{\gamma}$, Gofman *et al.* [45] reported $\gamma = 2.1 \pm 0.2$ and $\bar{\gamma} = 2\gamma$ using series expansions, and Monte Carlo simulations by Rieger *et al.* reported similar estimates [33, 36]. For the correlation length exponent ν, current theoretical estimates lie between 1.4 and 1.5 [47], and Monte Carlo work yields 1.6 ± 0.3 for binary random field distributions [33].

Exponents	3d Ising	3d REIM	3d RFIM
α	0.11 ± 0.005	-0.09,-0.04	≤ 0
β	0.325 ± 0.002	0.35 ± 0.01	$\simeq 0$
ν	0.63 ± 0.002	0.68 ± 0.02	$\simeq 1.4$
γ	1.24 ± 0.002	1.35 ± 0.04	$\simeq 2.1$

Table 1.1: Exponents of pure Ising, random exchange Ising and random field Ising models

1.2.3 Realization of the RFIM: Diluted Antiferromagnets in Applied Fields

Although the random field Ising model was first conceived by Imry and Ma as a purely theoretical construct and remained this way for years, we now know that it is in fact capable of describing the basic physics in a remarkable array of disordered systems in nature. These include binary fluid mixtures in porous media, charge-density-wave phases with impurity pinning, absorption onto two-sublattice substrates with surface impurities, random defects in vortex lattice in superconductors, structural phase transition in random alloys, and antiferromagnets diluted with non-magnetic ions and placed in uniform applied fields (DAFF). Each of these systems provides a platform for studying the random field phases and transitions, but most of the experimental work has been done on the DAFFs. This is because of the general advantages of using magnetic systems as a means of studying critical behavior, plus the convenience of a continuously tunable random field strength unique to the DAFFs. Single crystal mixtures such as $Mn_xZn_{1-x}F_2$ and $Fe_xZn_{1-x}F_2$ can be grown with exceptional quality and are ideal for a variety of experiments on the 3d RFIM.

That the RFIM may be realized in a DAFF was first demonstrated by Fishman and Aharony [48] based on an idea suggested by Imry and Ma [1] for an antiferromagnetic random *bond* Ising system in a uniform field. The applicability of an antiferromagnet with random *site* dilution was shown similarly by Wong *et al.* [49]. Cardy [50] later showed that the Hamiltonian of the site diluted Ising antiferromagnet in a field can be unambiguously mapped onto that of a ferromagnet with random fields.

The generation of random fields in a DAFF can be easily derived through simple substitutions [48, 49, 51]. Starting with the Hamiltonian of a random two-sublattice antiferromagnet in a uniform field H,

$$\mathcal{H} = \sum_{<ij>} \sum_{\alpha\beta} J_{ij}^{\alpha\beta} \epsilon_i^\alpha \epsilon_j^\beta S_i^\alpha S_j^\beta - H \sum_i \sum_\alpha \epsilon_i^\alpha S_i^\alpha \tag{1.6}$$

where two adjacent ions on opposite sublattices are grouped into a cell so that S_i^α denotes the spin in cell i and on sub-lattice α. $\epsilon_i^\alpha = 1$ for the presence of a magnetic ion and zero otherwise. Defining

$$\begin{aligned} m_i &= \frac{1}{\sqrt{2}}(S_i^1 + S_i^2) \\ m_i^\dagger &= \frac{1}{\sqrt{2}}(S_i^1 - S_i^2) \end{aligned} \tag{1.7}$$

for each cell i so that $< m_i^\dagger >$ is the sublattice magnetization, or the order parameter, and $< m_i >$ is the uniform magnetization, the Hamiltonian is rewritten as

$$\begin{aligned} \mathcal{H} &= \sum_{<ij>} \left[J_{ij}^- m_i^\dagger m_j^\dagger + J_{ij}^* m_i^\dagger m_j + J_{ij}^+ m_i m_j \right] \\ &\quad + \frac{1}{\sqrt{2}} \sum_i \left[(\epsilon_i^1 + \epsilon_i^2) H m_i + (\epsilon_i^1 - \epsilon_i^2) H m_i^\dagger \right] \end{aligned} \tag{1.8}$$

where

$$J_{ij}^- = \frac{1}{2} \sum_{\alpha\beta} \lambda^\alpha \lambda^\beta \epsilon_i^\alpha \epsilon_j^\beta J_{ij}^{\alpha\beta} \qquad J_{ij}^+ = \frac{1}{2} \sum_{\alpha\beta} \epsilon_i^\alpha \epsilon_j^\beta J_{ij}^{\alpha\beta} \tag{1.9}$$

$$J_{ij}^* = \sum_{\alpha\beta} \lambda^\alpha \epsilon_i^\alpha \epsilon_j^\beta J_{ij}^{\alpha\beta} \qquad \lambda^1 \equiv -\lambda^2 = 1 \tag{1.10}$$

The random fields are revealed in equation 1.8, where two of the five terms couple directly to the order parameter $< m_i^\dagger >$ and are site-random. One, H_{R1}, is the last term in 1.8:

$$H_{R1} = \frac{1}{\sqrt{2}}(\epsilon_i^1 - \epsilon_i^2) H \tag{1.11}$$

This term is clearly unique to site-random systems in a non-zero field H. It reflects

that, in any part of the lattice, which ever sublattice has more magnetic ions is favored to order parallel to H. H_{R1} is zero for pure ($\forall\epsilon \equiv 1$) or random exchange magnets ($H = 0$). In a DAFF, it assumes discrete values of 0, $\pm\frac{H}{\sqrt{2}}$ and its variance is $< H_{R1}^2 >= x(1-x)H^2$, where x is the concentration of magnetic ions. Clearly H_{R1} is directly proportional to the applied field. The other contribution to random fields comes from the second term in 1.8:

$$H_{R2} = \sum_{ij} J_{ij}^* < m_j > \tag{1.12}$$

This term is present because $< m_i > \neq 0$ in a finite applied field. It is proportional to the local uniform magnetization and has a continuous distribution. For an antiferromagnet, H_{R2} is a smooth function of the temperature. In general, the uniform susceptibility of Ising antiferromagnets are relatively small and the random fields generated in a DAFF is therefore largely due to H_{R1}.

A more comprehensive expression for the random field strength $< h_{RF}^2 >$ was derived by Cardy [50]:

$$< h_{RF}^2 >_{av} (H,T) = \frac{x(1-x)[T_N^{MF}(1)/T]^2(g\mu_B SH/K_B T)^2}{[1+\Theta^{MF}(x)/T]^2}, \tag{1.13}$$

where $T_N^{MF}(1)$ is the mean field transition temperature of the pure system and $\Theta^{MF}(x)$ is the mean field Curie-Weiss parameter. This expression applies to the low field situation where $H \ll J$. In the high field limit, the direct result $h_{RF} \propto H$ applies [50].

Cross-Over Behavior

The experimentally accessible DAFFs thus provide an ideal class of magnets for studying the RFIM. As the magnetic field is turned on, a diluted antiferromagnet crosses over from the random exchange regime to the random field Ising universality class [48]. Denoting the random field cross-over exponent by ϕ, the free energy assumes

the new scaling form

$$F(T,h) \sim t^{2-\alpha} f(\frac{Ah^2}{t^\phi}) \tag{1.14}$$

where α is the specific heat exponent at zero field, $h = \mu H/k_B T$, and

$$t = (T - T_N - Bh^2)/T_N \tag{1.15}$$

where T_N is the zero field Néel temperature and Bh^2 represents a mean-field shift so that t is measured with respect to a mean-field phase boundary. $A \approx x(1-x)/(k_B T)^2$ is a measure of the randomness due to the bond dilution. For $H \neq 0$, new random field critical behavior, drastically different from that of pure Ising or random exchange Ising, is expected and the new transition temperature is given by

$$T_N(H) = T_N(0) - bH^2 - aH^{2/\phi}. \tag{1.16}$$

The additional transition temperature depression due to the random fields, $aH^{2/\phi}$, is generally much larger than the mean field correction bH^2. The mean field term can be simply calculated as $b(x) = (g^2\mu_B^2(2S^2+2S+1))/(40k_B^2 T_N(0))$[52]. The cross-over exponent ϕ was originally equated to the pure Ising susceptibility exponent γ_{pure}=1.24 [48]. Further study [53] showed that, for cross-over from random exchange to random field Ising behavior, $\phi \approx 1.07\gamma_{REIM}$. Since $\gamma_{REIM} = 1.35$, this gives an estimate for $\phi \approx 1.44$.

1.2.4 Experimental Study of the RFIM

Fishman and Aharony's work stimulated intensive experimental research on the random field Ising problem using diluted antiferromagnets. The experiments have utilized techniques such as magnetic neutron and x-ray scattering, which measure the microscopic ordering of spins, direct ac and dc heat capacity, NMR, and other bulk techniques such as linear magnetic birefringence, Faraday rotation, SQUID magnetometry, capacitance, magnetostriction, thermal expansion, ultrasound, etc. Commonly studied are 2d samples such as $Rb_2Co_xMg_{1-x}F_4$ and 3d systems $Fe_xZn_{1-x}F_2$,

$Mn_xZn_{1-x}F_2$, $Co_xZn_{1-x}F_2$, $Fe_xMg_{1-x}Cl_2$, etc. Even though experimental reports on various aspects of the RFIM problem abound, agreement and insights into the fundamental questions are scarce. Here we summarize some notable experimental results that were obtained from studying diluted antiferromagnets.

d=2

Most experiments on the 2d RFIM have used the prototypical system $Rb_2Co_xMg_{1-x}F_4$ [54, 55, 56] which has a 2d square lattice with a percolation threshold of x_p=0.593. In zero applied field, a Néel transition to long range order occurs at finte temperature for Co concentrations above x_p and all the measured critical exponents for the two dimensional random exchange model are found to be identical to the corresponding pure 2d Ising exponents.

Neutron scattering reveals that a domain structure develops in $Rb_2Co_xMg_{1-x}F_4$ at low temperatures when a field is applied. The size of the domains decreases with increasing field. The domains are metastable and expand drastically over time following a certain power of a logarithm [56]. Hysteresis also exists, but only at temperatures *below* which short range order develops. Both birefringence and neutron scattering measurements reveal a systematic rounding of the zero field Néel transition as the field is turned on. All experimental evidences confirm that random fields destroy the equilibrium transition to long range order in two dimensions. Therefore d_l(RFIM) ≥ 2.

d=3

Hysteresis and the Lower Critical Dimension In principle, a neutron scattering study that probes the spin configuration in a 3d DAFF can straightforwardly determine the range of ordering and settle the controversy over the lower critical dimension. However, the experiments in three dimensions were severely complicated by hysteretic effects [57, 58, 59]. Different experimental protocols led to distinctly different spin structures. For example, when a DAFF is cooled from high temperature in a constant applied field, there occurs a transition towards a metastable domain state

without long range order. On the other hand, if the field is turned on after long range order establishes in zero field through the random exchange Néel transition, the long range order is preserved. As the system is heated up, the long range order decreases in an approximate power-law fashion and disappears at a well defined transition temperature. Although the former protocol (FC) suggests a destructed transition in 3d, similar to the 2d RFIM situation, the latter one (ZFC) shows that long range order is sustainable for 3d RFIM.

Related hysteretic effects have been observed in many other measurements, such as birefringence, uniform magnetization, thermal expansion, etc. Generally the ZFC protocol produces a cusp that is somewhat sharper than the FC one at the transition. The ZFC order parameter transition also appears increasingly rounded with growing applied field [60]. Metastability is present in the disparate configurations arrived at via both approaches. As we now understand, the strong hysteresis originates from the random field activated dynamics [23]. Thus neither protocol is able to probe the equilibrium phase transition in the 3d RFIM and, in fact, the complexity of the random field free energy distribution entails that the true transition to evade all experiments.

Historically, the first claim of observing the new random field critical behavior came from the linear magnetic birefringence data on $Fe_xZn_{1-x}F_2$ by Belanger *et al.*[61, 62]. These workers equated the thermal derivative of birefringence $\frac{d(\Delta n)}{dT}$ with the magnetic heat capacity C_m and stated that the data showed a symmetric logarithmic divergence of heat capacity, suggesting α(RFIM)=0 and an effective dimensionality $d \approx 2$ for this 3d DAFF. However, this claim was supported by data that covered less than two decades of reduced temperature and were measured in fields less than 2T. The effective random fields were so weak that these authors were apparently not able to observe any hysteretic effects. In view of the common difficulties associated with extracting α from heat capacity data even for pure systems, these claims obviously needed to be substantiated by more extensive measurements and analysis. Later studies utilizing birefringence [63, 64] and Faraday rotation [65, 66], both of which measure heat capacity indirectly, arrived at similar conclusions. Though ob-

vious hysteresis and rounding of the transition peaks were observed at higher fields in these studies, the authors dismissed the rounded region of the transition from the data analysis as dynamic effects and maintained that the remaining peak structures illustrated true random field critical heat capacity with α(RFIM)=0. This created a serious discrepancy between the indirect heat capacity measurements and the neutron scattering results [67], which showed that the correlation length saturated at finite values in the presence of random fields and thus the transition appeared to be destroyed. Further, most direct heat capacity measurements revealed a rounded finite cusp at the transition with little or no observable hysteresis [68, 69, 70]. Although it is natural to attribute the non-divergence of correlations, the smeared transition of the order parameter and the broadening of bulk thermodynamic peaks to the same physical mechanism, this discrepancy has lingered for a long time. In Chapter 3, we attempt to settle this issue through a comprehensive study using scattering, direct and indirect heat capacity techniques and a hypothesis that links the hysteresis in bulk measurements to the underlying spin configurations.

Order of the Transition and Exponents Although the activated dynamics obscures the random field transition and induces superheating effects, an order-disorder transition in the 3d RFIM unmistakably exists and experiments have attempted to explore the order of this transition and the associated exponents. First, all experiments have observed a continuous transition. For example, magnetic x-ray scattering study of the order parameter [60, 70] shows the long range order decreases to zero continuously. In addition, the correlation length measured by neutron scattering [67, 71] appears to follow a power-law trend with reduced temperature until it is interrupted by the onset of random field anomalous critical slowing down. In the presence of substantial random field strength, heat capacity shows a finte cusp or, in the case of strong random fields, a hump and no latent heat has been observed. All this evidence points to a transition that is of second order. However, an unambiguous determination of the order of the random field transition is made extremely difficult by the nonequilibrium effects near the transition. Therefore the true equilibrium behavior

of important quantities such as the order parameter at the transition is subject to speculation. For example, at least one experiment has suggested the possibility of a first-order transition[72].

Yet, since power-law like behavior has been observed for several physical quantities, one can assume that there is indeed a putative second order transition and attempt to extract equilibrium exponents for the RFIM. All approaches to this end are approximate, of course, in view of the difficulty in determining the appropriate reduced temperature window. The most direct measurement of β relies on magnetic Bragg scattering. Neutron scattering is known to suffer from large extinction effects at low temperatures and are therefore unreliable [67]. The technique of magnetic x-ray scattering has matured with the advent of synchrotron sources. Measurements on $Mn_{0.75}Zn_{0.25}F_2$ [60] and $Fe_{0.5}Zn_{0.5}F_2$ [70] at many fields after zero field cooling yielded $\beta_{ZFC} = 0.2 \pm 0.05$ and $\beta_{ZFC} = 0.13 \pm 0.05$ respectively using an empirical rounded power law. These numbers are significantly smaller than the corresponding values of the pure or random exchange Ising exponent. From an inverse piezomagnetic measurement on $Fe_{0.46}Zn_{0.54}F_2$, Ramos *et al.* [73] obtained $\beta \leq \frac{1}{8}$ at three different fields. An NMR study by Sartorelli [74] on the same crystal also yielded $\beta \approx \frac{1}{8}$. In a neutron scattering study at low random fields, Belanger *et al.* [75] estimated $\bar{\nu} = 1.0 \pm 0.15$, $\bar{\gamma} = 1.75 \pm 0.2$ and $\bar{\eta} \approx \frac{1}{4}$ in the temperature region above T_{eq}, the metastability boundary, in a ZFC measurement. The estimate for the 3d random field heat capacity exponent α is ≈ 0 according to the indirect measurements [61, 66], though more recent studies and direct measurements have indicated $\alpha < 0$ from the observed heat capacity cusps [76, 68, 70].

The random field cross-over exponent ϕ has been determined much more reliably. Assuming the metastability phase boundary observed experimentally scales as $T_N(H)$, one can readily measure ϕ by fitting the apparent transition temperature as a function of the field H according to equation 1.16. This has been performed on $Fe_xZn_{1-x}F_2$ [64], $Mn_xZn_{1-x}F_2$ [63] and $Fe_xMg_{1-x}F_2$ [66, 77] for a series of magnetic concentration x by bulk techniques. These studies yielded a consistent value of ϕ that is system and concentration independent: $\phi = 1.42 \pm 0.03$ [78]. This leads to the ratio $\phi/\gamma_{REIM} =$

1.08 ± 0.05, in good agreement with the theoretical estimate $1.05 \leq \phi/\gamma_{REIM} \leq 1.1$ by Aharony [53]. From neutron scattering experiments, Cowley *et al.* estimated $\phi = 1.5 \pm 0.2$ [71] in $Mn_xZn_{1-x}F_2$, and Belanger *et al.* [79] found $\phi = 1.42$ in $Fe_{0.46}Zn_{0.54}F_2$ for $H \leq 3$T.

Metastability

Since all the experimentally prepared states of 3d DAFF at low temperature - either the long range ordered state established after zero field cooling or the short range ordered state following field cooling - correspond to various metastable local free energy minima, time dependent behavior is expected in each of them. However, relaxation in the RFIM is extremely slow due to the pinning effects of the random fields. Therefore only observations that succeed in measuring the early moments after a change of external conditions (H or T) and covering a long period of time may be able to discern the time dependences.

The earliest indication of the metastability of the field cooled domains was reported by Wong *et al.* who noticed the peak intensity of scattering from $Fe_{0.7}Mg_{0.3}Cl_2$ to increase slightly over time [80]. Following the work by Villain [9] and Grinstein and Fernandez [26] that predicted a logarithmic growth of magnetic domain size for the RFIM, measurements of Faraday rotation [81, 82] and SQUID magnetometry [83, 84] showed the uniform magnetization, immediately after temperature or field quenching, to decay logarithmically over time in $Fe_xZn_{1-x}F_2$. This was interpreted as to reflect expansions of the underlying domains. Only recently has the field cooled domain morphology in $Fe_xZn_{1-x}F_2$ been studied directly by neutron scattering and the theoretical prediction of logarithmic expansion of domain size confirmed. A comprehensive discussion of neutron scattering and magnetometry analysis on the metastable field cooled domain state is presented in Chapter 5.

Unlike the field cooled state, where time dependences can be measured anywhere below the metastability phase boundary except at very low temperatures where the spins are practically frozen due to a finite Ising gap, the metastable behavior in the zero field cooled state is much less obvious. Discernible increase in uniform

magnetization [85] and in neutron scattering intensity [79] were only observed in a narrow temperature region near the transition. This may be an indication of the zero field cooled state being closer to the equilibrium ground state than the field cooled state. Supporting evidence comes from Monte Carlo simulations for 3d RFIM that indicate that the equilibrium state following zero field cooling has long range order except in the transition region, where short range order becomes the deeper free energy minimum [86, 87].

Chapter 2

Samples and Techniques

2.1 DAFF Samples

2.1.1 Structure

The DAFFs studied here are based on two isomorphic 3d Ising antiferromagnets: MnF_2 and FeF_2. The two systems are both of the body centered tetragonal structure. The body centered cation and the corner cation (Mn^{2+} or Fe^{2+}) are each surrounded by six F^- anions forming an octahedron, with the axis of the octahedron rotated by 90° about the [001] direction, making the two cations non-equivalent. Figure 2-1 gives a schematic of a chemical unit cell of MnF_2. Each cell has six ions at the following locations ρ_i: Mn ions at (0,0,0) and $(\frac{a}{2}, \frac{a}{2}, \frac{c}{2})$, F ions at $(au, au, 0)$, $(a-au, a-au, 0)$,$(\frac{a}{2}+au, \frac{a}{2}-au, \frac{c}{2})$ and $(\frac{a}{2}-au, \frac{a}{2}+au, \frac{c}{2})$, where u=0.305 [88]. The reciprocal lattice vectors are given by $\mathbf{G} = 2\pi(\frac{l}{a}, \frac{m}{a}, \frac{n}{c})$ where l, m and n are integers. Therefore the atomic structure factor (nuclear scattering for neutron and charge scattering for x-ray) is

$$S_A(\mathbf{G}) = \sum_i f_i exp(i\mathbf{G}\cdot\rho_i) \tag{2.1}$$

$$= \begin{cases} 2f_{Mn} + 4f_F cos(2\pi ul)cos(2\pi um) & l+m+n = even \\ -4f_F sin(2\pi ul)sin(2\pi um) & l+m+n = odd \end{cases} \tag{2.2}$$

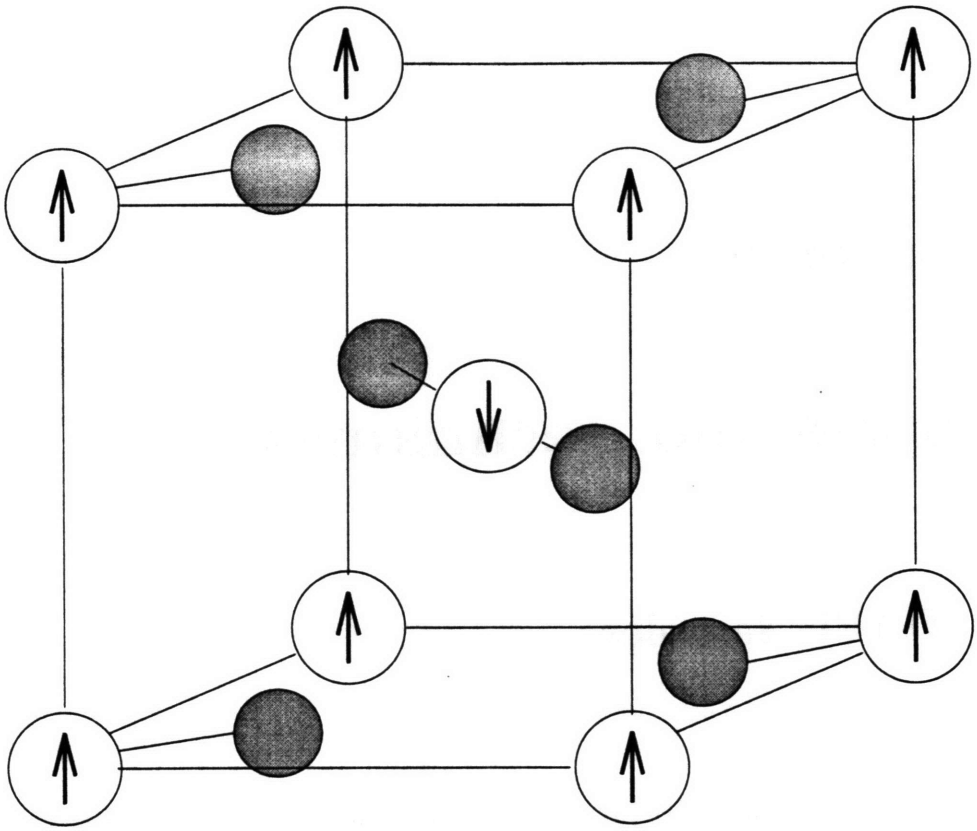

Figure 2-1: Chemical and magnetic cell schematic. Open circles: magnetic cations, i.e. Fe^{++} or Mn^{++}, where the arrows represent the orientation of magnetic moment. Filled circles: F^{-}.

where the sum is over all ions in a unit cell and f_{Mn} and f_F are form factors for Mn and F respectively. Below a certain temperature T_N, the Mn ions order antiferromagnetically so that the body-center Mn moment is anti-parallel to that of the corner Mn ion. The magnetic unit cell is therefore the same as the atomic cell and the magnetic structure factor is

$$S_M(\mathbf{G}) = \sum_i (\pm)_i f_M exp(i\mathbf{G}\cdot\rho_i) = f_M[1 - e^{i\pi(l+m+n)}] \tag{2.3}$$

$$= \begin{cases} 0 & l{+}m{+}n{=}even \\ 2f_M & l{+}m{+}n{=}odd \end{cases} \tag{2.4}$$

All the magnetic neutron and x-ray scattering data presented in this work are taken near the reciprocal lattice vector (100).

The $Mn_xZn_{1-x}F_2$ and $Fe_xZn_{1-x}F_2$ crystals were grown from melt mixtures of MnF_2 or FeF_2 and ZnF_2 using the Czochralski technique. The Zn ions displaces Mn or Fe ions randomly, and the crystal structures and lattice constants of the diluted compounds differ little from the corresponding pure ones. These samples were of outstanding crystallographic quality as x-ray scattering shows a very narrow mosaic spread of 0.04° HWHM for $Mn_{0.75}Zn_{0.25}F_2$ and 0.06° HWHM for $Mn_{0.45}Zn_{0.55}F_2$ and $Fe_{0.5}Zn_{0.5}F_2$.

2.1.2 Magnetism

MnF_2 and FeF_2 are both widely studied 3d Ising antiferromagnets. The exchange energies and the anisotropies have been carefully measured by inelastic neutron scattering experiments. The dominant interaction between the magnetic ions in each system is the antiferromagnetic super exchange between the body centered ion and the corner ion (next nearest neighbor) through the intervening F ions: $J(MnF_2)$ =0.305meV (T_N(MnF2) ≈67.3K [89]); $J(FeF_2)$=0.45meV ($T_N(FeF_2)$ ≈78.4K [90]).

In MnF_2, the Mn^{2+} ion has a $3d^5$ configuration and a ^{6}S ground term with $S = \frac{5}{2}$ whereas in FeF_2, the Fe^{2+} ion has a $3d^6$ configuration and a ^{5}D ground term with $S = 2$. This leads to drastically different magnetic anisotropies in these two systems. The tetragonal crystal structure gives rise to anisotropy through two mechanisms. First, the orbital moment of the magnetic ion is coupled to the crystalline field, which tends to align the spin along the c-axis. Secondly, the dipole-dipole interaction will favor an alignment along the c-axis because c ≈ $\frac{2}{3}$a. For MnF_2, the orbital moment is quenched and therefore the uniaxial anisotropy is mostly due to the weak dipole-dipole interaction at approximately 1% of the exchange. The zone center spin-wave gap is approximately 1meV [91]. In FeF_2, the octahedral crystal field removes the orbital degeneracy and spin-orbit coupling and spin-spin interaction further removes the spin degeneracy, giving rise to a strong uniaxial crystal field anisotropy $D \approx 0.84$meV for a spin Hamiltonian of the form $\mathcal{H} = \sum_{i,j} J\mathbf{S}_i \cdot \mathbf{S}_j + \sum_i DS_i^{z2}$ [92]. The zone center spin-wave gap is 6.5meV, much larger than that of MnF_2. FeF_2andMnF_2 have been widely studied as model 3d Ising magnets with strong and weak Ising anisotropies.

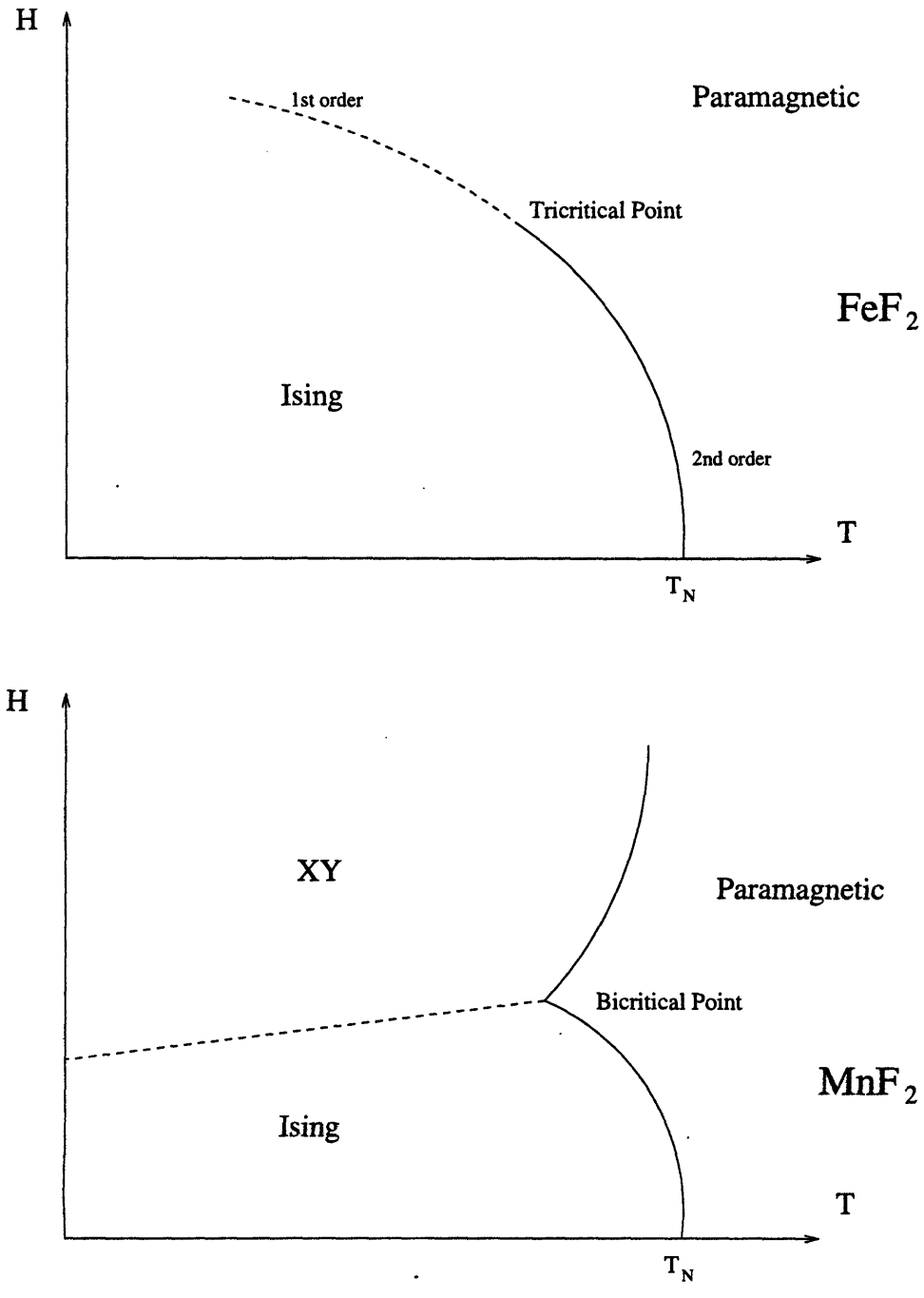

Figure 2-2: Schematic of phase boundaries of FeF_2 and MnF_2.

The different anisotropies in FeF_2 and MnF_2 have a direct bearing on their respective phase diagrams, as shown schematically in Figure 2-2. As the field applied along the c-axis increases, MnF_2 goes from the Ising phase into a spin-flop phase through a first order transition, where the spins lie largely perpendicular to the field with a small canting favored by energy. The phase boundaries meet at a bicritical point and have been carefully mapped out by Shapira *et al.* [52] and King *et al.* [93]. For FeF_2, however, the strong anisotropy suppresses the spin-flop state and the Ising phase persists into high fields where the second order phase boundary eventually converts into one which is first order through a tricritical point. It thus behaves as a metamagnet.

The dilution of the magnetic ions with non-magnetic ones such as Zn and Mg has nontrivial effects on the nature of the magnetic phase transitions. In zero applied field, the antiferromagnetic transition persists with T_N being depressed with increasing dilution until the percentage of magnetic ions, x, reaches the percolation threshold x_p. Based on simple geometric arguments, x_p=0.245 for a 3d system of the body-centered structure. For $x < x_p$, the magnetic ion density is so small that an infinite network of ions linked by exchange can not be sustained and the transition to long range order is thus destroyed. For $x_p < x < 1$, the transition temperature varies roughly linearly with the dilution, i.e. $T_N(x) \approx T_N(x - x_p)/(1 - x_p)$. However, the most important effect of the dilution is the crossover from pure 3d Ising to random exchange Ising universality class which has a rather different set of critical exponents and critical amplitudes.

Applying an external field that is parallel to the uniaxial anisotropy to a randomly diluted antiferromagnet causes the system to crossover further into the 3d random field Ising universality class [48]. Much work has been done on various types of DAFF using many different techniques to study the RFIM; yet the observed behavior has been so intriguing and complex that the problem is still not well understood. The phase transition in a DAFF is drastically different from that in a pure Ising system or a random exchange Ising system in zero field. In the next chapter, we will discuss in detail the anomalies that surfaced in studies of RFIM critical behavior and present a phenomenological conjecture that may shed some light on the nature of the phase

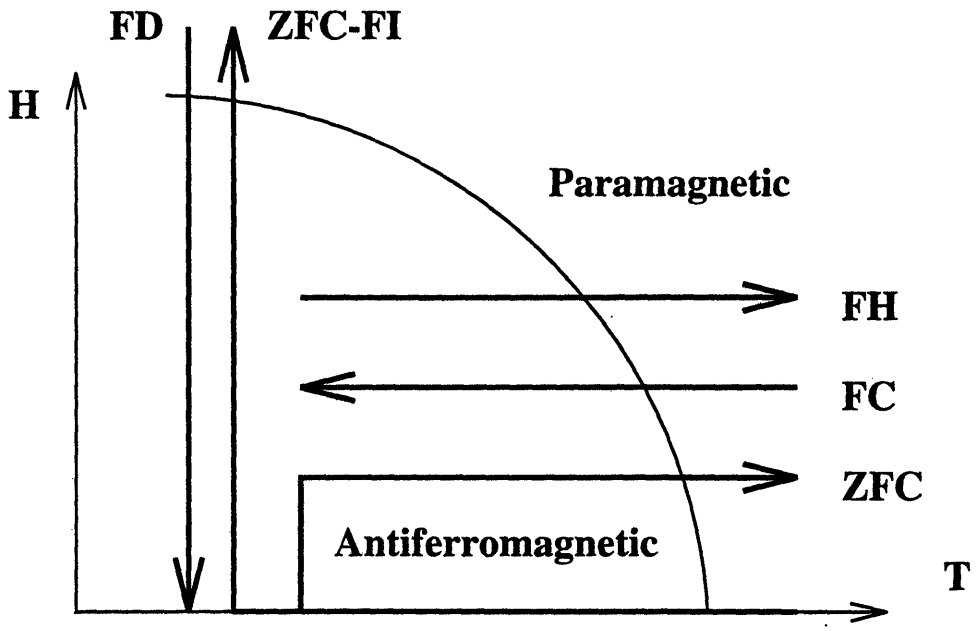

Figure 2-3: Schematic of the various experimental protocols applied in the study of DAFFs.

transition in RFIM.

2.2 Experimental Protocols

Figure 2-3 defines the various experimental protocols used in the current study. The importance of applying different protocols in studying the DAFFs is manifested by the strong hysteretic effects present in these systems. The hysteresis makes it difficult to compare experiments to theory and has led to some long standing controversies in interpreting various experimental findings. At the same time, it also provides clues to the reconciliation of these controversies.

2.3 Experimental Techniques

2.3.1 Magnetic Neutron Scattering

Principle

The technique of neutron diffraction has proven to be an extremely effective probe for studying condensed matter. Its wide application in physics is due to the unique properties of neutrons: neutrons interact with nuclei in matter through nuclear forces and with magnetic moments through interaction between neutron's moment and the orbital motion and spin of electrons. The nuclear and magnetic scattering processes can be differentiated by using polarized neutrons. Equally importantly, the thermal neutrons produced at research reactors possess wavelengths of the order of 2Å and energies of the order of 10meV, comparable to lattice spacings and excitation energies found in solids. The accessible wavevector and energy transfer are typically $0.05\text{Å}^{-1} < Q < 15\text{Å}^{-1}$ and $0.1\text{meV} < \hbar\omega < 100\text{meV}$. Neutron scattering is therefore an ideal tool for measuring both spatial and temporal correlations. In the study of magnetism, magnetic phase transitions in particular, neutron scattering has been indispensable not only in directly measuring magnetic configurations but also in the accurate determination of critical exponents.

We first review the general principle of magnetic neutron scattering technique which measures the differential scattering cross section. Consider a scattering process in which a neutron with wavevector $\mathbf{k}$ and spin μ is scattered by a magnetic ion from the state $|\mathbf{k}, \mu>$ into the state $|\mathbf{k}', \mu'>$. The corresponding initial and final states of the magnetic ion are ζ and ζ'. The energy and momentum loss of the neutron are defined as

$$\hbar\omega = \frac{\hbar^2}{2m_n}(k^2 - k'^2) = E - E' \tag{2.5}$$

$$\hbar\mathbf{Q} = \hbar(\mathbf{k} - \mathbf{k}') \tag{2.6}$$

Let $V(\mathbf{r})$ denote the interaction between the neutron spin and the moment of a magnetic ion. The probability of such an event is, in the first Born approximation

(valid when the average interaction energy is small compared with the kinetic energy of the neutron),

$$\frac{2\pi}{\hbar}|<\zeta',\mu'|\frac{1}{L^3}\int d\mathbf{r}e^{i\mathbf{Q}\cdot\mathbf{r}}V(\mathbf{r})|\zeta,\mu>|^2\delta(\hbar\omega+E_\zeta-E_{\zeta'}) \tag{2.7}$$

where L^3 is the volume of the sample. The number of neutrons scattered into the solid angle $d\Omega'$ with momentum between $\hbar k'$ and $\hbar(k'+dk')$ is $\frac{k'^2dk'd\Omega'}{(2\pi/L)^3}=\frac{m_nL^3k'}{8\pi^3\hbar^2}d\Omega'dE'$. The incident neutron flux is $\frac{\hbar k}{m_nL^3}$. Therefore the differential scattering cross section, after summing over the final states ζ' and μ' as well as averaging over the initial states ζ and μ with probability P_ζ and P_μ respectively, is

$$\frac{d^2\sigma}{d\Omega'dE'}=\sum_{\zeta,\mu}P_\zeta P_\mu\sum_{\zeta',\mu'}\frac{k'}{k}(\frac{m_n}{2\pi\hbar^2})^2|<\zeta',\mu'|V|\zeta,\mu>|^2\delta(\hbar\omega+E_\zeta-E_{\zeta'}) \tag{2.8}$$

Since the orbital momentum of electrons is quenched in many materials - especially for most transition metal ions - one may consider only the spin-spin interaction. Define s as the spin of an individual electron. The magnetic moment of neutron is $\frac{\gamma e\hbar}{m_nc}\mu$ with $\gamma=-1.91$. Then the matrix element in the cross section becomes

$$<\zeta',\mu'|V|\zeta,\mu>=\frac{4\pi\mu_B\gamma e\hbar}{m_nc}<\zeta',\mu'|\sum_i[\mathbf{s}_i\cdot\mu-(\mathbf{s}_i\cdot\mathbf{Q})(\mu\cdot\mathbf{Q})/Q^2]exp(i\mathbf{Q}\cdot\mathbf{r}_i)|\zeta,\mu>. \tag{2.9}$$

After the following algebra: (a) rewrite $\delta(\hbar\omega+E_\zeta-E_{\zeta'})$ as $\frac{1}{2\pi}\int dt(exp[i(\omega+(E-E')/\hbar)t])$; (b) based on the Wigner-Eckart theorem, the sum over all electrons in the sample $<\zeta'|\sum_i\mathbf{s}_iexp(i\mathbf{Q}\cdot\mathbf{r}_i)|\zeta>=\sum_nF(\mathbf{Q})exp(i\mathbf{Q}\cdot\mathbf{r}_n)<\zeta'|\mathbf{S}_n|\zeta>$ where n sums over all atoms, $F(\mathbf{Q})=\sum_l s_lexp(i\mathbf{Q}\cdot\mathbf{r}_l)$ which sums over electrons of a single ion is the magnetic form factor, and $\mathbf{S}$ is the total spin of an ion such that its magnetic moment is $g\mu_BS$; (c) sum over neutron spins for unpolarized neutron beam, one then arrives at the following expression for the differential cross section

$$\begin{aligned}\frac{d^2\sigma}{d\Omega'dE'} &= (\frac{\gamma e^2}{m_ec^2})^2\frac{k'}{k}(\frac{1}{2}gF(\mathbf{Q}))^2\sum_{\alpha,\beta}(\delta_{\alpha\beta}-Q_\alpha Q_\beta/Q^2)\\ &\quad\frac{1}{2\pi}\int dte^{i\omega t}\sum_{\mathbf{r}}<S_0^\alpha(0)S_{\mathbf{r}}^\beta(t)>e^{i\mathbf{Q}\cdot\mathbf{r}}\end{aligned} \tag{2.10}$$

excluding a Debye-Waller factor accounting for thermal vibrations. α and β are the Cartesian components of $\mathbf{Q}$. The central part of the cross section in the integral in equation 2.10 is the temporal and spatial Fourier transform of the correlation function of spin pairs in a sample. The bracket <> represent thermal average at a given temperature, so that $< S_0^\alpha(0) S_r^\beta(t) >$ is the probability of finding the β-component to be $S_r^\beta(t)$ for the spin at position $\mathbf{r}$ and time t given the α-component to be $S_0^\alpha(0)$ for the spin at origin and time 0.

In the experimental situation that concerns us, consider an ordered state in which magnetic moments are aligned in the uniaxial c (longitudinal) direction. During a neutron scattering scan, one measures the cross section by scanning the spectrometer along a trajectory in reciprocal space. Near a particular reciprocal lattice vector $\mathbf{G}$, letting $\mathbf{q} = \mathbf{Q} - \mathbf{G}$, the cross section we are concerned with is the $\mathbf{Q}$-dependent part of $\frac{d^2\sigma}{d\Omega' dE'}$

$$\mathcal{S}(\mathbf{Q},\omega) = \frac{k'}{k} F(\mathbf{Q})^2 \sum_{\alpha,\beta} (\delta_{\alpha\beta} - Q_\alpha Q_\beta / Q^2) \frac{1}{2\pi} \int dt e^{i\omega t} < S^\alpha(\mathbf{Q},t) S^\beta(-\mathbf{Q}) > \quad (2.11)$$

For a pure magnetic system, $\mathcal{S}$ is conveniently separated into a Bragg term

$$F(\mathbf{G})^2 (1 - G_z^2/G^2) < S >^2 \delta(\mathbf{q}) \delta(\omega) \quad (2.12)$$

which is a delta function whose amplitude is proportional to the square of the order parameter, and a diffuse term

$$\frac{k'}{k} \sum_{\alpha,\beta} (\delta_{\alpha\beta} - Q_\alpha Q_\beta / Q^2) \frac{1}{2\pi} \int dt e^{i\omega t} [< S^\alpha(\mathbf{Q},\mathrm{t}) S^\beta(-\mathbf{Q}) > - < S^\alpha(\mathbf{Q}) >< S^\beta(-\mathbf{Q}) >]$$
$$\sim \frac{k'}{k} \sum_{\alpha,\beta} (\delta_{\alpha\beta} - Q_\alpha Q_\beta / Q^2) \coth(\hbar\omega / 2k_B T) \chi''_{\alpha\beta}(\mathbf{Q},\omega)$$

where $\chi''_{\alpha\beta}(\mathbf{Q},\omega)$ is the imaginary part of the generalized susceptibility and gives the absorption spectrum of the system being studied. This is the fluctuation-dissipation theorem. As is apparent from the Kramers-Kronig relations that link χ' and χ'', the susceptibility may thus be obtained by integrating over energy (which is readily

achieved with the double-axis scattering arrangement). The neutron diffuse scattering directly measures these quantities. This is one of the main reasons why neutron scattering plays such an important role in studying magnetism.

For a pure uniaxial magnet, the susceptibility $\chi(\mathbf{q})$ can be further separated into a longitudinal part $\chi_L(\mathbf{q})$ and a transverse part $\chi_T(\mathbf{q})$. Therefore the energy-integrated $\mathbf{q}$-dependent intensity commonly used is [94]

$$\begin{aligned} \mathcal{S}(\mathbf{Q}) &= M^2\delta(\mathbf{q}) + \chi(\mathbf{q}) && (2.13) \\ &= c_1 M^2 \delta(\mathbf{q})\sin^2\phi + c_2[(\sin^2\phi)\chi_L(\mathbf{q}) + (1+\cos^2\phi)\chi_T(\mathbf{q})] && (2.14) \end{aligned}$$

where $\mathbf{M} =< \mathbf{S} >$ is the appropriate order parameter and ϕ is the angle between $\mathbf{Q}$ and the crystallographic c axis. c_1 and c_2 are prefactors that absorb the numerical factors and the form factor in the cross section. The intensity of the Bragg reflection is proportional to the squared order parameter, whereas the critical scattering gives the wave vector dependent susceptibility $\chi(\mathbf{q})$. χ_L and χ_T can be studied separately with different diffraction geometry and are generally described by Lorentzian functions in the Ornstein-Zernike approximation.

In an actual neutron scattering experiment, the energy and wave vector resolution are finite due to non-monochromatic neutron beam, imperfectly defined collimation, finite wave vector acceptance and mosaicity of the crystals. Therefore the measured intensity for a momentum transfer $\mathbf{Q}$ and energy transfer $\hbar\omega$ is the above calculated $\mathcal{S}(\mathbf{Q},\omega)$ convoluted with the resolution function $R(\mathbf{Q},\omega)$,

$$I(\mathbf{Q},\omega) = \int R(\mathbf{Q}'-\mathbf{Q},\omega'-\omega)\mathcal{S}(\mathbf{Q},\omega)\mathrm{d}\mathbf{Q}'\mathrm{d}\omega' \qquad (2.15)$$

The resolution function can be measured around a Bragg point as the Bragg scattering cross section is a delta function in $\mathbf{q}$ as well as in ω. For energy-integrated scattering, such as that achieved in two-aixs geometry, the convolution in the data analysis only needs to involves integration over the wave vector.

Structure Factor for RFIM

When quenched random disorders are introduced into a magnetic system, Grinstein, Ma and Mazenko (GMM) [95] were the first to point out the emergence of a new purely static spin-spin correlation function whose existence is unique to the random systems. They also showed this term to be proportional to the square of the dynamic susceptibility. For a random magnet such as a DAFF, considering longitudinal components only, the **q**-dependent structure factor near a reciprocal vector **G** is essentially

$$\mathcal{S}(\mathbf{q}) = [< S_L(\mathbf{q}) S_L(-\mathbf{q}) >] \tag{2.16}$$

where S_L is the spin component that is parallel to the order parameter $\mathbf{M} = [< \mathbf{S} >]$. Here <> denotes the usual thermal average at a specified temperature under a specified distribution of impurities or random fields; [ ] denotes the configurational average over the quenched random variables. This structure factor can now be separated into three terms,

$$\mathcal{S}_L(\mathbf{q}) = M^2\delta(\mathbf{q}) + \chi_L(\mathbf{q}) + C^{(s)}(\mathbf{q}) \tag{2.17}$$

The first term is again the usual Bragg peak giving a measure of the long range order. The second term is still the longitudinal spin correlation function as seen before, with the configurational average added,

$$\chi_L(\mathbf{q}) = [< S_L(\mathbf{q}) S_L(-\mathbf{q}) > - < S_L(\mathbf{q}) >< S_L(-\mathbf{q}) >] \tag{2.18}$$

It is also called the connected susceptibility. The function $C^{(s)}(\mathbf{q})$ is the GMM term, or the disconnected susceptibility, and it measures the fluctuations in the local quenched magnetization $m(\mathbf{q}) =< S_L(\mathbf{q}) >$,

$$C^{(s)}(\mathbf{q}) = [m(\mathbf{q})m(-\mathbf{q})] - M^2\delta(\mathbf{q}). \tag{2.19}$$

This term does not appear in the transverse part of the structure factor.

In a pure system, one obviously has $C^{(s)} = 0$. But in a system with quenched

disorder, whether it be random exchange or random fields, $C^{(s)}$ is not necessarily zero. Instead, as was first shown by GMM and later developed for diluted magnets and the random field problem by Kogon and Wallace [96], Lovesey [97], Kaufman and Kardar [98], Pelcovits and Aharony [99], $C^{(s)}(\mathbf{q}) = \chi_L^2(\mathbf{q})D(\mathbf{q})$ where $D(\mathbf{q})$ is a wave-vector dependent amplitude factor. In the mean-field theory, $D(\mathbf{q}) = \Delta M^2$ where Δ is a measure of the strength of the randomness. For the RFIM, $[h(x)h(x')] = \Delta\delta(x - x')$ where $h(x)$ is the site-random field at x. In general, to leading order in an Ising system, $C^{(s)}(\mathbf{q})$ is expected to be of a squared Lorentzian form. This term has been successfully applied to describe neutron scattering data on several DAFFs [100, 101, 67, 102, 103, 71]. The essential difference between the Lorentian and the Lorentzian-squared contributions to the cross section is that the former is dynamic while the latter is static. It has been shown that the static Lorentzian-squared intensity can be isolated from the dynamic Lorentzian susceptibility with a neutron scattering energy resolution of ~0.1meV [72, 104, 71]. Such high energy resolution may be achieved in a triple-axis scattering geometry.

Therefore the general form of the cross section used in interpreting neutron scattering profiles on RFIM systems is [105]

$$\mathcal{S}(\mathbf{Q}) = C\delta(\mathbf{q}) + \frac{B}{\kappa^2 + q^2} + \frac{A\kappa}{(\kappa^2 + q^2)^2} + \frac{B_T}{{\kappa_T}^2 + q^2}. \tag{2.20}$$

For the most commonly studied DAFFs, $\mathbf{q} = \mathbf{Q} - (100)$ expressed in reciprocal lattice units. The second term corresponds to the longitudinal dynamic susceptibility. κ is the inverse correlation length and B/κ^2 is the amplitude of this term. The third term is the Lorentzian-squared term arising from static fluctuations in the quenched random fields. Written this way, A is the integrated intensity of this term. The last term corresponds to the transverse dynamic susceptibility χ_T. It is clear that in order to separate χ_T from χ_L, one has to measure susceptibility around a reciprocal point $(00L)$. In principle, the transverse intensity at (100) can be subtracted by dividing the intensity observed at (001) by one-half (θ factor) and multiplying by the ratio of the form factors $|f(\mathbf{G} = (100))|^2/|f(\mathbf{G} = (001))|^2$. As Mitchell *et al.* pointed out,

the actual scaling factor is more complicated due to the asymmetric sample shape and differing scattering angle in the (100) and (001) directions [103]. They presented alternative ways of measuring this factor. In practice, because the DAFF systems we study all possess uniaxial anisotropy in the c direction, the transverse susceptibility is generally small compared to the longitudinal one. Further, B_T and κ_T vary only slowly with temperature and do not exhibit critical behavior [103]. Therefore neglecting the transverse term in $\mathcal{S}(\mathbf{Q})$ does not introduce any significant error.

In the actual data analysis for $H \neq 0$T, neutron scans are fitted by $\mathcal{S}(\mathbf{Q})$ convoluted with the instrumental resolution. For a two-axis setup satisfying the quasielastic condition [106], $\mathcal{S}(\mathbf{Q})$ includes the long range order term, longitudinal susceptibility and static fluctuations. For a triple-axis setup with sufficient energy resolution set for zero energy transfer, $\mathcal{S}(\mathbf{Q})$ includes the long range order term and the static fluctuations. In zero field, the scattering profile can be satisfactorily accounted for without the Lorentzian-squared term [103].

Experiments and Data Analysis

Figure 2-4 shows a schematic of the triple-axis neutron diffraction geometry. An appropriate energy is selected of the thermal neutrons emerging from the reactor vessel by a graphite monochromator. A pyrolitic graphite filter removes neutrons of higher energy that come from higher order scattering at the monochromator. The spatial resolution is further enhanced by the horizontal collimators. In the triple-axis geometry, a graphite analyzer selects a suitable energy for the outgoing neutrons scattered from the sample. High spatial and energy resolution can be arranged with this setup in order to study carefully the static lineshapes with the dynamic contribution excluded from the cross section. Triple-axis setup is used in studying time-dependence of magnetic domains, where an accurate measurement of the domain size is essential. In the two-axis geometry, the detector is positioned at a desired angle to collect outgoing neutrons without an analyzer. Although this geometry defines the direction of $\mathbf{k}'$, it does not define its magnitude and therefore the scattering process registers neutrons with different $\hbar\omega$. In order that this scattering geometry yields results that

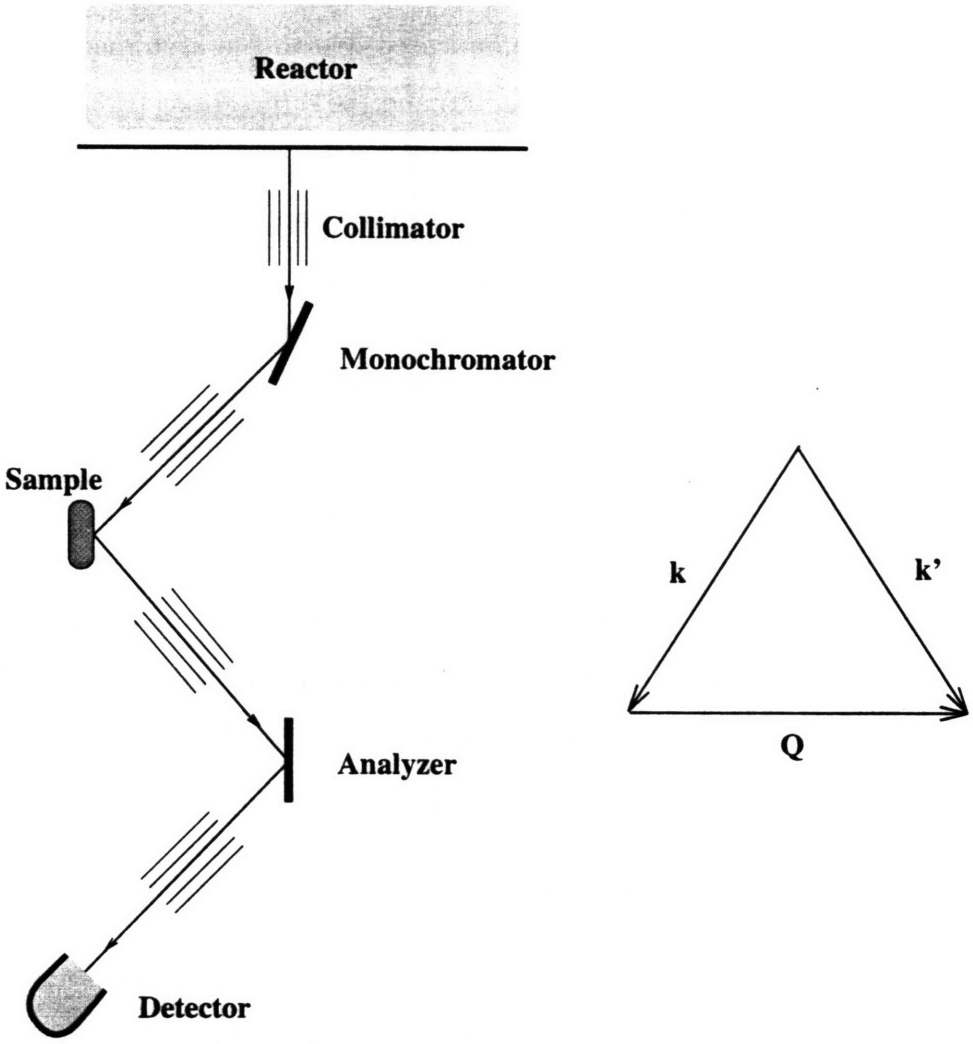

Figure 2-4: Schematic of Triple-Axis Neutron Diffraction Geometry.

are simple to interpret, the energy spread (described by the spectral shape function) should be small compared to the neutron energy and the resulting **q** spread should be small compared to the inverse correlation length of the system being studied. At temperatures close to T_C where the ω spread does indeed becomes very narrow, the scattering process is therefore almost elastic. This is the quasielastic approximation. Figure 2-5 shows a transverse two-axis neutron scan that exhibits all the Bragg, static Lorentzian-squared and dynamic Lorentzian components as described by equation 2.20.

During the experiments, the sample is mounted with c-axis vertical and parallel to the field direction. The alignment with the field is better than 3°. The sample is

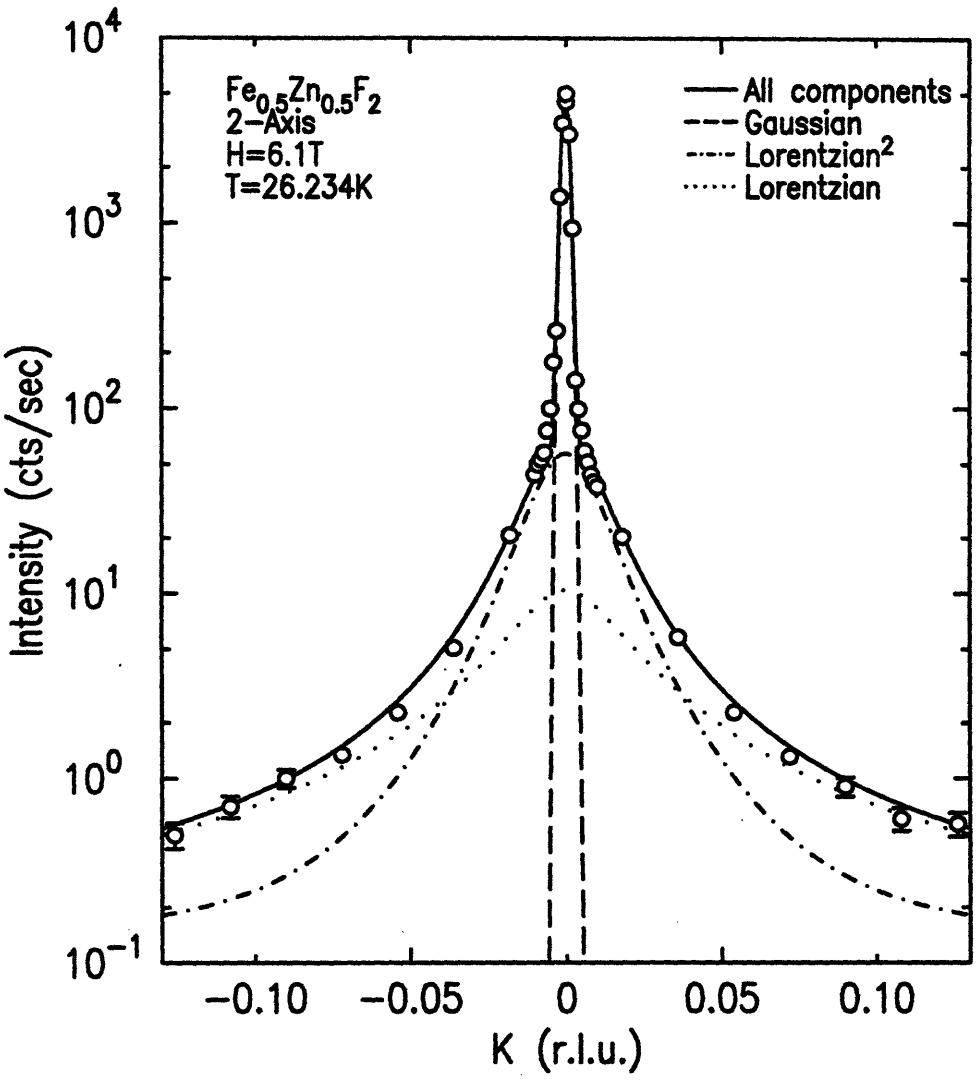

Figure 2-5: Components of a two-axis transverse neutron scan across the (100) magnetic peak.

cooled by He gas flow. Since the Carbon glass sensor is mounted inside the magnet and not in contact with the sample through a good thermal conductor, there may be a small temperature gradient between the sample and the sensor. Further, this gradient may vary depending on the level of liquid He in the cryostat. Therefore this arrangement may cause the measured transition temperature to differ by several tenths of a degree from experiment to experiment and between neutron measurements and other techniques.

Figure 2-6 compares 2-axis neutron scattering parameters at 0T and 6.1T taken on a sample of $Fe_{0.5}Zn_{0.5}F_2$. The 6.1T data were taken under zero field cooling (ZFC).

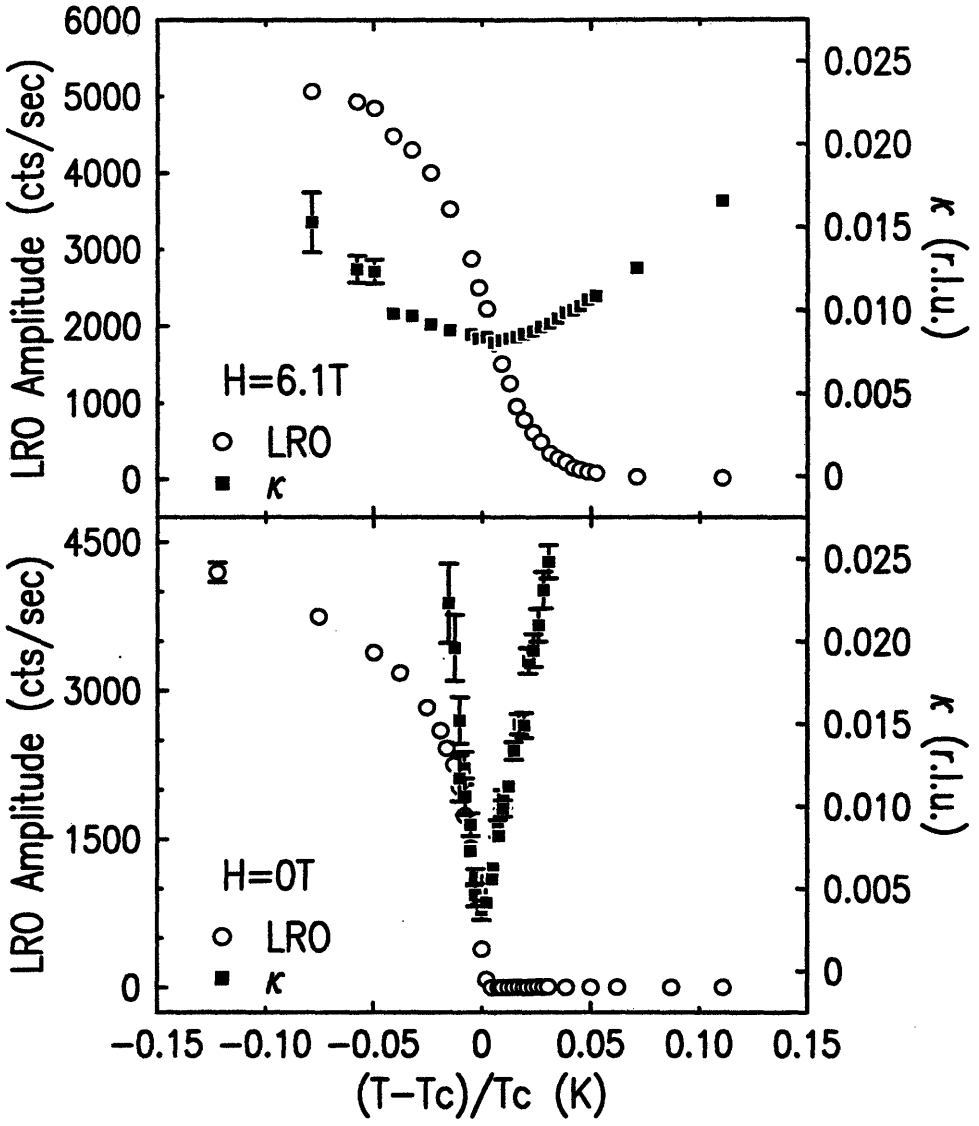

Figure 2-6: Comparison between 0T and 6.1T neutron parameters: LRO and κ.

The effects due to the presence of random fields are dramatic. The data are shown with T_C subtracted from the temperatures at both fields to facilitate comparison. Although there is long range order (LRO) at low temperature in both fields, the order parameter at 6.1T diminishes in a completely different fashion from a conventional second order transition, showing a smeared transition from the antiferromagnetic to the paramagnetic phase. Concordantly, the inverse correlation length, κ, while approaching zero in zero field reflecting a divergence of the spin-spin correlation length, displays severe broadening at 6.1T around a temperature T_C at which it reaches a

non-zero minimum (or a maximum in correlation length). Much can be learned about the transition of the RFIM from such studies, as will be discussed in the next chapter.

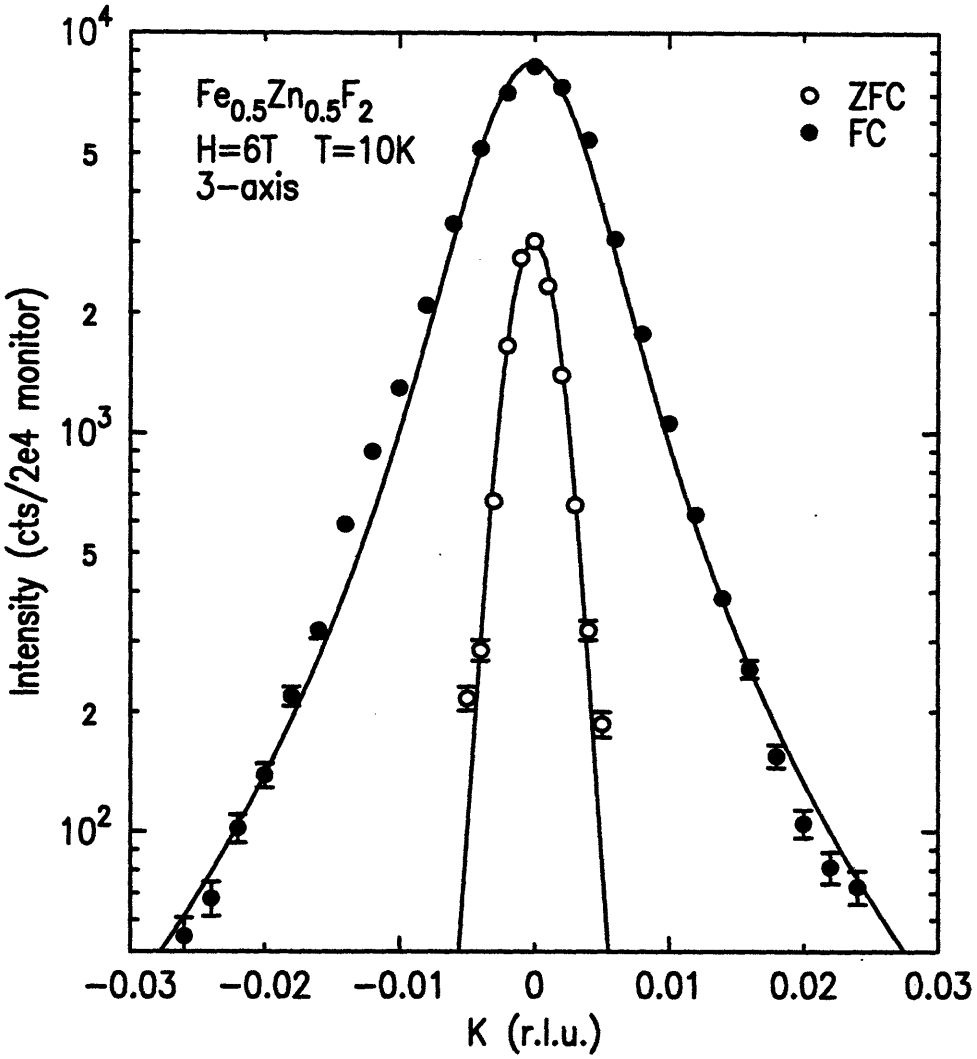

Figure 2-7: Hysteresis between ZFC and FC neutron scans.

Figure 2-7 is the most revealing demonstration of the strong hysteresis in the RFIM. It shows two scans at (100), both taken at H=6T and T=10K on a sample of $Fe_{0.5}Zn_{0.5}F_2$, one following the ZFC procedure and the other field cooling (FC). The ZFC lineshape is a resolution limited Gaussian peak representing long range magnetic order. The FC lineshape does not show a resolution limited central peak. The peak is much broader, suggesting a short range ordered (SRO) state. It is also higher in intensity because the extinction affects the ZFC state much more severely than the FC state. This finding, reported first in the early 80's, was most perplexing

and made it virtually impossible to identify the equilibrium lower critical dimension of the RFIM. The cause of such hysteresis, as will be discussed in greater detail in the following chapter, is the presence of a complex distribution of free energy minima and the anomalously slow critical dynamics. Related hysteretic effects can also be observed with other techniques, as are shown below.

2.3.2 Magnetic X-Ray Scattering

Principle

Immediately after their discovery by Wilhelm Conrad Röntgen in 1895, x rays became one of the most useful imaging tools known to humankind. In the next one hundred years, x rays have found wide applications in many aspects of our lives and have tremendously advanced our understanding of various states of matter through their interaction with electrons. X-ray spectroscopy enabled the nondestructive determination of chemical composition of samples through x-ray spectra which led to the completion of the periodic table before all the elements had been chemically separated. In crystallography, x-ray diffraction from powder or single crystal samples is the standard tool for structural characterization. X rays also elucidated the photon-electron interactions by making possible accurate comparisons between theory and experiments. In condensed matter physics, x-ray diffraction provides direct measurements of the electronic density-density correlation function which is essential in the study of phase transitions [107, 108].

Being an electro-magnetic wave, x rays interact with matter both electronically and magnetically. Charge x-ray scattering, arising from x rays interating with electronic charge, is the basis for mapping the electronic charge density distribution in matter and characterizing atomic and crystallographic structures. Such interaction is now well understood and the diffraction technique has been thoroughly treated by Warren [109]. The advent of synchrotron x-ray sources and their accompanying brilliance, high resolution and wave-length tunability has brought new applications of x-ray diffraction and spectroscopy. Among these is magnetic x-ray scattering which

originates from the interaction between x rays and the magnetic moments of electrons. The first calculation of the cross section for photons scattering from free charges that included magnetic interactions was done by Low [110] and Gell-Mann and Goldberger [111] in 1954. Sixteen years later, Platzman and Tsoar [112] worked out similar calculations and suggested studying magnetic properties in matter by means of x-ray scattering. In 1972, de Bergevin and Brunel while examining an NiO sample with a conventional x-ray source observed magnetic reflections with an intensity 10^7 times weaker than the charge Bragg reflection.

Detailed calculations of the magnetic x-ray scattering cross section has been given by Blume [113] and Blume and Gibbs [114]. The derivation of the cross section and its close relations with the magnetic correlation function partially parallels that of magnetic neutron scattering, though the different nature of the photon-electron interaction gives important ramifications that are affect the x-ray experiments. The weak photon-electron interaction is well suited for the Born approximation. First-order and second-order perturbation expansions, which contains both charge and magnetic terms, reveal that the magnetic scattering intensity is suppressed by many orders of magnitude compared to that of charge scattering. The ratio of the respective cross section of magnetic and charge scattering is

$$\frac{\sigma_{mag}}{\sigma_{charge}} = (\frac{h\nu}{mc^2})^2 \frac{N_m^2}{N^2} \frac{f_m^2}{f^2} < S >^2 \tag{2.21}$$

where ν is the x-ray frequency, m the electron mass, N_m the number of magnetic electrons per atom, N the number of electrons per atom and f_m and f the magnetic and charge form factors respectively. For 10keV x rays scattering off Fe atoms, this ratio is

$$\frac{\sigma_{mag}}{\sigma_{charge}} = 4{\times}10^{-6} < S >^2 . \tag{2.22}$$

Such low intensity renders traditional x-ray sources, such as rotating anode and tube generators which provide $\sim 10^6$/s after-monochromator photon flux, ineffective in studying magnetic scattering. Synchrotron x-ray sources, with its tremendous brilliance ($\sim 10^{12}$/s after-monochromator flux) and tunable energy, have opened up a

new era of magnetic x-ray scattering. Magnetic Compton scattering studies are now carried out at x-ray energies up to 100keV. Magnetic resonant scattering, suggested by Blume [113] in the second-order perturbation treatment of the photon-electron interaction, enables enhancement of scattering intensity by several orders of magnitude when the incoming x-ray energy is tuned to an excitation edge in the sample elements. This enhancement effect has been observed near the L-edges of rare earth elements and the M-edges of actinides and has made resonant scattering a useful tool in studying magnetic phase transitions in rare earth materials. However, the resonance enhancement is insignificant near the K-edge of transition ions such as Fe and Mn.

Because the energy scale of thermal fluctuations in magnetic systems is negligible compared to the experimental x-ray energy which is typically of the order of several keV to several tens of keV, x-ray detectors normally pick up both Bragg scattering and inelastic scattering even with an analyzer. X-ray scattering is thus similar to double-axis neutron scattering. However, x-ray scattering generally has spatial resolution far better than that of neutron scattering. For instance, x-ray scattering experiments on $Fe_{0.5}Zn_{0.5}F_2$ generally achieved 4×10^{-4}r.l.u. longitudinal and 5×10^{-5}r.l.u. transverse resolution, compared to approximately 4×10^{-3}r.l.u. longitudinal and 2×10^{-3}r.l.u. transverse with neutrons. This high resolution makes it very difficult to discern magnetic diffuse scattering with x rays.

In practice, the magnetic x-ray scattering cross section is similar to that of neutron scattering,

$$\mathcal{S}(\mathbf{Q}) = C\delta(\mathbf{q}) + \frac{A\kappa}{(\kappa^2+q^2)^2} + \frac{B}{\kappa^2+q^2} + \frac{B_T}{{\kappa_T}^2+q^2}. \tag{2.23}$$

The static random field fluctuations generally dominate over the dynamic fluctuations, and therefore the Lorentzian terms are much smaller in amplitude compared to the Lorentzian squared. The x-ray scans can be adequately fitted by using only the first two terms in equation 2.23. For zero field cooling data, where the spins are largely long range ordered, only the δ-function term is observable. Upon field cooling, both terms are present at lower fields, while at higher fields only a Lorentzian squared

profile can be observed.

One feature of magnetic x-ray scattering is that the orbital and spin contributions to the magnetic moment have different polarization dependencies. This further differs from neutron scattering and makes it possible to study these contributions separately [108]. Another important difference between neutron scattering, which is a bulk technique suffering from extinction effects, and x-ray scattering is in the penetration depth. Although x rays have small scattering cross section and therefore do not suffer from extinction, strong absorption reduces typical x-ray penetration depth to several microns. For example, the penetration depth in $Fe_{0.5}Zn_{0.5}F_2$ for x-rays of energy 9.58keV is 3.5μm. This makes x rays sensitive to effects peculiar to the near-surface region in a sample. On the other hand, the small illuminated volume helps to reduce side effects that stem from concentration gradient in a DAFF.

Experiments

All the magnetic x-ray scattering experiments discussed here were carried out on beam line X20 at the National Synchrotron Light Source at Brookhaven National Laboratory. The samples were mounted inside an Oxford superconducting magnet fitted with Be and aluminized mylar windows for the passage of x rays. The configuration of the beam lines, the horizontal four-circle spectrometer and the magnet has been described in detail by Hill[108]. The sample is cooled by He gas that flows from the liquid He reservoir and through an adjustable needle valve. A heater and a carbon glass thermometer is embedded in a copper block that couples to the copper sample mount to ensure good thermal conductivity. Generally, a double-crystal Ge(111) monochromator and a single Ge(111) analyzer is used in the experimental set-up.

Besides requiring an accurate line-up, the x-ray experiments were made particularly difficult by the presence of multiple charge scattering. As an example, at the magnetic (100) peak, although pure charge scattering is symmetry forbidden, one may observe a combined charge scattering of (011) and $(1\bar{1}\bar{1})$. This does not present a problem for neutron scattering experiments because the neutron charge and mag-

netic diffractions have comparable intensity. In x-ray scattering, however, multiple scattering with intensity on the order of one-millionth of direct charge scattering is enough to inundate the magnetic signal (no more than 300 counts per second at 200mA synchrotron ring current) with noise [108]. Therefore, it is necessary to adjust painstakingly the incoming x-ray energy and rotate the sample about the momentum transfer **Q** in order to minimize multiple scattering intensity. The resulting multiple scattering contamination is generally between 0-20 counts per second for each set-up. In studying the magnetic peak intensity as a function of temperature, we assume that the multiple scattering intensity does not change with temperature at least for the temperature range we are interested in , i.e. 10K-40K. This is verified by the two K scans taken on $Mn_{0.45}Zn_{0.55}F_2$ as shown in figure 2-8. The figure depicts a multiple scattering background at E=9.3keV and T=20K, above T_C, which displays several peaks at and about (100). The scan at T=8K, below T_C, shows the magnetic peak sitting on top of essentially the same multiple scattering background.

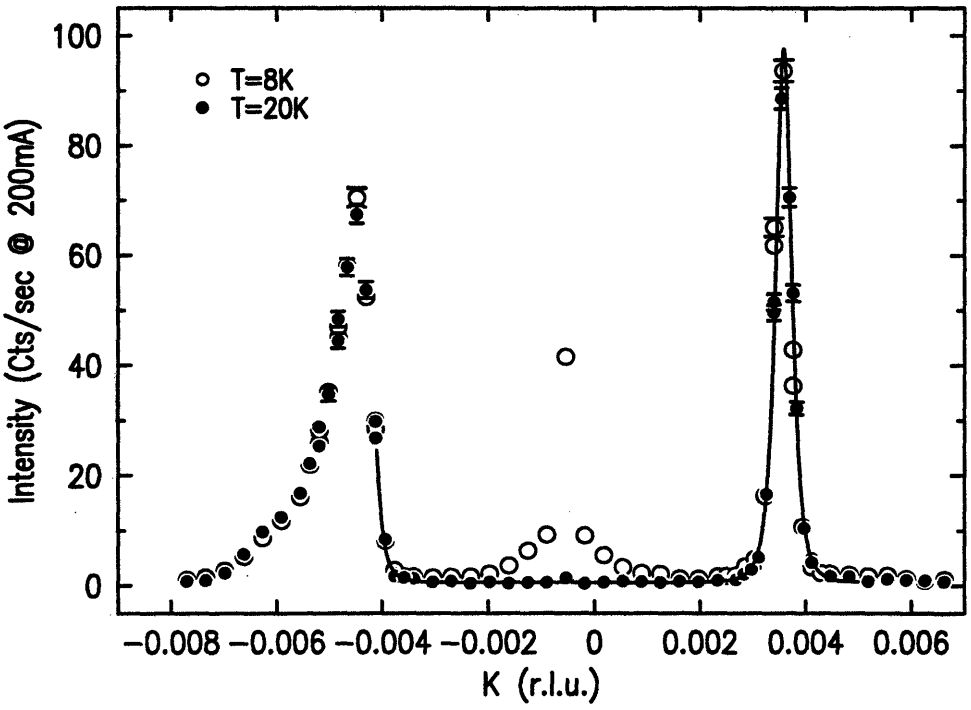

Figure 2-8: X-ray multiple scattering above and below T_C(1.5T) in $Mn_{0.45}Zn_{0.55}F_2$.

Figure 2-9 shows the temperature dependence of the fitted peak intensity at H=0T

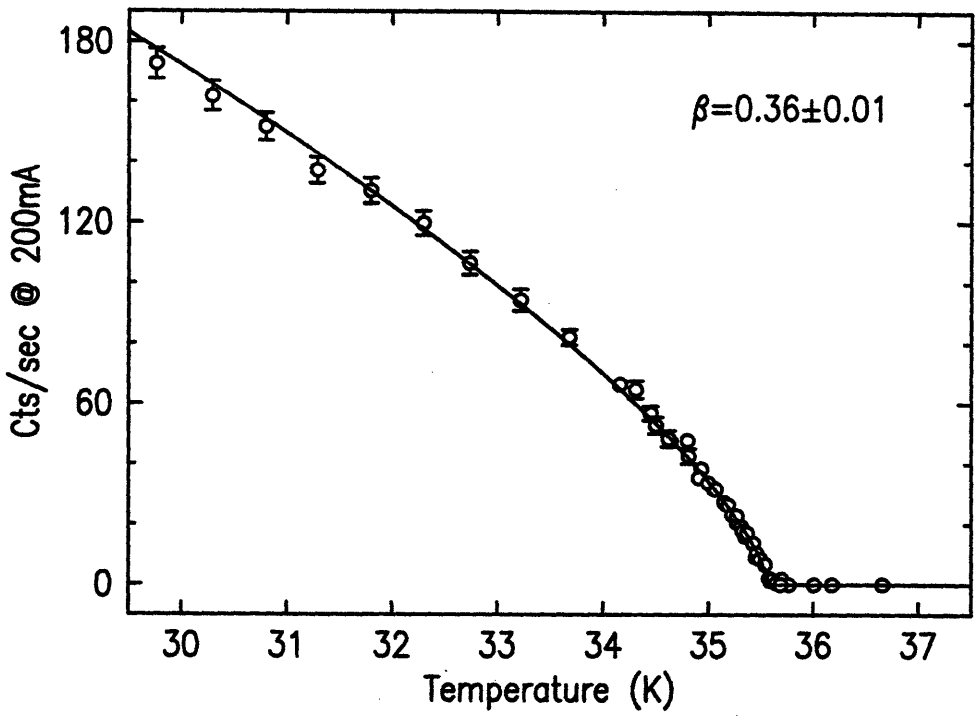

Figure 2-9: Fitted peak intensity of (100) magnetic peak of $Fe_{0.5}Zn_{0.5}F_2$ by x rays. The multiple scattering background has been subtracted in each scan before the fits.

taken on a sample of $Fe_{0.5}Zn_{0.5}F_2$. In general, it has been found that the peak profile can be best described by a Lorentzian squared in the H direction and a simple Lorentzian in the K direction. The use of these function forms is purely empirical. The peak intensity is proportional to the sublattice magnetization M_S squared, and because of its extinction-free nature, x rays therefore give an ideal measure of the order parameter. Fitted to a simple power law, we obtain an exponent $\beta = 0.36 \pm 0.01$, in excellent agreement with the value $\beta_{RE} = 0.35 \pm 0.01$ predicted for the random exchange Ising model. Order parameter studies in applied fields reveal properties of the RFIM that are qualitatively different from the REIM. This will be discussed in detail in the next chapter.

2.3.3 SQUID and High-Field Magnetometry

Principle

Uniform magnetization $M(\mathbf{Q} = 0)$ probes the thermal properties of a magnetic system. Although it can not give a direct measure of the order parameter for a simple ferromagnet, its usefulness in studying antiferromagnetic systems comes from the close relationship between the uniform longitudinal susceptibility χ and the magnetic heat capacity. This relation was first carefully treated and formulated by Fisher [115].

For a simple antiferromagnet, one in which there are two interpenetrating antiparallel sub-lattices and interaction only exists between adjacent neighbors, the zero field uniform susceptibility may be written as (taking z as the longitudinal direction)

$$\chi(T) = \frac{N\mu^2 g^2}{kT} \sum_i < S_0^z S_i^z > \tag{2.24}$$

where N is the total number of spins on the lattice, μ is the Bohr magneton, g is the gyromagnetic ratio, S is the total spin of the magnetic ion and the bracket denotes the thermodynamic mean. Let $G_0(T) = \sum_i < S_0^z S_i^z >= \sum_i w_i(T)$ be the zero wave-vector spin-spin correlation function such that $w_i(T)$ represents the correlation between the spin at the origin and its ith neighbor, Fisher showed that, to a first approximation, the leading contribution to G_0 is $1 - |w_1(T)|$ or more generally

$$G_0(T) \approx 1 - p|w_1(T)| \tag{2.25}$$

where w_1 describes correlation between adjacent spins on opposite sub-lattices and $p = p(T)$ is a slowly varying function of order unity.

On the other hand, the magnetic configurational energy for the Ising model is simply

$$E_M(T) \approx NqJ < S_0^z S_1^z >= NqJw_1(T) \tag{2.26}$$

where q is the number of nearest neighbors. Thus an approximate relation between

$\chi(T)$ and $C_m(T) = \frac{\partial E_M(T)}{\partial T}$ can easily be established:

$$C_m(T) \approx \frac{q|J|f}{g^2\mu^2}\frac{\partial(T\chi)}{\partial T} \tag{2.27}$$

where f is a relatively slowly varying function of temperature of order unity in the transition region that absorbs all the approximations made in arriving at this relation.

Equation 2.27 is the basis of all uniform magnetization studies of phase transitions in antiferromagnets. Its validity in zero field for pure antiferromagnets has been demonstrated by experiments on MnF_2 and MnO [116]. Similar arguments have been given for other indirect means of measuring magnetic heat capacity, i.e. temperature derivatives of linear magnetic birefringence ($d(\Delta n)/dT$) and capacitance ($d\epsilon/dT$) [117]. However, its applicability in studying an antiferromagnet with quenched disorder such as a DAFF is unclear. Although the above relation between χ and C_m should still hold for a diluted antiferromagnet in zero field, as shown by Wong [69], it becomes invalid in non-zero field even for a pure antiferromagnet. According to Fisher, a small uniform applied field H shifts the transition temperature T_N by an amount δH^v, so that the magnetization is approximately $M(T) \sim HG_0(T + \delta H^v)/T \sim H[1-p|w_1(T+\delta H^v)|]/T$. Thus $\chi(T,H) = \frac{\partial M(T,H)}{\partial H} \sim \frac{G_0}{T} - v\delta p H^v \frac{\partial w_1}{\partial T}$. The second term in the susceptibility expression is proportional to the heat capacity. Therefore $\frac{\partial(T\chi)}{\partial T}$ in a small field will yield a stronger divergence ($t^{-1-\alpha}$) than $C_m \sim t^{-\alpha}$ (or a narrow peak at T_N superimposed on the zero-field heat capacity).

For a DAFF where there is both dilution and non-zero magnetic field are present, the situation is more complicated (for example, the disconnected susceptibility is no longer zero) and it is doubtful the simple Fisher relation between χ and C_m is still maintained. We will re-examine this point later. However, the uniform magnetization M is still useful for at least two purposes. First, the $\frac{\partial(T\chi)}{\partial T}$ anomaly still defines the transition temperature between the antiferromagnetically ordered phase and the paramagnetic phase, and second, M provides an independent way of measuring magnetic domains other than diffraction.

Techniques and Experiments

We first briefly describe the techniques of superconducting quantum interference device (SQUID) magnetometry and vibrating sample magnetometry (VSM). Other techniques commonly used in measuring uniform magnetization include Faraday rotation.

SQUIDs are the most sensitive detectors of magnetic fields. The commercial dc SQUID magnetometer used in the measurements is manufactured by Quantum Design and has a sensitivity down to 10^{-7}emu. This sensitivity is adequate for measuring the samples of $Mn_{0.45}Zn_{0.55}F_2$ and $Fe_{0.5}Zn_{0.5}F_2$ used in this study for which the magnetization of interest ranges from 10^{-3}emu to approximately 2emu (the SQUID saturates at 2.5emu). During the measurement, the sample is translated through a pickup loop and the change of magnetic flux creates a current in the pickup loop. The current then flows to the SQUID input coil and produces a flux in the SQUID. The dc SQUID consists of two Josephson junctions with a bias current and is essentially a flux-to-voltage transducer. As the sample moves through the pickup loop, the flux through the SQUID varies, periodically changing the critical current in the Josephson junctions and producing a periodic swing of voltage across the SQUID. Each period of the voltage swing corresponds to variation of one flux quantum through the SQUID. Therefore by measuring the number of voltage swing periods during each sample movement, one measures the exact change of magnetic flux through the SQUID which is proportional to the change of current in the input coil and the pickup loop and is in turn proportional to the magnetization of the sample. With proper calibration, absolute magnetization can be obtained of any sample[118].

The Quantum Design SQUID is capable of producing any field from -5.5T to 5.5T and temperature down to 2K at a stability better than 0.05K. The field corrected Ge sensor is positioned about 18cm from the center of the field and is calibrated by the manufacturer. Magnetization can be conveniently measured as a function of temperature or field. Figure 2-10 shows a representative M vs. T measurement at H=2T on a sample of $Mn_{0.45}Zn_{0.55}F_2$. The derivative $\frac{dM}{dT}$ is plotted in the bottom panel and shows a cusp, indicating a phase transition. A series of M vs. T measurements

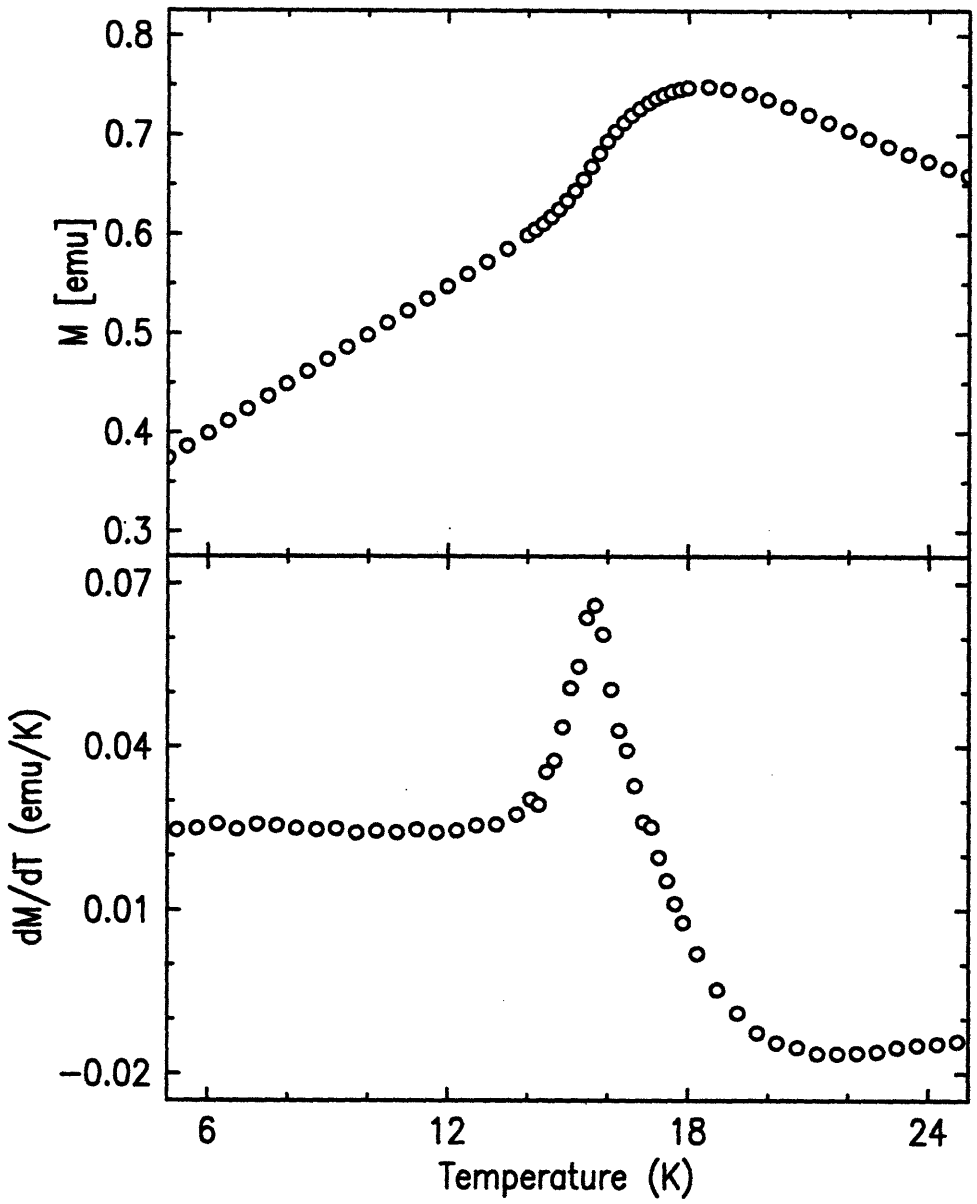

Figure 2-10: Upper panel shows uniform magnetization of $Mn_{0.45}Zn_{0.55}F_2$ at H=2T, measured by SQUID with increasing temperature after cooling in zero field to T=5K and raising the field to H=2T. Lower panel shows temperature derivative of M which displays a peak at T=15.7K signaling the crossing from the antiferromagnetic to the paramagnetic phase.

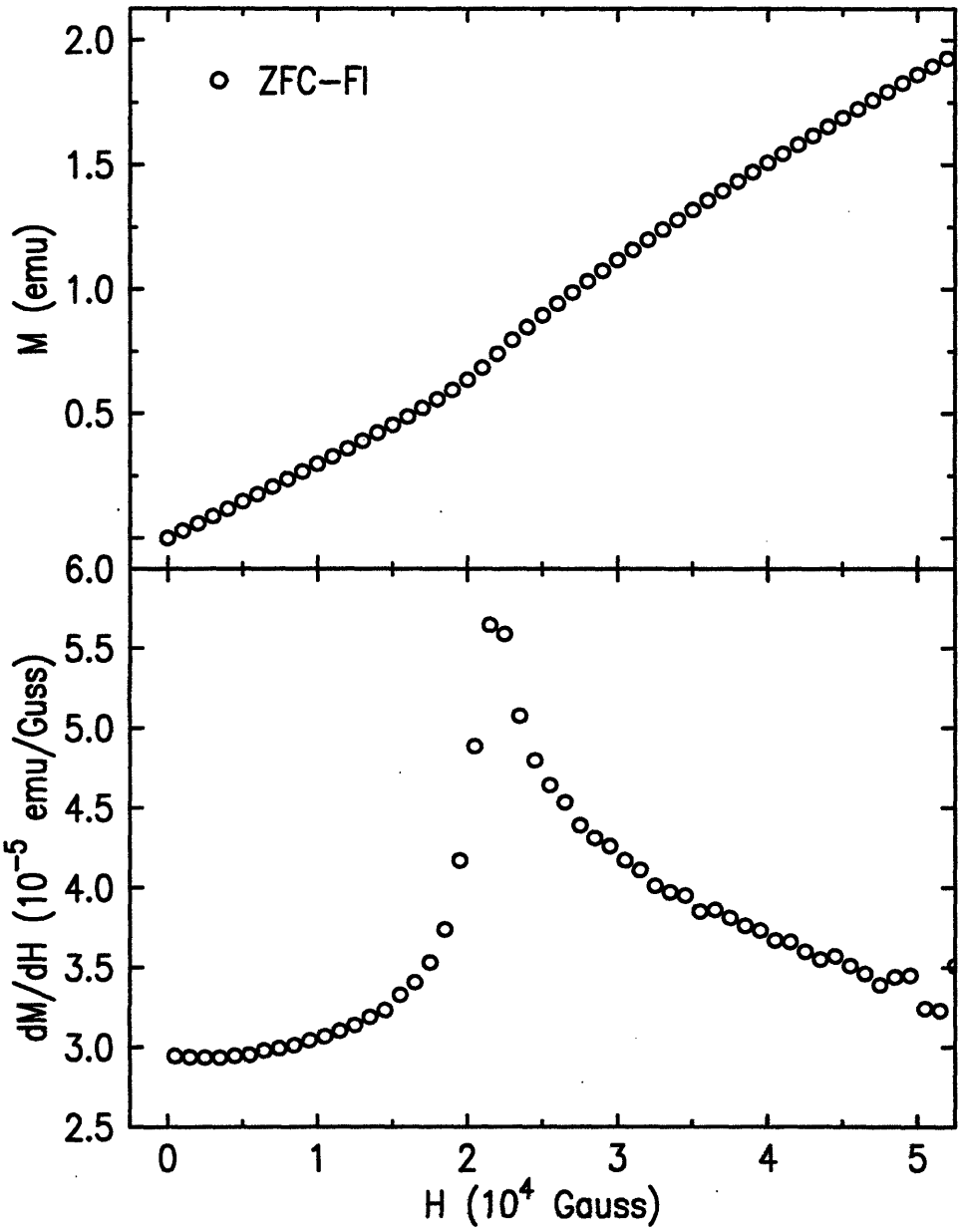

Figure 2-11: Upper panels shows uniform magnetization of $Mn_{0.45}Zn_{0.55}F_2$ at T=15K, measured by SQUID with increasing field after cooling in zero field through T_N to T=15K. Lower panel shows field derivative of M which displays a peak at H=2.15T signaling the crossing from the antiferromagnetic to paramagnetic phase.

at many fields can map out the phase boundary in the $H-T$ plane. One can also measure M vs. H at a constant temperature, as shown in figure 2-11. The $M-H$ curve is practically linear except for the region near the phase boundary. The derivative $\frac{dM}{dH}$ exhibits a peak similar to that of $\frac{dM}{dT}$ and provides an alternative way to study the phase boundary.

The VSM experiments were carried out at the Francis Bitter Magnet Lab where the vibrating sample magnetometry technique was developed by Foner *et al* [119, 120]. In a VSM experiment, the sample is attached by Duco cement to a rod of soft glass driven by a speaker operating at a constant sound frequency of 73.3Hz. The sample is positioned at the center of a water-cooled Bitter magnet capable of magnetic fields between -20T and 20T. The vibration of the sample induces a signal in the pickup loop that is proportional to the magnetization. The advantage of these measurements is that high magnetic fields of up to 20T can be accessed to complement data taken at relatively low fields with the SQUID. However, the VSM technique has two shortcomings - significantly greater measurement noise (making it suitable only for strongly magnetic samples) and less sophisticated temperature control. Thus all the data were taken in the M vs. H mode. The field can be swept from 0T to 20T with step $\Delta H \approx 0.07T$ at a specified rate as fast as 5 minutes. Each datum point is an average of many readings within one second.

Figure 2-12 shows VSM M vs. H data with increasing field after cooling in zero field to T=17.2K . Taking the field derivative of magnetization reveals a broad peak centered about 8.6T. Figure 2-13 shows data taken at a series of temperatures following the same procedure. These experiments provide approximate estimates for the transition fields and enable us to extend the measurable phase boundary. Figure 2-14 shows the complete phase boundary down to 10K measured with both the SQUID and the VSM technique. The agreement between the two sets of data is excellent.

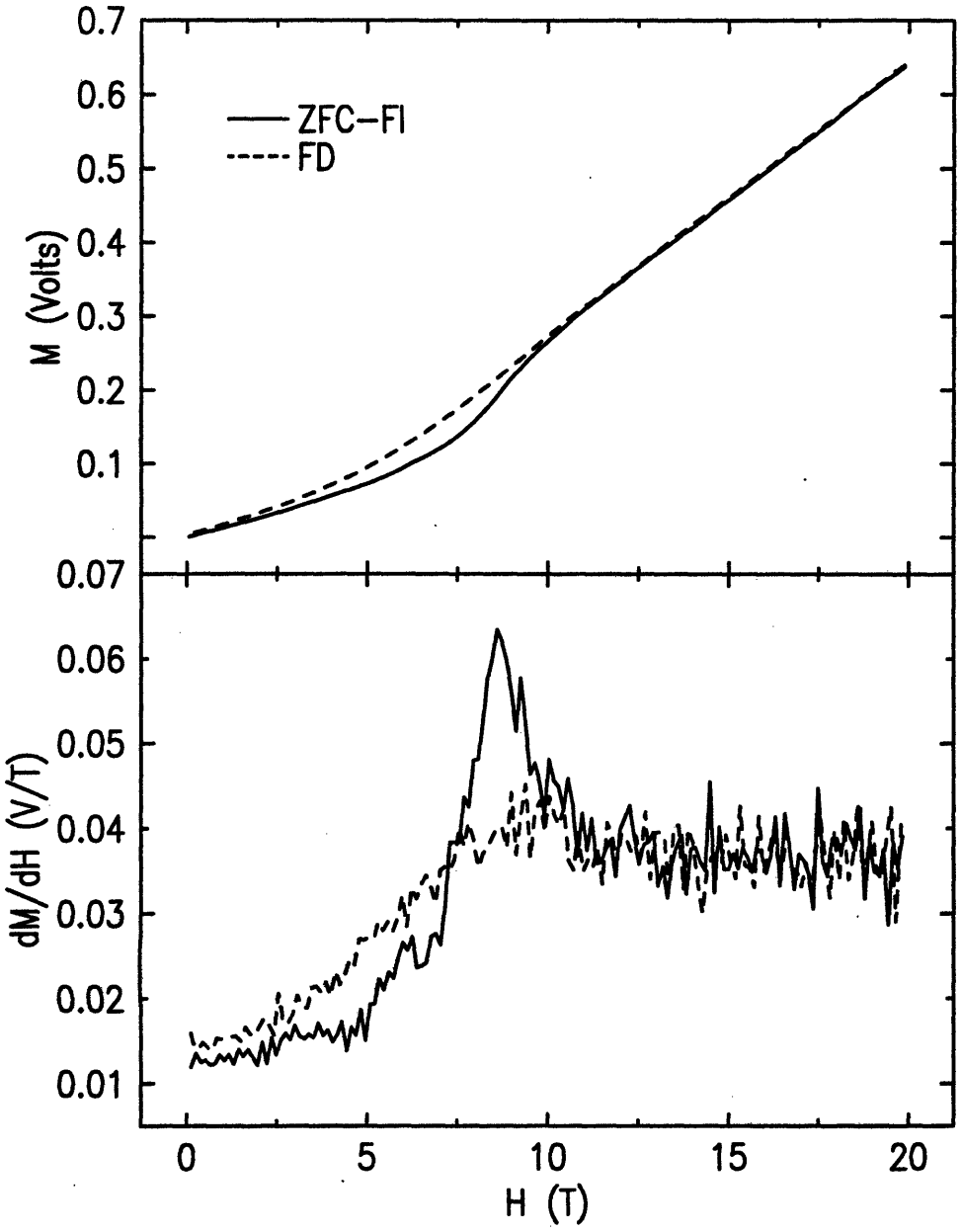

Figure 2-12: Upper panels shows uniform magnetization of $Fe_{0.5}Zn_{0.5}F_2$ at T=17.2K, measured by VSM with increasing field after cooling in zero field through T_N to T=17.2K (ZFC-FI) followed immediately by lowering field(FD). Lower panel shows field derivative of M which displays a peak at H=8.6T for the ZFC-FI data. Strong hysteretic effects are apparent.

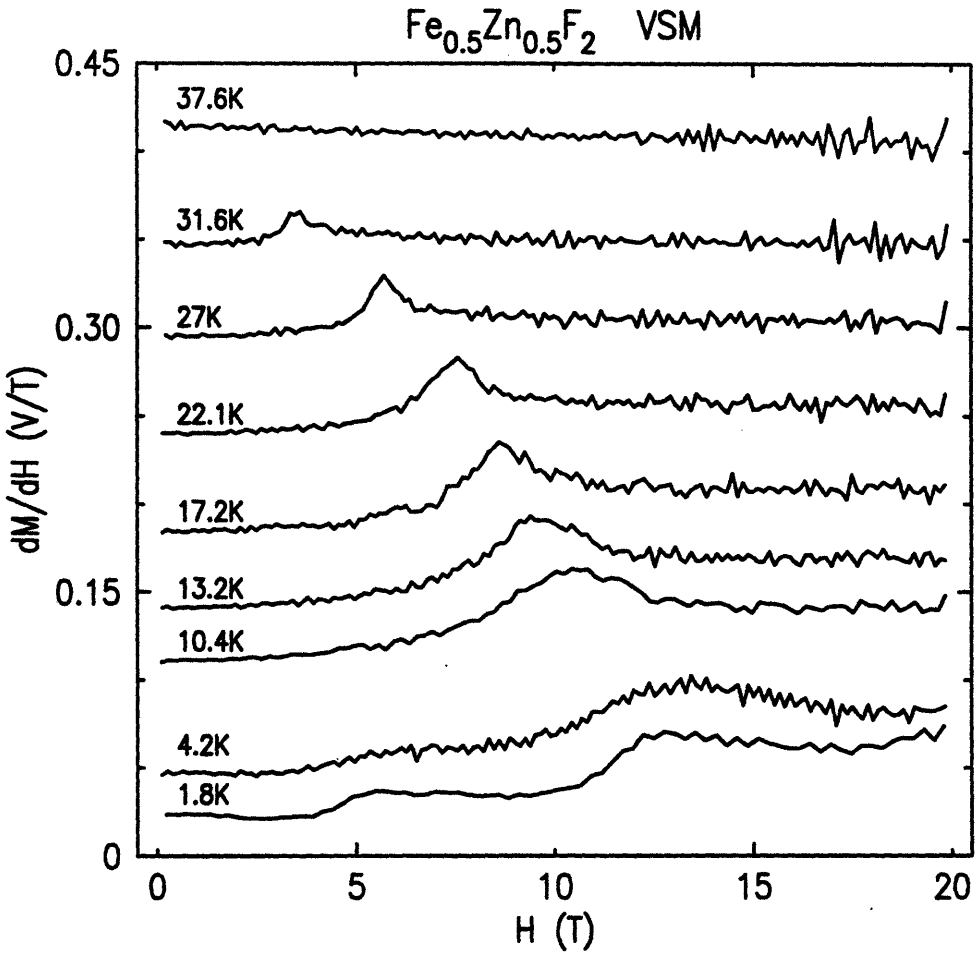

Figure 2-13: $\frac{dM}{dH}$ measured by VSM at a series of temperatures down to 1.8K. Each data set is shifted by adding the product of 0.01 and the temperature at which the magnetization is measured. A conspicuous cusp at temperatures above 4.2K signify the AF-PM transition. The data at 37.6K are completely in the paramagnetic phase.

2.3.4 Semi-Adiabatic Calorimetry

Principle

The direct heat-pulse semi-adiabatic technique is used in the heat capacity measurements. Data were taken on $Mn_{0.75}Zn_{0.25}F_2$ and $Fe_{0.5}Zn_{0.5}F_2$. The $Mn_{0.75}Zn_{0.25}F_2$ crystal measures approximately 2mm×2mm×7mm and weighs 0.19349g. The $Fe_{0.5}Zn_{0.5}F_2$ crystal measures approximately 6mm×5mm×2.5mm and weighs 0.430915g.

The calorimeter consists of a Cernox temperature sensor and a strain gauge heater both mounted on a sapphire plate (10mm×10mm×0.25mm) using Stycast 1266 epoxy. The $Mn_{0.75}Zn_{0.25}F_2$ crystal was attached to the sapphire plate with Dow Corning

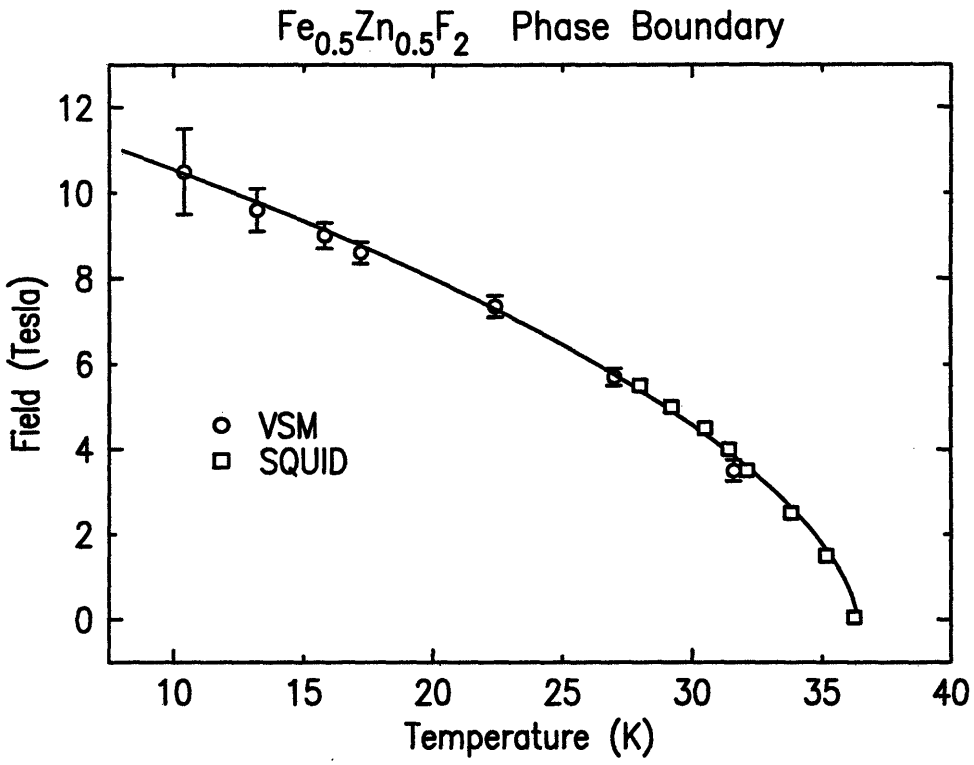

Figure 2-14: Phase boundary of $Fe_{0.5}Zn_{0.55}F_2$ measured by SQUID and VSM.

silicone high vacuum grease and tied down with a piece of cotton string, while the $Fe_{0.5}Zn_{0.5}F_2$ crystal was epoxied to the sapphire plate. Good thermal contact between the samples and all components of the calorimeter was manifested in the short internal equilibration time. The Cernox resistance was calibrated against a known platinum thermometer in zero field and a capacitance thermometer in the field. The magnetic field-induced errors were negligibly small. For instance, between H=0T and H=8T at T=46K, the Cernox resistance drifted less than 0.1% which corresponds to an error that is less than 0.03K. The calorimeter hung on four sets of Kevlar strings from an enclosing copper can that provided a constant ambient temperature. The advantage of the Kevlar strings is that they have low elasticity and a very thin strand can be used to support strong tension. This helped to minimize the thermal conductivity between the calorimeter and the copper can, which is essential for semi-adiabatic measurements. It also means the calorimeter could be tied down rigidly in order to avoid any movement of the sample under the magnetoelastic forces. Two twisted pairs of 0.001" Manganin wires were used on each of the Cernox sensor and

the strain gauge heater for four-wire measurements of their respective resistance. The calorimeter is surrounded by a vacuum better than 10^{-4}torr. For part of the experiment on $Mn_{0.75}Zn_{0.25}F_2$, the copper can enclosing the calorimeter was attached to the insert of an Oxford Instrument cryomagnetic system capable of a 10T field. A wire heater maintained the copper can at a desired temperature. For the rest of the measurements on $Mn_{0.75}Zn_{0.25}F_2$ and all the measurements on $Fe_{0.5}Zn_{0.5}F_2$, the copper can was mounted inside a Quantum Design Physical Property Measurement System (PPMS) capable of a 9T field and the can temperature could be accurately controlled by the PPMS.

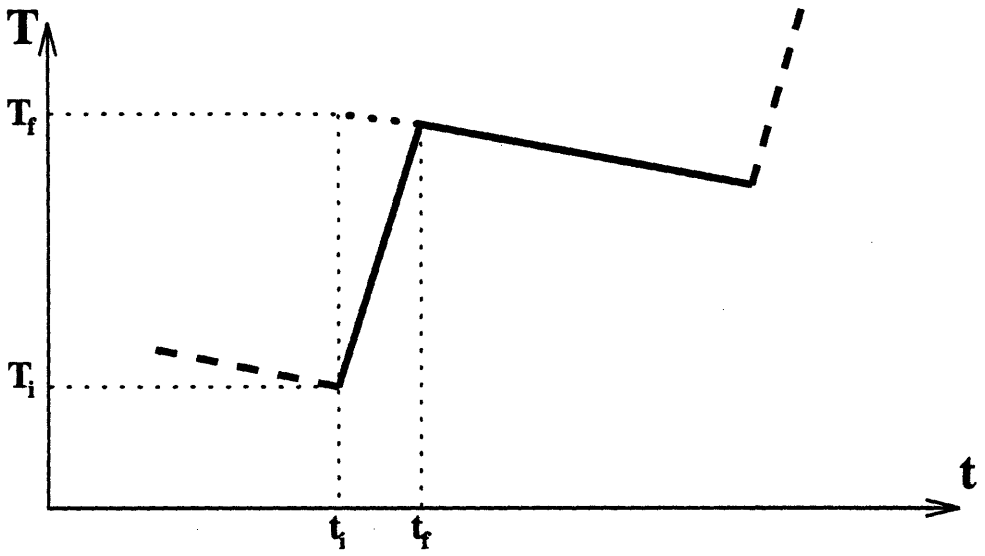

Figure 2-15: Schematic of semi-adiabatic heat pulse technique

The semi-adiabatic heat pulse technique is conceptually simple . The data acquisition procedure is schematically depicted in figure 2-15. A high precision current source connected to the strain gauge heater generated a heat pulse for a duration from t_i to t_f (normally a few seconds) that was clocked by the computer. After several seconds of equilibration time, the sample temperature was recorded repeatedly by the Cernox as it slowly drifted towards the ambient temperature. The drift was approximately linear due to the large thermal mass of the sample and the small heat loss from the calorimeter to its environment. The drift normally took 10-15 seconds, followed by the next heat pulse. As the heat pulse-drift cycle repeated, the sample temperature

progressively shifted upward or downward in a sawtooth fashion, controlled by the heat input and the duration of the drift. The quasi-linear temperature drift after each heat pulse was extrapolated backward to obtain T_f, a temperature that would have been reached by the calorimeter had the heat pulse been applied instantaneously. Taking the end temperature of the previous drift as the initial temperature T_i, the total heat capacity C of the sample and the calorimeter at temperature $T = \frac{T_i + T_f}{2}$ was calculated as $C = \frac{\Delta E}{T_f - T_i}$, where ΔE is the energy generated in the strain gauge heater during the heat pulse. As the temperature was raised, ΔE had to be increased accordingly to account for the general increase in the total heat capacity. C was measured in various temperature and field cycles. Most of the data presented here were taken following ZFC, FC and field heating (FH) protocols.

The total heat capacity C includes contributions from the magnetic heat capacity C_m of the sample, the lattice phonons of the sample and all other components of the calorimeter. Since we are only interested in C_m, the rest needs to be subtracted from C. The heat capacity of the calorimeter (without the sample) was measured separately and was found to be field-independent. The contribution from the phonon heat capacity can only be calculated through the corresponding states approximation proposed by Stout and Catalano [121], using the known heat capacity of ZnF_2. The corresponding states principle is based on the assumption that isomorphous compounds such as $ZnF_2, MnF_2, FeF_2, NiF_2$, etc. share a common temperature-dependent functional form for their lattice entropy, $S(\text{lattice}) = \Phi(T/\theta)$, and lattice heat capacity, $C_p(\text{lattice}) = (T/\theta)\Phi'(T/\theta)$, where Φ is the same function for all the compounds and θ is a characteristic temperature that differs for each compound. In order to establish a quantitative relationship between the lattice entropy and heat capacity of ZnF_2 and the magnetic compounds, one makes the following observation. From some temperature sufficiently above the Néel temperature up to room temperature, the splitting of the orbital states by the electrostatic crystalline fields (of tetragonal geometry in the case of MnF_2 and FeF_2) is large compared to kT which in turn is large compared to the splitting of the 2S+1 spin states, S being the spin quantum number. For these temperatures, one would expect there to be essentially an equal distribution

among the spin states and a negligible contribution of the electronic system to the heat capacity and a constant electronic contribution to the entropy of $R\ln(2S+1)$. If $S(MF_2, T)$ represents the entropy of an antiferromagnetic fluoride, denoted generally by MF_2, at temperature T, then $S^*(MF_2, T) = S(MF_2, T) - R\ln(2S+1)$ is equal to the lattice contribution to the entropy of MF_2 provided the electronic entropy is fully excited. One can then look up experimentally measured and tabulated entropy of ZnF_2 and find the temperature T' such that $S(ZnF_2, T')$ is equal to $S^*(MF_2, T)$. The ratio $T'/T = \theta(ZnF_2)/\theta(MF_2)$ is denoted by $r(MF_2, S)$. Similarly one finds a temperature T'' where ZnF_2 has the same heat capacity as does MF_2 at temperature T and denotes the ratio T''/T by $r(MF_2, C_p)$. If the principle of corresponding states were exactly followed one would expect to find that at the higher temperatures $r(MF_2, S)$ and $r(MF_2, C_p)$ were equal to one another and were both temperature independent. Stout and Catalano carefully measured the entropy and heat capacity of $ZnF_2, MnF_2, FeF_2, NiF_2$ and CoF_2 and found $r(S)$ and $r(C_p)$ for MnF_2, FeF_2 and NiF_2 to be indeed largely temperature independent over a significant temperature range between 100K and room temperature, though they are not exactly the same for each of these antiferromagnets. In each compound $r(C_p)$ is slightly higher than $r(S)$ and deviates more from the corresponding states principle. But in the neighborhood of the Néel temperature, the lattice contributions are comparatively small and the principle of corresponding states can be used to extrapolate curves of $r(MF_2, S)$ to low temperatures and obtain reliable values of the electronic contributions to the entropy and heat capacity of MnF_2 and FeF_2.

From tables compiled by Stout and Catalano, the values of $r(MnF_2)$ and $r(FeF_2)$ are approximately 1.0605 and 0.977 respectively in the temperature range of interest. The lattice contribution to the heat capacity is obtained from the thermodynamic relation

$$\begin{aligned} C_p(\text{lattice}, T) &= T\frac{dS(\text{lattice}, T)}{dT} \\ &= T\frac{dS(ZnF_2, rT)}{d(rT)}\frac{d(rT)}{dT} \end{aligned}$$

$$= C_p(ZnF_2, rT)(1 + \frac{d\ln r}{d\ln T}) \quad (2.28)$$

For MnF_2 and FeF_2, r changes very slowly with temperature and the term $\frac{d\ln r}{d\ln T}$ can thus be neglected. For a general diluted compound $M_xZn_{1-x}F_2$, the molar magnetic heat capacity C_m can be obtained from the total measure heat capacity C(total) as follows

$$\begin{aligned} C_m(T) &= C(\text{total}, T) - C(\text{calorimeter}, T) \\ &\quad -xC(MF_2, \text{lattice}, T) - (1-x)C(ZnF_2, T) \\ &= C(\text{total}, T) - C(\text{calorimeter}, T) \\ &\quad -xC(ZnF_2, r(MF_2)T) - (1-x)C(ZnF_2, T) \end{aligned} \quad (2.29)$$

All the terms being subtracted can be separated measured or looked up, and the true magnetic heat capacity can thus be obtained with negligible error. This procedure assumes that the entropy contributions of the lattice and of the electronic system are independent of one another so that any possible lattice changes associated with the antiferromagnetic ordering will not introduce additional errors in the estimation of the lattice entropy.

Figure 2-16 shows the total C in zero field together with the heat capacity of the calorimeter and the lattice for $Mn_{0.75}Zn_{0.25}F_2$.

Experiments

Both of the $Mn_{0.75}Zn_{0.25}F_2$ and $Fe_{0.5}Zn_{0.5}F_2$ samples are of exceptional crystallographic quality and the concentration gradients are small. Judging from the zero field transition peaks, the concentration gradient induced transition rounding is approximately 0.1K for $Mn_{0.75}Zn_{0.25}F_2$ and 0.2K for $Fe_{0.5}Zn_{0.5}F_2$ .The magnetic field is applied along the c-axis of the samples with an alignment better than 5°.

Figure 2-17 shows C_m vs. temperature at a series of fields following the ZFC procedure taken on $Mn_{0.75}Zn_{0.25}F_2$. A more or less conspicuous peak can be seen at each field. Data points away from the peaks have been diluted to improve clarity.

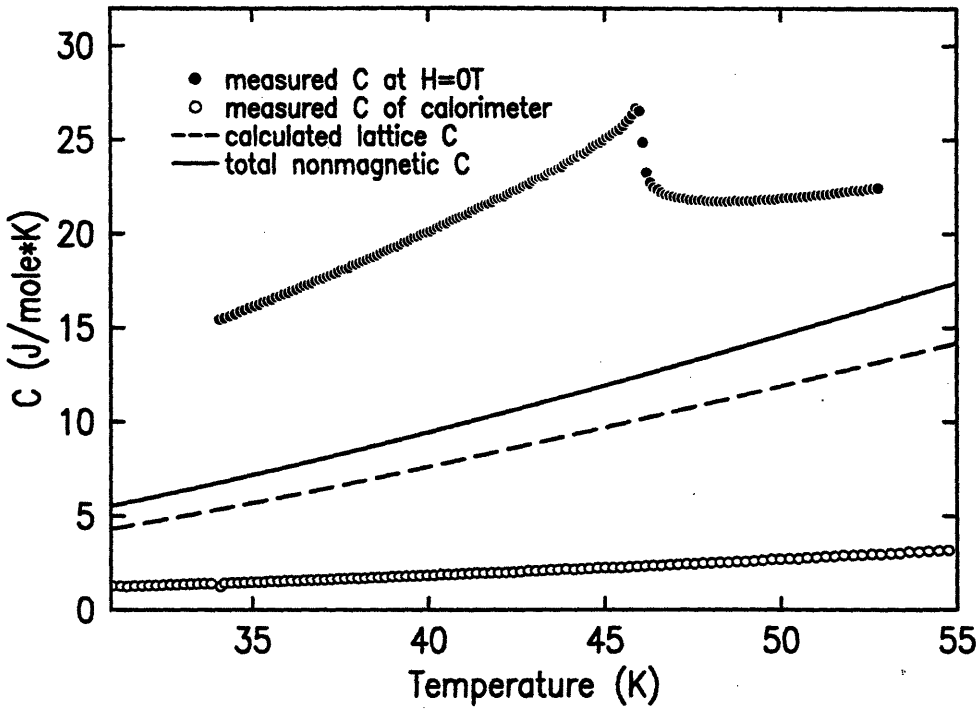

Figure 2-16: Contributions to the total measured heat capacity

The overall behavior of C_m shows strong similarity to the ac specific heat data on $Mn_{0.5}Zn_{0.5}F_2$ reported by Ikeda *et al.* [85, 68] and heat capacity data on $Fe_{1-x}Mg_xCl_2$ and $Fe_{1-x}Co_xCl_2$ by Wong *et al.* [122, 49, 51]. At H=0T, the system is described by the random exchange Ising model (REIM) and the heat capacity exhibits a strongly asymmetric cusp. Theoretical studies have yielded -0.09 [42] and -0.04 [43] for the random exchange heat capacity critical exponent α_{REIM}. Experimentally, the value of α_{REIM} has been measured with the indirect heat capacity techniques such as linear birefringence (-0.09±0.03 as reported in [123] and -0.10±0.03 as in [124]) and capacitance (-0.09±0.06) [125]. The zero field data on $Mn_{0.75}Zn_{0.25}F_2$ shown here are consistent with these values. The heat capacity cusp shifts to lower temperatures with increasing fields and becomes less asymmetric. There is no evidence of diverging C_m peaks. As the field approaches the bicritical point at approximately H=7T and T=40K, the peak broadens severely and the peak structure becomes complicated. Figure 2-18 shows C_m measured at a series of fields between $H = 6T$ and $H = 8T$. The anomaly near the transition develops a structure that seems to suggest two peaks at some fields. Although the data are not clear enough to make such assertion, they

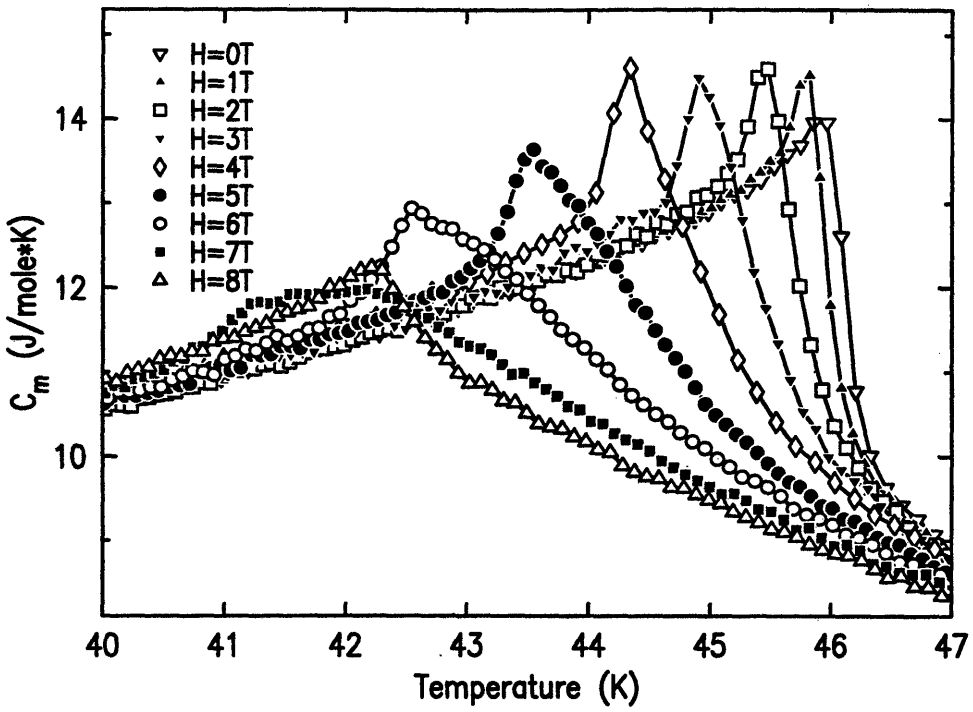

Figure 2-17: ZFC magnetic heat capacity of $Mn_{0.75}Zn_{0.25}F_2$. The solid lines connect the data points and serve as a guide to the eyes. Datum points away from the peaks have been diluted to improve clarity.

are reminiscent of the re-entrant behavior in the vicinity of the bicritical point reported by Shapira *et al.* [126]. Above the bicritical point, $Mn_{0.75}Zn_{0.25}F_2$ enters a spin-flop phase. Random field effects are not expected here because the spins mostly lie in the a-b plane and do not couple to the magnetic field applied in the c direction. Concordantly, the C_m peak above H=8T becomes sharp again. We measured C_m vs. T at H=7T down to T=6K and at H=5.7T down to 2.5K but did not see any anomaly signaling a transition between the Ising phase and the spin-flop phase. This has previously been attributed to the fact that the spin-flop phase boundary boundary has only a small slope with respect to the temperature axis [69]. The spin-flop boundary can be seen by measuring C_m vs. H, which is a series of C_m vs. T measurements within a narrow temperature range. Take at a series of fields, C_m vs H exhibits a cusp as the system crosses the phase boundary, as shown in figure 2-19. Figure 2-20 gives the phase boundary of $Mn_{0.75}Zn_{0.25}F_2$ as measured by the direct heat capacity technique. It agrees well with the $Mn_{0.75}Zn_{0.25}F_2$ phase boundary determined by

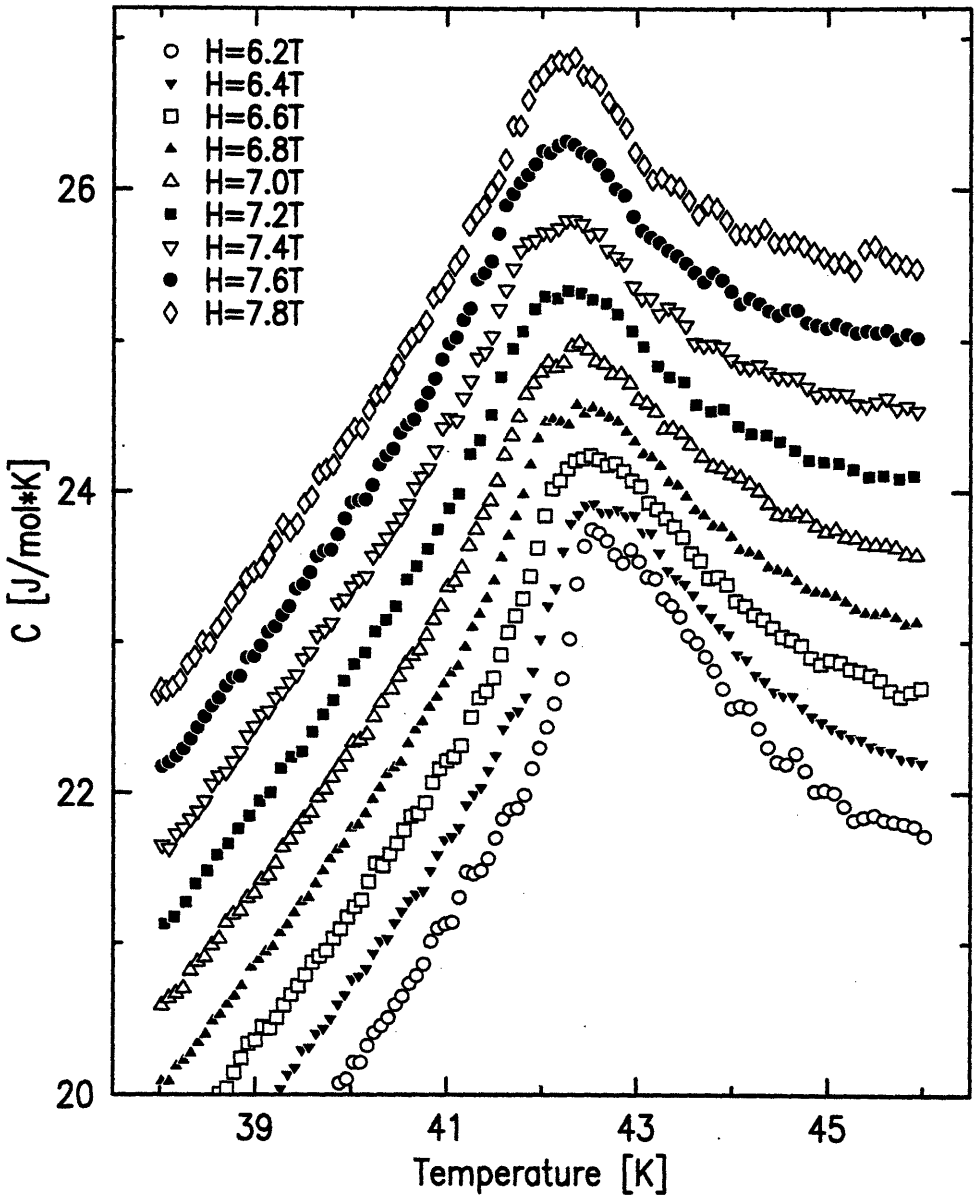

Figure 2-18: Magnetic heat capacity of $Mn_{0.75}Zn_{0.25}F_2$ near the bicritical point. Data shown are total heat capacity.

magnetic x-ray scattering [108].

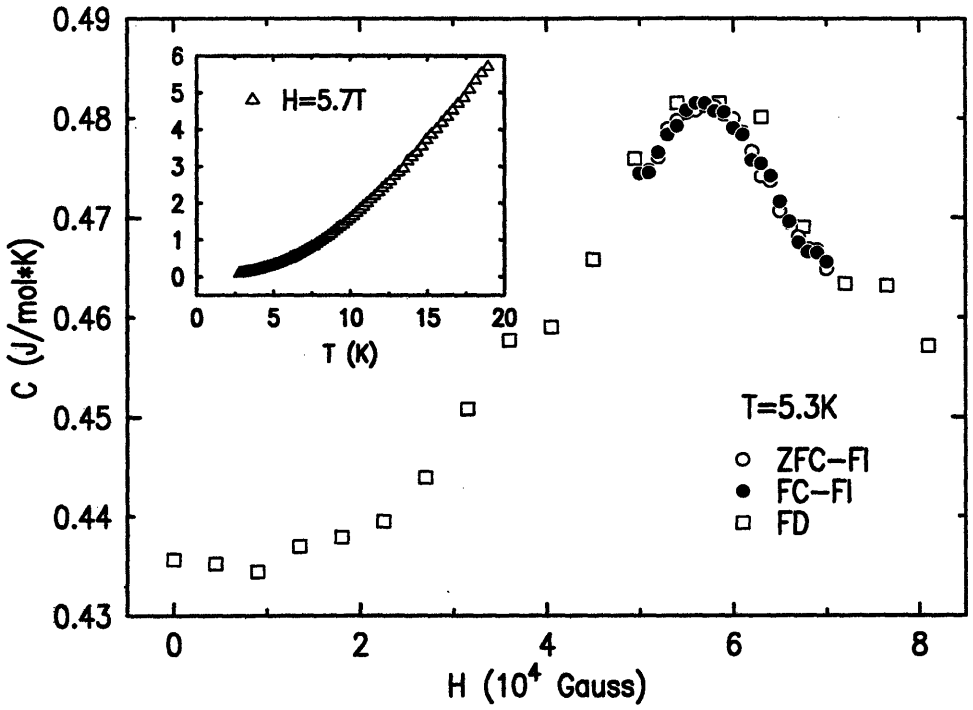

Figure 2-19: C_m vs H at 5.3K for $Mn_{0.75}Zn_{0.25}F_2$. The cusp near H=5.7T indicated the crossing between antiferromagnetic and spin-flop phases. The open circles are data taken with increasing field after first cooling the sample to zero field at 5.3K and raising the field to 5T. The closed circles are data taken with increasing field after first cooling the sample to 5.3K with the field held fixed at 5T. The open squares are data taken with decreasing field after first cooling the sample to 5.3K in a constant field of 8T. The inset shows C_m vs T at H=5.7T which shows no anomaly presumably because the spin-flop boundary is almost parallel to the temperature axis.

One remarkable fact that was found in the direct heat capacity study of the RFIM is the absence of hysteresis. This, along with heat capacity data of $Fe_{0.5}Zn_{0.5}F_2$, will be presented in the next chapter.

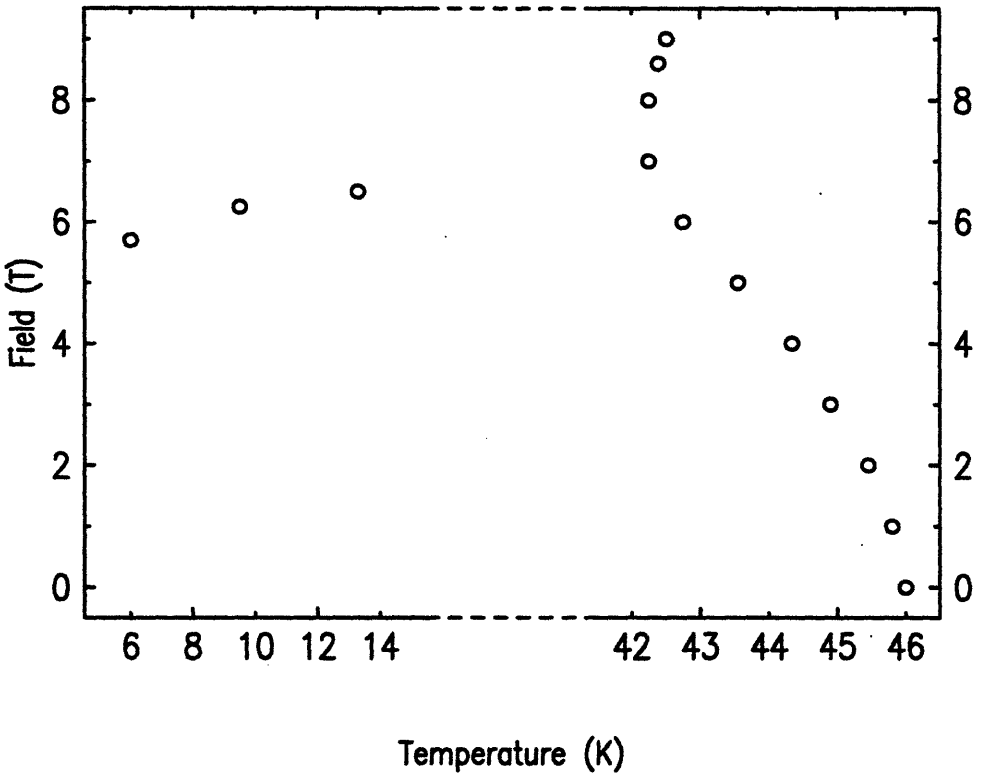

Figure 2-20: Phase boundary of $Mn_{0.75}Zn_{0.25}F_2$ measured by direct heat capacity.

Chapter 3

Nature of the Zero Field Cooled Transition

3.1 Introduction

At the heart of the Random Field Ising Model problem is the nature of its phase transition in three dimensions. Apart from being a fundamental model that addresses the effects of competing interactions and random disorder in various condensed matter systems, the RFIM has attracted much attention because of the contradicting interpretations of various experimental results and has presented significant challenges to theoretical studies. Although a disordered paramagnetic state exist in higher temperature and an ordered - whether over long range or short range - state is observed at low temperature, the way a RFIM system approaches the order-disorder transition is qualitatively different from that of a system free from random fields. This difference is attributed to anomalously slow dynamics which arise from a complex free energy distribution and large energy barriers due to the random fields. It prevents equilibrium from being attained for experimentally relevant time scales for $T < T_M(H)$ where $T_M(H)$ is the temperature below which metastability effects occur. The anomalously slow dynamics also cause the strong hysteretic effects observed in all RFIM systems.

It is commonly observed in experiments involving DAFFs that long range order is achieved following the ZFC protocol while a short range ordered domain state

sets in upon field cooling. In this chapter, we focus on what happens at the phase transition of a RFIM by studying the shedding of long range magnetic order in a ZFC procedure. The metastability of the RFIM, particularly that in the FC state, will be discussed in a later chapter. Although the ZFC state has LRO, as evidenced by magnetic neutron and x-ray scattering, it is in fact not the equilibrium ground state of the RFIM because an artificially high degree of order has been frozen in by the ZFC procedure. Were it possible to remain in equilibrium upon raising the field, the resulting LRO state would have significantly more disorder than the ZFC state since some patches of spins would follow their local random fields, despite the presence of a backbone of LRO. In addition, the ZFC transition is superheated and occurs at a T_C that is somewhat above the true equilibrium random field transition temperature T_N. Nevertheless, by studying the transition out of this metastable LRO state - presumably close to the equilibrium ground state - it is possible to gain insight into the disordering mechanism in the presence of random fields and in turn shed light on the problem of hysteresis in this system. In the current study, we combine the complementary techniques of magnetic x-ray and neutron scattering with direct and indirect heat capacity. These results provide a consistent phenomenological description of the transition process and the associated unusual critical behavior. They also lead to a new interpretation of indirect specific heat measurements in which the ZFC peak structure, previously attributed to critical fluctuations, is seen instead to arise entirely from a LRO contribution which is measured by scattering. This reconciles the conflicting views of the 3d RFIM in previous studies [127].

The chapter is organized as follows. Section 3.2 gives a brief survey of previous work on the random field transition. In section 3.3, we first present x-ray and neutron scattering measurements of the ZFC order parameter and short range correlations. These data demonstrate the extreme random field critical slowing down which results in a transition broadening that scales with the applied field squared. Measurements of the thermal derivative of the uniform magnetization and magnetic heat capacity are also presented. In section 3.4, we summarize the results and describe a new interpretation of the indirect heat capacity measurements that attribute the observed peaks

from these experiment to a static LRO contribution rather than critical fluctuations, thus resolving a long standing controversy in the study of the RFIM.

3.2 Previous Work on the Random Field Transition

Among the many systems that are modeled by the RFIM, the diluted antiferromagnets have the crucial advantage of offering a continuously variable random field strength that is typically inaccessible in other realizations of the model [48, 50, 128]. Diluted Ising-like antiferromagnets including $Mn_xZn_{1-x}F_2$, $Co_xZn_{1-x}F_2$ and $Fe_xZn_{1-x}F_2$ have therefore been the subject of much study over the last decade (for reviews see [129, 57, 130]). A variety of experimental techniques have been used including neutron scattering [131, 105, 72, 104, 132, 79, 133, 134], optical birefringence and Faraday rotation [132, 66, 63, 82, 64, 135], dilatometry [126], AC susceptibility [136, 137], SQUID magnetometry [138, 139, 134], NMR techniques [74] and more recently magnetic x-ray scattering [70, 140, 60, 141, 142]. Most of these work has focused on exploring the new random field critical behavior, particularly through the zero field cooling transition.

The experimentally observed effects of random fields on the phase transition for a 3d DAFF have been difficult to interpret. The first claim of the observation of true RF critical behavior came from an linear magnetic birefringence (LMB) study by Belanger *et al.* on $Fe_{0.6}Zn_{0.4}F_2$ [132]. These authors observed peaks in $\frac{d(\Delta n)}{dT}$ in magnetic fields up to 2T that appeared sharper and more symmetric than the zero field $\frac{d(\Delta n)}{dT}$ cusp. They went on to model these peaks with a logarithmic divergence and thereby mapping the apparent 3d RFIM critical behavior onto that of a 2d pure Ising system. However, it was not long before experiments started to review the unusual nature of the RFIM transition. The indication of a smeared transition was reported by Hagen *et al.* in a neutron scattering study on $Co_xZn_{1-x}F_2$ [101] and by Cowley *et al.* in their study of $Fe_xZn_{1-x}F_2$ [67]. These workers observed the

correlation length ξ, which diverges at T_C for a pure system, to saturate at a finite value in an applied field and the saturation value decreased with increasing field, indicating the destruction of a second order phase transition. Broadening of the ZFC transition with increasing applied field was also observed in the thermal expansion measurements of Shapira *et al.* [126], and subsequently with a range of optical and uniform magnetization techniques which indirectly measures magnetic heat capacity [66, 63, 143, 64, 65]. The authors of the indirect heat capacity studies maintain that the increasingly rounded transition anomaly is due to dynamic effects and that logarithmically divergent magnetic heat capacity is still observable from the peak structures outside the rounded region.

Faced with these anomalies, Villain [144] and Fisher [23] have developed ideas that attribute the transition rounding to the extremely slow dynamics at the transition. According to their derivation, the critical relaxation time $\tau \approx \tau_0 exp(C\xi^\theta)$, where τ_0 and C are constants that depend on the random field strength, and θ is an exponent such that the free energy barrier associated with reversing a block of spins of size R is $\sim R^\theta$. θ modifies the hyperscaling relation to $(d-\theta)\nu = 2-\alpha$. This form of relaxation time diverges much faster than the conventional critical slowing down, $\tau \approx \tau_0 \xi^z$. AC susceptibility experiments that reach over seven decades of frequency [136, 137] provided direct evidence of slow dynamics consistent with this exponential divergence of relaxation time. In addition, Monte Carlo simulations have also observed strongly divergent correlation times consistent with activated dynamics [34]. The apparent width of the transition, ΔT around $T_N(H)$, observed with measurements performed at frequency ω, is expected to scale as $\Delta T \sim |ln\omega|^{-1/\theta\bar{\nu}}$, where $\bar{\nu}$ is the RFIM correlation length exponent. For a crossover from REIM to RFIM, this scaling is modified to $\Delta T \sim h_{RF}^{2/\phi}[ln(\omega h_{RF}^{-2\nu z/\phi})]^{-1/\theta\bar{\nu}}$ where ν and z are the REIM correlation length and dynamical critical exponents respectively [63]. In a neutron scattering study, Belanger *et al* [79] found the broadening varied as $H^{2/\phi}$ with $\phi = 1.42$ for $H \leq 3.0$T in $Fe_{0.46}Zn_{0.54}F_2$. Similarly optical Faraday rotation data of Pollack *et al.* on $Fe_{0.47}Zn_{0.53}F_2$ [143] taken at four fields obeyed a $H^{2/\phi}$ power law with $\phi = 1.49 \pm 0.1$. However, magnetic x-ray scattering data showed that the

broadening of the transition in $Mn_{0.75}Zn_{0.25}F_2$ followed a H^2 field dependence [60] up to H=7.0 T. As discussed below, the same H^2 scaling is also observed on $Fe_{0.5}Zn_{0.5}F_2$ up to 7T.

3.3 Results and Interpretations

3.3.1 Magnetic X-Ray Scattering Measurements of the Order Parameter

We first present staggered magnetization data measured with magnetic x-ray scattering on a sample of $Fe_{0.5}Zn_{0.5}F_2$. The ZFC state is prepared by first cooling in zero field to 10K and then raising the field to the desired value. The resulting (100) magnetic peak was found to be completely resolution-limited for all fields studied, reflecting LRO with an antiferromagnetic domain size in excess of 1μm. The temperature was then raised holding the field fixed. Scans at each temperature took approximately 30 minutes in the transition region with an additional 5 minutes thermal equilibration time. Both longitudinal and transverse scans are taken at each temperature and then fitted to an empirical two-dimensional Lorentzian squared function. Figure 3-1 shows representative longitudinal scans using the ZFC protocol at selected temperatures taken at H=6.1T. The solid lines all have constant width equal to 4×10^{-4} r.l.u. The multiple scattering background was measured at a number of temperatures above the phase boundary and then subtracted from the raw data to obtain the data shown in figure 3-1. The fitted peak intensities at 6.1T are shown in the lower panel in figure 3-2. This figure compares the transition from ZFC LRO state into the paramagnetic state at H=0T and H=6.1T. The comparison captures the dramatic effects of random fields on the phase transition, where the shedding of LRO in the field is severely broadened. The zero field order parameter was adequately fitted with a simple power law and produced the REIM exponent β. The solid line fit to the 6.1T data in the

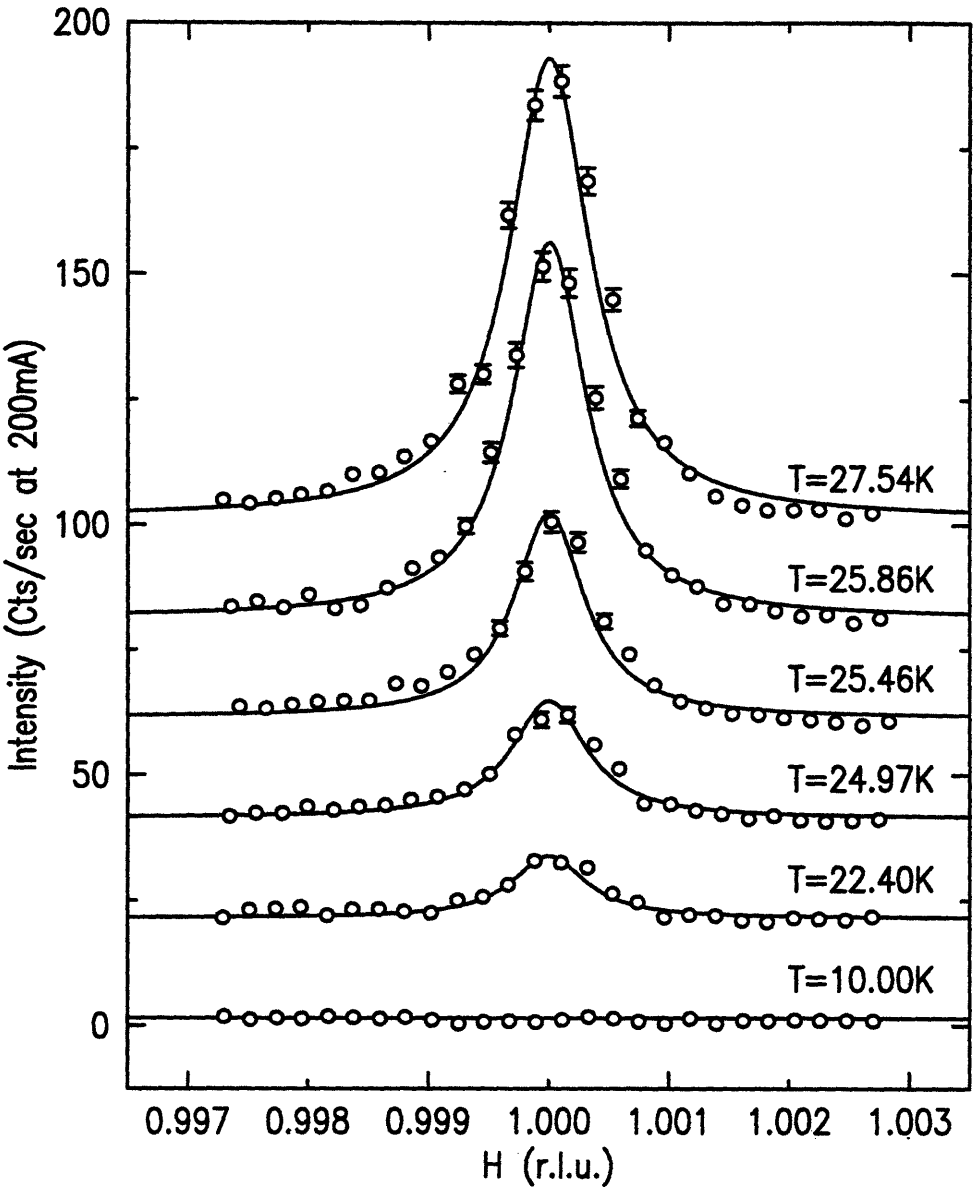

Figure 3-1: Representative longitudinal x-ray scattering scans. Data were taken at H=6.1T on warming, following a ZFC procedure. The solid lines are 2d fits to Lorentzian-squared of constant width, equal to 4×10^{-4} r.l.u.

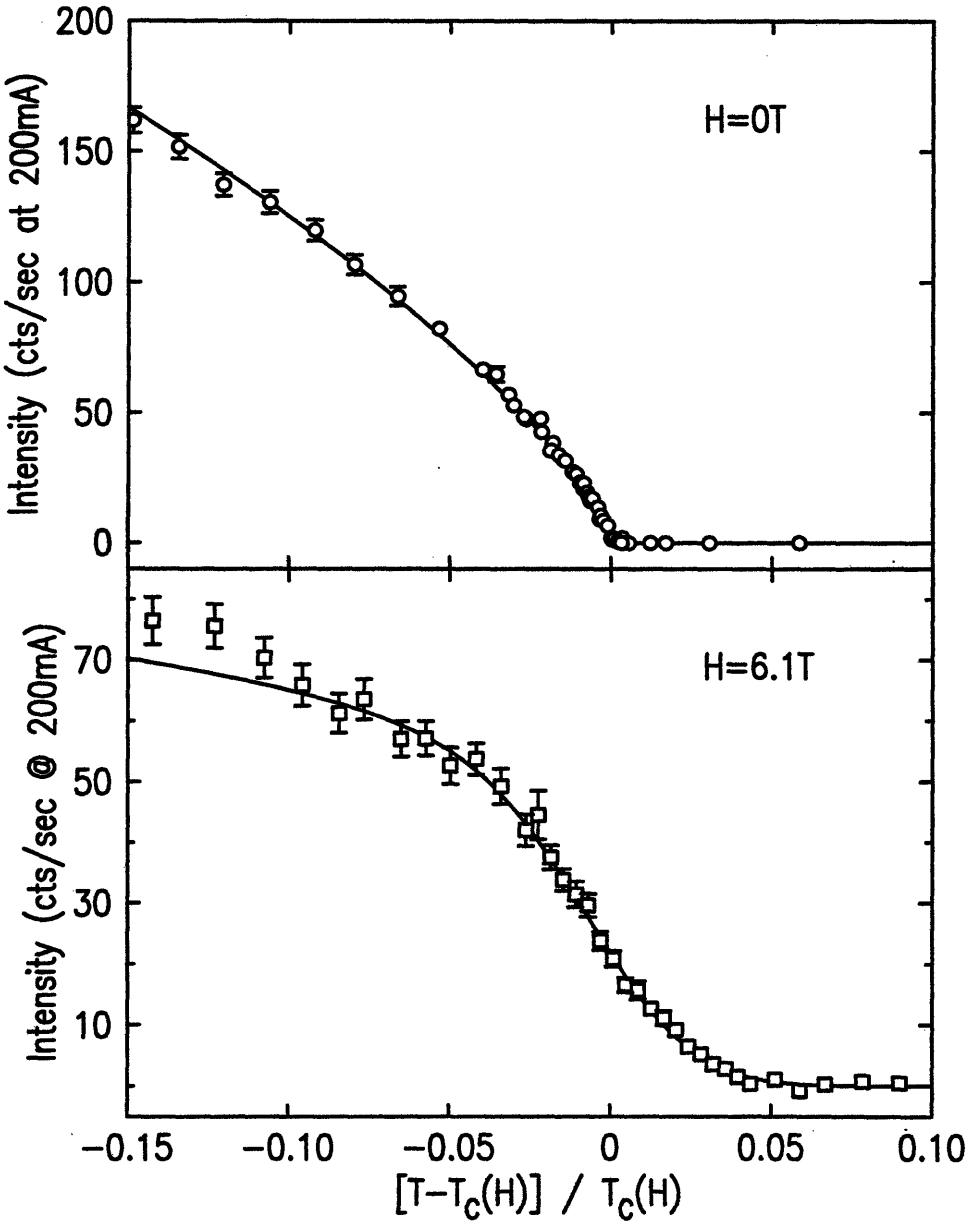

Figure 3-2: Comparison of x-ray-measured ZFC LRO at 0T and 6T. The horizontal axis is in reduced temperature.

bottom panel is of the form:

$$I(T,H) = \frac{1}{\sqrt{\pi\sigma_{ZFC}^2(H)}} \int \left(\frac{t_c - T}{t_c}\right)^{2\beta} exp\left(-\left(\frac{t_c - T_c(H)}{\sigma_{ZFC}(H)}\right)^2\right) dt_c. \qquad (3.1)$$

Equation 3.1 models the smeared transition by assuming a power law with a Gaussian distribution of transition temperatures (t_c) about a center $T_C(H)$ with a distribution width σ. As is apparent from figure 3-2, this function describes the broadening quite well. However, we emphasize that this is a heuristic form which has not yet been justified by any formal theory. Nevertheless, $\sigma_{ZFC}(H)$ provides a measure of the transition broadening and in turn the strength of the random fields.

Figure 3-3 displays the 2d-fitted (100) ZFC peak intensity obtained from a series of fields up to H=7T. For each field, the scattering remained resolution-limited at all temperatures and no critical scattering was observed. The progressive broadening of the transition region is apparent. The solid lines are all fits to equation 3.1. For $Mn_{0.75}Zn_{0.25}F_2$, $\sigma_{ZFC}(H)$ was found to be proportional to H^2 and this was also found to be the case in the present study of $Fe_{0.5}Zn_{0.5}F_2$. The field dependence of the transition width is shown in figure 3-4, where $\sigma_{ZFC}(H)$ is plotted against H^2. A straight line adequately fits the data. The dashed line represents a fit to $H^{2/\phi}$ behavior, with ϕ fixed to $\phi = 1.41$. The H^2 dependence gives a much better fit, reflected in the goodness of fit parameter, χ^2, which is about a factor of 3 worse for the $H^{2/\phi}$ fit. In fact, the power of H fits to 2.3 ± 0.4 if floated. As the inset of figure 3-4 shows , the order parameter exponent β_{ZFC} also displays field dependence, varying between 0.085 and 0.17 for fields ranging from H=3.5T to H=7T. The width is found to follow, $\sigma_{ZFC}(H) = AH^2 + B$ with $A = 0.021 \pm 0.002$ K/T^2 and $B = 0.10 \pm 0.02$K. In $Mn_{0.75}Zn_{0.25}F_2$, the equivalent results were $\beta = 0.2 \pm 0.05$ and A=0.0034 K/T^2 [108]. The observation of this field dependence in $Fe_{0.5}Zn_{0.5}F_2$ rules out the possibility that the H^2 scaling in $Mn_{0.75}Zn_{0.25}F_2$ was a consequence of the weak anisotropy or the close proximity of a bicritical point in the latter system.

Similar random field broadening effects were also observed in magnetic x-ray studies of $Mn_{0.45}Zn_{0.55}F_2$. Figure 3-5 shows ZFC order parameter squared measured at

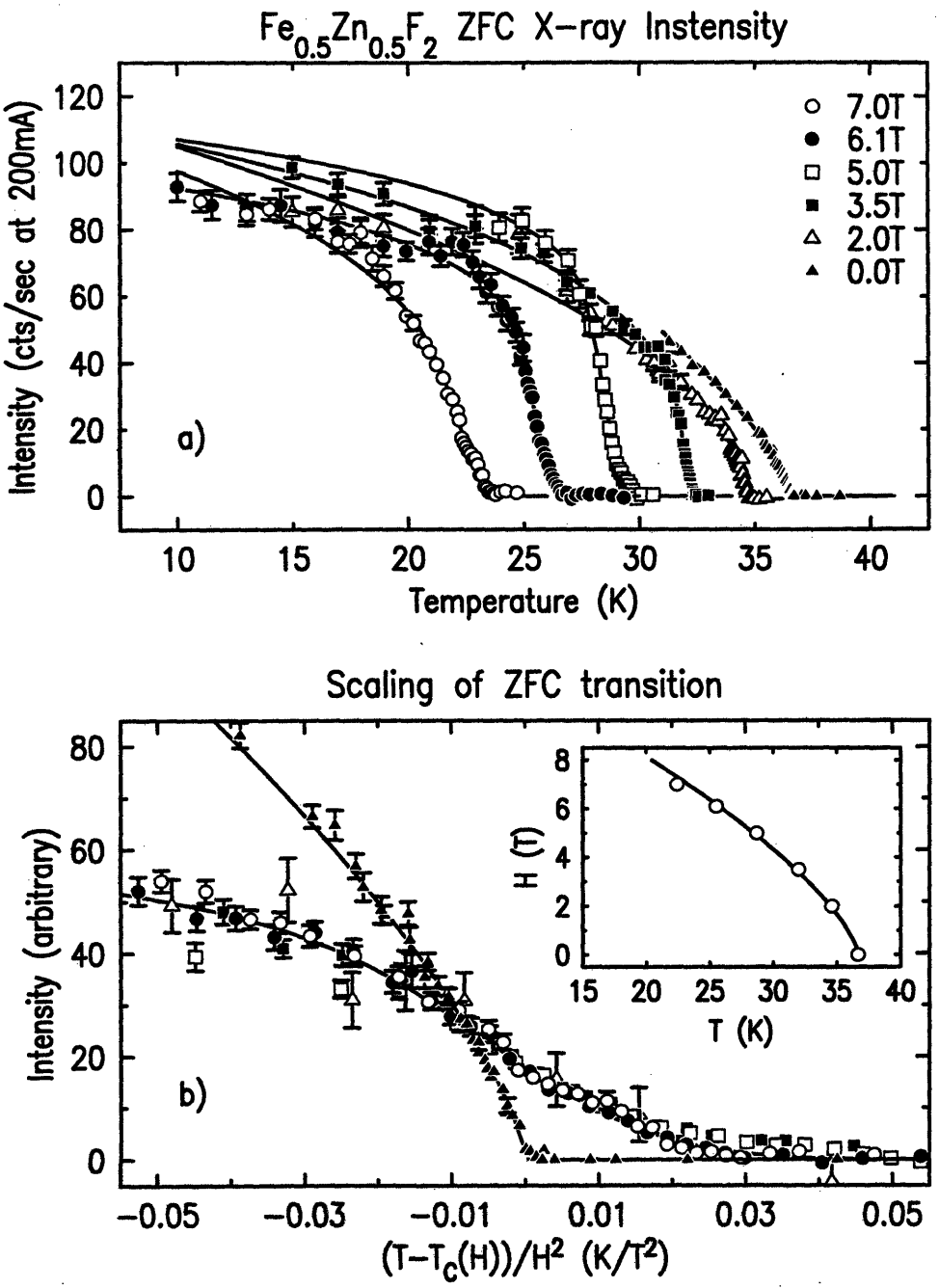

Figure 3-3: Top panel: The ZFC order parameter squared as measured at the (100) position with x-rays for five fields and H=0T. For H $\neq$ 0, the data are well described by a power-law-like behavior with a broadened transition region. The broadening is modeled by a Gaussian distribution of transition temperatures of width $\sigma_{ZFC}(H) \propto AH^2$ (see text). Bottom panel: The $H \neq 0$ data of Fig. 3a replotted as a function of the temperature interval away from T_C(H) as measured in units of H^2. This illustrates the rounding of the transition which is attributed to non-equilibrium effects arising from extreme critical slowing down and the universal scaling behavior of the *trompe l'oeil* critical phenomena. The inset shows the phase boundary of $Fe_{0.5}Zn_{0.5}F_2$ as determined from the x-ray fits.

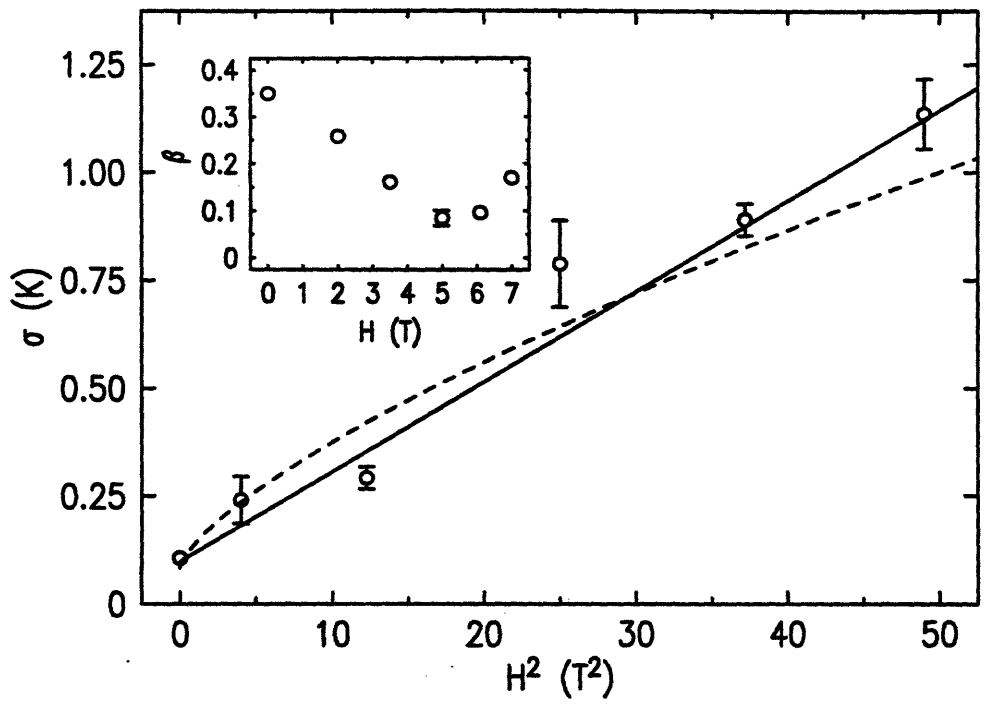

Figure 3-4: The parameter $\sigma_{ZFC}(H)$, which measures the observed x-ray ZFC transition width, plotted as a function of H^2. The inset shows β obtained at each field. Both $\sigma_{ZFC}(H)$ and $\beta_{ZFC}(H)$ are extracted from the order parameter fits shown as solid lines in Fig. 3-3. $\sigma_{ZFC}(H)$ appears to scale better with H^2 than with $H^{2/\phi}$.

fields between 0T and 2.5T. The solid lines are again fits to equation 3.1 and describe the data satisfactorily. The broadening effects are apparent. Figure 3-6 summarizes the order parameter exponent $\beta_{ZFC}(H)$ and transition width $\sigma_{ZFC}(H)$. What makes $Mn_{0.45}Zn_{0.55}F_2$ different from $Fe_{0.5}Zn_{0.5}F_2$ and $Mn_{0.75}Zn_{0.25}F_2$ is that the spin-flop occurs at approximately 2.7T and the phase boundary has a strong curvature and flattens rapidly as the applied field increases from 0T to 2.7T (see figure 4-16. This causes the broadening to occur much faster than the other two compounds. In fact, the solid line fit in figure 3-6 is for a power 6.6. The order parameter exponents obtained from the fits are as follows: β(0T)=0.35±0.01 which is in excellent agreement with REIM prediction; between 0T and 2T, β does not show much variance and averages to 0.19±0.02; above 2T, β decreases to 0.15±0.01 at 2.2T and 0.11±0.01 at 2.5T, though the transition is so severely smeared at 2.5T that there may not be enough data points far enough below T_C to determine these exponents accurately.

There is still a lack of consensus over whether the the RFIM transition is of first or

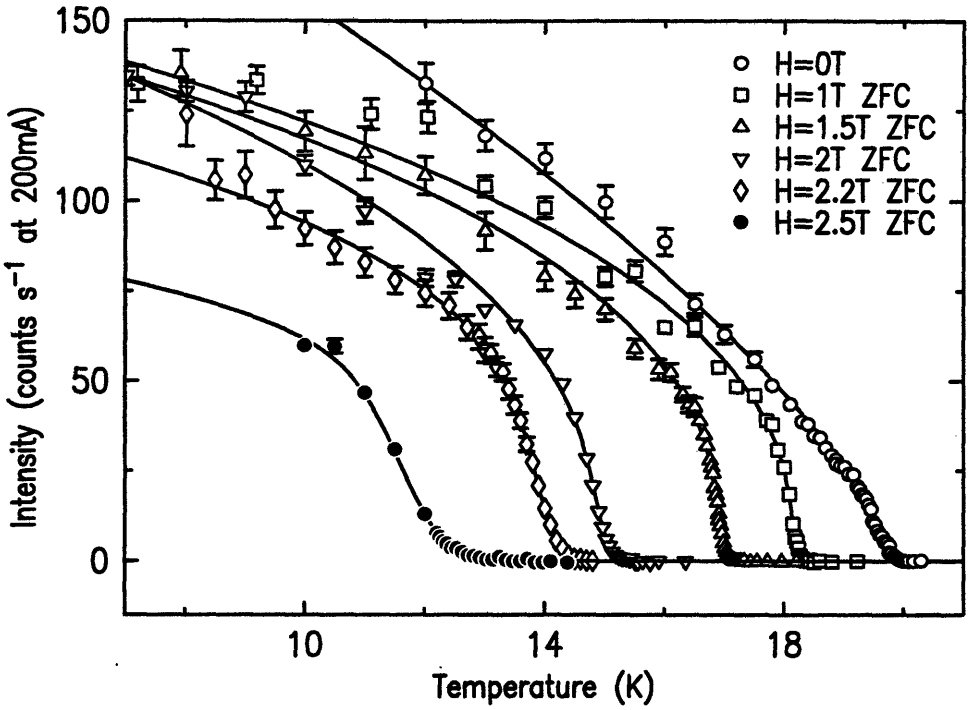

Figure 3-5: ZFC (100) 2d-fitted peak intensity of $Mn_{0.45}Zn_{0.55}F_2$ measured by x-ray scattering

second order. The theoretical prediction for the equilibrium exponent β is ≤ 0.05. X-ray scattering experiments, an ideal method of studying order parameter, estimated $\beta_{ZFC} = 0.2 \pm 0.05$ for $Mn_{0.75}Zn_{0.25}F_2$ [60]. The data presented here are consistent with a pseudo-second-order transition though they do not rule out the possibility of a first order ZFC transition with similar broadening effects due to the random fields. Specifically, modeled after a second order transition with a Gaussian-type transition broadening, we obtain estimates of $\beta_{ZFC} \approx 0.19 \pm 0.03$ for $Mn_{0.45}Zn_{0.55}F_2$, close to that of $Mn_{0.75}Zn_{0.25}F_2$, and $\beta_{ZFC} \approx 0.12 \pm 0.04$ for higher fields in $Fe_{0.5}Zn_{0.5}F_2$. Though these estimates are not uniform and the fits reflect β varying with the strength of the random fields, they are all small compared to the pure Ising or random exchange Ising exponents. In figure 3-7, we show staggered magnetization of $Fe_{0.5}Zn_{0.5}F_2$ from the current work in the top panel and previous data on $Mn_{0.75}Zn_{0.25}F_2$ in the bottom panel. For both sets of data, the horizontal axis has been rescaled so that temperature is measured with respect to $T_C(H)$ and in units of H^2. Vertically, data at each field is multiplied by an adjustable constant so that they conform to the same curve.

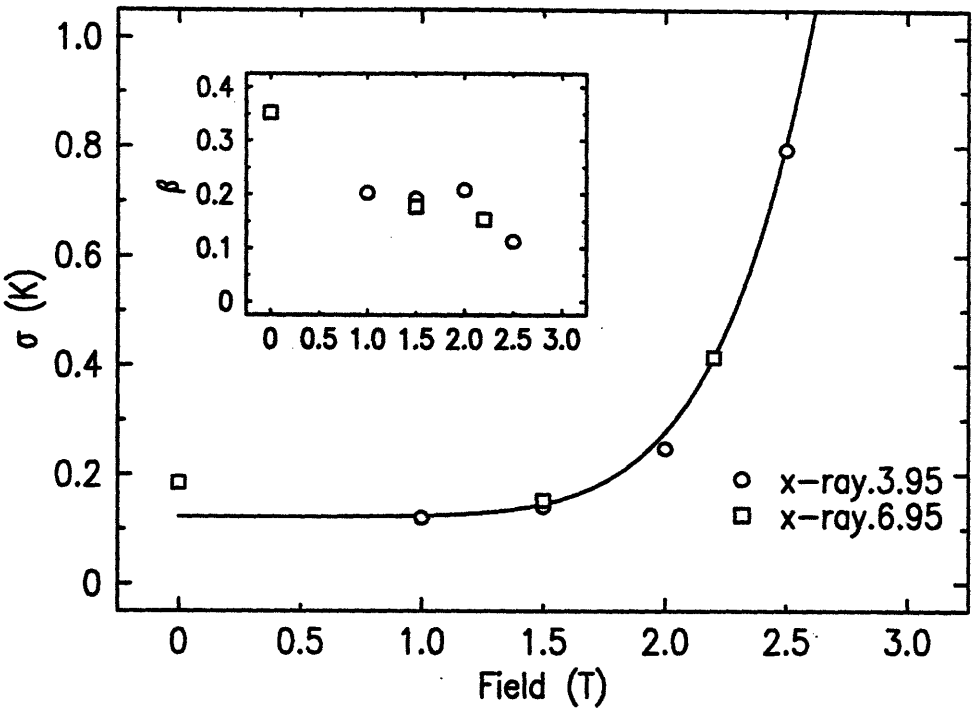

Figure 3-6: The parameter $\sigma_{ZFC}(H)$, which measures the observed x-ray ZFC transition width, is plotted vs. the field. The solid line is a fit to a power law. Since the phase boundary of $Mn_{0.45}Zn_{0.55}F_2$ flattens rapidly with increasing field, the broadening occurs much faster than in $Fe_{0.5}Zn_{0.5}F_2$ and the power (6.6) is strongly affected by the approach to spin-flopping. The inset shows β obtained at each field. Both $\sigma_{ZFC}(H)$ and $\beta_{ZFC}(H)$ are extracted from the order parameter fits shown as solid lines in figure 3-5.

The collapse of the data is excellent for both systems, illustrating the validity of the H^2 dependence of the broadening over a wide range of fields. The solid lines show simultaneous fits of the data at all fields to equation 3.1. This procedure yields the estimates for β_{ZFC} quoted above.

An alternative way to treat these order parameter data is to fit them to a Gaussian broadened first order transition,

$$I(T,H) = \frac{1}{\sqrt{\pi\sigma_{ZFC}^2(H)}} \int \left(A + B\left(1 - \frac{T}{t_c}\right)\right) exp\left(-\left(\frac{t_c - T_c(H)}{\sigma_{ZFC}(H)}\right)^2\right) dt_c \qquad (3.2)$$

where A and B are the discontinuity at and the slope of the order parameter squared below t_c respectively. The dashed lines in figure 3-7 are fits to equation 3.2. These fits appear to describe the data satisfactorily, though the quality of the fits are inferior

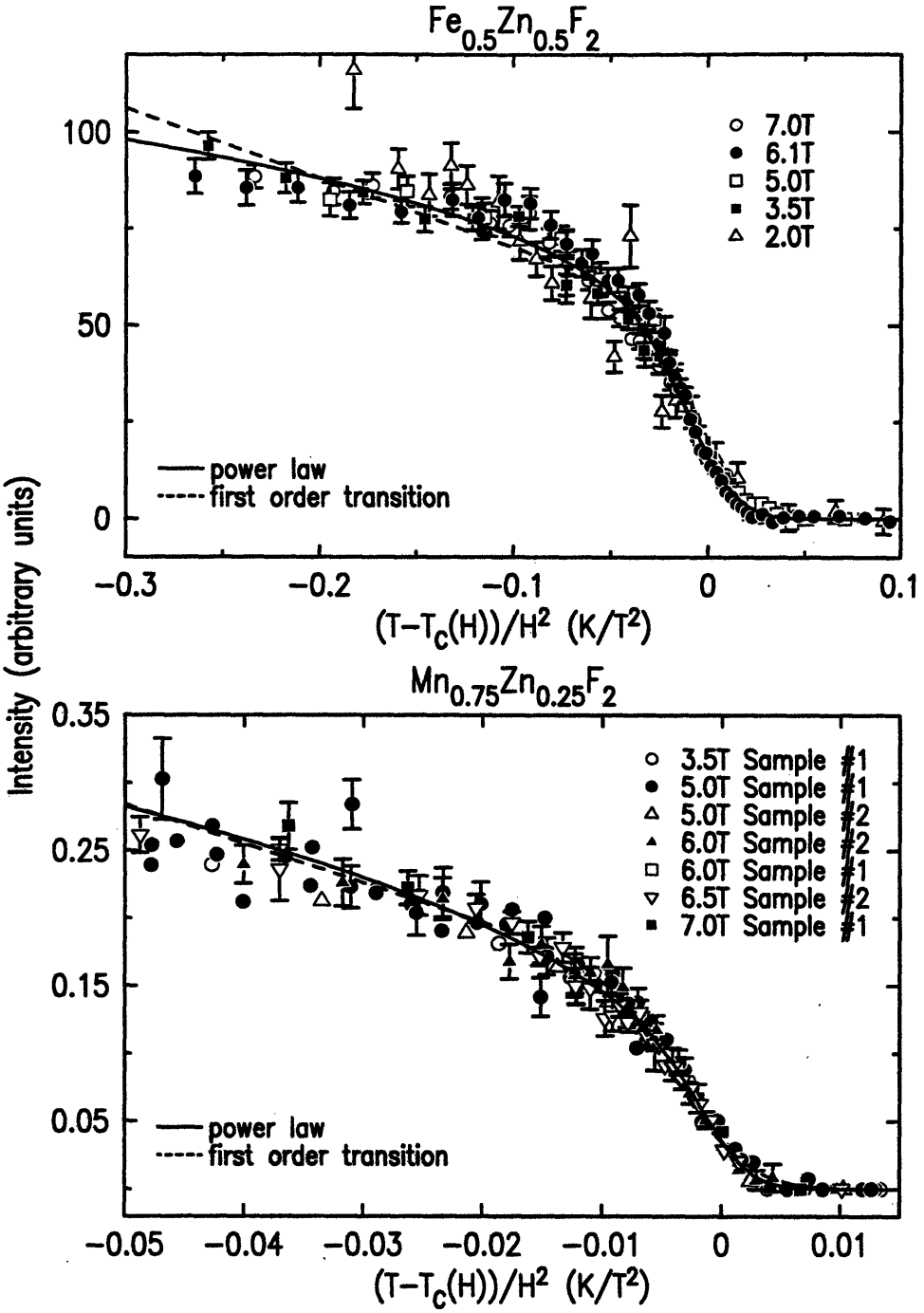

Figure 3-7: Comparison of a first-order and a second-order interpretation, with transition broadening, of the ZFC order parameters measured by magnetic x-ray scattering. Top panel: sublattice magnetization squared of $Fe_{0.5}Zn_{0.5}F_2$; bottom panel: sublattice magnetization squared of $Mn_{0.75}Zn_{0.25}F_2$. For both data sets, order parameter squared collapses onto one curve when the temperature scale is measured from $T_C(H)$ and rescaled with H^{-2}. The amplitude for data at each field is adjusted. The solid line is a fit to equation 3.1, representing a broadened second order transition. The dashed line is a fit to equation 3.2, representing a broadened first order transition.

to those of equation 3.1 in that the goodness of fits parameter χ^2 is larger and so are the errors of the fitted parameters. We have also attempted to fit these data using equation 3.1 while fixing β_{ZFC} at 0.05 or less in order to simulate a first order transition. These fits were entirely inadequate. Nevertheless, the x-ray data clearly do not favor one approach over the other. Fits to equation 3.2 yield comparable estimates for the broadening σ as equation 3.1. On general grounds, one might expect a discontinuity in the order parameter for random field systems especially in the ZFC superheated regime. However, the fit for $Fe_{0.5}Zn_{0.5}F_2$ data requires an temperature intercept greater than $T_N(0)$=36.7K which is unphysical. Further, critical correlation lengths appear to grow in a power-law-like fashion before saturating at T_C following either ZFC or FC in the rounded power law model. This indicates strong critical fluctuations at the equilibrium random field transition, which are not commonly associated with first order transitions. Therefore the first-order transition description for the ZFC transition is not entirely satisfactory. Clearly further experimental and theoretical work will be necessary in order to settle this issue.

It is interesting to note that the transition is broadened significantly more in $Fe_{0.5}Zn_{0.5}F_2$ and $Mn_{0.45}Zn_{0.55}F_2$ than was the case for $Mn_{0.75}Zn_{0.25}F_2$, at the same applied field. This difference arises from the larger random fields generated in $Fe_{0.5}Zn_{0.5}F_2$ by virtue of the greater dilution, and lower transition temperatures. In fact, h_{RF}^2 is $\approx$ 4 times larger in $Fe_{0.5}Zn_{0.5}F_2$ than in $Mn_{0.75}Zn_{0.25}F_2$ at the same applied field.

3.3.2 Magnetic Neutron Scattering Measurements

We next present neutron scattering results taken on the same sample of $Fe_{0.5}Zn_{0.5}F_2$. The data discussed in this chapter were all taken in the double axis mode so that both static and dynamic fluctuations are measured. Since the zero field transition temperature measured by neutron scattering is higher by 3.1K than that measured by x-ray scattering, magnetization and heat capacity techniques, most likely due to an error in thermometry or temperature gradient in the neutron experimental set-up, we shift all the neutron results uniformly by -3.1K. The large cross-section and broad resolution in neutron scattering enables one to measure the diffuse scattering in

addition to the LRO in the ZFC state. This diffuse component is observed to sharpen as the temperature is raised, reaching a maximum correlation length at $T_C(H)$. The 2-axis data were fitted to the cross section

$$S(\mathbf{Q}) = \frac{B}{(\kappa^2 + q^2)} + \frac{A\kappa}{(\kappa^2 + q^2)^2} + C\delta(\mathbf{q}), \tag{3.3}$$

which is a modified equation 2.20. Again, $\mathbf{q} = \mathbf{Q} - (100)$ is the deviation from the Bragg peak position, B is the amplitude of the longitudinal susceptibility (L), and A is the integrated intensity of the static longitudinal random field fluctuations (L^2). The LRO is fitted with the parameter C and the cross-section S($\mathbf{Q}$) is convolved with the full 3d resolution function.

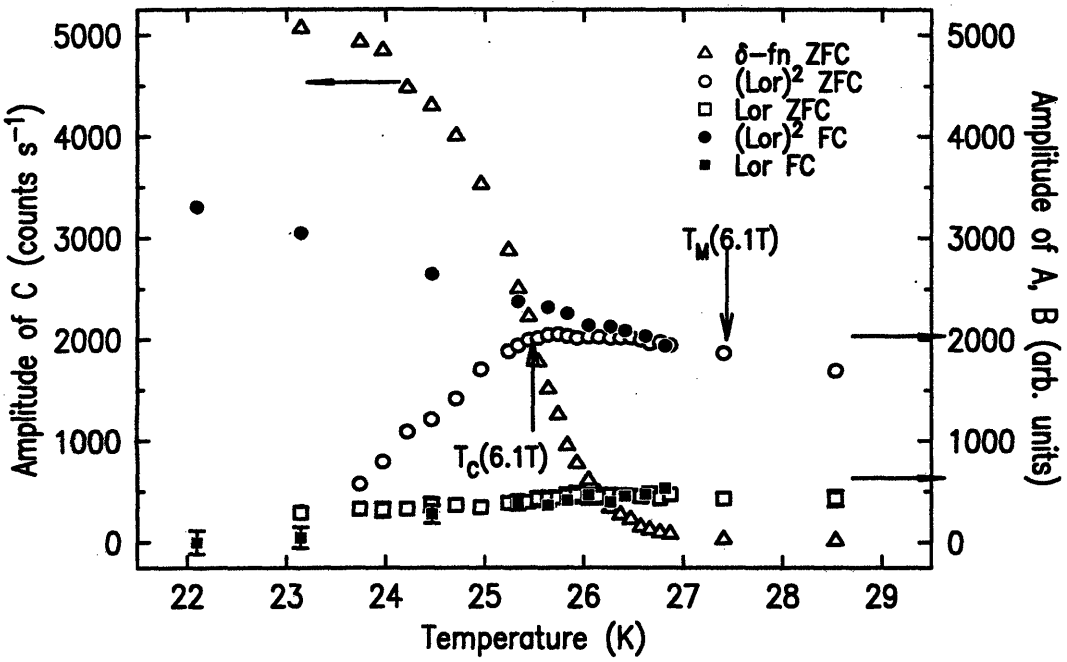

Figure 3-8: ZFC and FC lineshape components at H=6.1T for $Fe_{0.5}Zn_{0.5}F_2$. Top panel: ZFC LRO amplitude described by a δ-function. The intensity at (1,-0.003,0) is used to monitor the diffuse scattering intensity. Its maximum at T_C=25.5K indicates the phase boundary. Bottom panel: integrated intensity of Lorentzian-squared and amplitude of Lorentzian components in arbitrary units. T_M is an metastability temperature above which there is no hysteresis.

The temperature dependences of the parameters A, B and C of equation 3.3 are shown in figure 3-8 following both field cooled and zero field cooled protocols

at H=6.1T. Under FC there is no LRO and C is constrained to be zero in these fits. The intensity of the Lorentzian squared component rises smoothly as the sample is cooled through the metastability boundary. The closed symbols represent FC parameters. On warming from a ZFC state the data then require $C \neq 0$ in order to fit the LRO. The open symbols in figure 3-8 show the parameters from these fits. The results agree well in their general phenomenology with previous neutron studies on diluted antiferromagnets in an applied field [57, 130, 131, 79]. The metastability boundary, $T_M(H)$, is the point at which the amplitude of the LRO falls to zero. At H=6.1T, $T_M(6.1T) = 27.4 \pm 0.2$K. For $T > T_M(H)$ there are no history dependent effects and the system is in equilibrium. Note $T_M(H) > T_C(H) = 25.6$K, where T_C can be obtained by monitoring the wing intensity at (1,-0.003,0) (see figure 3-12). Unfortunately, extinction effects prevent reliable fitting of the amplitude of the LRO to an order parameter function such as equation 3.1. However, it is clear that qualitatively the behavior is similar to that observed with x-rays. Furthermore, in the transition region, where extinction effects are no longer expected to be significant, the x-ray and neutron measurements of the order parameter are found to be identical. In figure 3-9, we show both magnetic x-ray and neutron scattering order parameter measurements at H =6.1T. These data were taken on the same $Fe_{0.5}Zn_{0.5}F_2$ sample. As previously stated, the neutron data have been shifted by -3.1K in temperature so that the x-ray and neutron scattering measured T_N agree in zero field; the data of figure 3-9 serve to illustrate the validity of this procedure. No further adjustment has been made in the temperature scale. The only adjustment then is the rescaling of the neutron intensity by a constant multiplicative factor. As is apparent in figure 3-9, the two sets of data show excellent agreement within 2.5K of T_C(6.1T).

The ZFC diffuse scattering is largely Lorentzian squared in character, indicating that it arises from random field fluctuations. At H=6.1T the diffuse scattering peak amplitude reaches a maximum intensity $\sim$ 2K below the metastability boundary.

The field-induced rounding effects for diffuse scattering and correlation lengths are shown in figure 3-10 for fields ranging from 2T to 6.4T. The top panel shows the ZFC inverse correlation length $\kappa_{ZFC}(H)$ saturates at $T_C(H)$. The saturation

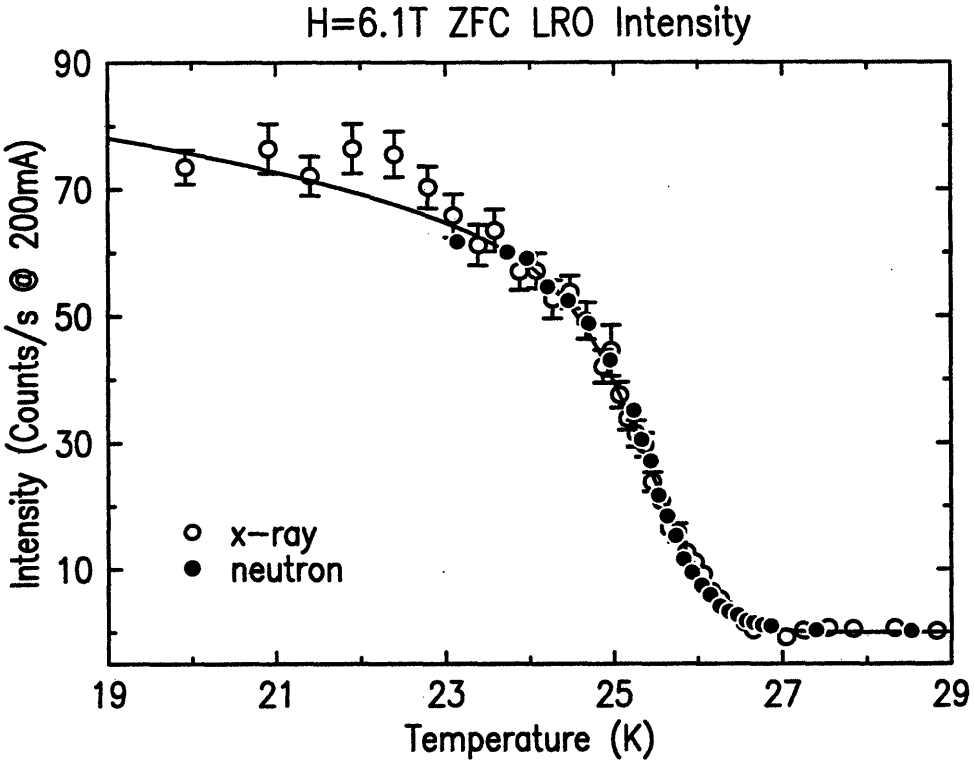

Figure 3-9: Neutron and x-ray (100) LRO intensities measured at 6.1T in the transition region after ZFC for $Fe_{0.5}Zn_{0.5}F_2$. The relative intensities have been adjusted so that they match in the temperature region around $T_C(H)$.

value of $\kappa_{ZFC}(H)$ increases with applied field, signaling the size of the clusters being flipped on experimental time scales becomes smaller in the shedding of LRO. This is a clear manifestation of the stronger random field dynamic effects at higher fields. The solid lines are guides to the eyes. The fits for the diffuse scattering terms become increasingly difficult for temperatures below $T_M(H)$ due to the growing presence of LRO, resulting in fewer data points below $T_C(H)$ and larger fitting errors. From the temperature dependence of κ above $T_M(H)$, one may obtain the critical exponent ν. Previously, estimates of ν have been given by neutron scattering experiments on both $Fe_xZn_{1-x}F_2$ and $Mn_xZn_{1-x}F_2$. For example, Cowley *et al.* found $Fe_xZn_{1-x}F_2$ κ vary linearly with T at temperatures sufficiently above the transition, suggesting $\nu \approx 1$ [67]. Similar results were later obtained by these authors on $Mn_xZn_{1-x}F_2$, though the fitted value of ν showed clear dependence on the temperature range chosen for the

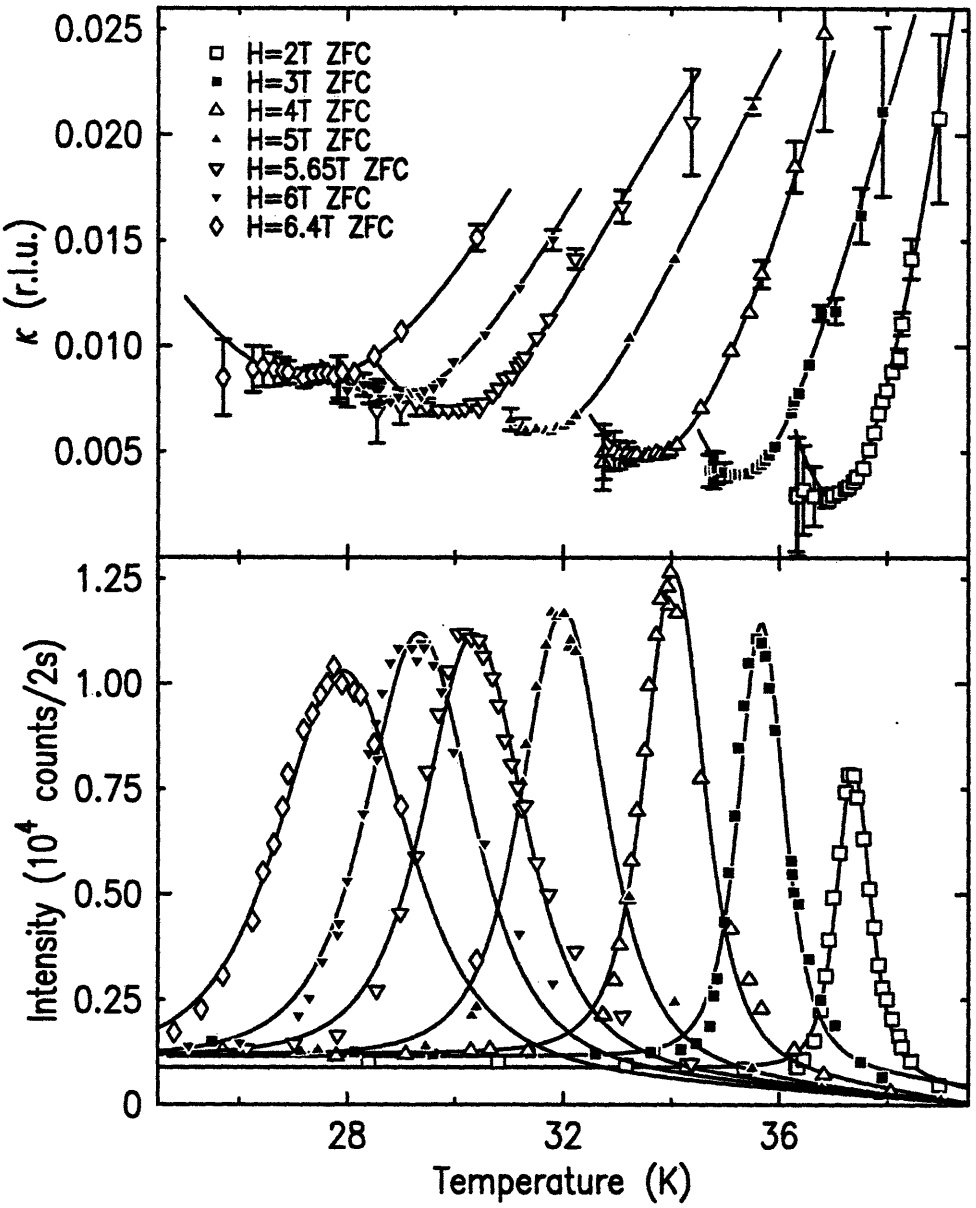

Figure 3-10: Inverse correlation lengths and intensity at (1,-0.003,0) of $Fe_{0.5}Zn_{0.5}F_2$ measured by 2-axis neutron scattering, after ZFC at fields 2T-6.4T. Top panel: Inverse correlation length $\kappa_{ZFC}(H)$ saturates at $T_C(H)$ at increasingly higher values for increasing fields, displaying stronger random fields dynamic effects for higher applied fields where the size of the clusters being flipped on experimental time scales becomes smaller. The solid lines are guides to the eyes. Bottom panel: The ZFC intensity at the (1,-0.003,0) position. The intensity reaches a maximum at $T = T_C(H)$ and occurs at lower temperatures as the field is increased. The peak broadens with increasing field. The solid lines represent empirical fits to a Lorentzian squared function as discussed in the text.

fits with an average value $\nu = 1.4 \pm 0.3$ [71]. Belanger *et al.* estimated $\nu = 1.0 \pm 0.15$ based on a neutron study of $Fe_{0.6}Zn_{0.4}F_2$ [75]. Recent Monte Carlo simulations by Rieger yielded $\nu = 1.1 \pm 0.2$ [36]. Our current data show that, at temperature sufficiently above $T_C(H)$, κ varies approximately linearly with T and is consistent with an estimate of ν that is close to but probably slightly greater than 1. However, one should be careful in extracting ν from the neutron data because first one needs to use the correct $T_N(H)$ in the fits and second, one has to choose an appropriate temperature range in order to avoid both nonequilibrium effects and the crossover to the random exchange critical behavior. These concerns considerably complicate the data analysis.

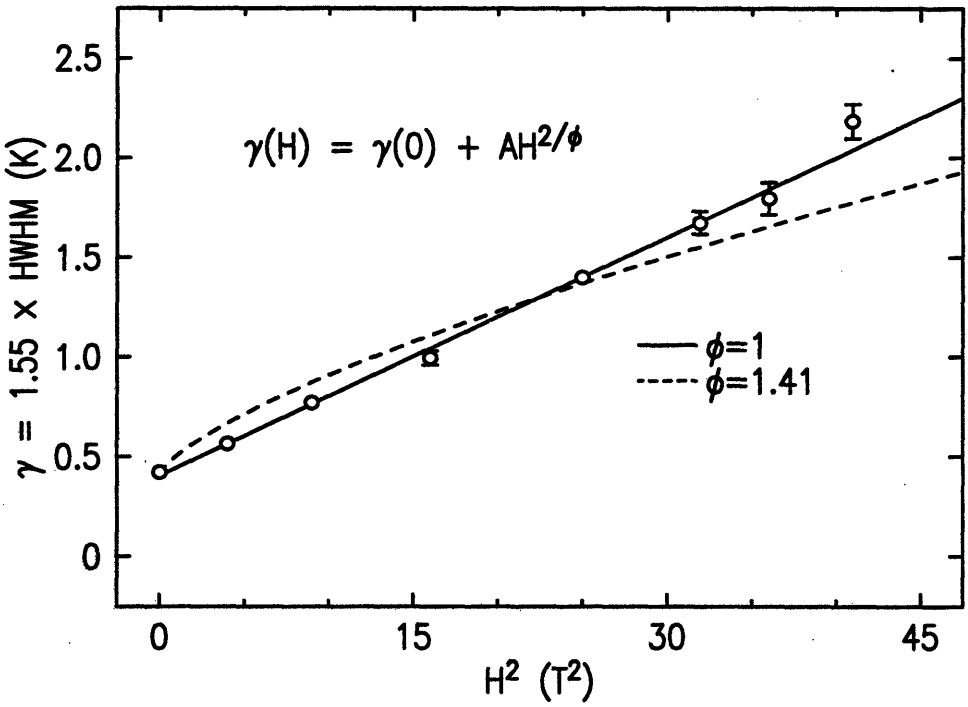

Figure 3-11: Width of neutron critical scattering at (1,-0.003,0) for $Fe_{0.5}Zn_{0.5}F_2$.

The bottom panel of figure 3-10 shows the ZFC intensity at the (1,-0.003,0) position. The intensity reaches a maximum at $T_C(H)$, the same temperature where $\kappa_{ZFC}(H)$ reaches a minimum at the corresponding field. The (1,-0.003,0) intensity peaks at lower temperatures as the field is increased. The peak broadens with increas-

ing field, and provides a measure of the apparent broadening effect of random fields. In figure 3-10, the solid lines are empirical fits to a Lorentzian squared function placed on a flat background which goes linearly to zero above the peak temperature. This form was used without theoretical motivation to parameterize the measured critical scattering and was found to fit the data well at all fields. Since the neutron order parameter in this temperature region agrees with those measured with x-rays, one would expect such a measure will also yield an H^2 dependence. The widths, $\gamma(H)$, obtained from these fits are plotted against applied field squared in figure 3-11. These data are indeed consistent with a $\sim H^2$ dependence. An $H^{2/\phi}$ dependence provides a less good description of the data. Interpretation of these widths is somewhat problematic because of the inherent, finite width at H=0T. It has been assumed to add linearly in this analysis.

3.3.3 Phenomenology of the Zero Field Cooling Transition

The phenomenology of the transition is clarified in figure 3-12 where we compare x-ray and neutron data all taken at H=6.1T. In the top panel of this figure, the x-ray intensity of the ZFC state is plotted. The solid line is a fit to equation 3.1 with $\beta = 0.12$ and σ_{ZFC}(6.1T) =0.85K. The dashed vertical line marks the center of the Gaussian distribution T_C(6.1T)=25.54 $\pm$ 0.02 K. In the center panel, the width κ of the diffuse scattering, as determined by fits of the neutron data to equation 3.3 at H=6.1T, is plotted for the ZFC and FC data. The closed squares represent the inverse correlation length of the FC domain state which decreases smoothly through the transition, flattening out at low temperatures around κ_{FC}(6.1T)=0.0075 r.l.u. This corresponds to a characteristic length of the FC domain state of $\sim$ 100Å. The width κ of the ZFC diffuse scattering decreases as $T_C(H)$ is approached, but does not go to zero as expected at an equilibrium second order transition. Rather, the correlation length of the fluctuations saturates at $T_C(H)$, at a value approximately equal to the FC length at that temperature. This temperature, at which the largest blocks of spins are being flipped, coincides precisely with the center of the transition region as determined by x-ray and neutron measurements of the order parameter.

It is the point of maximum rate of change of the sublattice magnetization. As the temperature is increased further, the correlation length begins to decrease, following closely the corresponding FC values and the rate of decay of the order parameter falls off. At $T_M(H)$, LRO diminishes to zero, the integrated intensity of Lorentzian squared static fluctuations becomes the same for ZFC and FC, and the system reaches equilibrium. In the bottom panel of figure 3-12, we plot the amplitude of the LRO, determined by the neutron scattering measurements, together with the wing intensity at (1,-0.003,0). This position, away from the Bragg peak, provides a measure of the "critical" scattering which is independent of any functional form used in the fitting. This pseudo-critical scattering also peaks precisely at $T_C(H)$.

We thus arrive at the following phenomenological description of the transition out of the LRO state. At low temperatures, the system is in a metastable state with frozen-in LRO. There is very little thermal energy to overcome the energy barriers that scale with the spin cluster sizes and therefore only very small clusters of spins flip as favored by the local distribution of random fields. As the temperature is raised, progressively larger static spin clusters are reversed and the decrease of order parameter accelerates. The dynamic fluctuations, measured by the Lorentzian term, is limited in size by the static one. As the transition is approached, the correlation length grows and the associated energy barriers for flipping correlated regions grow at a faster rate. Meanwhile, the time scale to relax such fluctuations increases exponentially and eventually grows well beyond observation time. Thus for an experiment performed in a finite time, the correlation length will appear to saturate at a finite maximum at a temperature $T_C(H)$. At this temperature, the order parameter decays at the fastest rate and diffuse scattering peaks, as reflected in the wing intensity in neutron studies. Above $T_C(H)$, the correlation length and the associated relaxation time gradually decrease and LRO decays at a slower rate. Finally, at $T_M(H)$, the system is once again able to relax on experimental time scales and all the LRO is removed. Beyond $T_M(H)$, the system is in an equilibrium paramagnetic state.

If the procedure is reversed and the system is cooled from a high temperature in a constant field H, it retraces the ZFC states down to $T_M(H)$. Below $T_M(H)$, because

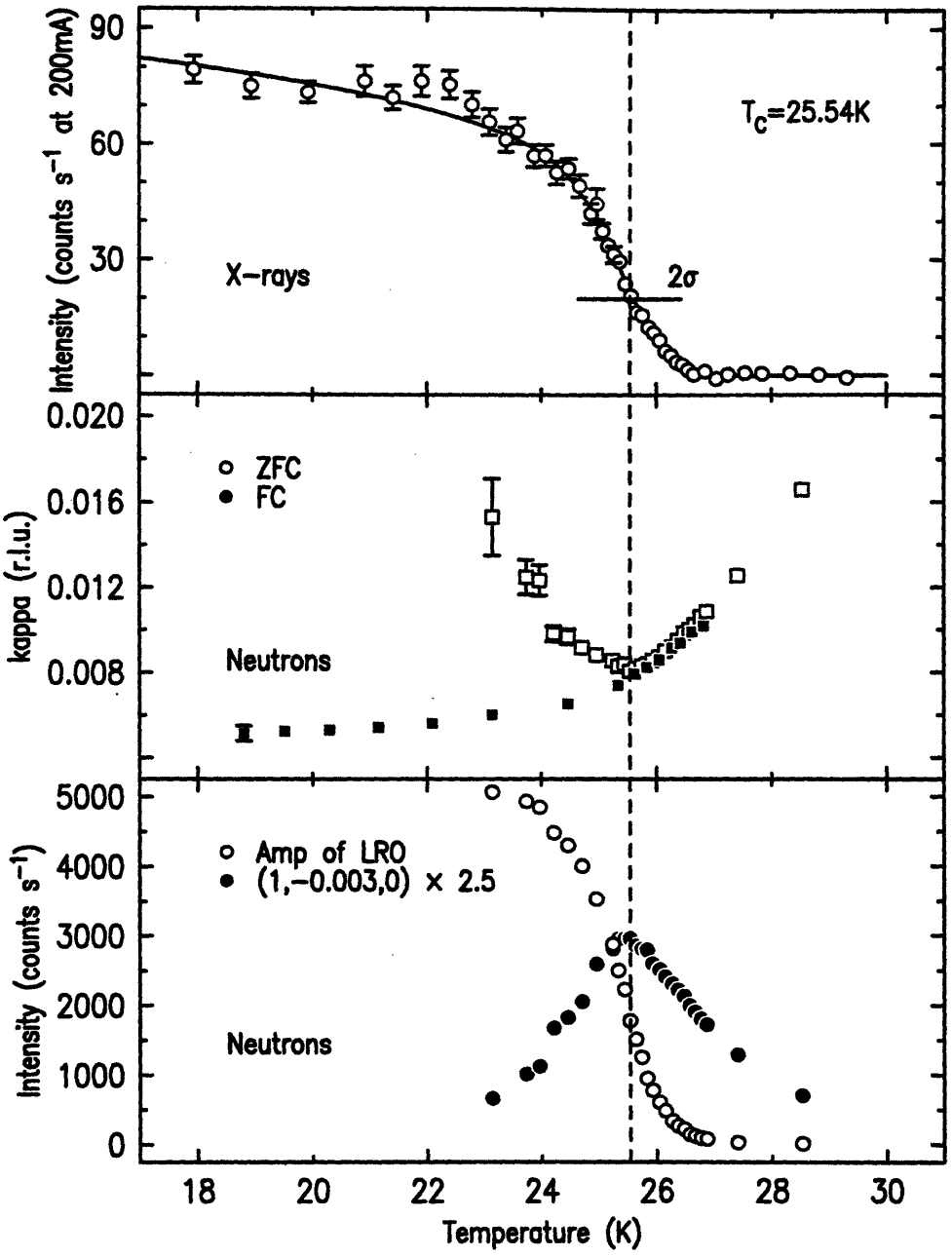

Figure 3-12: Top panel: The (100) x-ray magnetic ZFC peak intensity at H=6.1T. The solid line is a fit to equation 3.1. Center panel: The inverse correlation length,κ, of the diffuse scattering as measured by 2-axis neutron scattering. On FC, only a domain state is observed and the data are fit to a Lorentzian plus a Lorentzian squared form. A delta function Bragg peak (LRO) term is added for the ZFC data. κ is seen to saturate precisely at the temperature of maximal rate of change of the order parameter, $T_C(6.1T)$. The correlation length of the ZFC fluctuations agrees with the FC domain size at $T_C(6.1T)$. Bottom panel: The amplitude of the ZFC LRO as measured by neutron scattering. The intensity at (1,-0.003,0) also peaks around $T_C(6.1T)$.

of the anomalously slow dynamics, spin cluster reversals occur only on finite length scales and the system is unable to develop a LRO backbone which is present during ZFC at corresponding temperatures. However, the same random field dynamic effects are present and the size of the FC fluctuating clusters is the same as those during ZFC on comparable experimental time scales. This explains the agreement of the ZFC and FC correlation lengths at $T_C(H)$ and above. Below $T_C(H)$, the RFIM system is trapped in metastable energy states corresponding to domain-type spin configurations and LRO does not develop on finite time scales. The distribution of these energy states changes as the temperature is lowered and the correlation length grows. At a particular temperature below $T_C(H)$, the domains are metastable and in general larger ones are energetically more favorable, resulting in slow domain expansion over time. This last point will be studied in greater detail in a later chapter.

Discussion of the Broadening

The broadening of the transition in $Fe_{0.5}Zn_{0.5}F_2$ as observed by x-rays is in qualitative agreement with previous x-ray work on $Mn_{0.75}Zn_{0.25}F_2$ [141, 60]. However, as noted earlier, the broadening in $Fe_{0.5}Zn_{0.5}F_2$ is quantitatively much larger. This is true for the broadening obtained by fitting x-ray scattering data to equation 3.1, where $Fe_{0.5}Zn_{0.5}F_2$ gives a σ_{ZFC} that is about six times that of $Mn_{0.75}Zn_{0.25}F_2$ at corresponding fields. Related effects are observed in the saturation values of ZFC $\kappa(H)$. For example, $\kappa_{ZFC}(6.1T)$ of $Fe_{0.5}Zn_{0.5}F_2$ saturates at 0.0082r.l.u. while $\kappa_{ZFC}(6.15)$ of $Mn_{0.75}Zn_{0.25}F_2$ saturates at 0.0025r.l.u. [71].

These differences can be largely accounted for by the different random field strengths in the two systems. For an applied field H, the generated random field, h_{RF}, is [50];

$$< h_{RF}^2 >_{av} = \frac{x(1-x)[T_N^{MF}(1)/T]^2(g\mu_B SH/K_B T)^2}{[1+\Theta^{MF}(x)/T]^2}, \tag{3.4}$$

where $T_N^{MF}(1)$ is the mean field transition temperature of the pure system and $\Theta^{MF}(x)$ is the mean field Curie-Weiss parameter. For MnF_2 and FeF_2, Θ/T_N =1.24 and 1.48 [145], and $T_N(0T)$=67K and 77K respectively. For $Mn_{0.75}Zn_{0.25}F_2$, T_N(0T)=46.1K

and for $Fe_{0.5}Zn_{0.5}F_2$, $T_N(0T) = 36.7K$. We assume $\Theta^{MF}(x)$ scales with the zero field transition temperatures. As an example, at H=5T, we find the generated random field for $Fe_{0.5}Zn_{0.5}F_2$ is $\approx$ 4 times larger than that for $Mn_{0.75}Zn_{0.25}F_2$ at their respective transition temperatures, T_C(5.0T). The observed broadening is $\sim$ 6 times larger in $Fe_{0.5}Zn_{0.5}F_2$ compared with that in $Mn_{0.75}Zn_{0.25}F_2$ [60]. The effect of the larger random field can also be seen in the inverse correlation lengths of the FC domain state in the two materials. For example, at H=6.1T, figure 3-8 shows FC κ saturate at low temperatures to 0.0052r.l.u in $Fe_{0.5}Zn_{0.5}F_2$ whereas at H=6.5T, FC $\kappa \approx$ 0.0013r.l.u. at low temperatures in $Mn_{0.75}Zn_{0.25}F_2$ [131], a factor of approximately 4 smaller.

The data presented here are in qualitative agreement with the ideas of Villain and Fisher. However, the observed H^2 scaling of the x-ray and neutron transition region does not agree with $H^{2/\phi}$ scaling, with $\phi = 1.42$. However, the measured transition temperature $T_C(H)$, either from the center of transition broadening obtained from staggered magnetization or from the peak in the diffuse scattering, is consistent with the known $H^{2/\phi}$ scaling of the phase boundary. For instance, fitting the peak temperatures in the critical scattering to $T_C(H) = T_C(0) - AH^2 - BH^{2/\phi}$ with A held fixed at the calculated mean field value, A=0.0152 KT^{-2}, yields $\phi = 1.41 \pm 0.06$. This is in close agreement with the value obtained using birefringence techniques, $\phi = 1.40 \pm 0.05$ [132].

Fishman and Aharony first predicted that new random field critical behavior may be observed within a crossover region $t \leq t_{cr} \propto h_{RF}^{2/\phi}$ [48]. Ramos *et al.* later argued that the apparent width of the transition scales the same way as t_{cr} [63]. A $H^{2/\phi}$ scaling of the transition rounding has been reported previously [79, 143]. The neutron results presented here do not agree with previous neutron measurements [79] for which $H^{2/1.42}$ scaling was reported. However, these latter results were generated from three data points at relatively small fields, H <3T and a zero width was assumed at H=0T.

As discussed by Hill *et al.*[60], it is possible to derive empirically the H^2 field dependence. The rounding of the transition may be understood as a finite size effect in which the growth of the correlation length in the transition region is limited by the random fields to the FC domain size. One therefore expects the apparent broadening

ΔT to scale as $\Delta T \sim \xi_{max}^{-1/\nu}$. The inverse correlation length scales with the applied field as $\kappa \sim H^{\nu_H}$. Hence $\Delta T \sim H^{\nu_H/\nu}$. Using the experimentally obtained values, $\nu_H = 2.23 \pm 0.1$ [146] at T=8.0K and $\nu = 1.0 \pm 0.15$ [75] measured for the $Fe_{1-x}Zn_xF_2$ system, we obtain $\nu_H/\nu = 2.23 \pm 0.7$, in broad agreement with the observed field dependence. For $Mn_{0.75}Zn_{0.25}F_2$ similar agreement was observed. Using the measured exponents $\nu_H = 3.3 \pm 0.8$, $\nu = 1.4 \pm 0.3$ gives $\nu_H/\nu = 2.4 \pm 1.1$ [60].

Even from a theoretical point of view, the observed H^2 scaling for the apparent broadening should not be completely surprising. In principle, one expects to observe new random field behavior in a range that scales as $t \sim h_{RF}^{2/\phi}$. However, all experiments measure the broadening against the external field H. Although h_{RF} appears to be proportional to H in the derivation for the random fields in a DAFF, it is not exact for a wide range of applied fields. To see this clearly, we look more closely at Cardy's formula for h_{RF} (equation 3.4). As H increases, the transition is depressed and therefore the temperature at which we observe the transition, T, is lower. This means that h_{RF} effectively increases faster than H. Thus if a quantity scales as H^2 and h_{RF}^y, it is expected that $y < 2$. For the currents study which covers almost a decade of change in H, it should not be a surprise that this mechanism is at work and the observed H^2 broadening may therefore conceivably reflect the underlying $h_{RF}^{2/\phi}$ scaling.

3.3.4 Uniform Magnetization Measurements

We next turn to results from SQUID magnetometry, which provides a convenient bulk thermodynamic probe. We have performed a set of measurements of the uniform magnetization on samples of $Fe_{0.5}Zn_{0.5}F_2$ and $Mn_{0.45}Zn_{0.55}F_2$. The $Fe_{0.5}Zn_{0.5}F_2$ sample is cut from the same boule as that used in the x-ray and neutron scattering work. The $Mn_{0.45}Zn_{0.55}F_2$ sample is cut from the same boule as that used in the x-ray work. Measurements of the FC and ZFC uniform magnetization were made at a number of fields and the data are shown in figure 3-13. In accord with the hysteresis observed in scattering experiments, the domain state in the FC data is evidenced by an excess FC magnetization relative to the ZFC state. The excess magnetization

$M_{ex} = M_{FC} - M_{ZFC} > 0$ provides a measure of the density of the domain walls and thereby the domain size [138, 139]. As is apparent from figure 3-13, M_{ex} grows with increasing field, representing smaller domains at higher fields.

As discussed in the previous chapter, one can obtain information on magnetic heat capacity by measuring the thermal derivative of the uniform magnetization, $\frac{dM}{dT}$. Previously, workers have interpreted such measurements in terms of equilibrium phenomena. Specifically, taking the scaling form of the equilibrium free energy as $F = |t_H|^{2-\alpha_{REIM}} f(AH^2/|t_H|^{\phi})$, where $t_H = (T - T_N - BH^2)/T_N$ and assuming a sharp phase transition and random field behavior within a cross-over region, then $f(x) \rightarrow (x - x_o)^{2-\alpha_{RFIM}}$ is expected [48]. In this region it was argued that the thermal derivative of the uniform magnetization in equilibrium would have a singularity of the form [65],

$$\left(\frac{\delta M}{\delta T}\right)_H \sim H^{\frac{2}{\phi}(1+\alpha_{RFIM}-\alpha_{REIM}-\frac{\phi}{2})} |(T - T_C(H))/T_N|^{-\alpha_{RFIM}} \tag{3.5}$$

If $\alpha_{RFIM} > 0$, a divergence would be expected at the equilibrium transition. Some previous reports on bulk thermodynamic studies claimed to have observed logarithmically divergent heat capacity with $\alpha_{RFIM} = 0$ [132, 65, 147]. However, there lacks accurate predictions for α_{RFIM}. Recent theory suggests that $\alpha_{RFIM} = -0.1$ [45], so there should actually be a cusp in equilibrium.

Figure 3-13 also shows ZFC and FC $\frac{dM}{dT}$. The derivative is calculated from the difference between successive data points, ΔM divided by the temperature interval, ΔT. The ZFC data generally displays a more prominent peak compared to the FC data, emphasizing the hysteresis in the transition region. At low fields a relatively sharp peak is observed. The peak broadens and moves to lower temperatures as the field is increased. Similar to the fit to the neutron (1,-0.003,0) intensity, the ZFC $\frac{dM}{dT}$ data may be modeled with a square root Lorentzian, placed on a stepped background with a linear slope connecting the two levels [108]. The width of the squre root Lorentzian, as a measure of the transition broadening, is again found to be consistent with H^2 scaling. An alternative method of analysis is simply to subtract the FC $\frac{dM}{dT}$

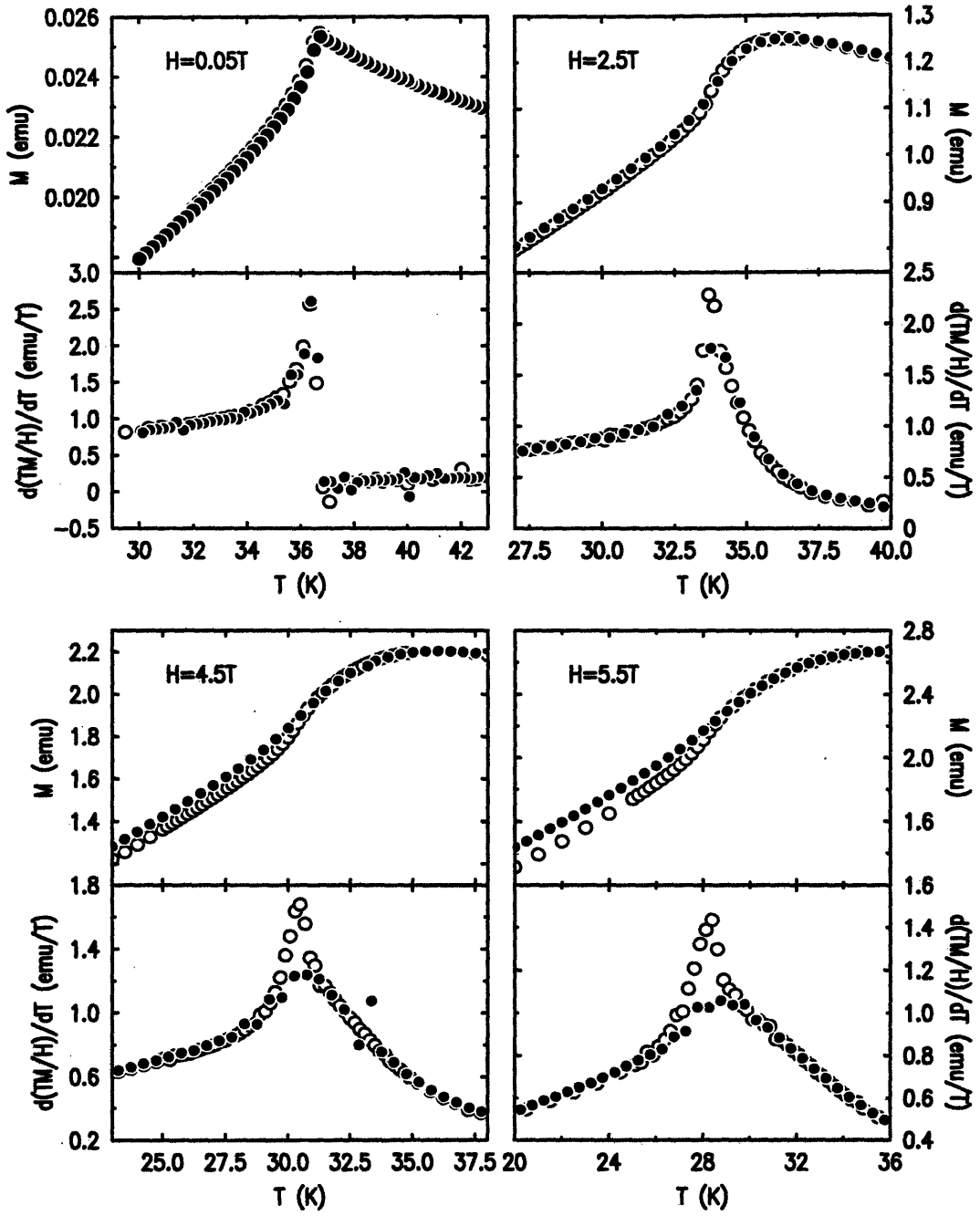

Figure 3-13: Hysteresis in uniform magnetization and its thermal derivatives measured on $Fe_{0.5}Zn_{0.5}F_2$. Data are taken at H=0.05T, 2.5T, 4.5T and 5.5T. Hysteretic effects, showing through an excess uniform magnetization, M_{ex}, for FC runs (closed circles) and more prominent thermal derivative peaks, $\frac{d(TM/H)}{dT}$, for ZFC runs (open circles), grow with increasing field.

from the ZFC $\frac{dM}{dT}$. The resultant peak width again scales as H^2. This agreement of the scattering and magnetization measurements of the field scaling of the transition widths is not coincidental and leads to ideas which are useful in interpreting the hysteresis of ZFC and FC protocols observed in indirect heat capacity measurements.

Similar hysteretic behavior was observed in SQUID measurements of $Mn_{0.45}Zn_{0.55}F_2$ as well. These data will be discussed in conjunction with additional x-ray scattering results in the next chapter.

3.3.5 Direct Heat Capacity Measurements

In this section we present direct semi-adiabatic heat capacity results obtained from two samples of $Mn_{0.75}Zn_{0.25}F_2$ and $Fe_{0.5}Zn_{0.5}F_2$. ZFC data between 0T and 9T for $Mn_{0.75}Zn_{0.25}F_2$ that led to a mapping of the phase boundary were presented in figure 2-17. The overall behavior of ZFC C_m is closely similar to the ac specific heat data on $Mn_{0.5}Zn_{0.5}F_2$ reported by Ikeda *et al.* [85, 68] and heat capacity data on $Fe_{1-x}Mg_xCl_2$ and $Fe_{1-x}Co_xCl_2$ by Wong *et al.* [122, 49, 51]. There is no evidence of diverging C_m peaks.

Little hysteresis was observed in the ZFC, FC and FH thermal cycles performed at various fields on $Mn_{0.75}Zn_{0.25}F_2$. Figure 3-14 shows ZFC and FC C_m data taken at fields between H=2T and H=7T. The only discernible hysteresis is that the FC peaks are slightly lower than the ZFC peaks for fields above H=3T. The FH peaks (not shown in figure 3-14) are virtually identical to ZFC peaks at all fields. The peak shape changes drastically near the bicritical point, as is apparent in the data taken at H=6T and H=7T, where the peaks seem to show some structure. Although there are some published results on LMB studies of $Mn_{1-x}Zn_xF_2$ [62, 148], only ZFC data have been reported. The insignificant hysteresis observed here is in agreement with direct heat capacity measurements on similar DAFFs $Mn_{0.5}Zn_{0.5}F_2$ [85, 68] and $Fe_{1-x}Mg_xCl_2$ [49, 51].

Neutron scattering has shown that, though the FC state has only SRO, the LRO state is recovered by lowering the field to zero after FC in the weakly anisotropic

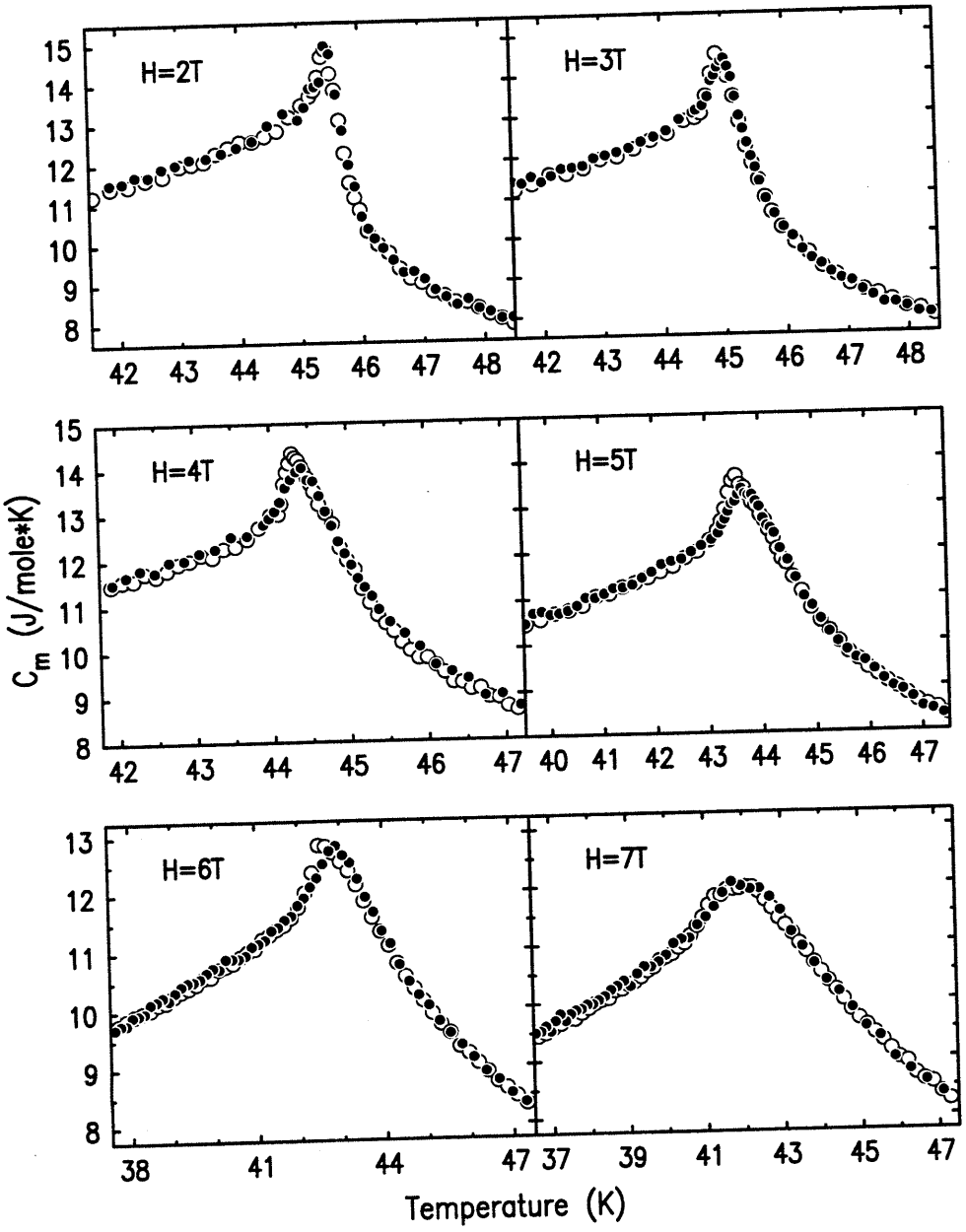

Figure 3-14: Direct heat capacity data on $Mn_{0.75}Zn_{0.25}F_2$ during ZFC (open circles) and FC (closed circles) between 0T and 7T. The data show little hysteresis.

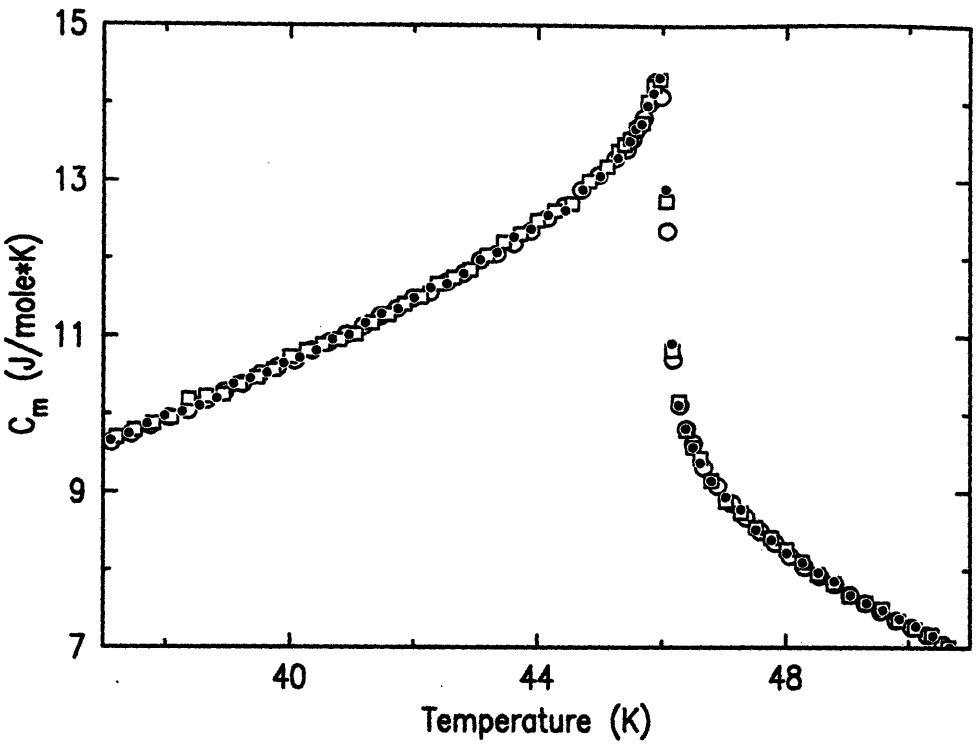

Figure 3-15: Direct heat capacity data on $Mn_{0.75}Zn_{0.25}F_2$ at 0T with various preparation: the open circles are data taken after cooling in zero field; the open squares and the closed circles are data taken after field cooling at 6T and 8T to 30K respectively and then the field removed. The three data sets are identical.

$Mn_{1-x}Zn_xF_2$. In figure 3-15, we compare $Mn_{0.75}Zn_{0.25}F_2$ C_m taken after cooling in zero field and that taken after cooling at H=6T and H=8T and then switching off the field. The three data sets are identical.

In figure 3-16, we present magnetic heat capacity of $Fe_{0.5}Zn_{0.5}F_2$ at H=0T, 1.5T and 5.5T. The zero field cusp of C_m is very similar to that of $Mn_{0.75}Zn_{0.25}F_2$. But the peak is much subdued at H=1.5T and almost completely disappears at H=5.5T. The data do not reveal any difference between the ZFC and the FC protocols. This is in drastic contrast to the strong hysteresis seen in LMB and magnetometry measurements of $Fe_{1-x}Zn_xF_2$ [149, 84], including the SQUID data presented above. This raises the doubt that the indirect techniques may not represent true magnetic heat capacity in these measurements. It is puzzling when we compare the heat capacity results here with those by Dow and Belanger [150], who used a similar technique but claimed to have observed hysteresis in $Fe_{0.46}Zn_{0.54}F_2$ resembling that in the LMB

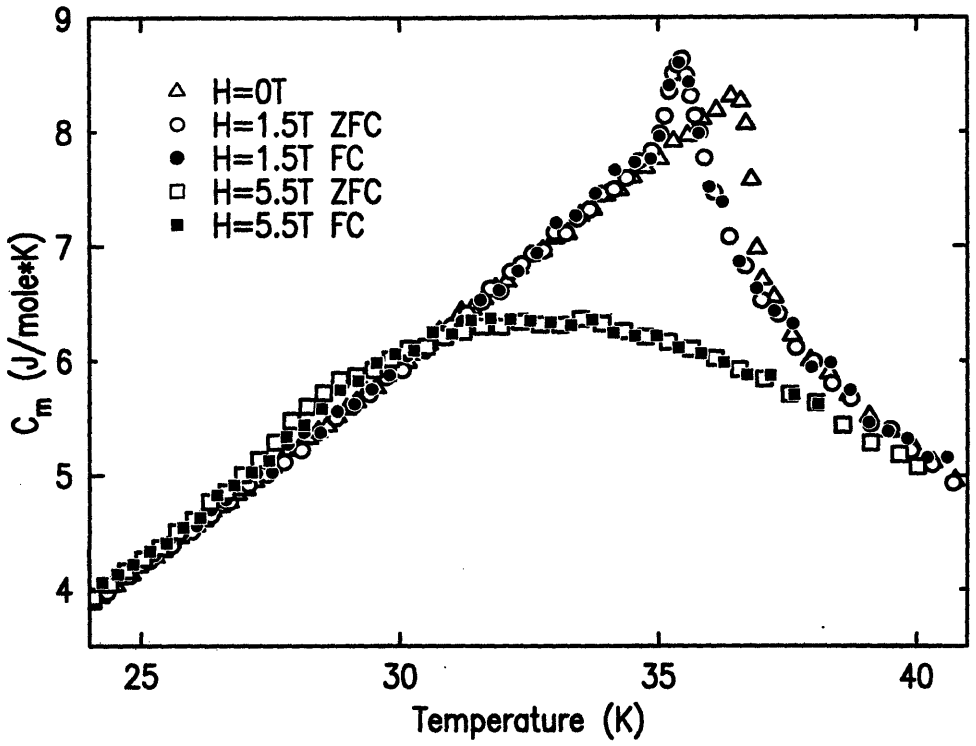

Figure 3-16: Direct heat capacity data on $Fe_{0.5}Zn_{0.5}F_2$ at 0T,1.5T and 5.5T. No hysteresis can be observed in the data.

results. We do not understand the cause of this discrepancy.

Two important results emerge from these measurements on $Mn_{0.75}Zn_{0.25}F_2$ and $Fe_{0.5}Zn_{0.5}F_2$. First, no clear evidence of a logarithmic heat capacity divergence is observed in either system. This is also the case for all the other direct heat capacity data known to us. However, evidence pointing to a diverging RFIM critical heat capacity was reported on LMB [61] and Faraday rotation [82] measurements. This has been a puzzle for a long time. For the direct ac heat capacity method used by Ikeda *et al.* which revealed non-diverging cusps at the transition [85, 68], Dow and Belanger[150] argued that the ac measurements were carried out on such short time scales that strong nonequilibrium effects had obscured any new critical phenomena or hysteresis. In the current study, each datum point is taken on a time scale of 20 to 30 seconds. Although time-dependent effects due to metastability near and below the transition will invariably affect measurements taken on any finite time scales, we believe that our data are taken on comparable time scales with those of the LMB

studies and nonequilibrium effects do not explain our inability to see the same critical anomalies as those in LMB and Faraday rotation. What may have had an adverse effect on our measurements, however, is the temperature drift at each datum point and the concentration gradient in the samples. The temperature drift effectively causes a smearing of $\Delta T \approx 0.05$K and $\Delta T \approx 0.1$K in the ZFC and FC C_m peaks respectively. The concentration gradient, though small as evidenced by the sharpness of the zero field C_m peak, can also contribute to the rounding of the transition. We estimate the concentration smearing to be $\Delta T \leq 0.1$K for the $Mn_{0.75}Zn_{0.25}F_2$ sample and $\Delta T \leq 0.2$K for the $Fe_{0.5}Zn_{0.5}F_2$ sample. Although the combined effects may have obscured certain features of the low field data, they should have had negligible influence on the appearance of the C_m cusps or any hysteresis at high fields. We note that $Fe_{0.5}Zn_{0.5}F_2$ displays observable hysteresis over a temperature range of approximately 2.5K near the transition at 5.5T, as evidenced in the uniform magnetization data presented above, much broader compared to the inherent smearing due to the heat pulse technique or the sample concentration gradient.

As noted before, at the same applied field, the effective strength of the random fields is very different in $Mn_{0.75}Zn_{0.25}F_2$ and $Fe_{0.5}Zn_{0.5}F_2$[50]. This may explain why the $Mn_{0.75}Zn_{0.25}F_2$ sample shows clear C_m peaks all the way up to H=6T while the random fields have completely destroyed any anomaly in the $Fe_{0.5}Zn_{0.5}F_2$ sample at H=5.5T. This, and the onset of the spin-flop phase at $H \approx 7$T, makes $Mn_{0.75}Zn_{0.25}F_2$ less ideal a RFIM system than $Fe_{0.5}Zn_{0.5}F_2$. Below H=5T in $Mn_{0.75}Zn_{0.25}F_2$, the effective RF in the sample is relatively small and one might observe crossover effects between REIM and RFIM. For H >5T, the C_m peak changes drastically and reflects the closeness of the bicritical point as well as RF effects. On the other hand, $Fe_{0.5}Zn_{0.5}F_2$ clearly exhibits strong random field effects. The C_m cusp at H=1.5T and the disappearance of any peak at H=5.5T is in keeping with Monte Carlo results by Ogielski and Huse [35] and with real space RG work by Dayan *et al.* who noted that the magnetic specific heat saturated and showed "no tendency to diverge" at the phase boundary [46]. This necessitates a negative α_{RFIM} (if there is indeed a second order phase transition). More recent Monte Carlo simulations by Rieger *et al.*[33, 36]

demonstrated the transition in RFIM to be weakly first order and the specific heat to show no "indication of a divergence, even logarithmic", with $\alpha_{RFIM} = -1$ and $\alpha_{RFIM} = -0.5$ for binary and Gaussian random field distributions respectively. Recent series expansion work by Gofman *et al.* suggested $\alpha_{RFIM} = -0.1$ [45]. These results, together with most of the direct heat capacity data available, strongly disagree with the logarithmic divergence suggested by LMB [61] and Faraday rotation experiments [82]. This brings to attention the applicability of the optical and magnetometry techniques in studying magnetic heat capacity in a system characterized by randomness and impurities. We look at these indirect techniques more carefully in the next section.

The second prominent feature of the direct heat capacity data is the absence of any significant hysteresis in both the strongly and the weakly anisotropic systems studied here. This is in sharp contradiction with results from indirect magnetic heat capacity tools. Most of the techniques that are applied in the study of the RFIM, such as magnetic x-ray and neutron scattering which probe the staggered magnetization M_S or LMB, Faraday rotation and magnetometry which probe the uniform magnetizations M, are all sensitive to the microscopic spin configurations and the long range correlations. Therefore the presence of LRO in the ZFC state and its absence in the FC state, and the difference in average sizes of the FC and FH magnetic domains are reflected directly and indirectly in these measurements and give rise to the observed hysteresis. The direct heat capacity technique, on the other hand, measures local energy fluctuations. In a DAFF, large domains are frozen on experimental time scales due to the anomalous RF dynamics [151, 152] and C_m reflects energy required to flip local spin clusters. Further, a characteristic feature of the RFIM is that, at temperatures close to the phase boundary, there exist many different spin configurations (with or without LRO) that differ little in free energy [122, 153]. It is therefore not surprising that C_m appears to be insensitive to the differing spin configurations and long range correlations, and hence manifests little detectable hysteresis. This explains the seemingly contradictory results from direct heat capacity and other bulk thermodynamic techniques. Monte Carlo simulations

and mean field theoretical studies by Grest *et al.* [153] showed little difference between the ZFC and the FC specific heat, though the authors speculated that the small hysteresis at lower fields might have been a finite-size effect. In view of our current data on C_m at a variety of fields and the reports by other direct technique experiments [122, 85, 68], the small hysteresis is to be expected of the DAFFs.

3.4 Indirect Heat Capacity Results Revisited

The comprehensive results presented above emphasizes the apparent discrepancy between interpretations of indirect heat capacity measurements and all the other experimental techniques. Specifically, bulk thermodynamic probes, such as birefringence and SQUID measurements, show sharp ZFC peaks that have previously been interpreted as reflecting equilibrium critical behavior, described by a critical exponent α_{RFIM}, together with some small dynamic rounding. On the other hand, the x-ray and neutron scattering data demonstrate that the transition from the ZFC LRO state is not an equilibrium transition characterized by critical exponents, but rather proceeds with a smooth, rounded power-law decay of the order parameter and a finite maximum correlation length. This is corroborated by direct heat capacity data that exhibit rounded cusps rather than diverging peaks in the presence of random fields. Further, the conspicuous hysteresis revealed by indirect techniques is not observed in direct heat capacity measurements.

This conflict necessarily leads to a re-interpretation of the indirect heat capacity measurements. Motivated by the similarity in the field scaling of the ZFC transition broadening between the thermal derivative of the magnetization data and the scattering data, one is led to speculate that the strong hysteresis of the bulk thermodynamic measurements arises from the presence of the non-equilibrium LRO in the ZFC state. The hypothesis is as follows: For indirect specific heat measurements, which are based on measuring quantities proportional to the two spin correlation function, there are two contributions to the signal. The first term is proportional to the magnetic energy, arising from the local energy fluctuations. The second, new term, is proportional to

the staggered magnetization squared M_s^2, the LRO. In a conventional second order transition, $M_s^2 \sim t^{2\beta}$. For derivative measurements this LRO term is typically the stronger singularity for $T < T_N$ and should be especially important in the current case for which the heat capacity fluctuations are not divergent due to the dynamics. Most importantly, the LRO term for RFIM systems will contribute to ZFC but not FC measurements where only SRO exits. We make the additional assumption that the fluctuation contribution to $\frac{d(TM)}{dT}$, which is determined by short range correlations, is not very different for FC and ZFC measurements. This is evidenced by neutron measurements of the correlation length which is the same for ZFC and FC at and above T_C. Therefore, as a first approximation the ZFC $\frac{d(TM)}{dT}$ should be equal to the FC result plus the $\frac{dM_s^2}{dT}$ contribution.

In figure 3-17, we demonstrate how to apply this hypothesis quantitatively by comparing neutron and SQUID data taken at H=5.0T on $Fe_{0.5}Zn_{0.5}F_2$. The top panel shows the neutron data for the LRO (C in equation 2.20) and the (1,-0.003,0) critical scattering amplitudes. The solid line is the Gaussian-rounded power law. The bottom panel shows the temperature derivative of both the ZFC and FC magnetization data. The temperature scales are normalized so that they agree at zero field. In figure 3-17 we have shifted the neutron data by an additional 0.3K, as indicated by the small arrow at the top of the figure. This is motivated by the physically compelling argument that $\frac{d(TM)}{dT}$ should have its maximum at the same temperature for which the correlation length is a maximum [139], a point made clear by figure 3-12. It is important to note that this subtle temperature shift also serves to bring $T_M(H)$ into agreement for the two techniques. In any case, that the temperature scale shift is within the combined temperature uncertainties of the neutron and the SQUID measurements. The ZFC $\frac{dM}{dT}$ data are reconstructed by taking the neutron measurement of M_s^2 (solid line, top panel), differentiating with respect to T and adjusting the amplitude of $\frac{dM_s^2}{dT}$ (dashed line, bottom panel) and adding it to the SQUID FC data. This procedure results in the solid line in the bottom panel. The agreement with the actual data is excellent.

Since we have demonstrated earlier that the LRO measured by neutron and x-

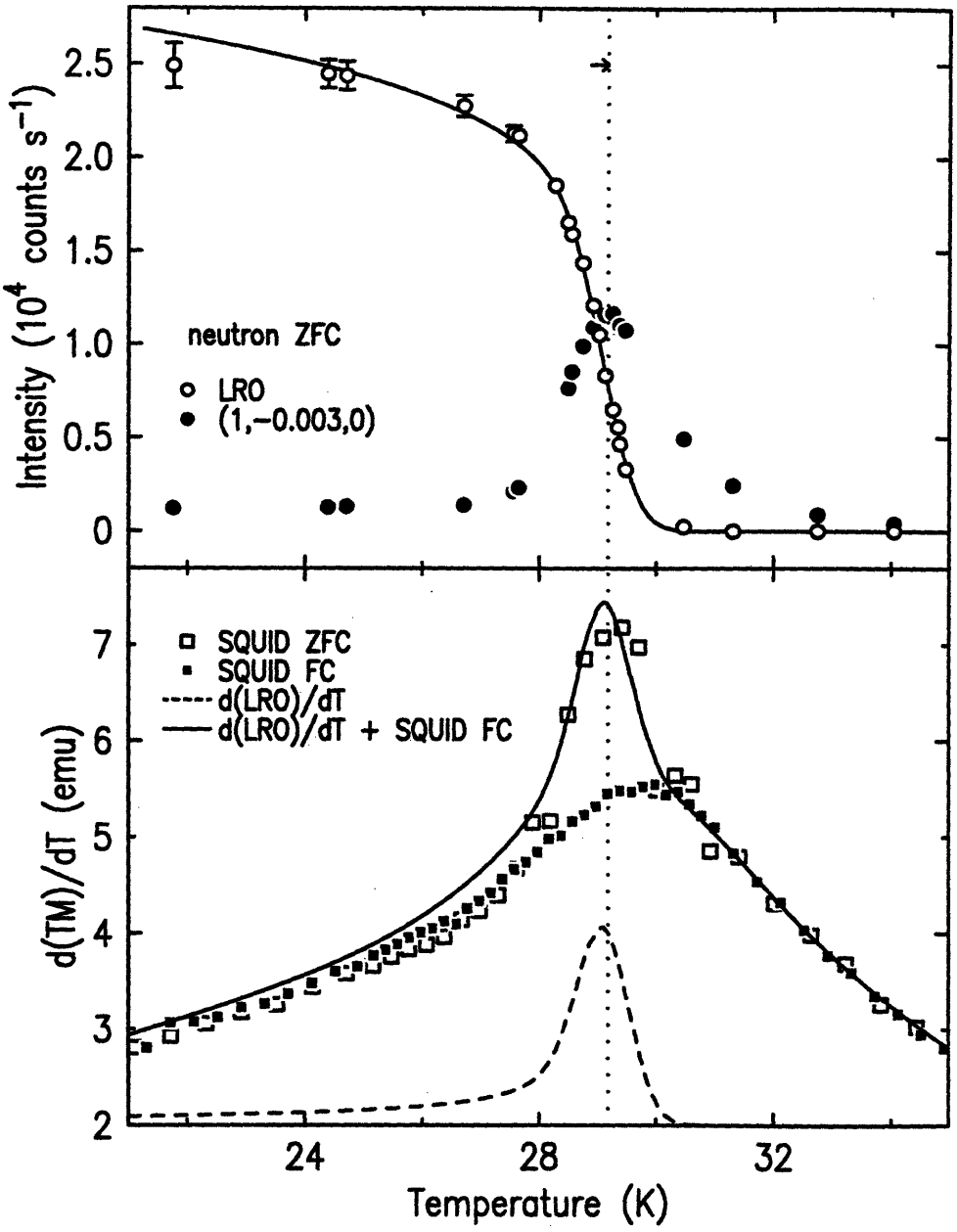

Figure 3-17: Top Panel: Neutron scattering intensity at (1,0,0) and (1,-0.003,0) at H=5T. The solid line is the result of a fit to the rounded power-law decay of equation 3.1. The small arrow at the top indicates the 0.3K shift in the neutron data temperature scale. Bottom panel: FC and ZFC data for $\frac{d(TM)}{dT}$ at H=5T. The dashed line is the $\frac{dM_s^2}{dT}$ contribution. Only the amplitude has been adjusted. The solid line is the sum of the FC data plus the $\frac{dM_s^2}{dT}$ term.

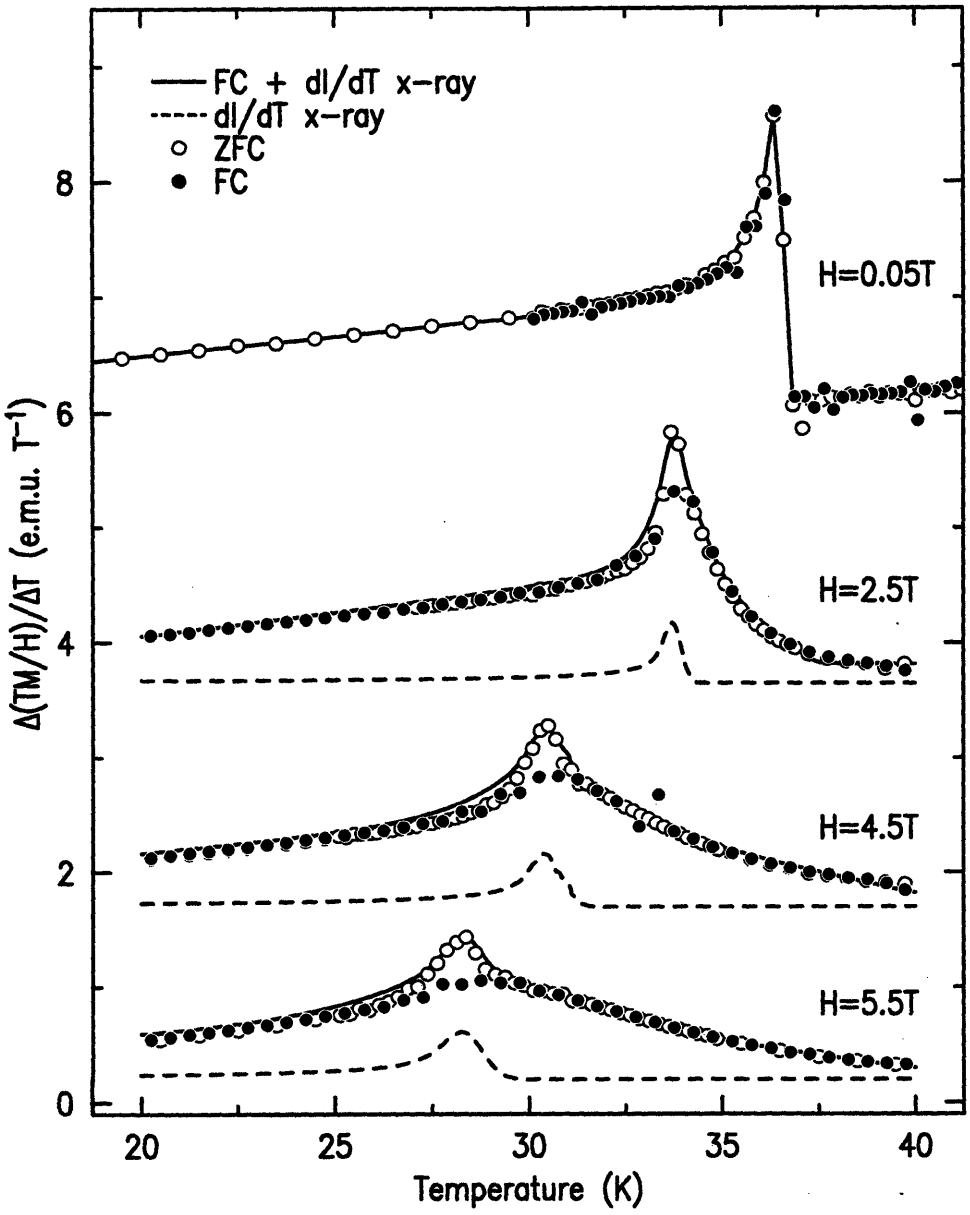

Figure 3-18: The temperature derivative of the uniform ZFC and FC susceptibilities, as measured by SQUID magnetometry. The dashed line corresponds to the temperature derivative of the x-ray intensity scaling function, with the intensity scaled to match the difference in the ZFC and FC results. The solid line is the sum of the FC $\frac{d(TM/H)}{dT}$ and $\frac{d(M_s^2)}{dT}$.

ray scattering are equivalent in the transition region, it is expected that this model also works in comparing x-ray and SQUID data. The results of such analysis are shown in figure 3-18 , in which we use the scaling function obtained from the x-ray data to reconstruct the ZFC $\frac{dM}{dT}$ data for a series of fields, based on the FC data at corresponding fields. Again, only the amplitude of the $\frac{dM_s^2}{dT}$ contribution has been adjusted. The width of the $\frac{dM_s^2}{dT}$ piece is held fixed at the value obtained from the H^2 scaling law of the x-ray data (figure 3-4). The agreement is very good at all the fields where there is observable hysteresis.

We further test this approach on published birefringence data, as shown in figure 3-19. In the upper panel, we show data of Ferreira *et al.* [64] taken on a sample of $Fe_{0.46}Zn_{0.54}F_2$ of very high quality. The solid line is the prediction for the ZFC $\frac{d\Delta T}{dT}$ data. The $\frac{dM_s^2}{dT}$ piece is determined from the H^2 scaling of our x-ray measured transition width for $Fe_{0.5}Zn_{0.5}F_2$ and with the H=0T width taken to be zero to account for the higher quality crystal. The FC data are used as the background that arises from non-critical fluctuations. $T_C(H)$ was adjusted slightly from the value determined in our experiments on $Fe_{0.5}Zn_{0.5}F_2$. The agreement is satisfactory. In the lower panel of figure 3-19 we show similar birefringence data [154] and analysis for $Fe_{0.6}Zn_{0.4}F_2$. In this case, the the peak width is fitted at H=4T and the width at the other fields are then determined in the construction using the H^2 law with respect to the 4T width. The agreement between the constructed lines the and the actual ZFC data is compelling.

This remarkable success of the simple phenomenological re-interpretation of the indirect heat capacity measurements is not incidental. Although there is no theory behind this idea that is rigorously applicable to the DAFFs, a number of authors have previously considered the presence of a LRO term for various types of bulk measurements in other systems. For example, Fisher and Langer noted the presence of a LRO term in $\frac{d\rho}{dT}$ for $T < T_C$ in resistive measurements of the specific heat [155]. For a diluted antiferromagnet, Fishman and Aharony [48] argued that a M_s^2 term needs to be included in the uniform susceptibility even in zero field. This term arises from bond disorder and is absent in pure systems. It is not the same as the

M_s^2 term in the postulate presented here, which arises from random fields and goes to zero at H=0T for a diluted antiferromagnet. For measurements performed on diluted systems in a field, Wong [156] has speculated that there is an additional singularity that arises from the Zeeman energy in the indirect heat capacity techniques. Finally, for birefringence measurements on Ising systems, Ferre and Gehring showed that $\Delta n^{zx} \sim \sum_r g(r) < S_0^z S_r^z > \sim AU + BM_s^2$, where U is the magnetic energy and B=0 only under two stringent conditions [157]: First, $g(r)$ and $J(r)$ (exchange interaction) are strictly proportional for all r, and second, correlation length is long compared with the range of both $g(r)$ and $J(r)$. It is not clear that these conditions are strictly satisfied for the RFIM. Therefore, on general grounds, one is led to expect that all these indirect specific heat measurements may contain a LRO term unless it is symmetry forbidden. Such a term may cancel under certain particular conditions, for instance in zero field. But both theoretical ideas and experimental evidence strongly suggest that in general a $\frac{dM_s^2}{dT}$ term is present in measured quantities such as $\frac{dM}{dT}$ and $\frac{d\Delta T}{dT}$.

3.5 The Nature of the RFIM Transition

Although it was determined a long time ago that the equilibrium ground state of the 3d random field Ising model is one of long range ordering for weak field strength [158], an equilibrium transition from the disordered paramagnetic state to a long range ordered low temperature state has not been observed experimentally. Instead, on cooling in a field, diluted antiferromagnets freeze into a short range ordered metastable domain state. This is one of the symptoms of the pathologically slow random field dynamics which make a direct observation of the equilibrium critical behavior impossible. However, a state presumptively closer - in energy and magnetic configuration - to the LRO ground state can be prepared by first letting LRO evolve in zero field through the random exchange Néel transition and then introducing the random fields. Although this ZFC state has retained certain frozen-in magnetic ordering and is in fact metastable, the shedding of its LRO may offer some insight on true RFIM critical

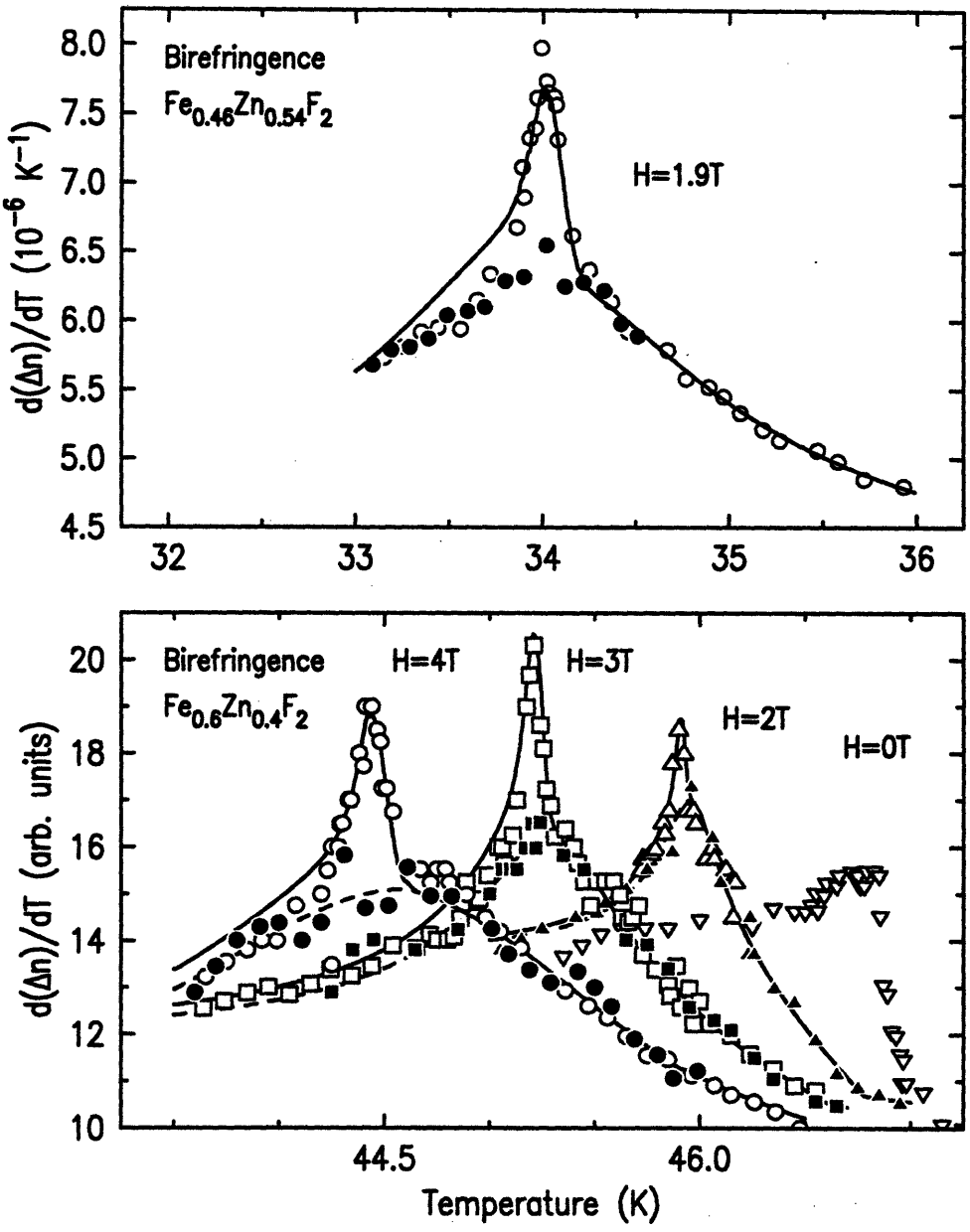

Figure 3-19: Top panel: Linear magnetic birefringence data taken from Ferreira, King and Jaccarino [64] for $Fe_{0.46}Zn_{0.54}F_2$. The solid line is the FC data plus the contribution from the $\frac{d(M_s^2)}{dT}$ term. Bottom panel: Similar results and analysis for $Fe_{0.6}Zn_{0.4}F_2$ [154]. In each panel, the open symbols are ZFC data and the closed symbols are FC results.

behavior. Yet the same anomalous critical slowing down that prevents the build-up of LRO during field cooling also obscures the ZFC transition, the effects of which include a rounded diminution of the order parameter, a non-diverging correlation length, broadened bulk thermodynamics peaks and smeared magnetic heat capacity - all happening in a superheated temperature regime. These symptoms worsen as the random field strength increases. In this chapter we have presented a comprehensive study of the ZFC transition utilizing x-ray and neutron scattering, uniform magnetization and direct heat capacity techniques. The scattering measurements of the order parameter and correlation length suggest that the ZFC transition is weakly second order in nature. Although the anomalous dynamics preclude an accurate measurement of the critical exponents, the order parameter is observed to decay through a continuous power-law-like transition with an average exponent, $\beta_{ZFC} = 0.12 \pm 0.04$ for $Fe_{0.5}Zn_{0.5}F_2$ and $\beta_{ZFC} = 0.19 \pm 0.03$ for $Mn_{0.45}Zn_{0.55}F_2$. The rounded transition may be modeled by a Gaussian distribution of transition temperatures, centered at $T_C(H)$. The progressively larger rounding observed with increasing field is reflected in $\sigma_{ZFC}(H) \sim H^2$, contrary to the previously reported field dependence of $H^{2/\phi}$ with $\phi = 1.41$ [79]. Using finite size arguments and empirical scaling relations for the correlation length, it can be shown that $\sigma_{ZFC} \sim H^{2.2\pm0.7}$, in approximate agreement with experiments. In addition, the width of the transition may also be estimated from the temperature width of the peak in the neutron critical scattering and from the thermal derivative of the uniform magnetization. Both yield an $\sim H^2$ dependence. The correlation length is found to reach a finite maximum at $T_C(H)$, but it does not diverge as expected of an equilibrium second order transition.

These results lead us to believe that there is no equilibrium phase transition after zero field cooling a random field system. The observed pseudo-critical behavior simulates ordinary critical phenomena at a second order transition, but in fact reflects a finite size effect due to nonequilibrium local fluctuations limited in size by random fields. This has previously been labeled the *trompe l'oeil* critical behavior. This interpretation differs from that given in some previous studies of ZFC behavior in DAFFs, mostly with indirect heat capacity methods [132, 79, 66, 63, 143, 64, 135]. In these

papers, the ZFC behavior is argued to largely reflect true equilibrium critical behavior of the RFIM with the addition of a relatively small amount of dynamic rounding. Since the data presented here and those reported in refs. [132, 79, 66, 63, 143, 64, 135] are entirely consistent with each other and only the interpretations differ, we attempt to reconcile the discrepancy by introducing a new understanding of the sharp ZFC peaks and ZFC-FC hysteresis in the thermal derivatives of physical quantities measured (M, Δn, θ, etc.) in these bulk thermodynamic techniques. Taking the thermal fluctuations in the ZFC and FC state to be similar, we postulate that the ZFC data are the sums of the FC fluctuations and a LRO piece which may be derived from the x-ray measurements. This model is physically motivated and yields a satisfactory agreement with both our own SQUID magnetization data and published birefringence data. In this phenomenology, the ZFC peaks of indirect heat capacity measurements arise solely from the decay of the superheated LRO and not from critical fluctuations. This is also confirmed by the direct heat capacity measurements presented above that show neither a critical contribution nor measurable hysteresis.

Chapter 4

Field Cooled Ordering: In Search of the Equilibrium Transition

4.1 Introduction

In this chapter we study the ordering process during field cooling a DAFF. The hysteresis in the RFIM has been a well studied subject by many techniques. The underlying difference in spin configurations between the ZFC and the FC states has been directly clarified by neutron and x-ray scattering. In particular, it is well established by neutron scattering results on several DAFF systems [67, 71, 75, 159, 72, 160, 102] that, well below the phase boundary, the ZFC state maintains a long range ordered state reflected by resolution limited scan profiles while the FC state is short range ordered resulting in line shapes that are broader than the resolution. The range of the ordering, or the size of the domains, can be determined by fitting the profiles to the cross section suitable for a RFIM system, i.e. equation 4.1. The disparate behavior of the ZFC and the FC protocols has also been observed in Monte Carlo simulations [161, 162, 163, 164, 86]. It is believed that the SRO in the FC state develops because of the anomalous dynamics in the RFIM. Such dynamics obscure the underlying phase transition, particularly for FC, and make it difficult to determine the order of the transition or obtain accurate measurements of the critical exponents.

Since the ZFC state is presumptively close to the equilibrium long range ordered

ground state of the 3d RFIM and the ZFC transitions sometimes display sharp and distinctive features in observable quantities, they have been under intense study by many experimental methods. The interpretation of the ZFC transition behavior has been a long standing controversy. The problem arises from the contradiction between some early indirect heat capacity measurements, such as linear magnetic birefringence, which were interpreted in terms of new equilibrium random field critical behavior [62, 61] and neutron scattering measurements that found the correlation length did not diverge [67]. This discrepancy has been reconciled in the previous chapter. At moderate random fields, the ZFC transition is apparently a superheated one that differs from the true random field transition, even though some of its features (such as a small β_{ZFC}) may reflect the underlying equilibrium transition.

On the other hand, experiments in the field cooled state have mostly concentrated on measuring the scaling of domain size with random field strength [67, 71] and the time dependent behavior [134, 82, 83, 84]. The field cooling transition, severely out of equilibrium and usually revealing little feature, has not been studied as much as the ZFC transition. However, there exists a well defined metastability temperature, $T_M(H)$, above which no hysteresis is ever observed. As the sample is cooled from the paramagnetic state into the domain state, it is expected to remain in equilibrium for $T > T_M(H)$ and critical behavior dominated by random fields is observable within a certain temperature range above T_M. From the correlation length measured by neutron scattering above $T_M(H)$, one may be able to extract the exponent ν unique to the RFIM and even extrapolate the equilibrium random field Néel temperature $T_N(H)$, assuming the existence of a second order phase transition. This approach has been attempted previously by several workers [75, 71] and the values of several random field critical exponents were estimated, though the metastability temperature was not well defined in these studies and there were signs of random exchange crossover behavior either due to weak random field strength or inappropriate temperature ranges. In the current study, we continue to pursue this viable approach through a double-axis neutron scattering study on the prototypical DAFF $Fe_{0.5}Zn_{0.5}F_2$ and measure the correlation length above $T_M(H)$ but below the zero field T_N. From the data, we are able

to extract the correlation length exponent ν, the connected susceptibility exponent γ, the disconnected susceptibility exponent $\bar{\gamma}$ and identify an equilibrium random field transition temperature $T_N(H)$. We compare these values with previous experimental results and current theoretical estimates.

The advent of synchrotron magnetic x-ray scattering has brought new excitement to the RFIM research. It has proven to be an ideal tool for measuring the order parameter in the ZFC transition [165, 70], and has also led to unexpected discoveries on the field cooling transition. In their magnetic x-ray scattering study on a sample of $Mn_{0.75}Zn_{0.25}F_2$, Hill *et al.* first discovered long range ordering in the field cooled state [140, 60]. This directly contradicted neutron scattering results. The observation of the FC LRO raised questions regarding its origin and opened up the prospects of studying equilibrium critical properties of the RFIM. In the current study, we further the x-ray investigation on the ordering process and the magnetic configurations following the FC protocol by studying two different compounds, $Fe_{0.5}Zn_{0.5}F_2$ and $Mn_{0.45}Zn_{0.55}F_2$. The results reported here not only confirm that FC LRO exists in systems other than $Mn_{0.75}Zn_{0.25}F_2$, but also provide more detailed information on how it varies with temperature and applied fields.

In the current work, we have carried out an x-ray study on two different DAFFs, $Fe_{0.5}Zn_{0.5}F_2$ and $Mn_{0.45}Zn_{0.55}F_2$, in order to address the following issues: First, is the FC LRO unique to the LRO sample of $Mn_{0.75}Zn_{0.25}F_2$, or a feature of weakly anisotropic Ising systems, or is it more universal? Second, what are the temperature and field dependences of the LRO and SRO that coexist in the field cooled state?

4.2 Previous Results on $Mn_{0.75}Zn_{0.25}F_2$

The approach of measuring correlation length and susceptibility in the equilibrium temperature region above the metastability boundary has been previously used in the analysis of neutron scattering measurements by Cowly *al.* on $Mn_{0.75}Zn_{0.25}F_2$ [71], and by Belanger *et al.* on $Fe_{0.6}Zn_{0.4}F_2$ [75]. Although this was a logical approach in search of the equilibrium random field critical behavior, some caveats existed in these

studies. For example, the metastability temperature was not well defined, and the analysis might have included data outside of the random field critical region, raising concerns about random exchange crossover. We will compare our own analysis with these existing results later in the chapter.

The first and only evidence of long range magnetic order in a field cooled DAFF has, until the current work, been observed in the magnetic x-ray scattering experiments on one sample of $Mn_{0.75}Zn_{0.25}F_2$ by Hill *et al.* For the two $Mn_{0.75}Zn_{0.25}F_2$ samples used in their study, completely different ordering was observed. In one sample, labeled the SRO sample, hysteretic behavior similar to that in neutron scattering was observed - LRO in the ZFC state and the FC state is completely occupied with SRO. However, another sample, labeled the LRO sample and obtained from the same boule as the SRO sample, demonstrated LRO in the FC state as well as in the ZFC state. The FC state indicated a coexistence of LRO and SRO, reflected in some diffuse tails and a smaller LRO intensity compared to the ZFC state. At H=6T, for example, the intensity of the resolution-limited peak in the LRO sample showed that approximately half of the illuminated volume in the sample achieved long range order, with domain size in excess of 20000Å.

Several important results emerged from the x-ray study on the LRO sample. First, because neutron scattering did not discern any LRO at H=6T in $Mn_{0.75}Zn_{0.25}F_2$ [71], it was suggested that the observed LRO came from the near surface region of the sample which dominates the signal in an x-ray experiment but makes a vanishingly small contribution to neutrons. The temperature dependence of the FC LRO intensity was found to fit to a power law, $I \sim t^{2\beta}$, with $\beta_{FC} \approx 0.3$, which is close to the pure Ising or random exchange Ising value. Further, the long range order was found to develop at a temperature, labeled $T_N(H)$, below the metastability boundary, $T_M(H)$. At H=6T, $T_M - T_N \approx$1.2K.

The apparent contradiction in the x-ray results from the two $Mn_{0.75}Zn_{0.25}F_2$ samples were attributed to the different surface qualities of the two samples that resulted from different polishing processes. The LRO sample went through a less refined polishing and had a surface with far more scratches than the SRO sample. Several

scenarios were invoked to describe how the surface defects might have nucleated ordering or caused an asymmetric distribution of the random fields that induced the formation of FC LRO in the near surface region. However, during subsequent field heating, the LRO intensity was found to be higher than that of FC and go to zero at T_M rather than T_N. This raised doubt about whether the transition to the LRO state in the near surface region was an equilibrium process. Although the ordering occurred close to T_C, it was unlikely that the appearance of LRO during field cooling represented a true equilibrium RFIM transition, at least not an equilibrium one in the usual sense.

4.3 Experimental Details

The room temperature lattice constants are a=b=4.71Å, c=3.24Åfor $Fe_{0.5}Zn_{0.5}F_2$, and a=b=4.87Å, c=3.31Åfor $Mn_{0.45}Zn_{0.55}F_2$. The samples used in the neutron and the x-ray study were cut from the same boules from which we obtained the crystals used for magnetization and heat capacity experiments reported in this work. Since surface preparation appeared to have made a decisive difference in the ordering in the two $Mn_{0.75}Zn_{0.25}F_2$ samples, we paid special attention to the polishing of the x-ray samples. Both the $Fe_{0.5}Zn_{0.5}F_2$ and the $Mn_{0.45}Zn_{0.55}F_2$ went through preparation processes similar to that applied to the SRO sample of $Mn_{0.75}Zn_{0.25}F_2$ which had a smooth surface with sparse scratches. The crystal surfaces were polished on a polishing wheel covered with *Buehler* felt and lubricant, and successively finer grit was used in each step. The final polishing was accomplished with 0.05μm Alumina powder on *Polytek Supreme* felt. In figure 4-1 and figure 4-2, we show surface images of the $Fe_{0.5}Zn_{0.5}F_2$ and $Mn_{0.45}Zn_{0.55}F_2$ samples taken with an environmental scanning electron microscope. The surfaces show some scratches that result from the polishing processes, most of which have a width (and a depth) of approximately 0.1μm. The surface quality is closer to that of the SRO $Mn_{0.75}Zn_{0.25}F_2$ sample.

The concentration homogeneity of the two samples is reflected in the zero field transition. A concentration gradient will reduce the sharpness of the transition. By

Figure 4-1: Image on the surface of the $Fe_{0.5}Zn_{0.5}F_2$ sample used for x-ray scattering, taken with an environmental scanning electron microscope. The white bar represents a length of 5μm.

fitting the temperature dependence of the zero field x-ray peak intensity at (100) to a rounded power law such as equation 3.1, one obtains a measure of the transition broadening, σ, and thereby the concentration variance in the illuminated volume. The fitted σ is 0.18K and 0.12K for the $Mn_{0.45}Zn_{0.55}F_2$ and the $Fe_{0.5}Zn_{0.5}F_2$ respectively. The crystallographic quality of the samples is illustrated by the transverse scan profile of the x-ray charge scattering peaks. At (200), the measured mosaic spread is 0.006° HWHM for both samples.

4.3.1 Experiments

The neutron scattering experiments were carried out on spectrometer H7 at the Brookhaven High Flux Beam Reactor. The data were taken in the energy integrating 2-axis mode with incoming energy of 14.7meV and 10'-10'-sample-10' collimations.

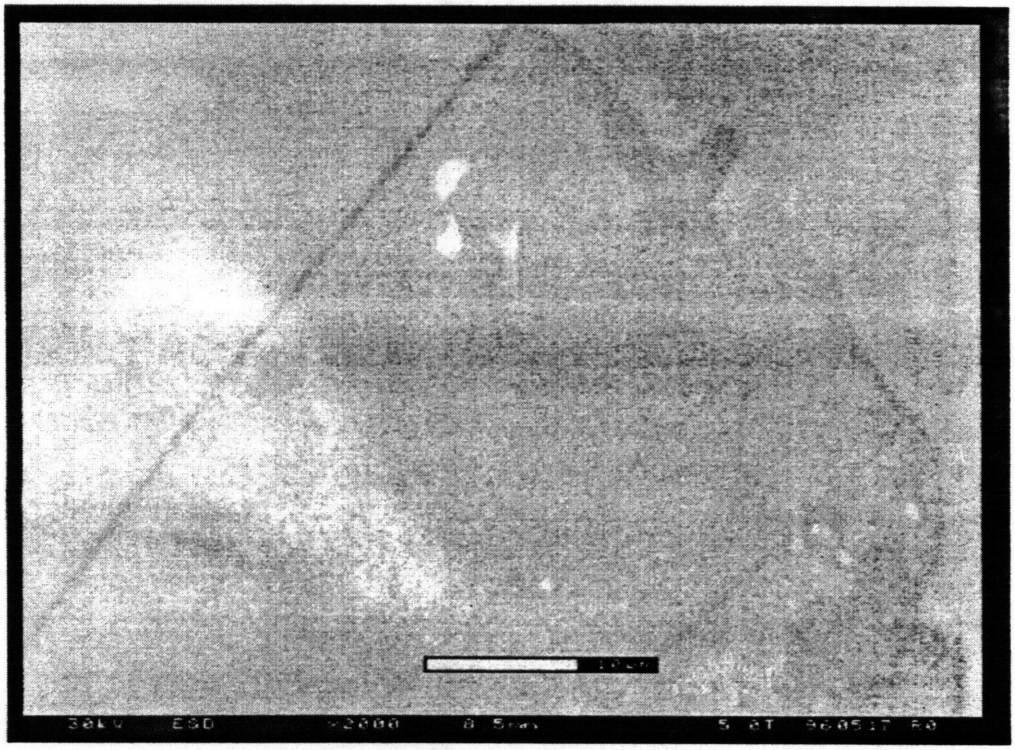

Figure 4-2: Image on the surface of the $Mn_{0.45}Zn_{0.55}F_2$ sample used for x-ray scattering, taken with an environmental scanning electron microscope. The white bar represents a length of 10μm.

The resulting resolutions at the (100) Bragg reflection are 0.0072 r.l.u. (FWHM) longitudinal, 0.0019 r.l.u. transverse in-plane, and 0.05 r.l.u. vertical. Pyrolitic graphite filters were used to remove higher harmonics. The sample was mounted inside a superconducting magnet capable of fields up to 6.1T.

All the x-ray experiments were performed on Beamline X20A at the National Synchrotron Light Source. The beamline utilized a platinum coated, bent silicon mirror to focus the x-ray beam horizontally and vertically to a cross section of approximately 1mm by 1mm at the sample position. The mirror also removed the higher harmonic contaminations from the beam, of which $\lambda/2$ photons were the most detrimental for the current experiments. For each experiment, the x-ray energy was chosen to minimize the multiple scattering intensity at the magnetic peak position (100). The double-bounce monochromator and the analyzer utilized single crystals of Ge(111). The in-plane resolution of approximately 4×10^{-4}Å^{-1} HWHM

and 5×10^{-5}Å^{-1} HWHM in the longitudinal (H) and transverse (K) direction respectively. The out of plane (L) resolution, controlled by collimating slits, was $\sim 2\times10^{-3}$Å^{-1} HWHM. The x-ray scattering spectrometer has an inherent energy resolution of ~10eV. The samples were mounted in an x-ray compatible superconducting magnet. The alignment between the c-axis of the samples and the vertical field was better than 3° in both the x-ray and neutron experiments.

4.3.2 Data Analysis

Figure 4-3 shows representative transverse neutron scattering scans at 5T during field cooling. All the data were taken above the metastability temperature, T_M(5T). It is apparent that, as the temperature is decreased, the scattered intensity increases and the scan profiles become sharper, though they remain much broader than resolution. The general form of the neutron scattering cross section for RFIM systems is [105]

$$S(\mathbf{Q}) = C\delta(\mathbf{q}) + \frac{B}{\kappa^2 + q^2} + \frac{A\kappa}{(\kappa^2 + q^2)^2} + \frac{B_T}{{\kappa_T}^2 + q^2} \tag{4.1}$$

where $\mathbf{q} = \mathbf{Q} - (100)$. As discussed in Chapter 2, the transverse term in $S(\mathbf{Q})$ can be neglected without introducing any significant error. For data taken following field cooling, the scans do not contain a resolution-limited component. Therefore, the FC neutron data were analyzed by fitting the sum of the longitudinal Lorentzian and the static Lorentzian squared terms in $S(\mathbf{Q})$ convoluted with the instrumental resolution. This analysis has resulted in the solid lines in figures 4-3.

The cross section for magnetic x-ray scattering is essentially the same as equation 2.23 with the dynamic susceptibility (Lorentzian) terms set to zero,

$$S(\mathbf{Q}) = \frac{A\kappa}{(\kappa^2 + \mathbf{q}^2)^2} + C\delta(\mathbf{q}) \tag{4.2}$$

where $\mathbf{q} = \mathbf{Q} - (100)$. C is the intensity of long range magnetic order and is proportional to the staggered magnetization squared, M_S^2. A is the integrated intensity of the short range order, described by a Lorentzian squared. The absence of the dy-

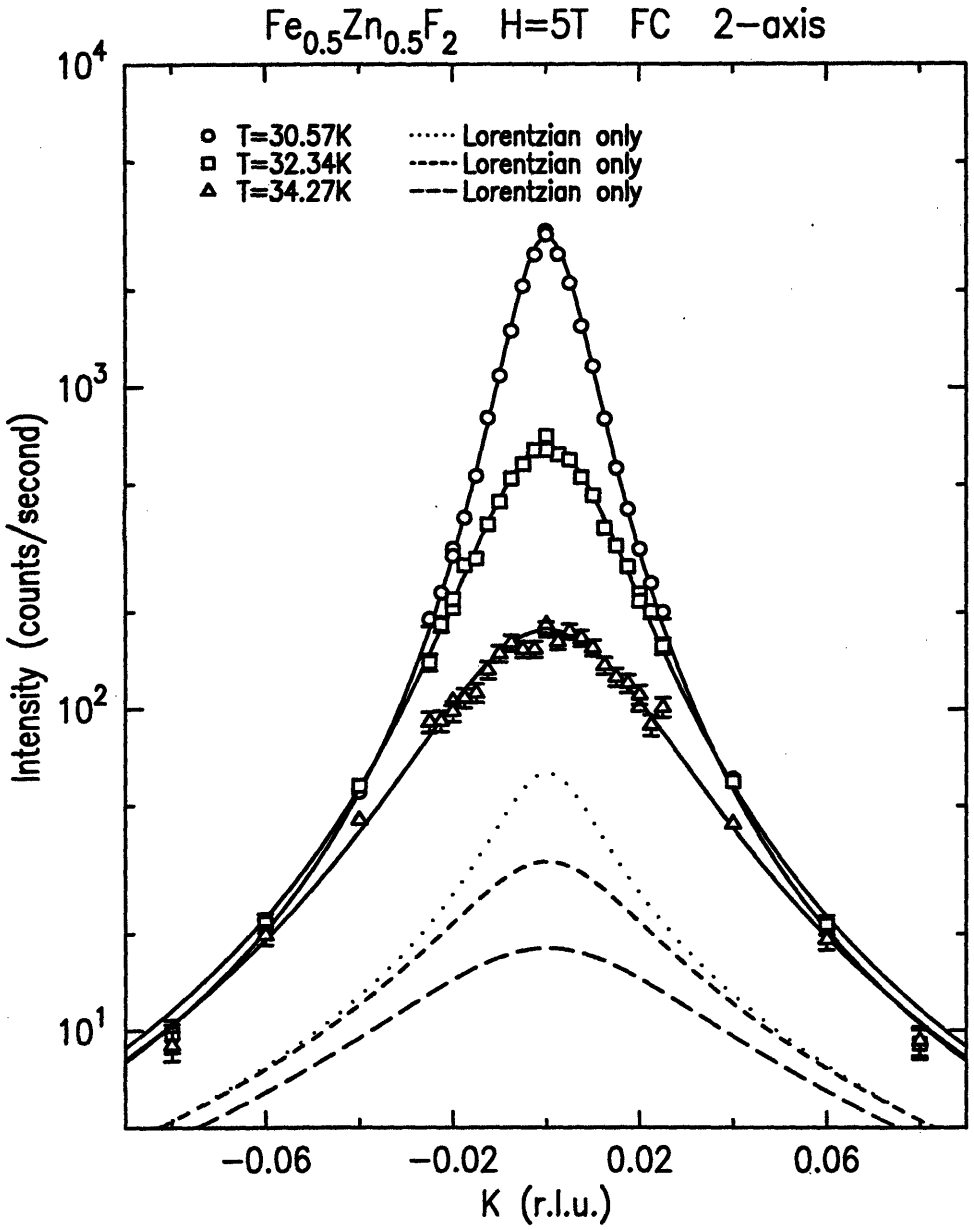

Figure 4-3: Transverse neutron scans taken with $Fe_{0.5}Zn_{0.5}F_2$ at three temperatures 33.57K, 35.34K and 37.27K above T_M at 5T. The solid line fits are given by equation 4.1. The dotted, short-dash and long-dash lines are the dynamic Lorentzian susceptibility components of the structure factor for the three respective temperatures.

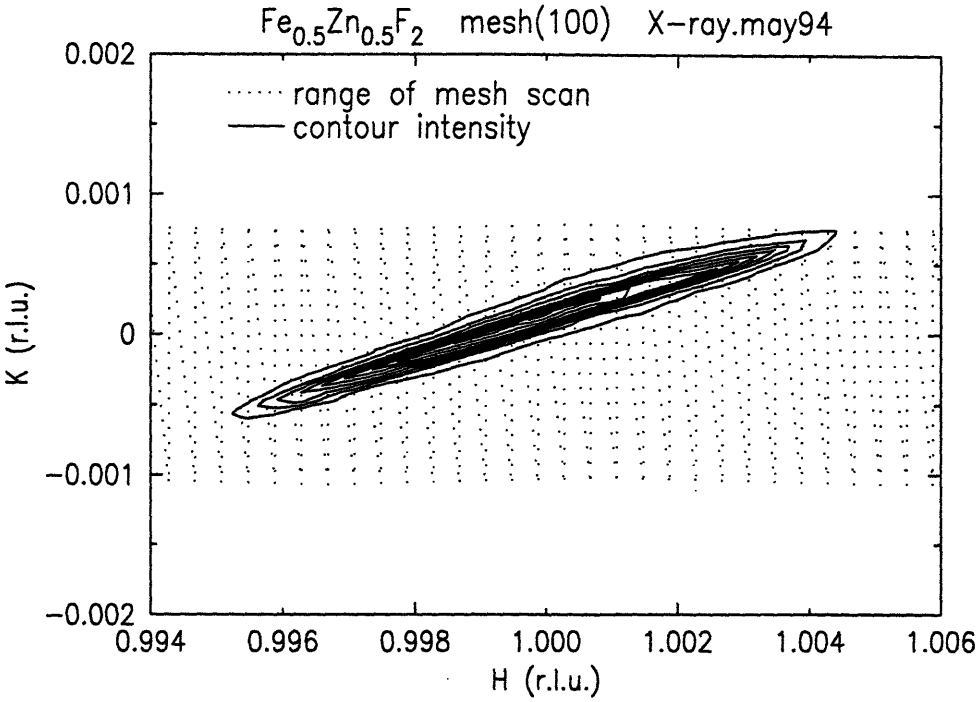

Figure 4-4: X-ray resolution mesh in the H-K plane at (100). The dotted line shows the range of the mesh scan, which is a series of K scans. The solid line gives the contour of the scan intensity. Notice that the horizontal scale is 3 times broader than the vertical scale.

namic susceptibility terms is due to the following reasons. First, x-ray scattering from transverse susceptibility is negligible. Second, as the field increases, the random field term (Lorentzian squared) dominates over the dynamic terms and makes distinguishing the latter difficult. Finally, as was found in the data analysis of $Mn_{0.75}Zn_{0.25}F_2$ and also in the current study, the scans were adequately described by equation 4.2 convoluted with the resolution function $R(\mathbf{Q}-\mathbf{q})$.

In fitting the data obtained on $Mn_{0.45}Zn_{0.55}F_2$ and $Fe_{0.5}Zn_{0.5}F_2$, the convolution integral was carried out in only the K direction. This is because the diffuse scattering in the H scans was asymmetric with respect to the central δ-function peak. The x-ray results on the correlation length are therefore qualitatively, but not necessarily quantitatively correct. Figure 4-4 shows the x-ray resolution measured by carrying out a mesh scan in the H-K plane about (100).

Figure 4-5 shows scans taken after field cooling $Mn_{0.45}Zn_{0.55}F_2$ to T=5K at H=1.5T. The K scan consists of a distinct resolution limited central peak, demonstrating LRO,

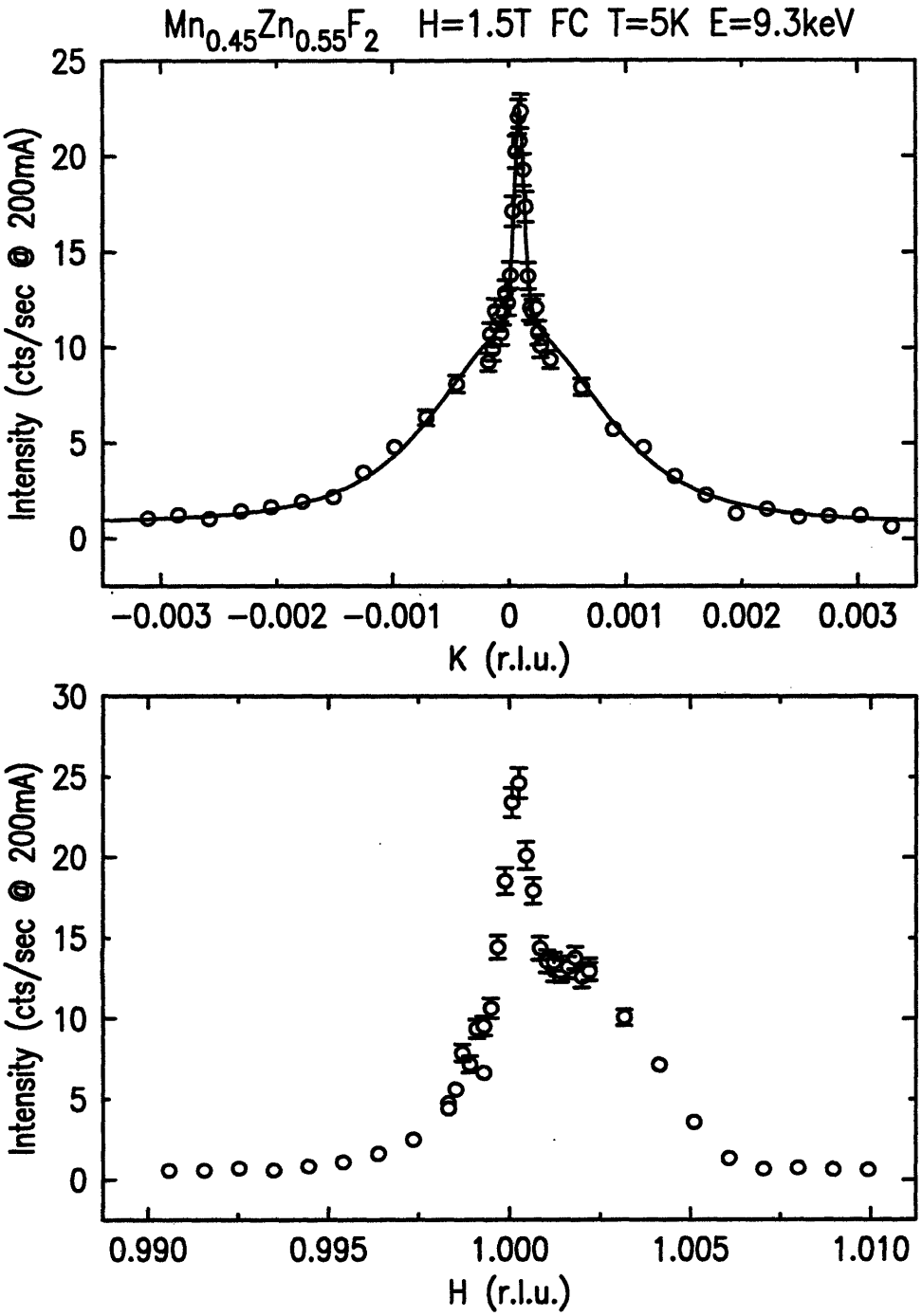

Figure 4-5: Representative FC scans at (100) for $Mn_{0.45}Zn_{0.55}F_2$. The K scan consists of a resolution limited central peak, demonstrating LRO, on top of broad diffuse scattering reflecting SRO. The solid line is a fit to equation 4.2. The H scan shows of the same two components, but the position of the two peaks of different length scales are shifted with respect to each other. The multiple scattering, at 4.4 counts/second for this particular run, is included in the data.

on top of broad diffuse scattering reflecting SRO. The diffuse scattering is well described by a Lorentzian squared function. The H scan shows of the same two components, but the positions of these two peaks of different length scales are shifted with respect to each other. The solid line is a fit for the K scan to equation 4.2 convoluted with the K resolution function.

4.4 Neutron Scattering Results

We first report neutron scattering results taken on $Fe_{0.5}Zn_{0.5}F_2$ at H=5T and 6T. From the fitted parameters κ, A and B, one can easily calculate the correlation length $\xi \sim 1/\kappa$, the connected susceptibility $\chi \sim B/\kappa^2$, and the disconnected susceptibility $\chi_{dis} \sim A/\kappa^3$. Assuming these parameters reflect the approach toward an equilibrium second order transition, one can readily extract the exponents ν, γ and $\bar{\gamma}$ using data above $T_M(H)$. In the current study, $T_M(H)$ has been unambiguously defined as the temperature at which the ZFC long range order goes to zero. Note that $T_M(H)$ is different from the pseudo-critical temperature of the ZFC transition, $T_C(H)$, where ZFC critical scattering peaks and the ZFC correlation length reaches a finite maximum. This choice of $T_M(H)$ is justified by the fact that no nonequilibrium effects or hysteresis has ever been observed above this temperature. Below $T_M(H)$, the activated random field dynamics set in, the experimental system becomes trapped in local free energy minima and is unbale to relax fully. Above $T_M(H)$, one expects a temperature range in which the system displays new equilibrium random field critical behavior, undisturbed by the anomalous dynamics. It is on data taken in this regime that we carry out our analysis.

We found that κ, χ_{dis} and χ at both fields could all be described adequately by simple power laws. For κ, least squares fits yielded ν(5T) =1.59 $\pm$ 0.14 and ν(6T)=1.44 $\pm$ 0.27. We therefore estimate that $\nu = 1.5 \pm 0.3$, respecting the fitting errors at both fields. In fact, forcing ν at 1.5 results in satisfactory fits to the data. This is illustrated in the top panels of figure 4-6 and figure 4-7, where the solid lines are fits with $\nu = 1.5$ being fixed. It is important that this value of ν is significantly

larger than 1 and is in keeping with the current theoretical estimates for ν [47, 2, 166]. Further, we are able to define a new temperature by extrapolating the power law fits till they reach zero. This is the temperature at which, assuming the correctness of the power law description of the critical behavior, the correlation length would have diverged had it been able to equilibrate on experimental time scales. Therefore we designate this temperature $T_N(H)$, the random field Néel temperature. The arrows in figures 5 and 6 indicate the positions of $T_N(H)$, which lies substantially below $T_M(H)$. We found that T_M(5T)-T_N(5T)$\approx$3.4K, and T_M(6T)-T_N(6T)$\approx$5.8K. In fact, based on preliminary analysis for data at lower fields, the increase in $T_M(H) - T_N(H)$ with increasing field appears to be a general trend.

As the temperature is decreased toward $T_M(H)$, χ_{dis} and χ grow drastically. We found that meaningful least squares fits could be obtained only by fixing $T_N(H)$ at the values determined by the fits of κ. Following this approach, we estimate $\bar{\gamma} = 5.7 \pm 1$ and $\gamma = 2.6 \pm 0.5$, where the large errors reflect the strong dependence of the exponents on the data and the choice for T_N. In the middle and bottom panels of figures 5 and 6, we show χ_{dis} and χ at H=5T and 6T. The solid lines are power law fits where T_N's have been fixed at the values determined by the fits to κ, and the exponents $\bar{\gamma}$ and γ fixed at 5.7 and 2.6 respectively. Hence the only adjustable parameter is the amplitude. Clearly the fits describe the data well. We note that these fitted values for $\bar{\gamma}$ and γ are considerably larger than those previously reported, but are consistent with most current theoretical predictions [45, 166].

4.5 Magnetic X-Ray Scattering Results

The results presented below show that both $Fe_{0.5}Zn_{0.5}F_2$ and $Mn_{0.45}Zn_{0.55}F_2$ demonstrate LRO together with SRO under field cooling for relatively low fields. The correlation length of the SRO decreases with increasing field, a fact previously observed by neutron and x-ray scattering. Interestingly, the LRO that coexists with the SRO also decreases in intensity as the applied field increases and disappears completely above a certain threshold field. We discuss experimental findings on $Mn_{0.45}Zn_{0.55}F_2$

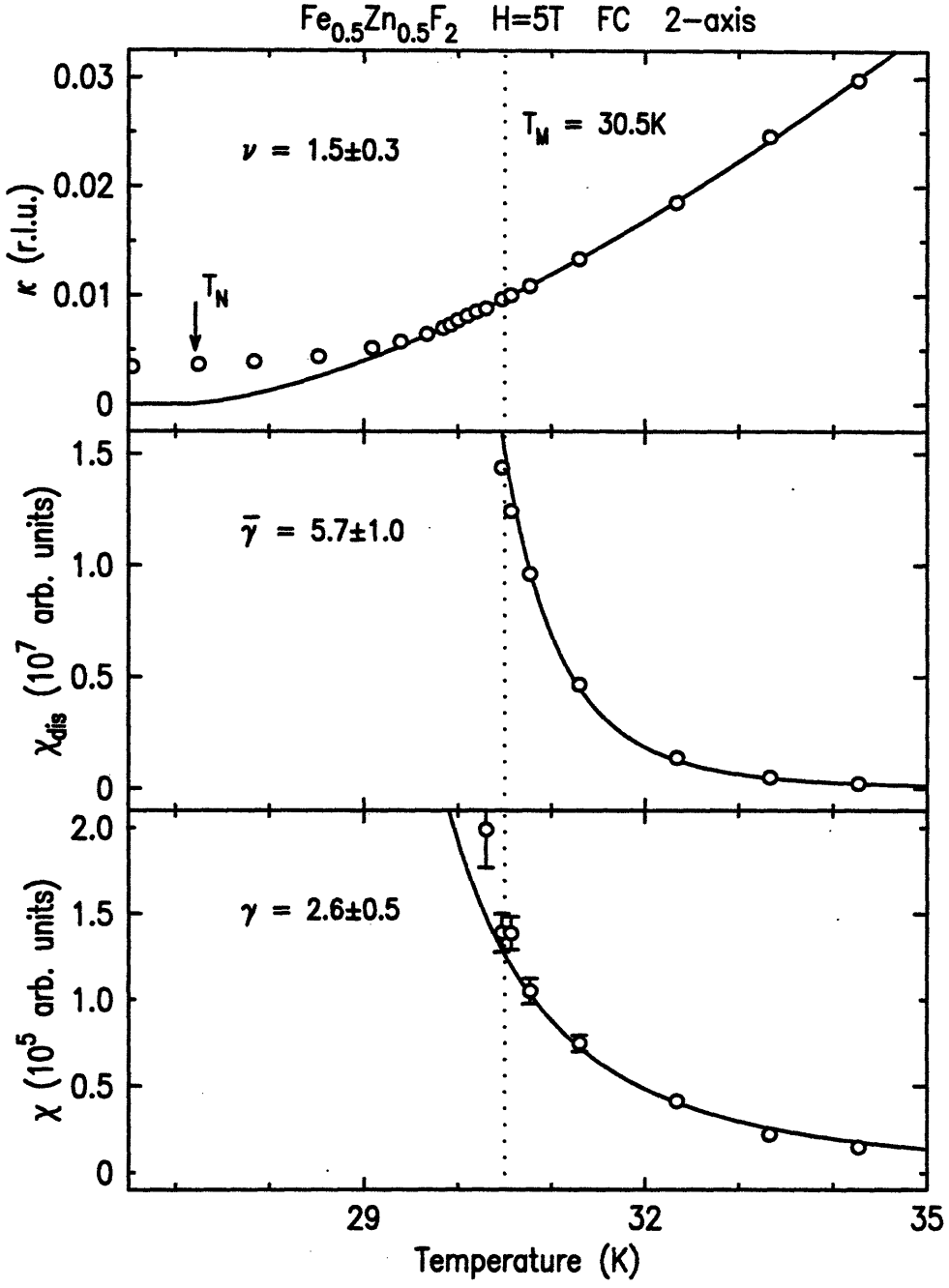

Figure 4-6: Inverse correlation length κ, disconnected susceptibility χ_{dis} and connected susceptibility χ measured by neutron scattering for $Fe_{0.5}Zn_{0.5}F_2$ at 5T. The dotted line shows the metastability temperature. T_N is the temperature at which the solid line fit for κ reaches zero. The estimated critical exponents are given.

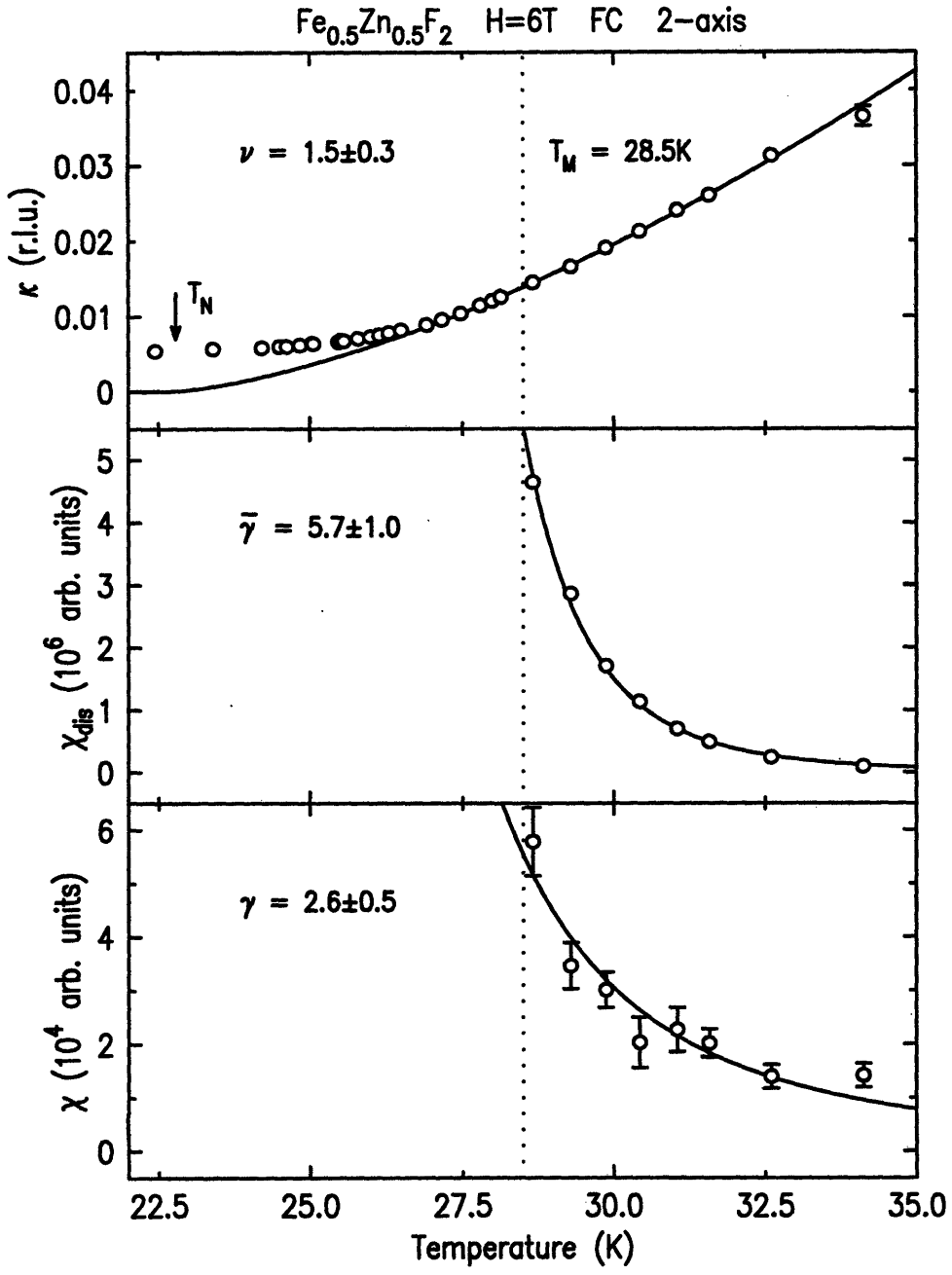

Figure 4-7: Inverse correlation length κ, disconnected susceptibility χ_{dis} and connected susceptibility χ measured by neutron scattering for $Fe_{0.5}Zn_{0.5}F_2$ at 6T. The dotted line shows the metastability temperature. T_N is the temperature at which the solid line fit for κ reaches zero.

and $Fe_{0.5}Zn_{0.5}F_2$ separately.

4.5.1 $Mn_{0.45}Zn_{0.55}F_2$

Figure 4-8 shows FC K scans at H=1T, 1.5T and 2T at temperatures well below $T_C(H)$ performed on $Mn_{0.45}Zn_{0.55}F_2$. The peak intensity of the scans decreases drastically for higher fields. The LRO component decreases from 62 counts/s at H=1T to 7 counts/s at H=1.5T, and all but disappears at 1.3 counts/s at H=2T. At the same time, the Lorentzian squared diffuse tails broaden, as are more clearly illustrated in semi-logarithmic format in the bottom panel of figure 4-8. The FC inverse correlation length, κ, appears to be proportional to H^2, as shown in the inset. This is in agreement with neutron scattering results on $Fe_{1-x}Zn_xF_2$ that show FC κ to scale with H^{ν_H} and $\nu_H = 2.2 \pm 0.1$ [67].

Temperature dependence of the LRO and SRO was measured during ZFC, FC and FH runs at H=1T and 1.5T. Figure 4-9 is a summary of the fitted parameters in equation 4.2 for a FC run at H=1T. Although the convolution is carried out only in the K direction, narrow H scans were also performed and fitted together with the K scans to ensure that the scans did not fall off the peak in the H direction. The top panel shows the inverse correlation length κ that decreases as the sample is cooled through $T_C(1T)$ and saturates at 0.0005Å at low temperature. The middle panel shows the integrated intensity of the diffuse scattering. The bottom panel is the temperature dependence of the LRO component. The rise of the FC LRO, fitted to equation 3.1, yields β_{FC}(1T) =0.28±0.04, σ_{FC}(1T)=0.4±0.1K and $T_{C,FC}$(1T)=17.7± 0.1K, compared with the ZFC β_{ZFC}(1T)=0.18 ± 0.03, σ_{ZFC}(1T)=0.13 ± 0.02K, and $T_{C,ZFC}$(1T)=18.17±0.1K. Insets in figure 4-9 display data in the corresponding panels near the transition region. Comparing the three panels, it is obvious that though there is measurable SRO at and above $T_C(1T)$K, LRO develops only after the sample is cooled to approximately 0.4K below T_M ≈18.3K. This agrees with the observation on $Mn_{0.75}Zn_{0.25}F_2$ [60] by Hill *et al.* who designated the temperature at which FC LRO first develops T_N. Figure 4-10 compares the LRO amplitude between the ZFC and the FC states for $Mn_{0.45}Zn_{0.55}F_2$ at H=1T.

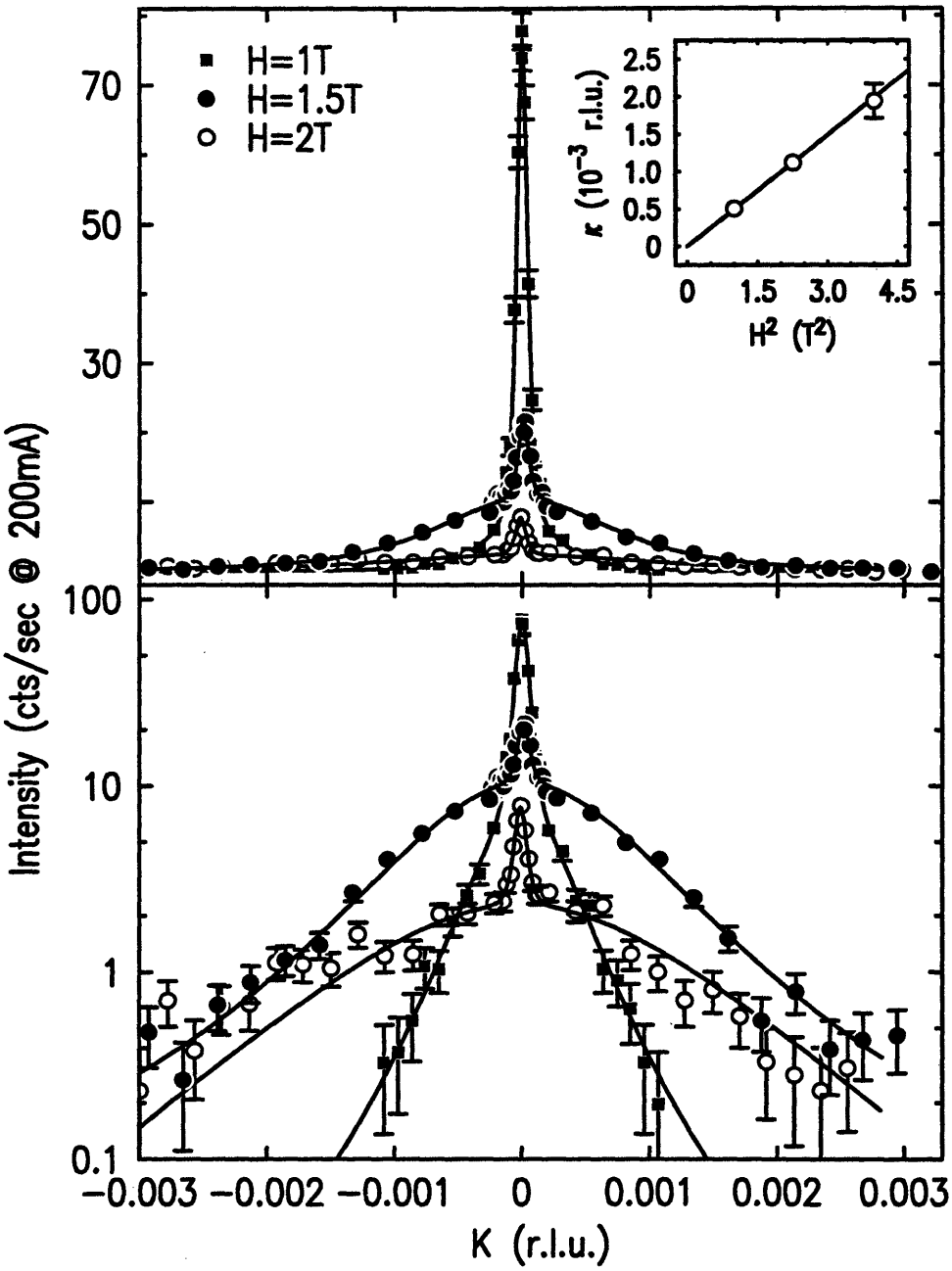

Figure 4-8: FC scans well below $T_C(H)$ at several fields for $Mn_{0.45}Zn_{0.55}F_2$. The peak intensity of the scans drops drastically for higher fields, reflecting contributions to the total scattering intensity being converted from LRO to SRO. The multiple scattering component, included in the data, is 7.7counts/s at 1T, 4.4 counts/s at 1.5T and 4.1 counts/s at 2T. The bottom panel shows the same data in semi-log format. The inset plots FC κ vs. applied field squared.

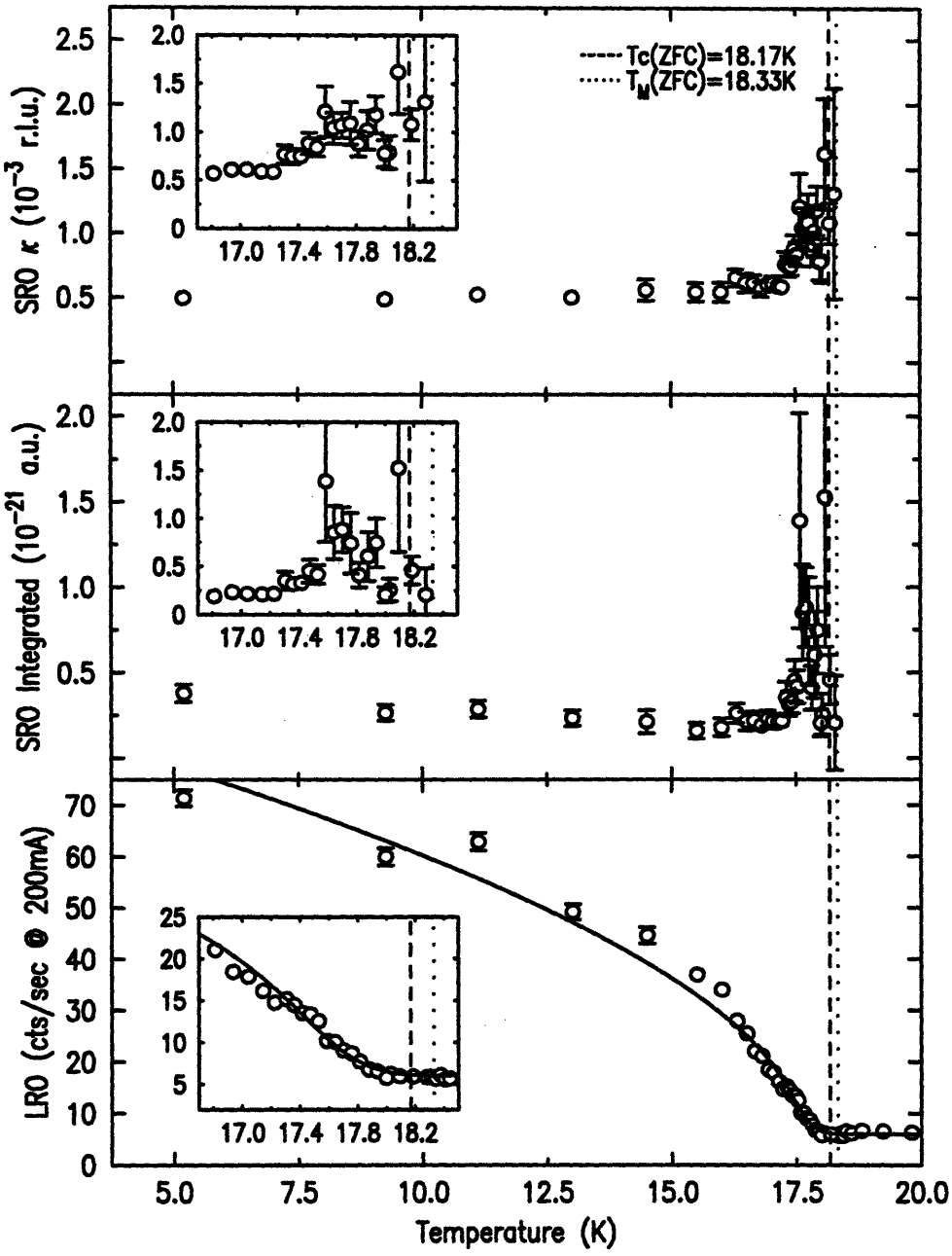

Figure 4-9: X-ray parameters of $Mn_{0.45}Zn_{0.55}F_2$ for H=1T FC. Top panel: inverse correlation length (κ) of SRO measured from diffuse scattering. Middle panel: integrated intensity (A) of SRO. Bottom panel: LRO component. The solid line is a fit to a simple power law that gives $\beta_{FC} = 0.35 \pm 0.02$.

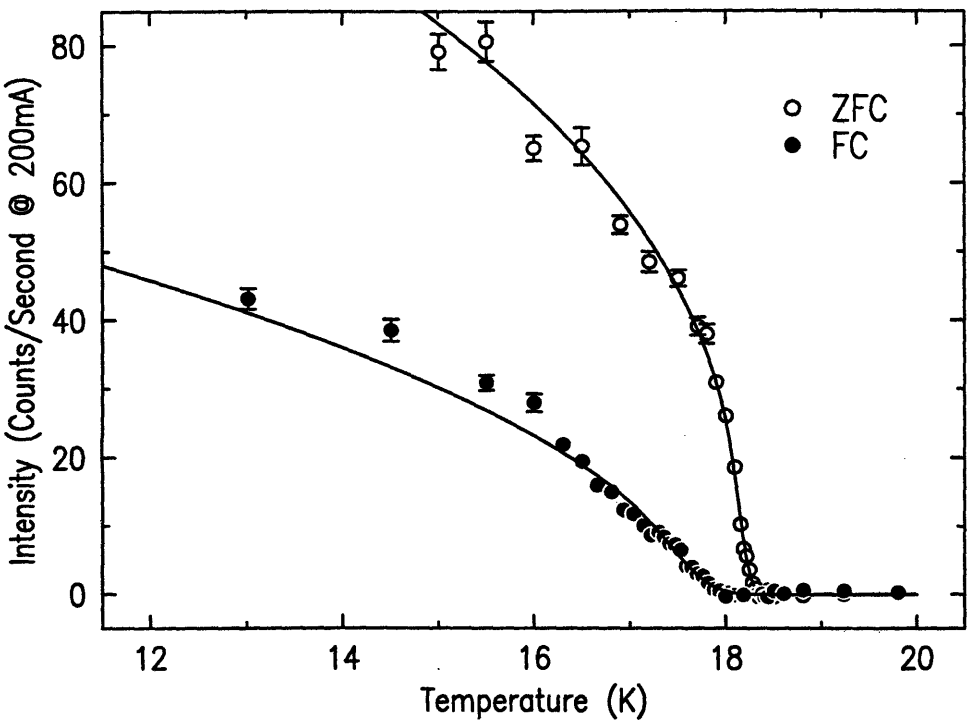

Figure 4-10: ZFC and FC LRO of $Mn_{0.45}Zn_{0.55}F_2$ at H=1T.

It is obvious from figure 4-8 that the FC intensity at H=1T is dominated by LRO. At H=1.5T, κ is larger and the LRO and SRO are of comparable amplitude. Fitting the scans to two peaks of different length scales therefore yields parameters that are more reliable. Figure 4-11 gives a summary of the fitted parameters. The features of κ, SRO integrated intensity A and LRO amplitude are essentially similar to those at H=1T. κ(FC) saturates at 0.0012Å at low temperature. The FC LRO appears to be rather rounded. Fitting to 3.1 yields $\beta_{FC}(1.5\text{T})=0.31\pm0.04$, $\sigma_{FC}(1.5\text{T})=1.0\pm0.2$K, and $T_{C,FC}(1.5\text{T}) = 16.3\pm0.2$K, compared with $\beta_{ZFC}(1.5\text{T}) = 0.19\pm0.03$, $\sigma_{ZFC}(1.5\text{T}) = 0.14\pm0.03$K, and $T_C(1.5\text{T})$=16.93K. The rise of the FC LRO is again slightly below $T_M(1.5\text{T})$=17.2K.

A field heating run was taken immediately following field cooling at H=1.5T. A summary of the FH parameters are presented in figure 4-12. Although both LRO and SRO are present during FH, the temperature dependence of κ, A and LRO are significantly different from those of FC. FH κ, shown in the top panel, remains a constant until about 0.2K below $T_{C,ZFC}(1.5\text{T})$ when it starts to rise, though it still

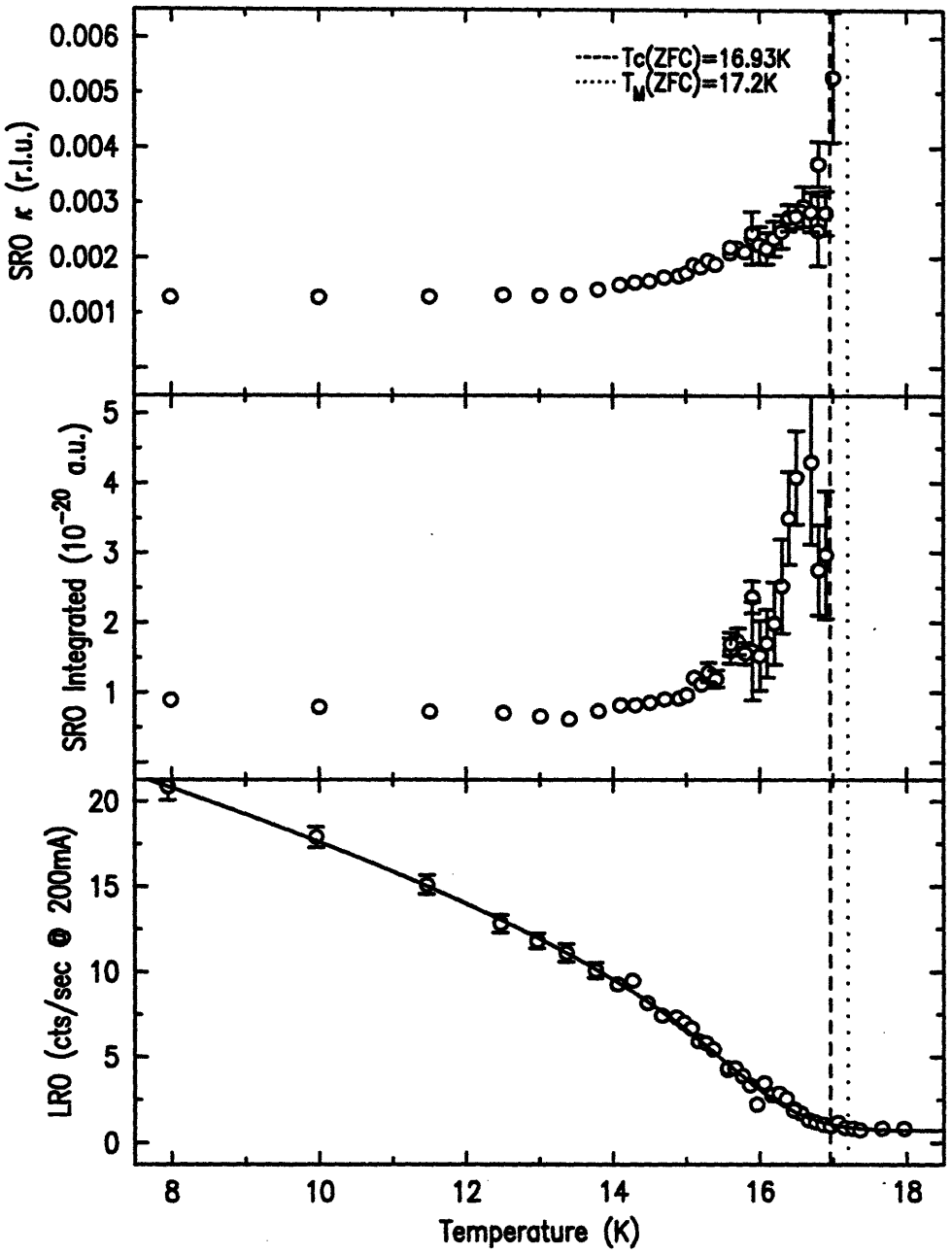

Figure 4-11: X-ray parameters of $Mn_{0.45}Zn_{0.55}F_2$ for H=1.5T FC. Top panel: inverse correlation length (κ) of SRO. Middle panel: integrated intensity (A) of SRO. Bottom panel: LRO component. The solid line is a fit to a simple power law that gives $\beta_{FC} = 0.34 \pm 0.01$.

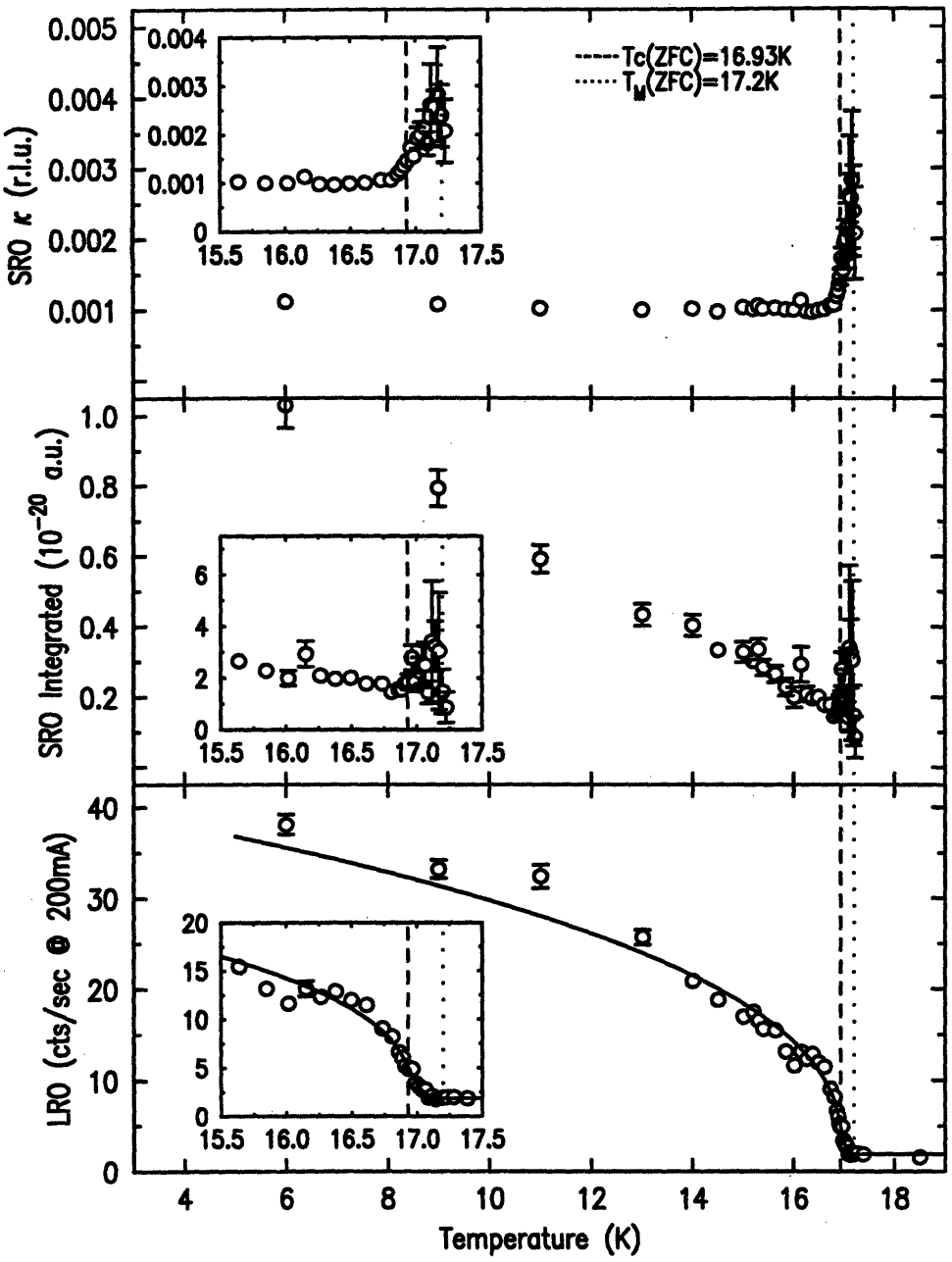

Figure 4-12: X-ray parameters of $Mn_{0.45}Zn_{0.55}F_2$ for H=1.5T FH. Top panel: inverse correlation length (κ) of SRO. Middle panel: integrated intensity (A) of SRO. Bottom panel: LRO component. The solid line is a fit to the rounded power law that gives $\beta_{FH} = 0.20 \pm 0.01$.

lies below the FC κ measured at corresponding temperatures. The SRO integrated intensity A is shown in the middle panel. It decreases significantly with increasing temperature. Both κ and A are observable up to $\sim T_M(1.5\mathrm{T})$ with x-rays, though they can be measured up to much higher temperatures with neutron scattering which has broader resolution. The LRO intensity, in the bottom panel of figure 4-12, resembles that of the ZFC intensity at H=1.5T except for its lower amplitude. The solid line is a fit to the rounded power law equation 3.1 and gives comparable estimates of $\beta_{FH}(1.5\mathrm{T})=0.20 \pm 0.02$ and $\sigma_{FH}(1.5\mathrm{T})=0.12 \pm 0.03\mathrm{K}$. The FH LRO component remains observable up to within 0.1K of $T_M(1.5T)$ where the ZFC LRO diminishes to zero. Figure 4-13 summarizes the ZFC, FC and FH parameters at H=1.5T. The hysteretic effects agree qualitatively with those observed by neutron scattering [67, 71] and earlier magnetic x-ray scattering experiments on DAFFs including $Mn_xZn_{1-x}F_2$ [140, 108, 60].

Before discussing the interesting dynamic effects in the Ising phase, we first digress to discuss the intriguing phase boundary of $Mn_{0.45}Zn_{0.55}F_2$ which is not completely understood. It is well known that, in $Mn_{0.75}Zn_{0.25}F_2$, there is a clearly defined first-order transition between a low field antiferromagnetic (AF) phase and a high field spin-flop (SF) phase, and a LRO established in the SF phase is preserved as the system moves into the AF phase through decreasing field or increasing temperature [71, 60]. The situation in $Mn_{0.45}Zn_{0.55}F_2$ is less clear. Specifically, the boundary between the SF phase and the AF phase is not well understood, as neutron scattering study showed that the system exhibited a Lorentzian squared profile on entering the AF phase from the SF phase that resembles the profile obtained with field cooling [71]. The phase boundary of $Mn_{0.45}Zn_{0.55}F_2$ has also been studied by magnetization [167, 168] and heat capacity [167, 169]. In our x-ray experiments, we have cycled the sample through various regions of the phase diagram of $Mn_{0.45}Zn_{0.55}F_2$ to explore the rich behavior at its transitions.

We first present a map of the phase diagram measured by SQUID magnetometry. This was carried out by cycling the sample in temperature and field through ZFC, FC, increasing field at constant temperature after cooling in zero field (FI) and

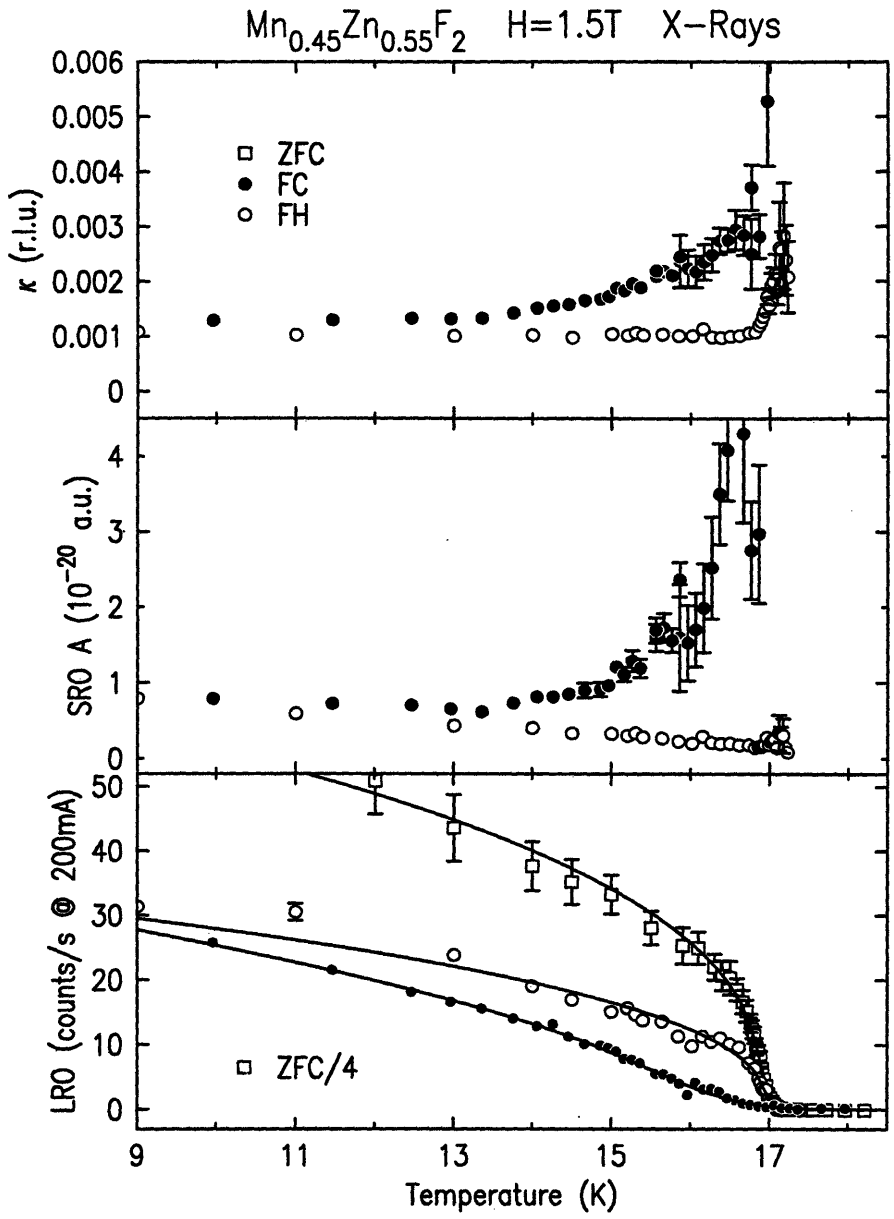

Fig. 12

Figure 4-13: Comparison of ZFC, FC and FH parameters of $Mn_{0.45}Zn_{0.55}F_2$ at H=1.5T measured by x-ray. The open squares, closed circles and open circles correspond to ZFC, FC and FH parameters respectively. Top panel: inverse correlation length (κ) of SRO. Middle panel: integrated intensity (A) of SRO. Bottom panel: LRO component.

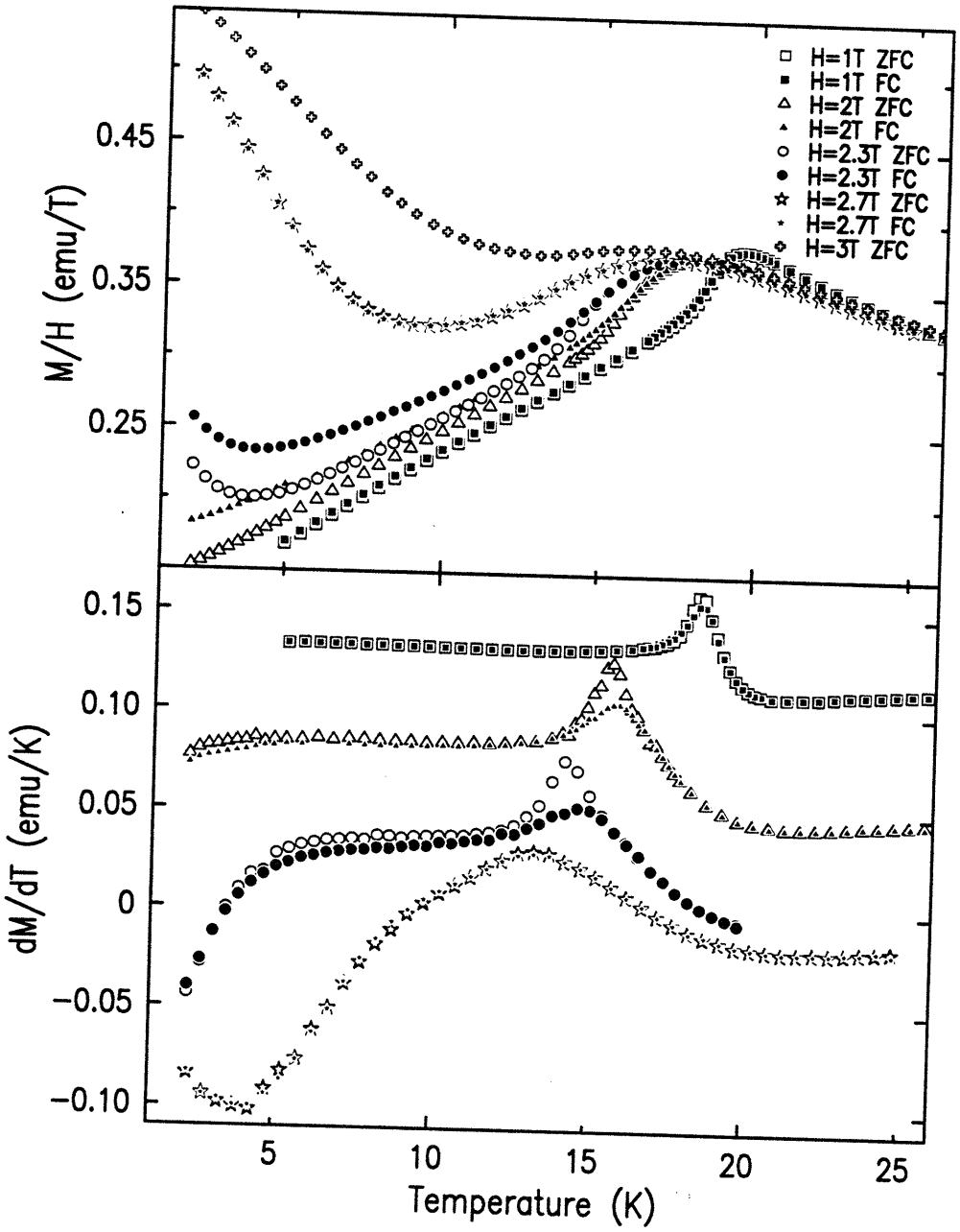

Figure 4-14: SQUID data of $Mn_{0.45}Zn_{0.55}F_2$ some representative fields. Upper panel: uniform magnetization M. Lower panel: temperature derivatives of M. The data at H=1T,2T,2.3T are shifted vertically by 0.12, 0.06, 0.01 to respectively to improve clarity.

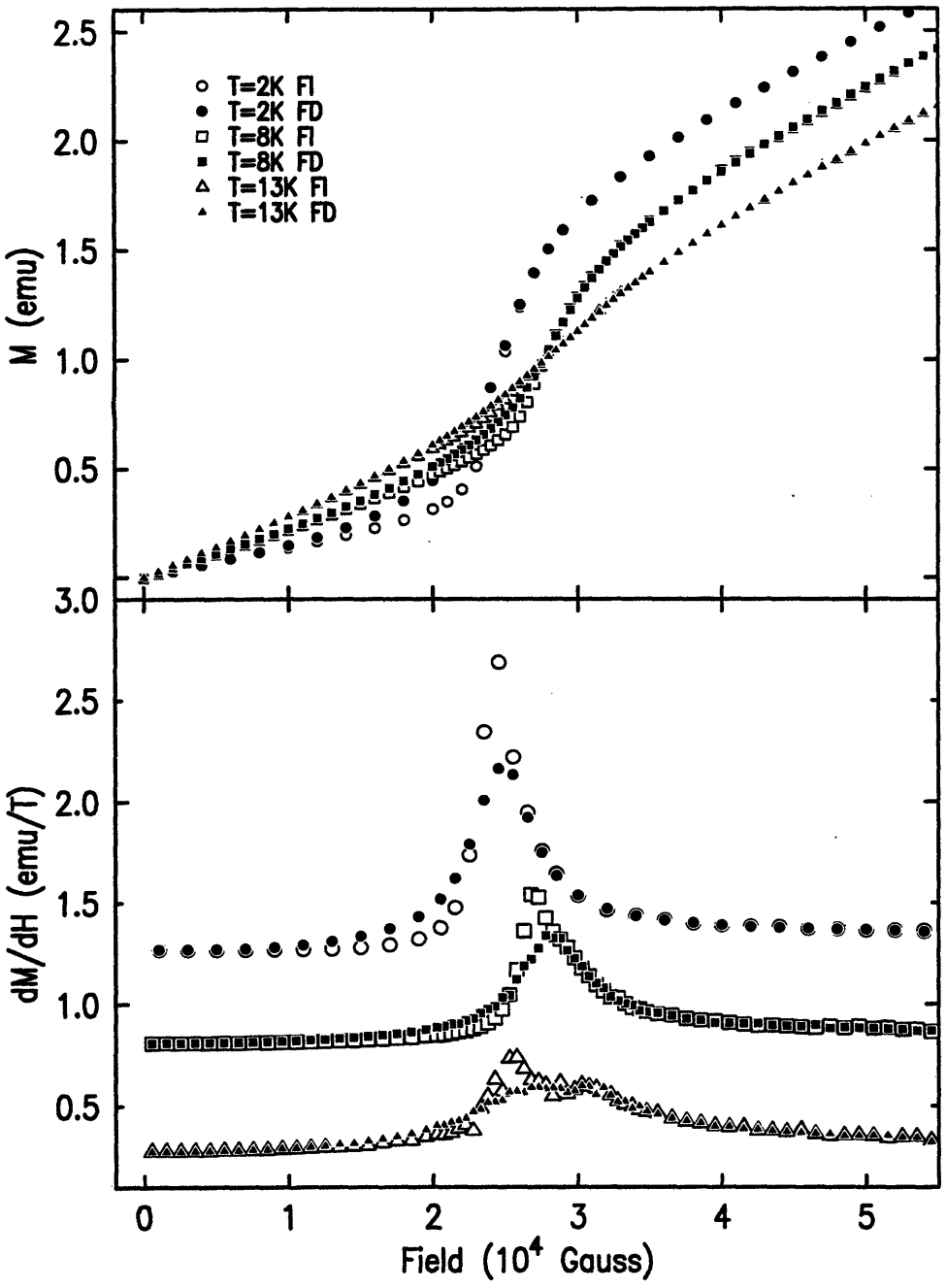

Figure 4-15: SQUID of $Mn_{0.45}Zn_{0.55}F_2$ at some representative temperatures. Upper panel: uniform magnetization M. Lower panel: field derivatives of M and data at 8K and 2K are shifted vertically by 0.7emu/T and 1.2emu/T respectively after dividing by 2 to improve clarity.

subsequently decreasing the field (FD). Representative data from thermal cycling at H=1T, 2T, 2.3T, 2.7T and 3T. are presented in figure 4-14. At H=1T and 2T, the transition is one between the AF and paramagnetic (PM) state and is represented by an inflection in the ZFC data on M (upper panel) or a peak in the temperature derivative of the uniform magnetization $\frac{dM}{dT}$ at the corresponding fields (lower panel). At H=2.3K, the system is in the SF phase at low temperatures, $T < 4$K, and in the AF phase between 4K and 15K. The minimum in M may characterize the AF-SF transition [168]. At 2.7T and 3T, M first decrease, signaling a SF phase; it then increases before finally decreases as it is heated into the PM phase. There is clearly observable hysteresis at H=1T, 2T and 2.3T, but no hysteresis at or above H=2.7T. The SF-PM boundary at higher fields can be estimated from cusps in $\frac{dM}{dT}$.

Representative field cycling data are shown in figure 4-15 at T=2K,8K and 13K. Transitions are indicated by inflections in M vs. H and by peaks in $\frac{dM}{dH}$. Hysteresis can be observed in the AF-SF and the AF-PM transition. At T=2T, there is a well defined $\frac{dM}{dH}$ peak following FI that appears sharper than the FD $\frac{dM}{dH}$ peak. The AF-SF transition field H_{SF}(2K) is defined by the FI $\frac{dM}{dH}$ peak. The stability limit of the AF phase, at H_c^{AF}, above which the FI and FD values of M coincide, can be easily identified at about 0.2T above H_{SF}(2K) [168]. However, the stability limit of the SF phase is not as easily determined. In fact, FD M appears slightly above FI M down to zero field. Since we know the FI state has long range magnetic order, this small excess magnetization means that the system attains some short range order after going through the SF-AF transition upon field decreasing. The observation at T=8K is largely similar, except that the FD $\frac{dM}{dH}$ peaks at a field approximately 0.2T above the FI peak. The existence of SRO upon lowering the field through the SF-AF transition can be easily confirmed by comparing several numbers. During thermal cycling, M_{ZFC}(1T,8K) =0.20868 $\pm$0.00012 emu, M_{FC}(1T,8K) =0.21089 $\pm$0.00005 emu, M_{ZFC}(2T,8K) =0.44902 $\pm$0.00023, M_{FC}(2T,8K) =0.47778 $\pm$0.00004 emu. Therefore the thermal excess magnetization at 1T and 2T due to hysteresis is $M_{ex,T}$(1T,8K) =0.00221 $\pm$0.00017 emu and $M_{ex,T}$(2T,8K) =0.02876 $\pm$0.00027 emu respectively. On the other hand, during field cycling, M_{FI}(8K,1T) =0.21829 $\pm$0.00007

emu, M_{FD}(8K,1T) =0.22275 ±0.00001 emu, M_{FI}(8K,2T) =0.46973 ±0.00006 emu M_{FD}(8K,2T) =0.50744 ±0.00004 emu. Therefore the field excess magnetization a 1T and 2T is $M_{ex,H}$(8K,1T) =0.00446 ±0.00008 emu and $M_{ex,H}$(8K,2T) =0.037 ±0.0001 emu respectively. Two observations can be made from these numbers. First we note that M_{FI}(8K,2T) > M_{ZFC}(2T,8K), where the former is reached by cooling i zero field to 8K and then raising the field to 2T while the latter is reached by coolin in zero field to 5K and then raising the field to 2T before heating to 8K. It is obviou that the AF state reached through the ZFC protocol is prone to hysteresis since ther appears to be less short range order in the latter protocol, which first cools the sampl to a lower temperature. This is but one example of the pinning effect of the randon fields and random bonds in a DAFF - the higher ordering in zero field is more o less frozen in and is preserved as the field is applied. This confirms that the lon range ordered ZFC state is indeed not an equilibrium state. The second observatio is that the excess magnetization is greater for field cycling than for thermal cyclin at the same temperature and field. For example, $M_{ex,H}$(8K,2T) > $M_{ex,T}$(2T,8K) This would mean that, as the sample leaves the SF phase and enters the AF phase it acquires more short range order than following field cooling to the same tempera ture and field. We explore this point with x-ray scattering below. At T=13K, $\frac{dM}{dH}$ displays two peaks, one at $H \approx$ 2.5T and the other at $H \approx$ 3T signaling AF-PM an PM-SF transitions respectively. Comparing FI and FD field derivatives, it is obviou that the AF-PM transition shows hysteresis as expected of a RFIM system while th PM-SF transition does not because the field is largely decoupled from the spins in th spin-flopped phase and no random field effects are expected. Figure 4-16 summarize the phase diagram of $Mn_{0.45}Zn_{0.55}F_2$.

We now present further x-ray investigations on the ordering and disordering pro cesses in $Mn_{0.45}Zn_{0.55}F_2$ following various paths in the $H-T$ plane. Figure 4-17 show the drastic decrease in intensity as the sample approaches the AF-SF boundary afte being cooled in zero field to 10K. From H=2.5T to 2.65T, the peak intensity decrease from 75 counts/s to 3 counts/s as the spins rotate into the a-b plane to minimize tota energy. Since the a-b plane largely coincides with the horizontal scattering plane, th

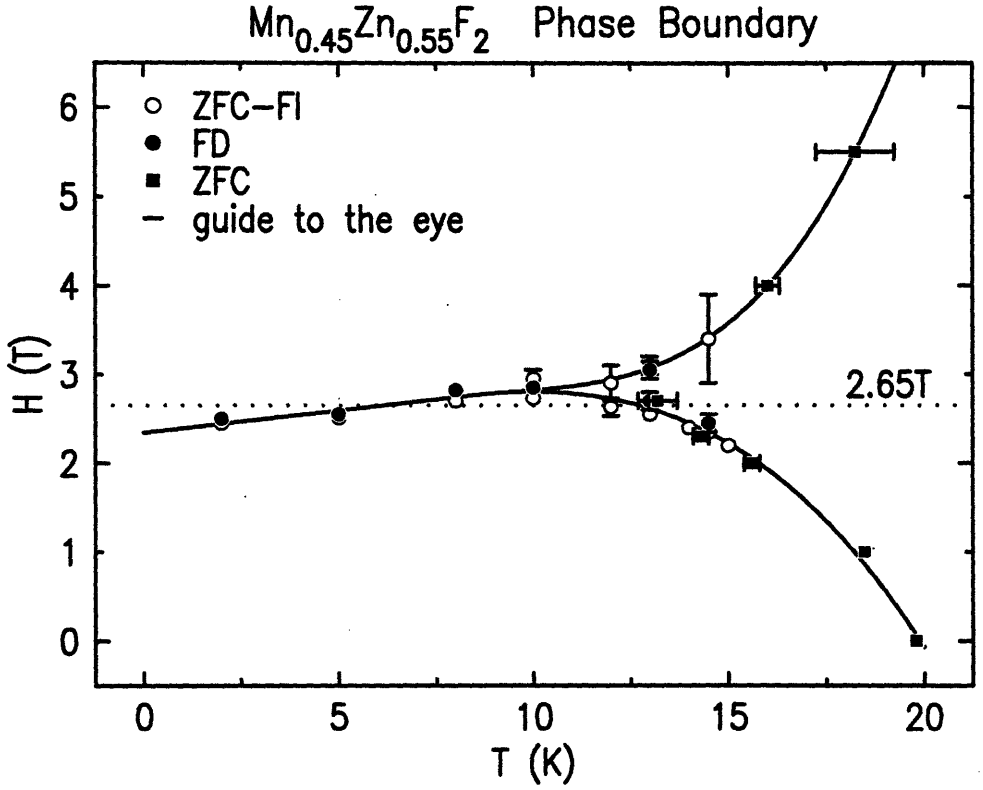

Figure 4-16: Phase diagram of $Mn_{0.45}Zn_{0.55}F_2$ measured by SQUID. Oper circles, closed circles and close squares are phase boundaries obtained from peaks in $\frac{dM}{dH}$ in FI, FD and $\frac{dM}{dT}$ in ZFC respectively. The dotted line at 2.65T is a reference for discussion.

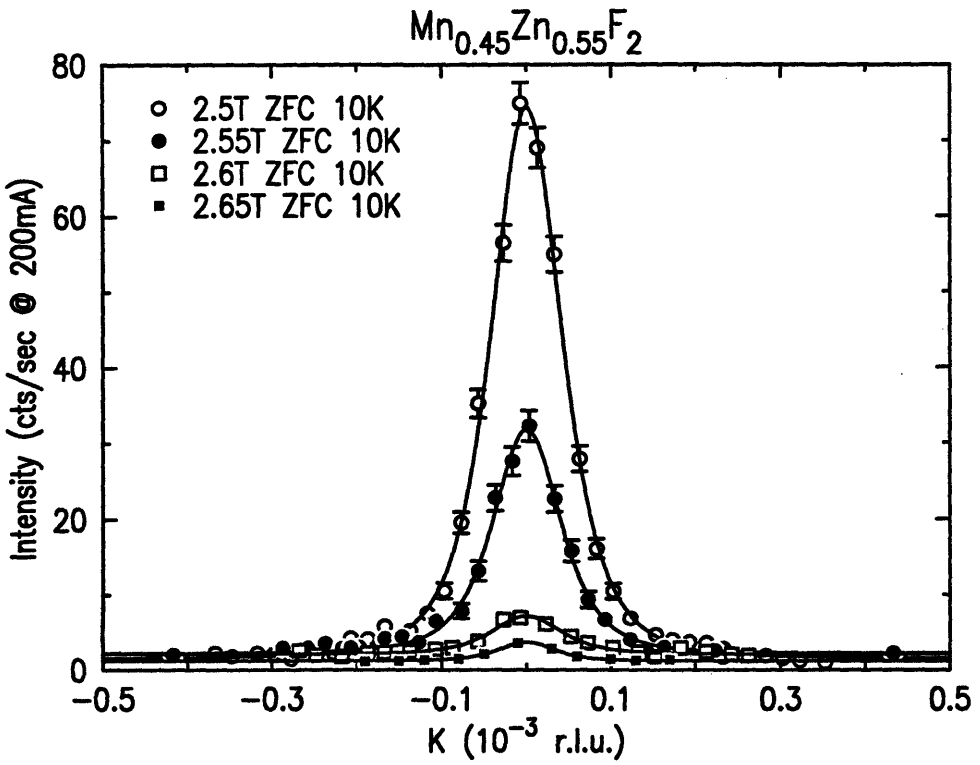

Figure 4-17: Approach to the AF-SF transition in $Mn_{0.45}Zn_{0.55}F_2$. Solid lines are fits to a Lorentzain squared function. All scans are resolution limited.

scattering intensity is reduced by a factor of $sin^2\theta \sim 0.01$ due to the polarization dependence of x-rays [60, 170], where $\theta \sim 8°$ is the Bragg angle at (100) for the x-ray energy used in the current study. This results in magnetic scattering intensity on the order of 1 count/s in the SF phase. In figure 4-18 we present H and K scans in the SF phase at H=4T together with the multiple scattering background measured in the PM phase at the same field. There is indeed approximately 1 count/s magnetic signal on top of the background. The low intensity and signal to noise ratio precluded a careful study of the temperature dependence of the SF scattering.

In figure 4-19, we compare K scans taken at H=1.5T and T=5K after taking the sample through three different paths in the $H - T$ diagram (see figure 4-16: open circles - field cooling to 5K at 1.5T (path 1); closed circles - cool the sample to 5K in zero field, raise the field to 4T and then lower it to 1.5T (path 2); closed squares - cool the sample to 10K in zero field, raise the field to 2.6T, cool further to 5K and lower the field to 1.5T (path 3). Path 2 and path 3 both take the sample through

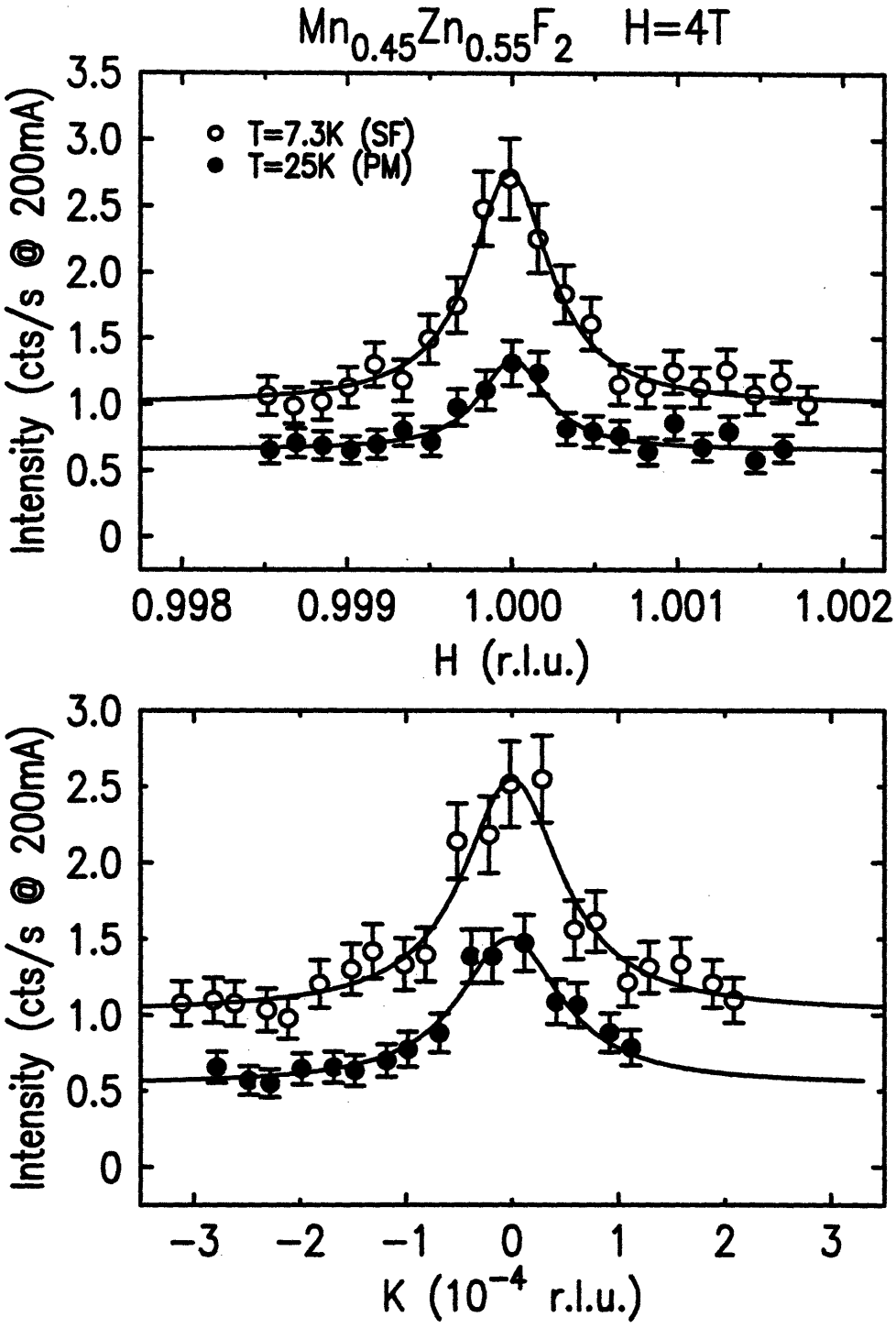

Figure 4-18: X-ray scattering in the XY phase, $Mn_{0.45}Zn_{0.55}F_2$. The solid lines are empirical fits to a Lorentzian, though the choice is not unique. Peaks are resolution limited.

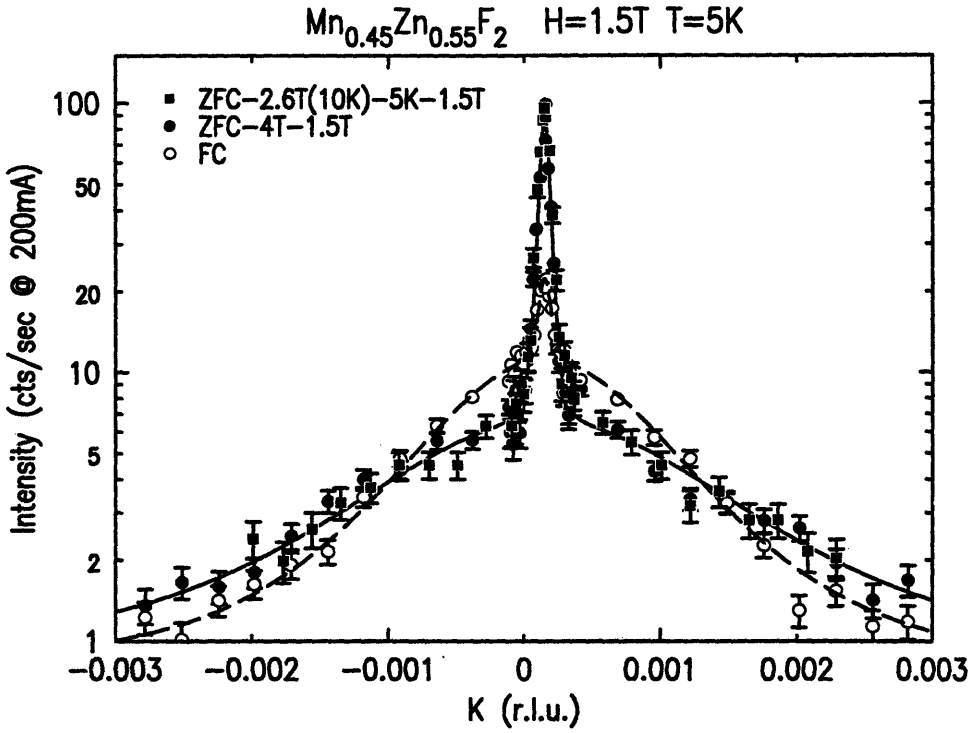

Figure 4-19: X-ray scans of $Mn_{0.45}Zn_{0.55}F_2$ taken at H=1.5T, T=5K following different protocols. Open circles: field cooling to 5K at 1.5T. Closed circles: cool the sample to 5K in zero field, raise the field to 4T and then lower it to 1.5T. Closed squares: cool the sample to 10K in zero field, raise the field to 2.6T, cool further to 5K and lower the field to 1.5T.

the SF-AF transition and the data show that the end results are practically identical. Compared to the FC scan, they both show a much stronger LRO component while at the same time preserving some SRO. In fact, the resultant SRO following path 2 and path 3 has a correlation length of approximately 2/3 of that following FC (path 1). All this is in qualitative agreement with the observation from SQUID magnetometry as discussed above. Similarly results were found by carrying the sample through various trajectories to H=2T and T=6K. The AF-SF boundary of $Mn_{0.45}Zn_{0.55}F_2$ therefore appears to be quite different from that of $Mn_{0.75}Zn_{0.25}F_2$ for which the LRO established in the XY phase is preserved as the field is lowered through the spin-flop value [71, 60].

In previous neutron scattering study on $Mn_{1-x}Zn_xF_2$ [71] and $Fe_{1-x}Zn_xF_2$ [159], it has been found that the field lowered state and the field cooled state correspond to similar spin configurations and have comparable domain sizes. The FD domain

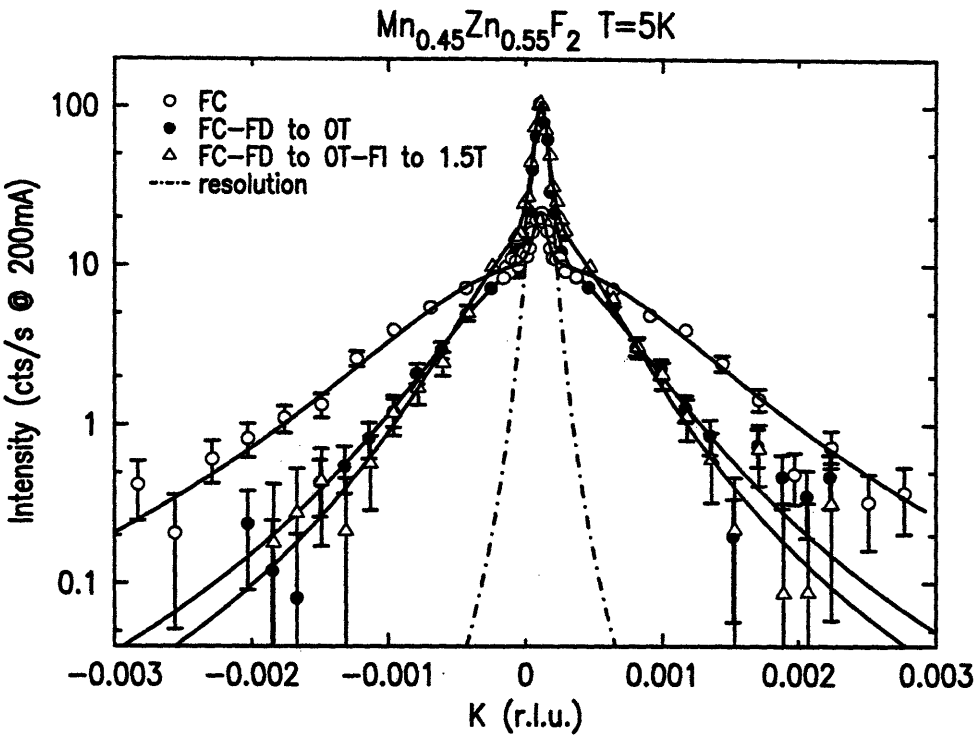

Figure 4-20: Hysteresis in FC, FD and FI in $Mn_{0.45}Zn_{0.55}F_2$ observed by x-rays. Open circles: field cooling to 5K at 1.5T. Closed circles: reduce the field to 0T after FC to 5K at 1.5T. Open triangles: raise the field back to 1.5T, keeping the temperature at 5K. The solid lines are fits to equation 4.2.

size increases if the magnetic field is decreased. LRO is recovered as the field goes to zero and is preserved even if the field is raised again. In order to verify these effects on $Mn_{0.45}Zn_{0.55}F_2$ with x-rays, we compare the data shown in figure 4-20. The open circles represent a K scan after field cooling to 5K at 1.5T. Upon ramping the field to zero, the scattering profile becomes dominated by LRO, the amplitude of which grows by approximately ten fold. In addition, there are lingering magnetic domains contributing to the diffuse tails, though the domains are twice as large as the FC ones. This shows that the pinning is largely due to the random fields in this weakly anisotropic DAFF. When the random fields are introduced again by raising the field back to 1.5T, the configuration remains largely the same as that at zero field except that the domains have further grown by about 20%. The findings are in agreement with observations by neutron scattering which concluded that the ordering increases in the AF phase as field decreases but does not decrease with either increasing field

or temperature.

4.5.2 $Fe_{0.5}Zn_{0.5}F_2$

Magnetic x-ray scattering results on $Fe_{0.5}Zn_{0.5}F_2$ are similar to those on $Mn_{0.45}Zn_{0.55}F_2$ and the presentation here parallels that in the previous section. Again, LRO and SRO are found to coexist in the FC data at relatively low fields. LRO can be observed in $Fe_{0.5}Zn_{0.5}F_2$ following FC up to at least H=2T. Detailed temperature dependence of LRO and SRO components were studied at H=1T and 1.5T.

Figure 4-21 shows K and H scans after field cooling to 15K at H=1.5T. The features of these scans are very similar to those taken with $Mn_{0.45}Zn_{0.55}F_2$. The FC K scan displays a LRO central peak in addition to diffuse scattering tails and is well described by equation 4.2. The FC H scan similarly suggests two length scales, though the two peaks appear to be slightly offset from each other, as with $Mn_{0.45}Zn_{0.55}F_2$. One-dimensional convolution was carried out for a series of K scans following FC at H=1.5T and the resultant parameters for LRO intensity, SRO inverse correlation length κ and SRO integrated intensity are shown in figure 4-22. $\kappa(T)$ decreases sharply as the sample is cooled through the transition and gradually saturates at low temperature. The LRO component starts to rise at approximately 0.3K below T_M(1.5T). Fitting to equation 3.1 yields β_{FC}(1.5T)=0.27 $\pm$ 0.06, σ_{FC}(1.5T)=0.65$\pm$0.1K, and $T_{C,FC}$(1.5T)=34.2$\pm$0.2K, compared with β_{ZFC} = 0.19$\pm$ 0.03, σ = 0.09 $\pm$ 0.03K, and T_C = 34.95 $\pm$ 0.1K obtained from the ZFC data at the same field. Parameters from a field heating run at H=1.5T are presented in figure 4-23. The FH κ stays constant up to T_C(1.5T) and then starts to rise as the diffuse scattering broadens. The integrated intensity of the SRO decreases with increasing temperature. Again, diffuse scattering at temperatures much higher than T_M can be detected with neutron diffraction. The FH LRO intensity, remarkably similar to the ZFC LRO at 1.5T, diminishes to zero at T_M and is well described by β_{FH} = 0.21$\pm$0.03, σ_{FH} = 0.13 $\pm$ 0.03K, and $T_{C,FH}$ = 34.95 $\pm$ 0.1K. Therefore, the FH LRO transition appears to be driven by the same mechanism as that of the ZFC transition in both $Fe_{0.5}Zn_{0.5}F_2$ and $Mn_{0.45}Zn_{0.55}F_2$. We summarize the ZFC, FC and FH data at 1.5T

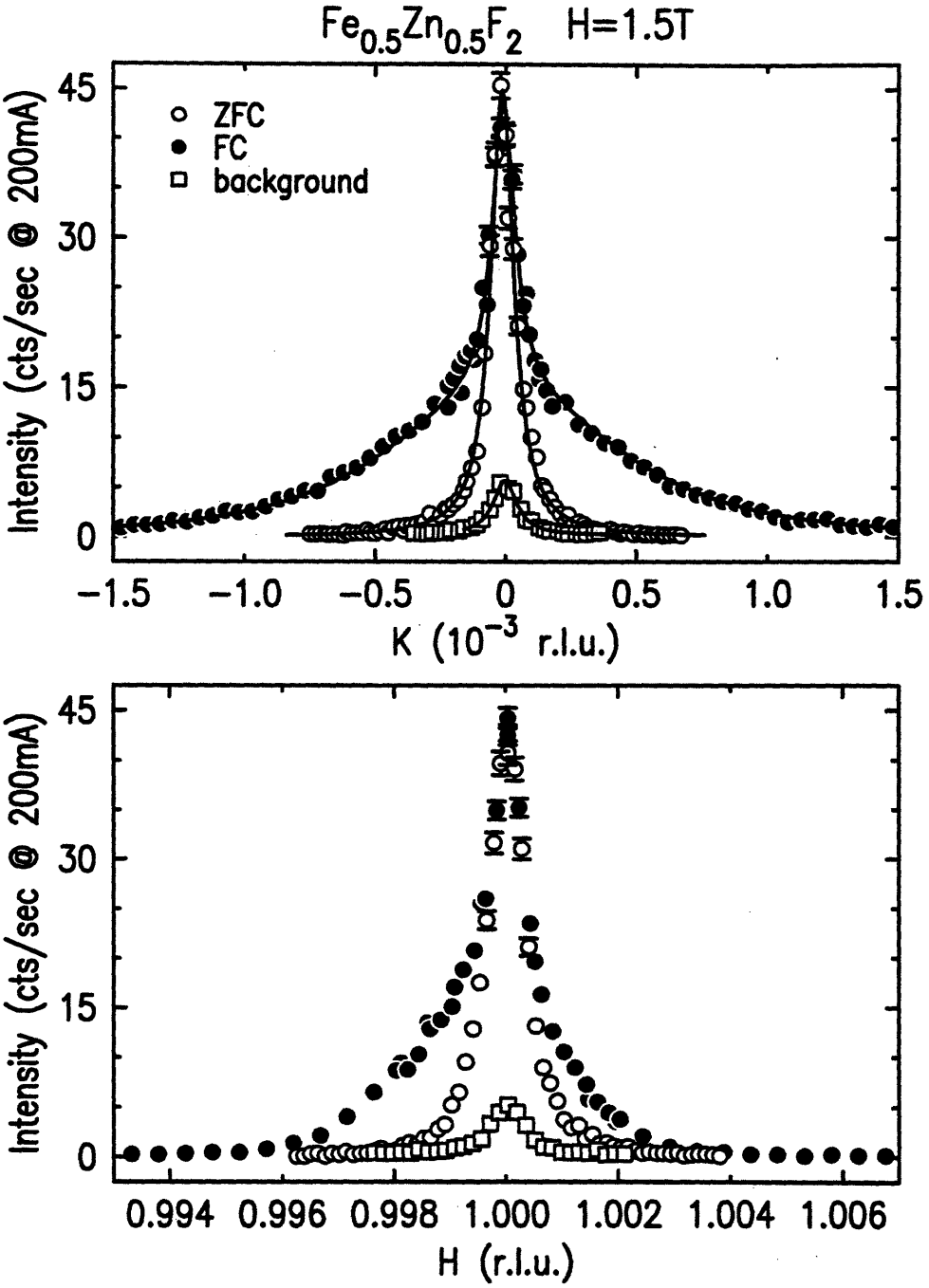

Figure 4-21: Representative FC scans at H=1.5T and T=15K for $Fe_{0.5}Zn_{0.5}F_2$, compared with ZFC data and background. T_C(1.5T)=34.98K. Upper panel: the K scan, fitted to equation 4.2, consists of a resolution limited central peak, demonstrating LRO, on top of tails of broad diffuse scattering reflecting SRO. Lower panel: the H scan shows of the same two components, but the position of the two peaks of different length scales are shifted with respect to each other. The ZFC scans and the multiple scattering background are all resolution limited. The ZFC data are scaled to match the FC peak intensity for comparison.

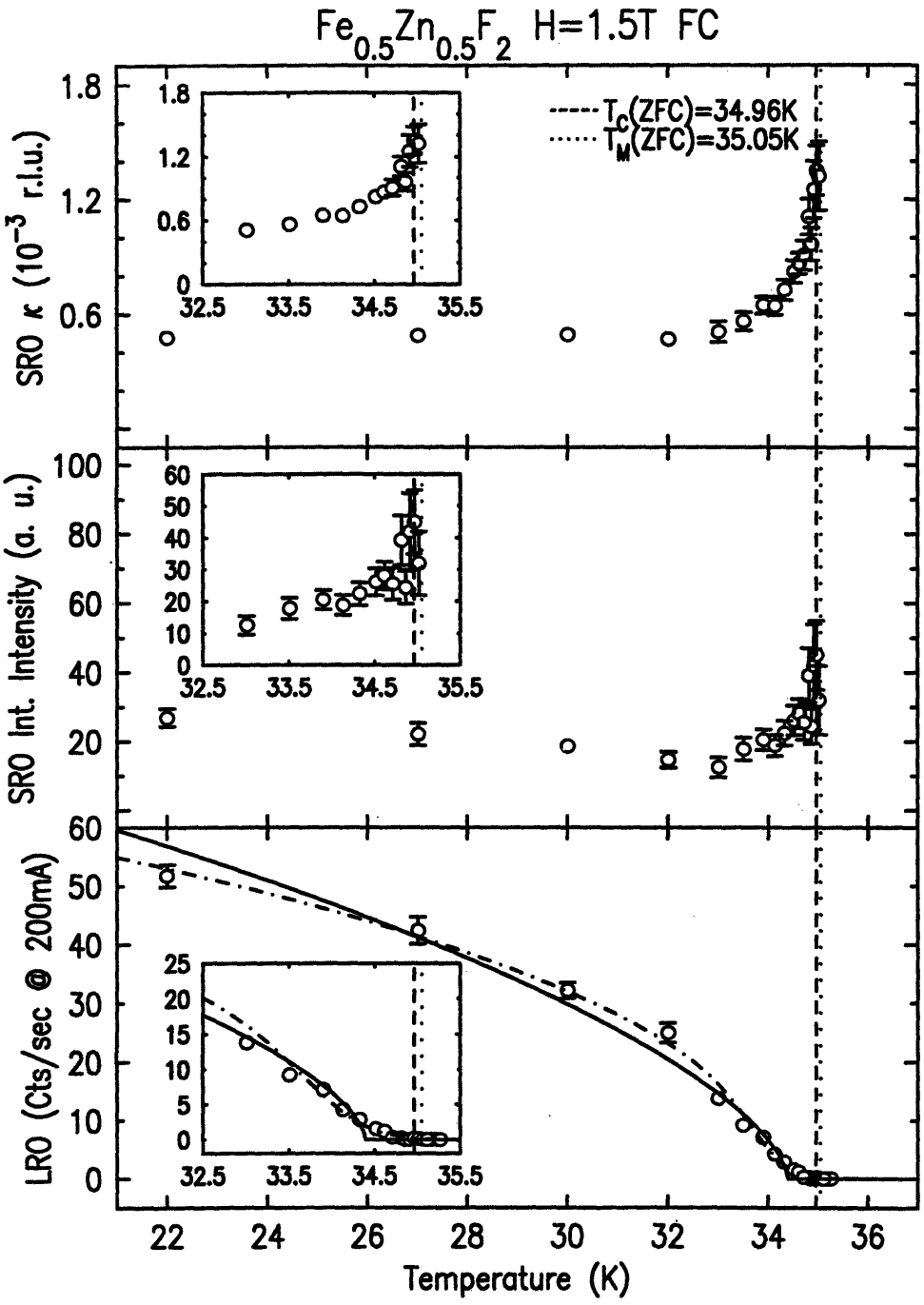

Figure 4-22: X-ray parameters of $Fe_{0.5}Zn_{0.5}F_2$ for H=1.5T FC. Top panel: inverse correlation length (κ) of SRO. Middle panel: integrated intensity (A) of SRO. Bottom panel: LRO component. The solid line is a fit to a simple power law that gives $\beta_{FC} = 0.31 \pm 0.03$. The dot-dash line is an alternative fit to a rounded power law which yields $\beta_{FC} = 0.23 \pm 0.02$.

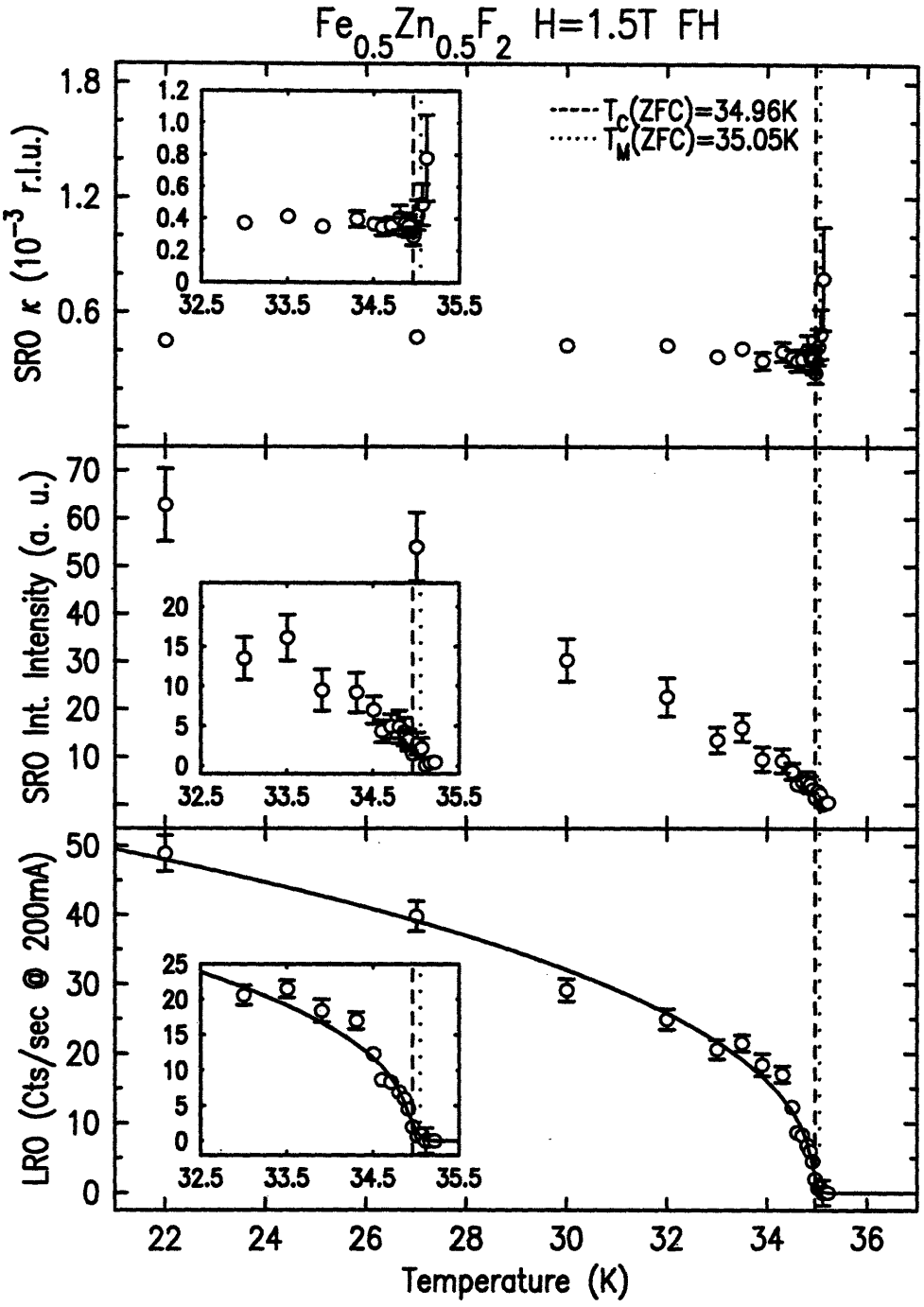

Figure 4-23: X-ray parameters of $Fe_{0.5}Zn_{0.5}F_2$ for H=1.5T FH. Top panel: inverse correlation length (κ) of SRO. Middle panel: integrated intensity (A) of SRO. Bottom panel: LRO component. The solid line is a fit to a rounded power law which yields $\beta_{FH} = 0.21 \pm 0.03$, in good agreement with the ZFC parameter of $\beta_{ZFC} = 0.2 \pm 0.02$. The same β is obtained if the FC LRO is fitted to a simple power law. The insets illustrate the transition region more clearly.

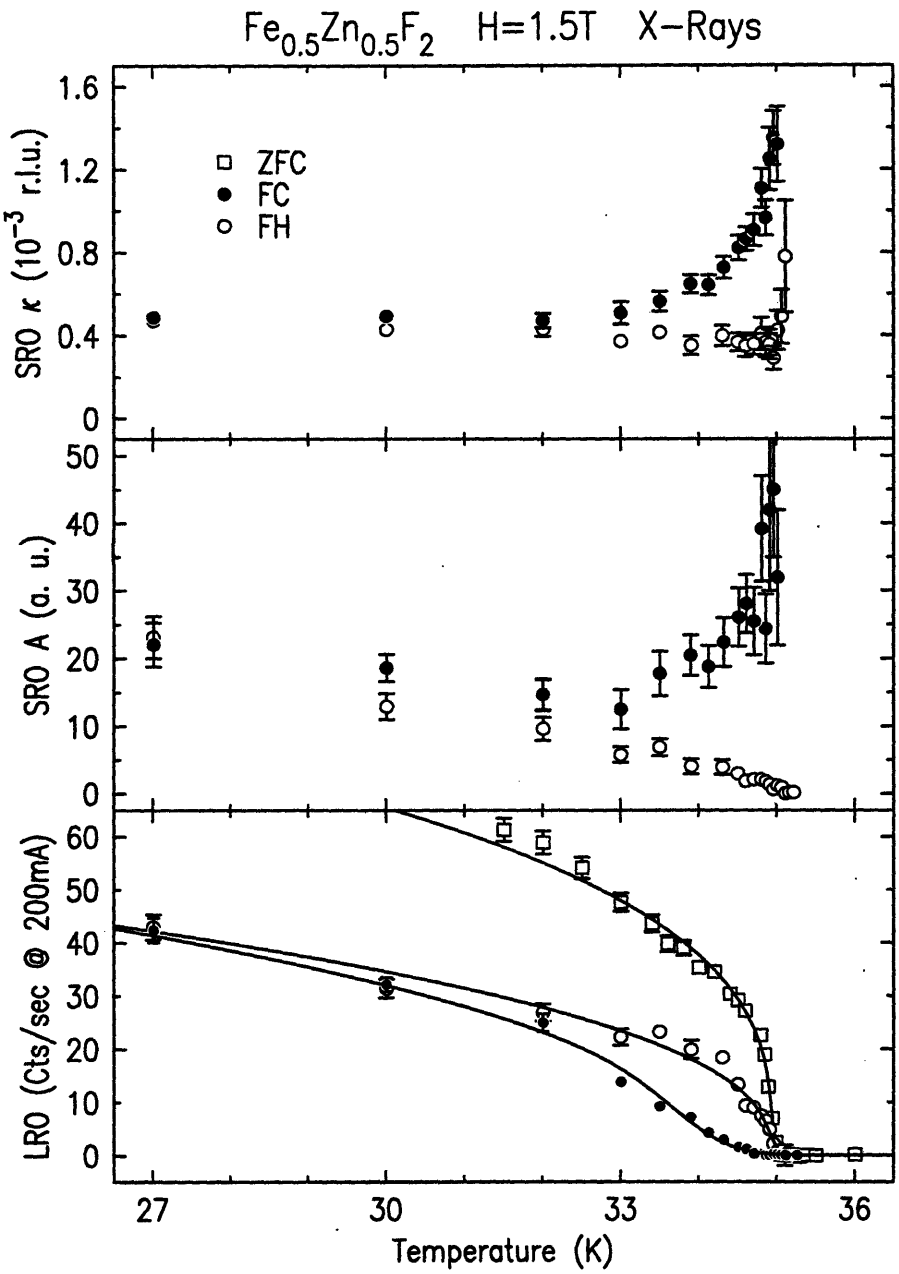

Fig. 8

Figure 4-24: Comparison of ZFC, FC and FH parameters of $Fe_{0.5}Zn_{0.5}F_2$ at H=1.5T measured by x-ray. The open squares, closed circles and open circles correspond to ZFC, FC and FH parameters respectively. Top panel: inverse correlation length (κ) of SRO. Middle panel: integrated intensity (A) of SRO. Bottom panel: LRO component. The solid lines are fits to equation 3.1.

in figure 4-24.

In figure 4-25, we summarize fitting parameters for data taken following FC at H=1T. The insets emphasize the transition region. κ saturates at 0.0002 r.l.u. at low temperature. As the temperature decreases, the LRO component rises in a rather rounded fashion at a temperature indistinguishable from the temperature at which LRO diminishes to zero following ZFC. Fitting the FC LRO to a rounded power law gives $\beta_{FC}(1\text{T})=0.26\pm0.05$, $\sigma_{FC}(1\text{T})=0.37\pm0.06$K, and $T_{C,FC}(1\text{T})=35.3\pm0.1$K. The ZFC data yielded $\beta_{ZFC}=0.17\pm0.03$ and $T_C=35.6\pm0.1$K, fitted to either a simple power law or to a rounded power law with a small σ. A comparison of the ZFC and FC LRO is shown in figure 4-26. Clearly, the LRO component dominates the scattered intensity, as shown by a comparison of the ZFC and FC K scans at 15K in the inset. Coupled with a large FC domain size which results in narrow diffuse tails, this might introduce uncertainties when fitting the FC scattering profile to two length scales.

To illustrate the rich hysteretic effects in the AF phase of $Fe_{0.5}Zn_{0.5}F_2$, field cycling as well as temperature cycling was performed and some representative results are presented below. In figure 4-27, we show K scans taken after field cooling to 15K at 3T, followed by lowering the field to 1.5T and then to 0T, together with the multiple scattering background. The FC state at 3T has broad tails due to the domains and zero LRO on top of background. As the field is decreased while maintaining the temperature at 15K, both the LRO and correlation length grow. From 3T to 1.5T, LRO increases to 5 counts/s and the inverse correlation length κ decreases from 0.0027 r.l.u. to 0.0023 r.l.u. When the field is completely removed, LRO further increases to 6 counts/s and there is still substantial SRO with κ further reduced to 0.0019 r.l.u. On the other hand, at the higher temperature T=30K, the domains are able to relax significantly when the field is removed after first field cooling the sample in 3T. The scan, shown by closed squares in figure 4-27, shows mostly LRO and some tails that can be attributed to a Lorentzian squared with a much smaller $\kappa=0.0004$ r.l.u. The higher temperature and the correspondingly stronger thermal fluctuations have clearly helped the ordering to grow. We note that field cooling in H=1.5T to

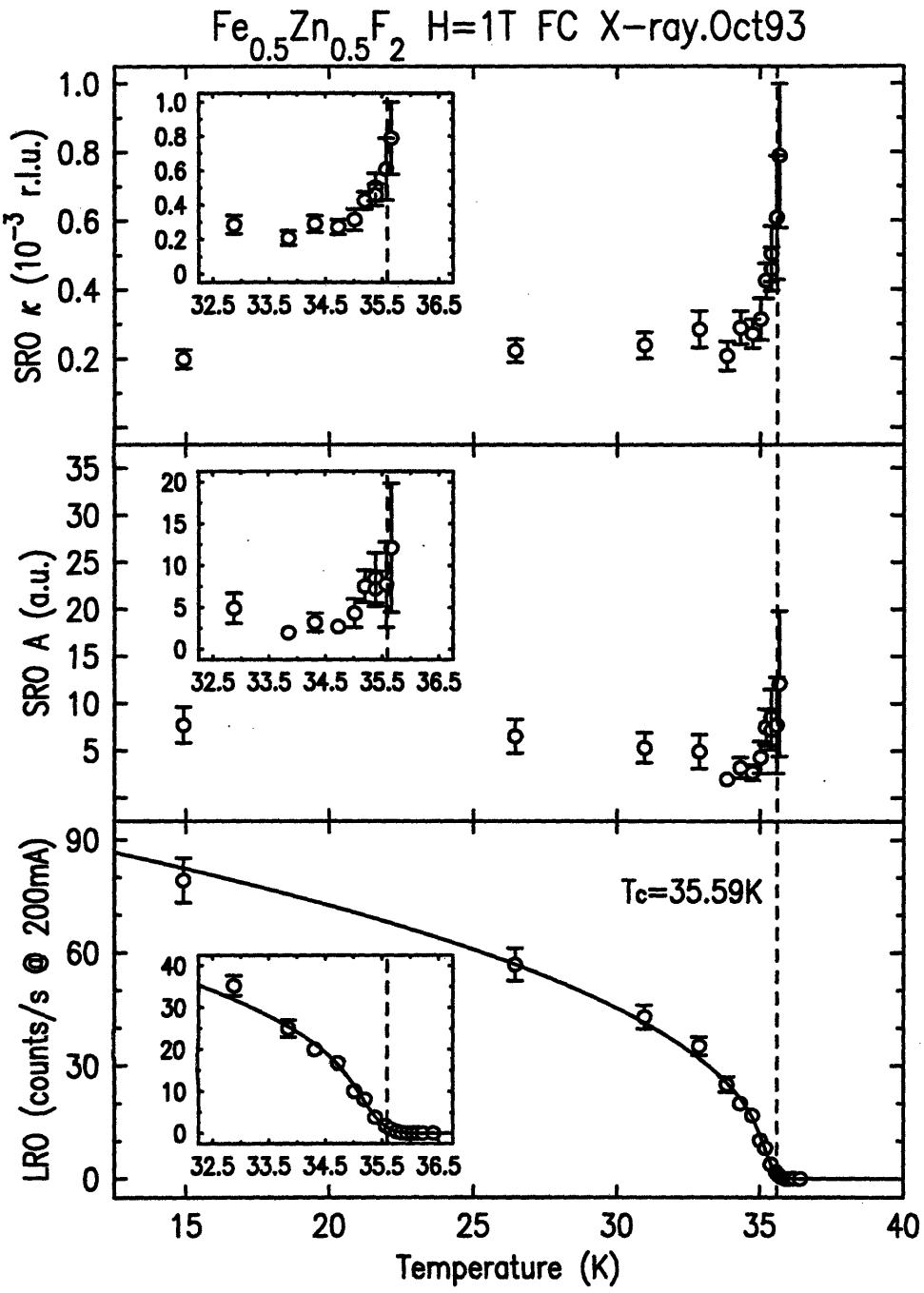

Figure 4-25: X-ray parameters of $Fe_{0.5}Zn_{0.5}F_2$ for H=1T FC. Top panel: inverse correlation length (κ) of SRO. Middle panel: integrated intensity (A) of SRO. Bottom panel: LRO component. The solid line is a fit to a rounded power law that gives $\beta_{FC} = 0.25 \pm 0.04$. The dash line shows the position of $T_C(1\text{T}) = 35.59\text{K}$ determined from ZFC data.

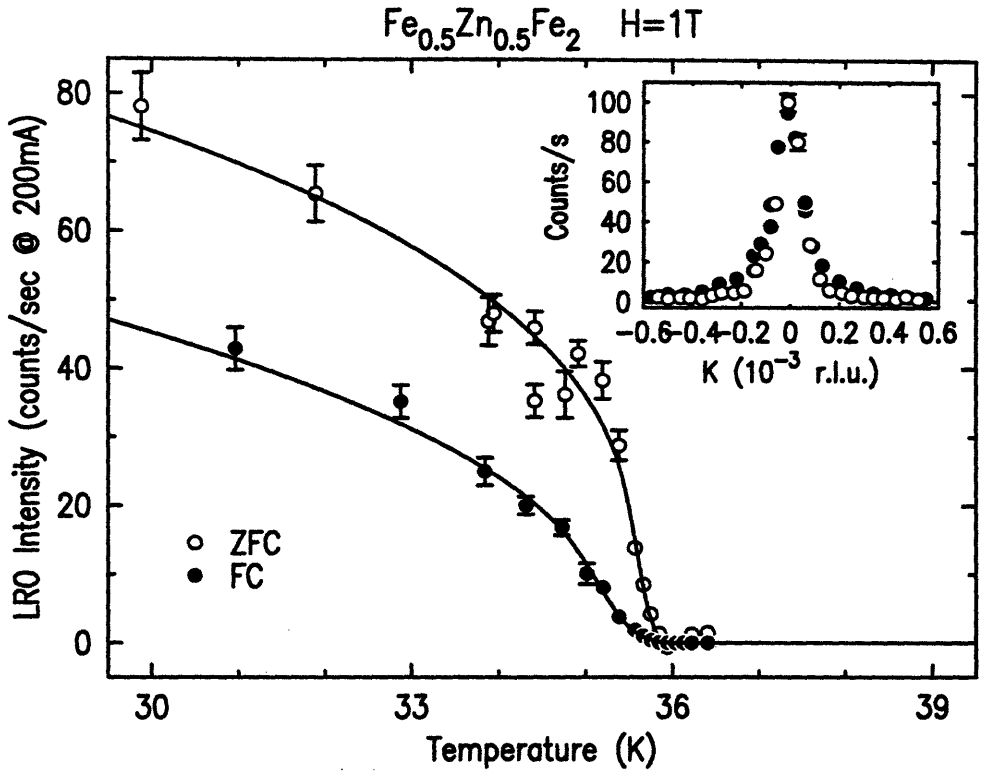

Figure 4-26: Comparison of ZFC and FC LRO at 1T in $Fe_{0.5}Zn_{0.5}F_2$. The solid lines are fits to equation 3.1 yielding $\beta_{ZFC} = 0.17 \pm 0.03$ and $\beta_{FC} = 0.25 \pm 0.04$.

15K, shown in figure 4-21, results in a much stronger LRO component and smaller κ compared to field cooling in 3T to 15K first and then lowering the field to 1.5T. This clearly shows that, at 15K, the domain state formed during FC at 3T is largely frozen even when the field is lowered. This demonstrates the different end configurations at a given temperature and field setting in the AF phase when the sample comes from the PM phase through different trajectories. The opposite has been claimed by a neutron scattering study on $Mn_xZn_{1-x}F_2$ [71], where generalizations were made based on a few scans between FC and FD protocols and the experiment may not have explored extensively enough in the phase diagram to observe the significant hysteresis discussed here.

Figure 4-28 shows similar hysteretic behavior following field cooling at H=5T. After subtracting multiple scattering and constant background, the K scan (open circles) following FC to 15K at 5T does not display any feature except that the constant intensity is at 0.6 counts/s above background. This shows that the FC domains at

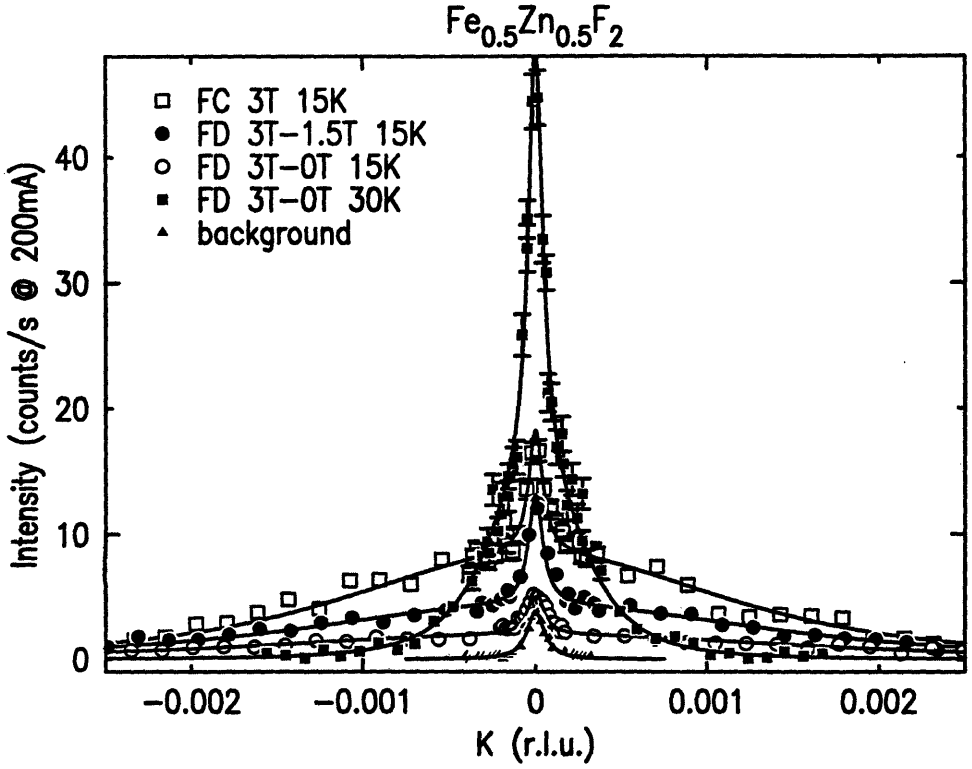

Figure 4-27: Hysteresis in FC and FD in $Fe_{0.5}Zn_{0.5}F_2$ observed by x-rays. Open squares: field cooling to 15K at 3T. Closed circles: reduce the field to 1.5T after FC to 15K at 3T. Open circles: reduce the field further to 0T after FC to 15K at 3T. Closed squares: reduce the field to 0T after FC to 30K at 3T. Closed triangles: multiple scattering background. The solid lines through the data are fits to equation 4.2, except the multiple scattering data which are fitted to the resolution function.

5T are so small that x-ray scattering, with its sharp reciprocal space resolution, is not able to discern a Lorentzian squared profile. When the field is removed while keeping the temperature constant at 15K, the K scan (closed squares) does not reveal obvious LRO or SRO features. But the intensity has grown to 2.3 counts/s and seems to form part of broad diffuse tails, reflecting stronger SRO contribution from expanded domains. This is another example of the strong pinning effects at low temperature in a RFIM system. In this strongly anisotropic DAFF, the pinning seems to be largely due to random bonds. If the field is removed after field cooling to 25K (open squares), which is within 3K of $T_C(5T)$, thermal fluctuations may overcome the pinning forces and the domains relax to much larger sizes (κ=0.00064 r.l.u.), with some LRO (13 counts/s) recovered.

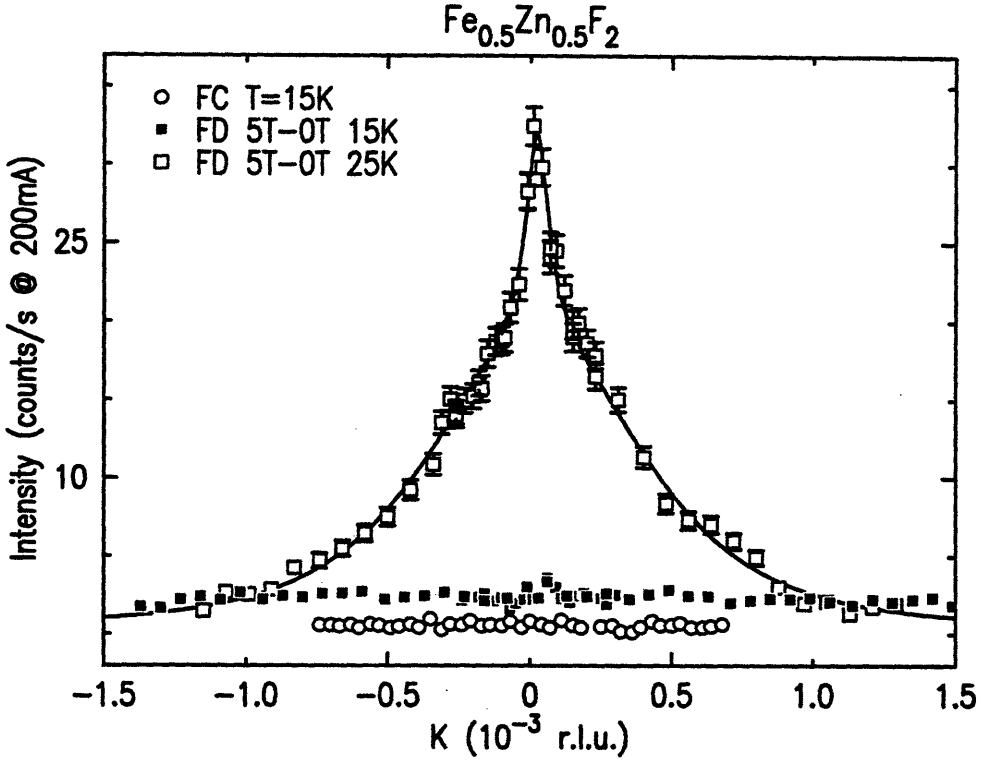

Figure 4-28: Hysteresis in $Fe_{0.5}Zn_{0.5}F_2$ observed by x-rays. Open circles: field cooling to 15K at 5T. Closed squares: reduce the field to 0T after FC to 15K at 5T. Open squares: reduce the field to 0T after FC to 25K at 3T. $T_C(H)$=28K. The multiple scattering together with the constant background due to noise has been subtracted from all the data. The solid line is a fit to equation 4.2.

4.6 Discussion

The neutron and x-ray scattering data presented above together suggest the existence of an equilibrium random field transition that lies below the metastability temperature $T_M(H)$ and the pseudo-critical ZFC transition temperature $T_C(H)$. This is first shown to be implied in the neutron scattering data, where the correlation length, connected and disconnected susceptibilities all demonstrate power law behavior in the equilibrium regime above $T_M(H)$. Extrapolating the power law fits naturally leads to the equilibrium random field Néel temperature $T_N(H)$. It is obvious from the data that, as a result of the random field activated dynamics, the measured FC κ deviates from the power law behavior well before the temperature is lowered to $T_N(H)$. Concordantly, a transition to long range order observed by x-ray scattering also occurs at a temperature below T_M and T_C, measured at lower fields. It seems natural to

designate this temperature $T_N(H)$, though we can not make a direct comparison between the neutron and the x-ray results as they are measured at different fields.

4.6.1 On the Neutron Results

Besides predicting T_N, the neutron data also yield estimates for the critical exponents $\nu = 1.5 \pm 0.3$, $\gamma = 2.6 \pm 0.5$ and $\bar{\gamma} = 5.7 \pm 1$. Similar approach has been taken previously with neutron measurements. For example, Belanger *et al.* estimated, without performing least squares fits, $\nu = 1.0 \pm 0.15$ and $\bar{\gamma} = 1.75 \pm 0.2$ based on data taken at H=1.4T and 2T on $Fe_{0.6}Zn_{0.4}F_2$ [75]. These authors went on to claim that the 3d RFIM thus exhibited 2d pure Ising critical behavior, as they had previously claimed based on birefringence measurements [132]. We believe the gaping discrepancy between these estimates with our current results is mainly due to the crossover to random exchange criticality in the $Fe_{0.6}Zn_{0.4}F_2$ study. The effective random field strength at 2T in $Fe_{0.6}Zn_{0.4}F_2$ is much smaller than that in a x=0.5 sample at the same applied field, due to the smaller dilution of Zn [171]. With such weak random fields, one obviously expects random exchange crossover and this explains the smaller value of ν reported. In fact, Yoshizawa *el.* examined exactly the same data on $Fe_{0.6}Zn_{0.4}F_2$ and concluded they were not sufficient for making any predictions about equilibrium critical exponents.

In an extensive neutron study on $Mn_{0.75}Zn_{0.25}F_2$, Cowley *et al.* carried out a similar approach in order to determine the exponent ν and the equilibrium Néel temperature [71]. As these authors noticed, the values of ν and $T_N(H)$ vary significantly depending on the temperature range chosen for the fits. Specifically, fits limited to data below $T_N(0)$ yielded values of ν that were substantially above 1, while including data at higher temperatures in the fits drew the value close to 1. This is apparently due to random exchange crossover effects. The authors thus concluded that $\nu = 1.4 \pm 0.3$ and excluded the possibility of $\nu = 1$. We note that studies on $Mn_{0.75}Zn_{0.25}F_2$ at high fields general suffer from the proximity of a bicritical point. In addition, $T_M(H)$ in reference [71] was named for what we now know as the ZFC pseudo-critical temperature $T_C(H)$ [70, 171]. Although κ appears to be the same

above $T_C(H)$ for ZFC and FC protocols, the system is clearly not in equilibrium between T_C and T_M because the ZFC state has LRO while the FC state does not. However, the fitting errors for ν and T_N due to this misnomer is mitigated by the fact that first, $T_M - T_C$ is small due to relatively weak random fields in $Mn_{0.75}Zn_{0.25}F_2$ and second, κ within a certain temperature range below T_M appears to fall onto the power law prediction based on κ above T_M, as shown in figures 3 and 4.

Therefore, we believe the current neutron study, performed on the model random field Ising magnet $Fe_{0.5}Zn_{0.5}F_2$ of excellent crystallographic quality, at fields that are among the highest used in random field experiments and within the temperature range $(T_M(H), T_N(0))$, is the most logical approach to studying asymptotic equilibrium random field critical behavior. The exponents directly determined from the fits are comparable to current theoretical predictions. For the susceptibilities, recent accurate series expansion calculations by Gofman *et al.* [45] proved two exponent scaling for the RFIM and predicted $\gamma = 2.1 \pm 0.2$ and $\bar{\gamma} = 2\gamma$ in 3d. Monte Carlo simulations by Rieger *et al.* yielded $\gamma = 2.3 \pm 0.3$ and $\bar{\gamma} = 4.8 \pm 0.9$ for binary random field distributions, and $\gamma = 1.7 \pm 0.2$ and $\bar{\gamma} = 3.3 \pm 0.6$ for Gaussian distributions. [172, 166]. Our measured values of γ and $\bar{\gamma}$, though slightly larger, generally agree well with these predictions. They are also consistent with two-exponent random field scaling which requires that $\bar{\gamma} = 2\gamma$. For the exponent ν, we have the predictions of $\nu = 1.6$ by Bruce and Wallace [173], $\nu = 1.3 \pm 0.3$ by Ogielski and Huse [34], $\nu = 1.4 - 1.5$ by Schwartz [47], and $\nu = 1.6 \pm 0.3$ and $\nu = 1.1 \pm 0.2$ by Rieger for binary and Gaussian random field distributions respectively [172, 166]. Our measured $\nu = 1.5 \pm 0.3$ is clearly in excellent agreement with most of these theoretical values.

4.6.2 On the X-Ray Results

The x-ray data presented here display the following general features. First, long range magnetic order, together with short range order, is observed during field cooling and subsequent field heating for fields below a certain threshold in both $Mn_{0.45}Zn_{0.55}F_2$ and $Fe_{0.5}Zn_{0.5}F_2$. Second, the amount of the FC LRO, or the intensity of the FC and FH LRO relative to that following zero field cooling, decreases with increasing

fields. The FH and the ZFC protocols at the same field appear to shed LRO in the same way. They can both be described by the same power law with the same β and $T_C(H)$. On the other hand, the temperature dependence of the FC LRO is less well depicted by a power law. This may be partially due to the lower scattered intensity during FC. The average value $\bar{\beta}_{FC} = 0.3 \pm 0.5$ is close to the pure or the random exchange Ising exponent. The FH LRO intensity is generally comparable to the FC LRO intensity at temperatures far below $T_C(H)$, but remains above the FC LRO as the temperature approaches $T_C(H)$. Concordantly, the FH SRO is characterized by a lower integrated intensity and longer correlation length compared to the FC SRO at corresponding temperatures and fields. This shows that thermal fluctuations help the system overcome free energy barriers, thereby enabling domains to relax and long range order to grow. Third, the size of the field cooled domains decreases at higher fields. Villain predicted that the minimum metastable domain size would scale with field as $\kappa \sim H^{\nu_H}$ with ν_H=2 at low temperature and $\nu_H = \frac{2}{2-\eta}$ at $T = T_N(0)$ [9]. Previous neutron scattering has yielded $\nu_H = 3.4 \pm 0.4$ for $Mn_{0.5}Zn_{0.5}F_2$, $\nu_H = 3.3 \pm 0.8$ for $Mn_{0.75}Zn_{0.25}F_2$ [71], $\nu_H = 2.18 \pm 0.05$ for $Fe_{0.5}Zn_{0.5}F_2$ [67], and $\nu_H = 3.63 \pm 0.12$ for $Co_xZn_{1-x}F_2$ [101]. Our own estimates from x-ray scattering is $\nu_H = 1.9 \pm 0.1$ for $Mn_{0.45}Zn_{0.55}F_2$ and $\nu_H = 1.7 \pm 0.3$ for $Fe_{0.5}Zn_{0.5}F_2$. However, the accuracy of these x-ray estimates are compromised by the fact that the data analysis only involved de-convolution in the K direction. The neutron analysis is generally complicated by extinction effects. The most reliable estimate for ν_H remains to be that obtained by neutron scattering on $Fe_{0.5}Zn_{0.5}F_2$. We note that Hill *et al.* found their FC x-ray data on $Mn_{0.75}Zn_{0.25}F_2$ to be compatible with $\nu_H = 2.0$.

A fourth feature of the x-ray data is that the FC LRO starts to grow at a temperature *below* the ZFC metastability temperature $T_M(H)$ above which there is no LRO or hysteresis. Hill *et al.* designated this temperature "$T_N(H)$", believing the FC transition to LRO is an equilibrium Nèel transition. However, this designation remains a speculation without understanding the origin of the FC LRO or independent means of confirmation. On warming through a ZFC transition, the system sheds LRO gradually. Because of the complicated distribution of many free energy min-

ima and the pinning due to random fields and random bonds, it is unable to relax into the ground state which becomes paramagnetic at the equilibrium random field $T_N(H)$. This results in "superheating" and the residual LRO does not diminish until the temperature reaches $T_M(H) > T_N(H)$. Based on symmetry, one would expect just the opposite to happen during field cooling. As the temperature is decreased, metastable domains start to form above $T_N(H)$. At $T_N(H)$, where in equilibrium a long range ordered ground state is expected, the system is trapped in a free energy minimum corresponding to a domain state and is unable to reach LRO. This causes "supercooling" and, in the weak random field limit, a certain LRO might start to form only when the sample is cooled further to a temperature, which we will refer to as $T_U(H)$. Upon further cooling, the LRO grows and the SRO domains expand slightly till they saturate at low temperature. Some SRO may be converted into LRO by flipping domains and attaching them to the LRO backbone. If the FC LRO we have observed in $Fe_{0.5}Zn_{0.5}F_2$ and $Mn_{0.45}Zn_{0.55}F_2$ is a manifestation of this type of random field behavior, it is possible that the equilibrium T_N lies somewhere between T_M, where LRO disappears on ZFC, and T_U, where LRO appears on FC. Upon subsequent FH, the observed LRO does not retrace the FC LRO, this corroborates the suspicion that the FC transition to LRO is not in equilibrium and is unlikely to be any closer to the true RFIM transition than the one observed during ZFC or FH protocols. At higher fields, LRO never develops and only SRO is observed during FC. One important observation is that both $(T_M(H) - T_C(H))$ and $(T_C(H) - T_U(H))$ increase with applied field, further demonstrating that these are effects attributable to the random fields. We note that T_U may indeed be the random field Néel temperature $T_N(H)$ in view of the above analysis of the neutron data, though a quantitative comparison is not available at the time being. However, even if the equilibrium random field transition does occur at $T_U(H)$, the observed critical behavior appears to reflect pure Ising or random exchange Ising criticality because the measured β_{FC} is approximately 0.3 ± 0.05.

There remains the question concerning the origin of the field cooled long range order. Two possible scenarios exist. The first one is that the LRO we observe with x-

rays is in fact a bulk phenomenon. Indeed, it should not be a surprise to observe LRO during FC at lower fields. Since the ordering in a RFIM is a result of the competition between the exchange interaction which favors long range order, and the site random local fields which favor disorder, it is expected that LRO can be achieved for relatively weak random fields, the strength of which is proportional to the applied field. The FC LRO is unexpected mostly because it was never seen in neutron scattering. For $Fe_{0.5}Zn_{0.5}F_2$, as studied by Cowley *et al.*, the FC κ for $H \leq 3$T becomes smaller than the transverse resolution (HWHM) and there exists considerable extinction [67]. Besides the FC bulk domains, Cowley *et al.* claimed that there is no threshold field for the destruction of long range order based on the observation that the extinction was significantly relieved, reflected in a marked increase in intensity, even when a field as low as 0.25T was applied. In our own triple-axis neutron scattering experiment, with respective longitudinal and transverse resolution (HWHM) of 0.002 r.l.u. and 0.0017 r.l.u., we found that the FC data at H=1.5T yield $\kappa = 0.00037$ r.l.u. if fitted only with a Lorentzian squared component. This κ is much smaller than the resolution. Clearly, extinction plays an important role at the low fields and its correction is an involved procedure that is not always successful, as demonstrated by Cowley *et al.* Although a Lorentzian squared seems to fit the 1.5T neutron data data, it does not rule out the possibility that a fit to two length scales may also work if the extinction is adequately accounted for. For $Mn_{0.45}Zn_{0.55}F_2$, the FC κ at 1.5T is comparable to the HWHM of the transverse resolution in the neutron study by Cowley *et al.* [71]. However, the intensity of the FC LRO is only approximately one eighth of that of the ZFC LRO at low temperatures in the same field and it may have been overshadowed by strong SRO intensity in the neutron scans.

Although our current data do not rule out this bulk FC LRO scenario, it is in disagreement with available neutron results and with the observation by Hill *et al.* on the SRO sample of $Mn_{0.75}Zn_{0.25}F_2$ [60]. Since the SRO $Mn_{0.75}Zn_{0.25}F_2$ differed from the LRO one only in its surface smoothness, we need to examine the surface quality of our x-ray samples more closely. In figure 4-29, we present a three dimensional image of the $Fe_{0.5}Zn_{0.5}F_2$ sample taken with an atomic force microscope. The image shows

that, instead of being flat over large areas on the surface as the two dimensional images suggest, the surface is strewn with tiny "knolls" and "stalagmites" with an average height of no more than 100 nm. The root-mean-square of the vertical variation is 9 nm. These numbers are small compared to the penetration depth of x-rays which is approximately 3.5μm at (100) at x-ray energy 9.5KeV for both $Fe_{0.5}Zn_{0.5}F_2$ and $Mn_{0.45}Zn_{0.55}F_2$. The surface quality of the $Mn_{0.45}Zn_{0.55}F_2$ sample is very similar to that of the $Fe_{0.5}Zn_{0.5}F_2$ sample.

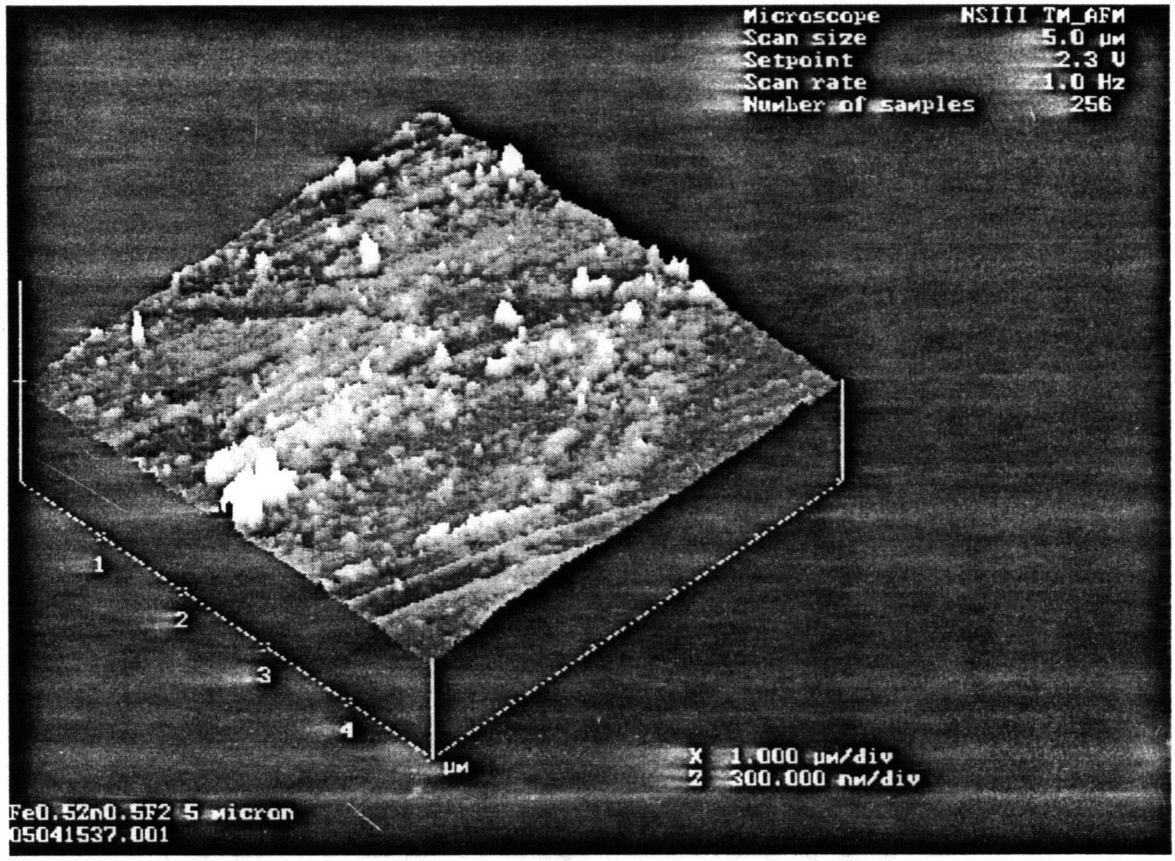

Figure 4-29: Three dimensional AFM image of representative areas on the surface of the $Fe_{0.5}Zn_{0.5}F_2$ sample used for x-ray scattering. The scales of the horizontal and vertical axes are 1μm/division and 300nm/division respectively.

A second scenario for the origin of the FC LRO, first presented by Hill *et al.* [60], derives the LRO from defects on the sample surfaces. These defects may play a role in aiding the formation of LRO by, for instance, providing nucleation center for large magnetic clusters or generating an asymmetric distribution of random fields near the surface. In fact, theoretical studies by Maritan *et al.* for the case of asymmetric

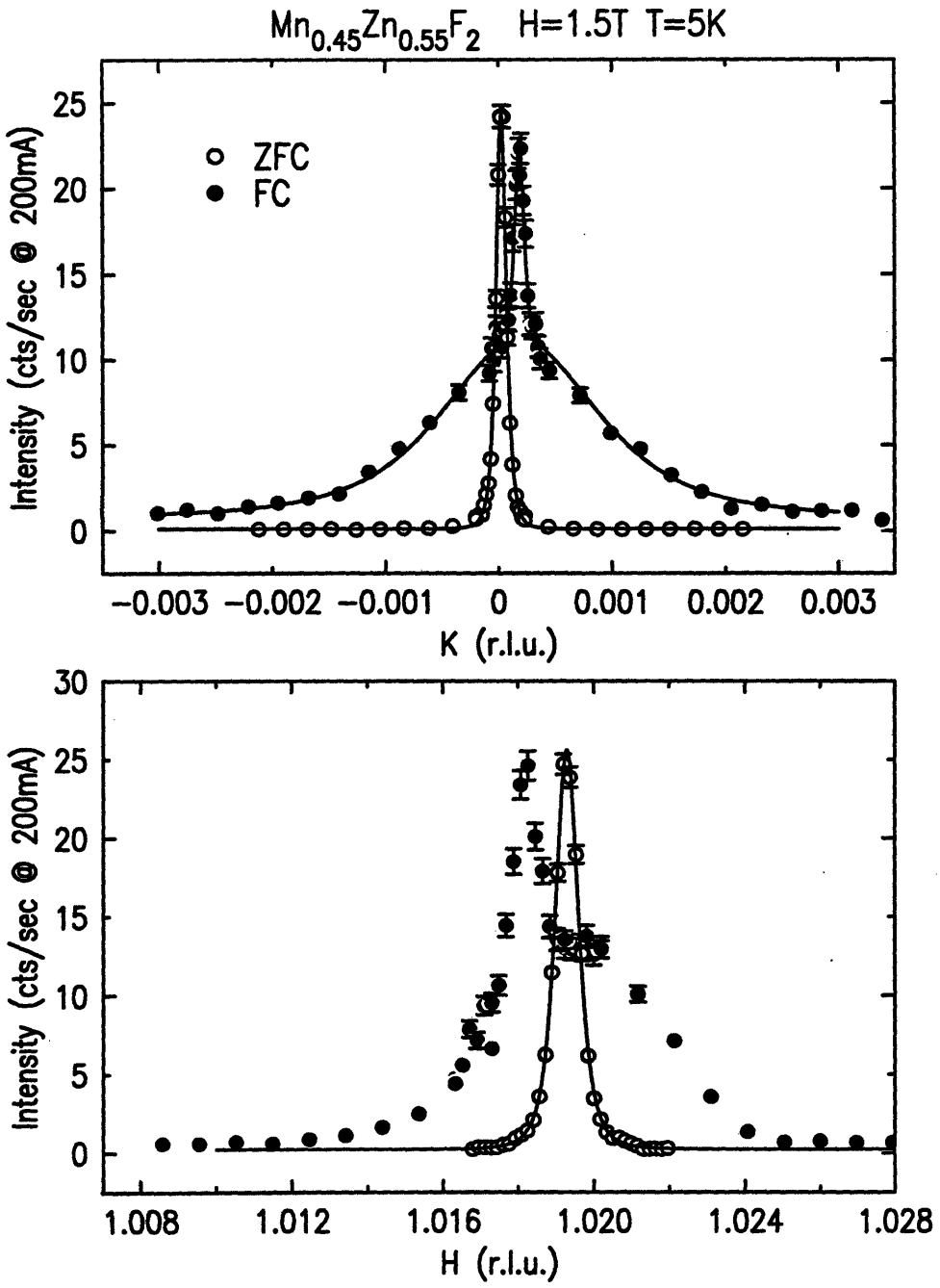

Figure 4-30: Position of ZFC and FC H and K scans of $Fe_{0.5}Zn_{0.5}F_2$ by x-ray scattering. Note, the FC data are the same as those presented in figure 4-21, but the H and K scan positions in that figure have been shifted to center at (100) for demonstration purpose. Open circles: ZFC resolution-limited scans with intensities scaled to 1/10 to facilitate comparison with FC scans. Closed squares: FC scans taken immediately after the ZFC scans.

random fields predict that the observed value of β should be that of the pure Ising model and not the RFIM [174]. In our case, this means that the REIM β=0.35 would be observed. Indeed, β_{FC} estimated above is in broad agreement with this prediction and is generally higher than those obtained from β_{ZFC} and β_{FH}. An additional observation that may shed some light on the origin of the LRO component is the different position of the LRO piece and the center of the SRO peak in the longitudinal scans. In figure 4-30, we plot the original H and K scans taken on $Fe_{0.5}Zn - 0.5F_2$ after ZFC and FC protocols, both at H=1.5T and T=15K. The peak positions of the K scans are slightly offset due to a small movement of the sample during the temperature changes. As is apparent from the plot for H scans, the FC SRO peak coincides with the ZFC resolution limited peak while the FC LRO peaks at a slightly smaller H position. Note that the H direction is perpendicular to the crystal surface. This seems to suggest two different underlying lattice constants for the two different length scales - a situation that may conceivably occur because of a concentration of defects near the surface. However, this shift in the H peak position was not reported for $Mn_{0.75}Zn_{0.25}F_2$. Furthermore, the ZFC H peaks are all resolution limited and do not seem to suffer from two offset components.

The problem of anomalous large-scale fluctuations in the near-surface region is not unique to the RFIM. Other x-ray and neutron scattering studies of structural [175, 176] or magnetic [177, 178, 179, 180, 181] phase transitions have revealed the co-existence of two distinctively different length scales in the correlation length. Altarelli *et al.*, in their recent theoretical treatment of this problem, proposed that the narrow component (or the one with the larger length scale) comes from the quenched long-range disorder in the region damaged during the polishing of the samples [182]. In our case, though the visible surface roughness fluctuations due to polishing is only on the order of 100nm, it is conceivable that the region affected by the resulting long-range strain can extend for a few microns into the depth of the sample - a length scale comparable to the x-ray penetration depth.

4.7 Summary

In summary, we have studied the field cooling transition of the 3d RFIM with neutron and x-ray scattering. Double-axis neutron scattering measurements taken with $Fe_{0.5}Zn_{0.5}F_2$ yield $\nu = 1.5 \pm 0.3$, $\gamma = 2.6 \pm 0.5$ and $\bar{\gamma} = 5.7 \pm 1$ for the random field correlation length, connected and disconnected susceptibility exponents. All the analysis are carried out above the metastability temperature and below the zero field Néel temperature. The equilibrium random field transition can be found by extrapolating the power law fits to κ to zero. The $T_N(H)$ determine this way is well below $T_M(H)$ and $T_C(H)$, both determined through the ZFC transition at the corresponding fields. Obviously, in order to determine the critical exponent more accurately, experiments need to go to higher fields where new random field behavior can be observed in a wider accessible temperature range. Alternatively, one can take detailed measurements through the transition while varying the external field.

The x-ray data from $Fe_{0.5}Zn_{0.5}F_2$ and $Mn_{0.45}Zn_{0.55}F_2$ reveal the coexistence of long range order and short range order for weak random field strengths. The nucleation of the long range order occurs below $T_M(H)$ and $T_C(H)$. The intensity of the long range order component decreases with increasing field. Its temperature dependence can be described by a power law with $\beta_{FC} \approx 0.3 \pm 0.05$. The origin of this field cooled long range order is not completely understood. To thoroughly settle the lingering questions, a high resolution neutron scattering study equipped with reliable extinction corrections is probably the most viable approach.

Chapter 5

Metastability of the Field Cooled Domains

5.1 Introduction

In this chapter, we discuss the metastability in the field cooled state of a DAFF and in particular the time dependence of magnetic domains. Systems modeled by the RFIM generally display a variety of intriguing phenomena, including particularly rich dynamic behavior [183, 184]. This was first discovered by experiments on diluted antiferromagnets in applied fields. Early neutron scattering experiments on $Fe_{0.7}Mg_{0.3}Cl_2$ by Wong *et al.* showed hysteresis in the scattering intensity following different paths in the $H-T$ plane[80]. They interpreted this as a result of the existence of a domain phase. Soon afterwards, Cowley *et al.* carried out a more careful study on $Fe_xZn_{1-x}F_2$[185]. They confirmed that a short range ordered domain state was formed as the system was cooled in the presence of random fields or field-lowered at a constant temperature across the phase boundary. Related hysteretic effects were observed by Shapira *et al.* in $Mn_{0.75}Zn_{0.25}F_2$ using various bulk thermodynamic techniques[186]. These nonequilibrium effects made it virtually impossible to answer important questions such as the lower critical dimension of the RFIM through experiments.

Following the experimental discoveries, theoretical work by Fisher and Villain

indicated that the anomalously slow dynamics in the RFIM causes its true equilibrium behavior to evade investigation on experimental time scales[151, 187]. As a RFIM system is cooled through the transition from the disordered paramagnetic phase, it falls out of equilibrium and is trapped in a metastable domain state[152, 153]. The structure of the FC domains is determined by the competition between energy costs due to unsatisfied bonds between neighboring spins and gains due to random fields (RF) and random bonds (RB) in a DAFF. The experimentally observed metastability results from the presence of multiple free energy minima corresponding to differing spin configurations. For $T < T_C(H)$, where $T_C(H)$ is the pseudo-critical temperature defined in the ZFC transition, there exist metastable spin clusters that, if flipped, the free energy may be lowered. However, an energy barrier of the order $\Delta E \sim pL^D$ needs to be overcome. The multiplicative factor p is dependent upon the exchange J, the spin S, the temperature T and the field H. D is a scaling exponent that depends on the roughness of domain surfaces. Based on the Arrehnius law, these energy barriers ΔE may be overcome through thermal activation on a time scale $t \sim exp(\frac{\Delta E}{kT})$ and the domains are expected to relax with the larger ones generally expand at the expense of the smaller ones. The expansion of domains extend towards a LRO equilibrium state, and the time dependence of the average domain size can be easily deduced from the above relations for ΔE and t. For a RFIM system in the field cooled state, Villain has argued that the dynamic lower critical dimension is 4 and that the domain relaxation time in three dimensions is infinite[152]. On general grounds, it is expected that the average size of these field cooled domains grows logarithmically with time[152, 26].

An indication of such metastable effects was first observed by Wong *et al.* [80] in their study on $Fe_{0.7}Mg_{0.3}Cl_2$, where the FC peak intensity showed a clear increase over a period of six hours (though most of the change occurred within the first hour). No attempt was made by these authors to measure the evolution of the domain size itself. A similar effort to study the time dependence of the FC domains in $Mn_xZn_{1-x}F_2$ by neutron scattering yielded negative results. In particular, Cowley *et al.* [188] carefully studied the FC domains in $Mn_xZn_{1-x}F_2$ at several fields and temperatures and did not discern any notable change in either the peak intensity or the domain

size over two decades in time. However, optical Faraday rotation [81, 82] and SQUID magnetometry [84, 83] performed on $Fe_xZn_{1-x}F_2$ with various levels of dilution have shown the FC uniform magnetization M_{FC} to decay logarithmically over time. This has been interpreted as a manifestation of domain wall motion in the metastable state.

Following these apparently contradictory experimental results on the time dependence in 3d DAFFs, Nattermann and Vilfan (NV) developed ideas stressing the role of broad and narrow domain walls and concluded that there was disparate time dependent behavior for DAFFs with weak and strong anisotropy[28]. In systems with weak anisotropy and therefore broad domain walls, for example, $Mn_{0.75}Zn_{0.25}F_2$ in which the dipolar anisotropy is only about 1% of the exchange energy, they predict that no domain relaxation should be observable within the usual experimental time scale of several hours. Conversely, NV predict that strongly anisotropic DAFFs with narrow domain walls should show a decaying uniform magnetization due to adjustments in the domain surfaces. $Fe_xZn_{1-x}F_2$ and $Fe_xMg_{1-x}Cl_2$ are examples of 3d systems with strong anisotropy. The NV theory can qualitatively describe the neutron scattering findings in $Mn_{0.75}Zn_{0.25}F_2$ and $Fe_{0.7}Mg_{0.3}Cl_2$ and the magnetometry results in $Fe_xZn_{1-x}F_2$. In their measurements on $Fe_{0.46}Zn_{0.54}F_2$, Lederman *et al.* mapped out the dynamic behavior in the $H-T$ plane based on systematic time dependence and field-cycling studies[189]. However, up to now, there has been no direct evidence of the predicted underlying domain evolution. In this chapter, we present systematic measurements of the FC domain at a series of fields and temperatures. We first discuss neutron scattering experiments on $Fe_{0.5}Zn_{0.5}F_2$ that were designed to study the metastable effects by directly measuring the correlation length in the FC state. We find a notable increase in the FC domain size for $T \leq T_C(H)$. No time dependence is observed at very low temperatures, $T \ll T_C(H)$, as a result of the frozen dynamics. This explains why domain relaxation was not detected in earlier experiments by Cowley *et al.* on a sample of the same composition[185]. In their experiment, the sample was quenched to low temperatures ($T \approx 8$K). Our results are then compared with further SQUID magnetometry measurements of the uniform

magnetization, M. At H=5.5T, at several temperatures below T_C(5.5T), the excess magnetization $M_{ex} = M_{FC} - M_{ZFC}$ and the inverse correlation length, $\kappa(T)$, exhibit identical time dependences.

5.2 Experimental Procedure

As mentioned earlier, the temperature scale of the neutron data was found to be offset by +3.01K from the SQUID or x-ray data. We believe this discrepancy arises solely from an error in the magnet thermometer calibration in the neutron study and therefore the neutron data have been shifted by $\Delta T = -3.1K$ throughout this discussion. The zero field transition measured by neutron scattering shows a smearing that is less than 0.1K (FWHM), corresponding to a concentration gradient of less than 0.1% per mm. The crystal has a mosaic spread of approximately 0.01° FWHM given by x-ray diffraction.

The neutron scattering experiments were performed at the High Flux Beam Reactor at Brookhaven National Laboratory. Measurements were carried out in the triple-axis mode. The data at H=5.5T were taken on spectrometer H7. A PG(002) monochromator selected incident neutrons with an energy of 14.7meV. The horizontal collimations were 10'-10'-sample-10'-80'. At the (100) reciprocal lattice point, this configuration gave rise to an in-plane resolution of 0.0031 r.l.u. (HWHM) parallel to the momentum transfer, 0.0012 r.l.u. perpendicular to the momentum transfer and a 0.044 r.l.u. vertical resolution. The energy resolution was 0.17meV HWHM. The neutron data at all other fields were taken on spectrometer H9 also used triple-axis geometry with two set-ups: a 5meV 60-40-30-sample-20-20 configuration resulting in 0.0032 r.l.u. (HWHM) longitudinal, 0.0019 r.l.u. transverse and 0.05meV energy resolution, and a 3.5meV 60-40-15-sample-20-20 configuration resulting in 0.0023 r.l.u. (HWHM) longitudinal, 0.0017 r.l.u. transverse and 0.03meV energy resolution.

In all the neutron scattering and the SQUID magnetometry experiments, the FC quenches begin with the system brought to equilibrium at 10K above $T_C(H)$ and then cooled rapidly through the transition to the target temperature with the field held

constant. Time-zero is taken to be the time at which the sample temperature crossed the metastability temperature $T_M(H)$ associated with the phase boundary[190]. By definition, this is the point at which metastability is first established[84]. Immediately after the temperature is stabilized at the target value, scans are taken repeatedly through the (100) peak in the neutron scattering experiment while in the SQUID measurements the uniform magnetization, M, is measured repeatedly. The time scales probed by both types of experiments are approximately 5 minutes to 5 hours.

5.3 Neutron Scattering Results

5.3.1 Initial Results at H=5.5T

The first direct evidence of domain expansion comes from neutron scattering results on $Fe_{0.5}Zn_{0.5}F_2$ at H=5.5T [134]. In this section, we discuss in detail the experimental results at three temperatures below the T_C(5.5T): T=6.8K, 21.5K and 27.1K. As we shall see, these temperatures represent three distinct metastability regimes. No LRO component is observed in these measurements. In figure 5-1, we show the peak intensities of K scans taken after quenching to each of these temperatures. Over the time period studied, the (100) peak intensity is constant at T=6.8K, but increases notably at T=21.5K and T=27.1K.

Before discussing these results further, we first present a brief outline of the data analysis techniques. As discussed in Chapter 3, the scattering cross section near a magnetic reciprocal lattice point **G** is basically determined by the spin-spin correlation function of the z-components $< S_i^z S_j^z >$ and, for field cooling of a random field Ising system, is typically represented by the square of a Lorentzian [185, 191, 192]

$$\mathcal{S}(\mathbf{Q}) = \frac{A\kappa}{(\kappa^2 + (\mathbf{q})^2)^2} \tag{5.1}$$

where $\mathbf{q} = \mathbf{Q} - \mathbf{G}$ is expressed in reciprocal lattice units. Written in this form, A is the integrated intensity and the correlation length is equal to $1/\kappa$. We have ignored the δ-function for LRO and the Lorentzian term for dynamic susceptibility. Trans-

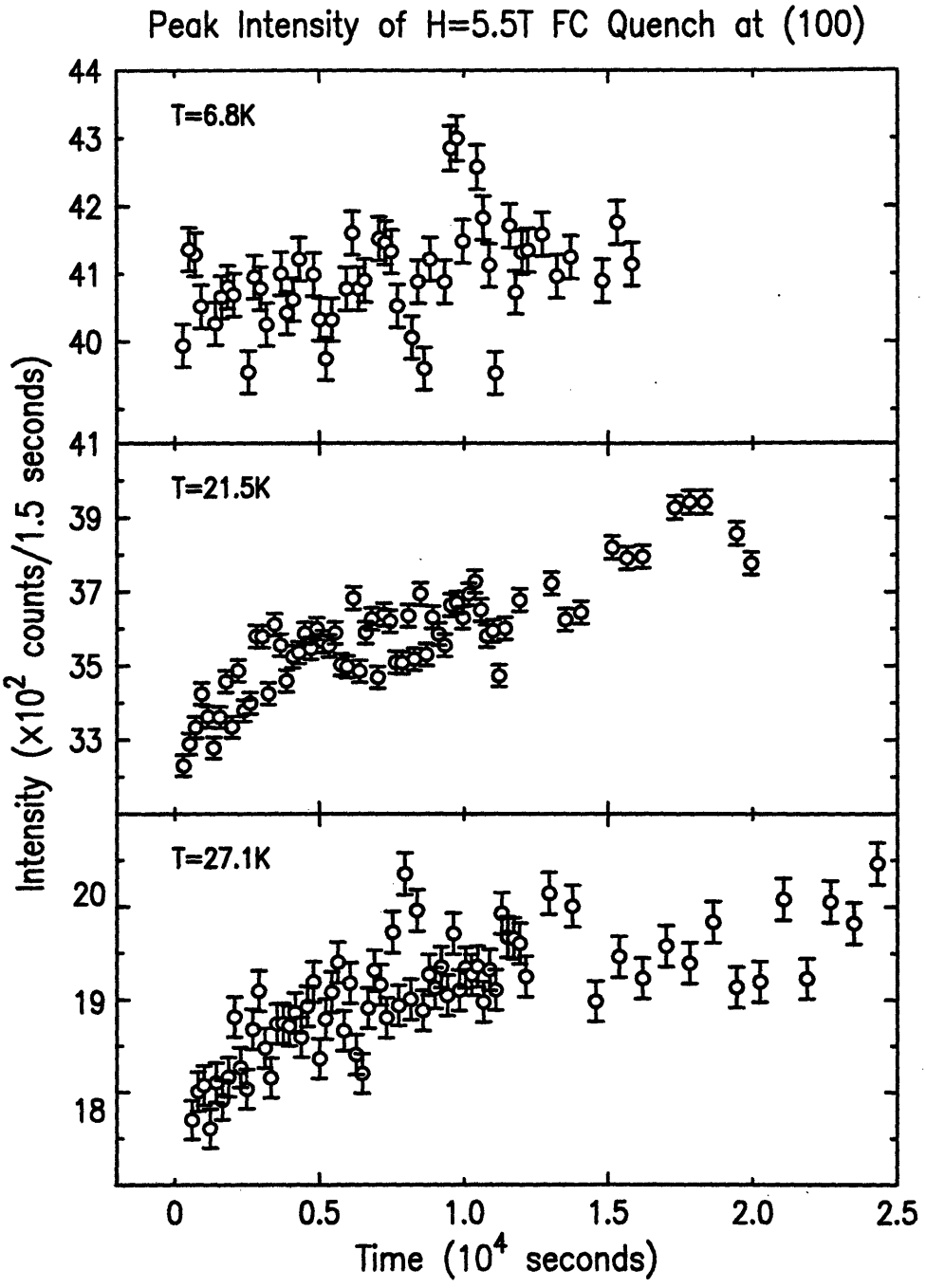

Figure 5-1: The time dependence of the (100) magnetic peak intensity following FC quenches at H=5.5T to three temperatures T=6.8K (top panel), T=21.5K (middle panel) and T=27.1K (bottom panel) . There is no detectable time-dependence at T=6.8K, which is attributed to a freezing of the domain dynamics at low temperatures due to the Ising gap. At T=21.5K and T=27.1K, a pronounced increase in peak intensity is observed.

verse scans through (100) were fitted to equation (1) convolved with the instrumental resolution, plus a time-independent constant background, in order to determine the parameters A and κ. The results of this analysis, shown in figure 5-2, shows that κ decays significantly over a period of five hours at T=21.5K and T=27.1K, but remains constant to within errors at T=6.8K. The fitted integrated intensity A remains constant over time at all temperatures.

However, upon closer scrutiny of the quality of each fit, it was found that equation 5.1, while providing excellent fits to the data at T=27.1K, showed small but systematic deviations from the data for large $\mathbf{q}$ at T=6.8K and T=21.5K. As shown in figure 5-3, the fits (dashed line) overestimate the intensity in the wings. This cannot be attributed to the absence of a dynamic Lorentzian term in the cross-section which would account for thermal fluctuations, because such a term can only increase the large $\mathbf{q}$ intensity. Further, the energy resolution of the triple axis mode is sufficiently high as to make the experiments insensitive to these fluctuations. As discussed previously by Cowley *et al.*[185, 188], the deviations are due to extinction effects which are commonly observed in neutron scattering experiments on nearly perfect crystals. The κ's obtained from the fits at T=6.8K and T=21.5K are then in fact overestimates of the intrinsic widths. Therefore, we experimented with re-fitting these scans using only points that were below one third or one quarter of the peak intensity, since extinction effects were expected to be much smaller for these data points. The κ's obtained this way were 50% smaller than those obtained from the earlier fits, but they displayed similar time dependences. However, the maximum value of the fitted curve exceeded the measured peak intensity in the data by more than a factor of five, which was expected because of the pronounced effects of the extinction. To maintain satisfactory fitting quality and at the same time to account for extinction, we introduced a simple correction formula for secondary extinction[193],

$$I_c = \frac{I}{1 + gI} \tag{5.2}$$

where I_c is the corrected intensity, I is the result of equation 5.1 convolved with the

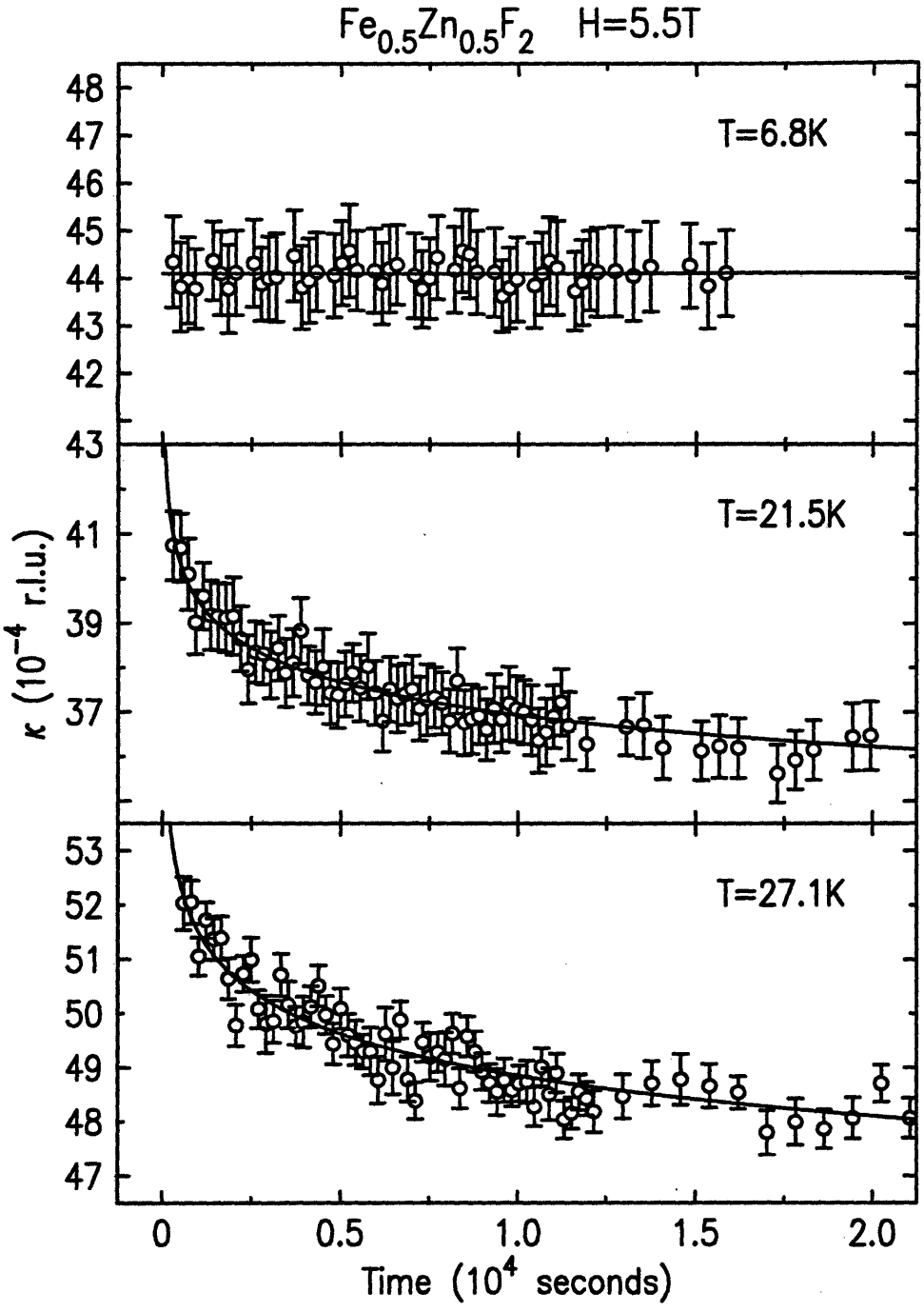

Figure 5-2: Time dependence of the inverse correlation length, κ, obtained from fits to equation 5.1. The growth of the FC domains at T=21.5K and T=27.1K is significant. The domain size does not change at T=6.8K. The solid lines are fits to equation 5.4.

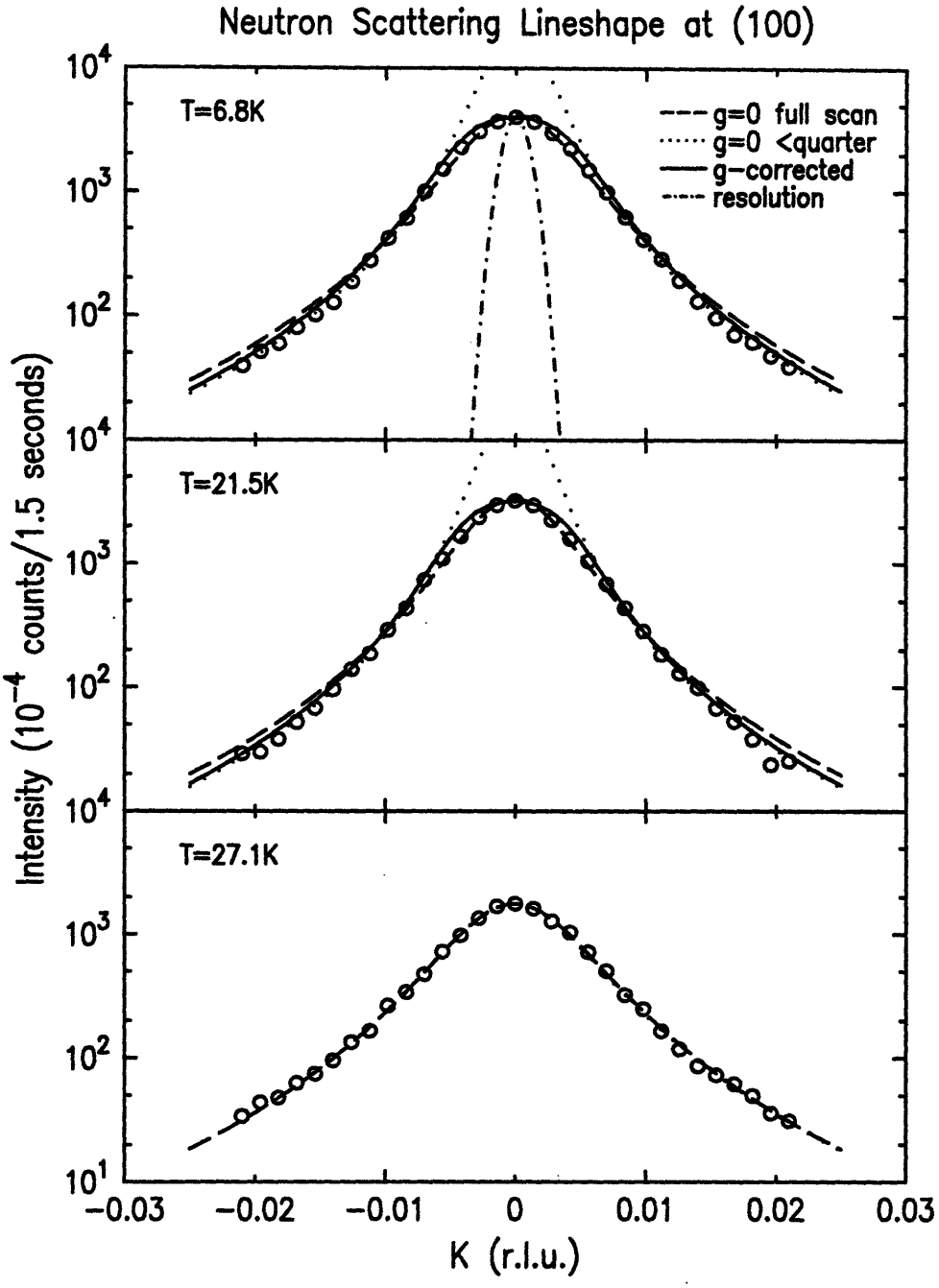

Figure 5-3: Typical neutron scattering transverse scans through the (100) Bragg peak during FC quenches to the temperatures T=6.8K (t=290s), T=21.5K (t=298s) and T=27.1K (t=605s) at H=5.5T. The solid lines show the extinction corrected fits at T=6.8K and T=21.5K as discussed in the text. The dashed-lines represent fits to all data points and dotted-lines are fits to points below one quarter of the peak intensity, both without extinction correction. At T=27.1K, good fits were obtained without correction for extinction, and the fit to points below one quarter of the peak intensity is essentially identical to the fit to the full scan.

instrumental resolution and g is an empirical extinction correction parameter. A is then held constant for all the scans of a given quench. Excellent fits were obtained at T=6.8K and T=21.5K by varying g and κ. Figure 5-3 also shows typical scans with the extinction corrected fits at the three temperatures (solid lines). The extinction corrected results for the inverse correlation length at H=5.5T are shown in figure 5-4. Again, κ is constant at T=6.8K but has pronounced time dependence at T=21.5K. Apparently the time dependences seen here are *not* artifacts of the fitting function used. g is constant over time at T=6.8K but decreases slightly with increasing time at T=21.5K. Note that equation 5.1 is adequate at T=27.1K, indicating the absence of extinction at this temperature due to thermal fluctuations near T_C (g=0, bottom panel, figure 5-3).

Although the extinction correction formula above provides a better fit to the data at the lower temperatures, it also changed the fitted value of κ drastically. For example, at 21.5K, the extinction corrected κ is less than one half of that obtained from the original fits. Therefore the absolute value of the κ obtained from equation 5.2 may be questionable. However, it serves to verify that the observed time dependences are a real effect independent of the method of fitting. It appears as a general feature that the correlation length at T=6.8K is smaller than that at T=21.5K, in qualitative agreement with the expectation that domains attain smaller size for quenches to lower temperatures because the energy barriers are less easily overcome through thermal activation. At T=27.1K, within 0.8K of T_C(5.5T), the correlation length is less than those at both T=6.8K and T=21.5K because the ordering of spins is broken up by thermal fluctuations.

Theory for the dynamics of a RFIM system quenched from high temperatures predicts that the typical domain radius expands logarithmically with time. In a model developed by Grinstein and Fernandez [26],

$$R(t) \approx \frac{2JT}{h^2} ln \frac{t}{\tau}, \tag{5.3}$$

where J is the exchange energy, T is the temperature and h is the root-mean-squared

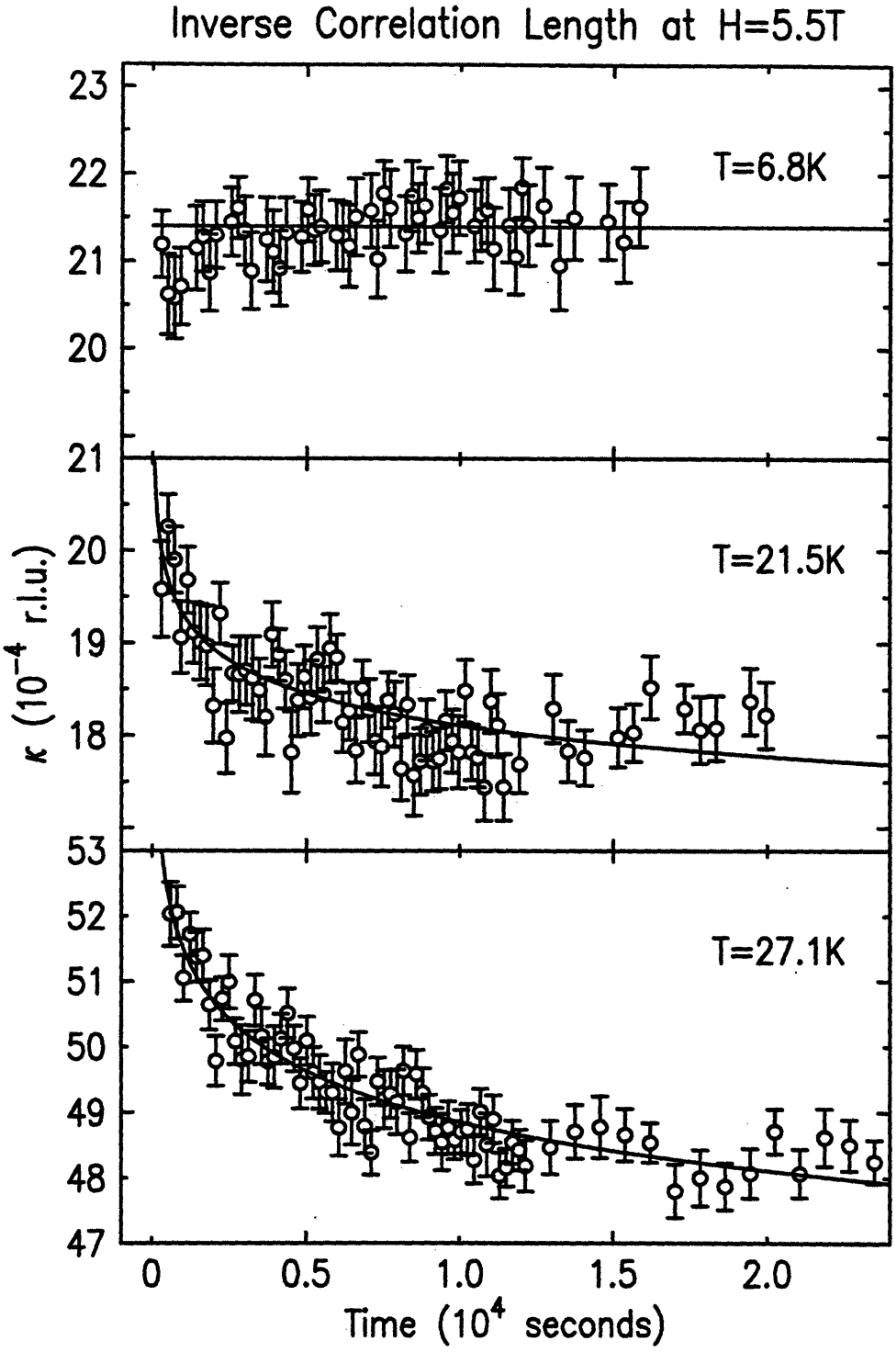

Figure 5-4: Time dependence of the inverse correlation length, κ. κ at T=6.8K and T=21.5K are obtained from extinction-corrected fits. The properties of the decay of κ remain similar to those in figure 5-2. The solid lines are best fits to equation 5.4 and show satisfactory agreement between the data and the logarithmic time dependence predicted by RFIM theory.

random field strength. τ is a characteristic microscopic attempt time[152, 28, 194]. For $Fe_{0.5}Zn_{0.5}F_2$, we estimate $\tau = \frac{\hbar}{E} = 7.7 \times 10^{-13}$s, where E is derived from the (111) zone boundary magnon energy of FeF_2[195, 196]. For a DAFF, the domain expansion may be modified to a certain power of a logarithmic function, depending on how the activation energy scales with the characteristic length scale of the system at time t and temperature T[28, 18]. With the assumption $\kappa(t) \sim R(t)^{-1}$, we fit κ vs. t to the following equation

$$\kappa(t) = c(ln\frac{t}{\tau})^{-\psi_\kappa} \tag{5.4}$$

with τ fixed at the value 7.7×10^{-13}s. c is a multiplicative constant for a quench to a specific temperature at the specific field. For the quenches at T=21.5K and T=27.1K, we obtain ψ_κ=1.0±0.2 and 0.74±0.3 respectively. For extinction corrected fits at 21.5K, we estimate $\psi_\kappa = 0.9 \pm 0.4$. They are all compatible with a pure logarithmic decay and are within the range of estimates given by Huse *et al.* [197] and Fisher[151], but differ from the value of 1.82 calculated by Lai *et al.* [18]. Equation 5.4 yields the solid lines shown in figure 5-4. At T=6.8K, the inverse correlation length does not change with time. This is in agreement with the freezing of the dynamics at low temperatures observed by others and is attributed to the non-zero Ising excitation energy gap[84].

5.3.2 Comprehensive Neutron Scattering Results

A more comprehensive study of the time dependence of FC domains was carried out on spectrometer H9 of the HFBR on a larger piece of $Fe_{0.5}Zn_{0.5}F_2$ crystal. This crystal was found to have a wider mosaic spread than the one used in the previous study at H7, as reflected in the slightly worse transverse resolution. In the analysis, it was found that the data could be adequately fitted by equation 5.1 without invoking the extinction correction formula 5.2. At lower fields where the transverse scan profiles are narrower, a second peak of much smaller intensity due to mosaic was observed, at a position -0.01 r.l.u. from the main K peak. All quenches are studied with

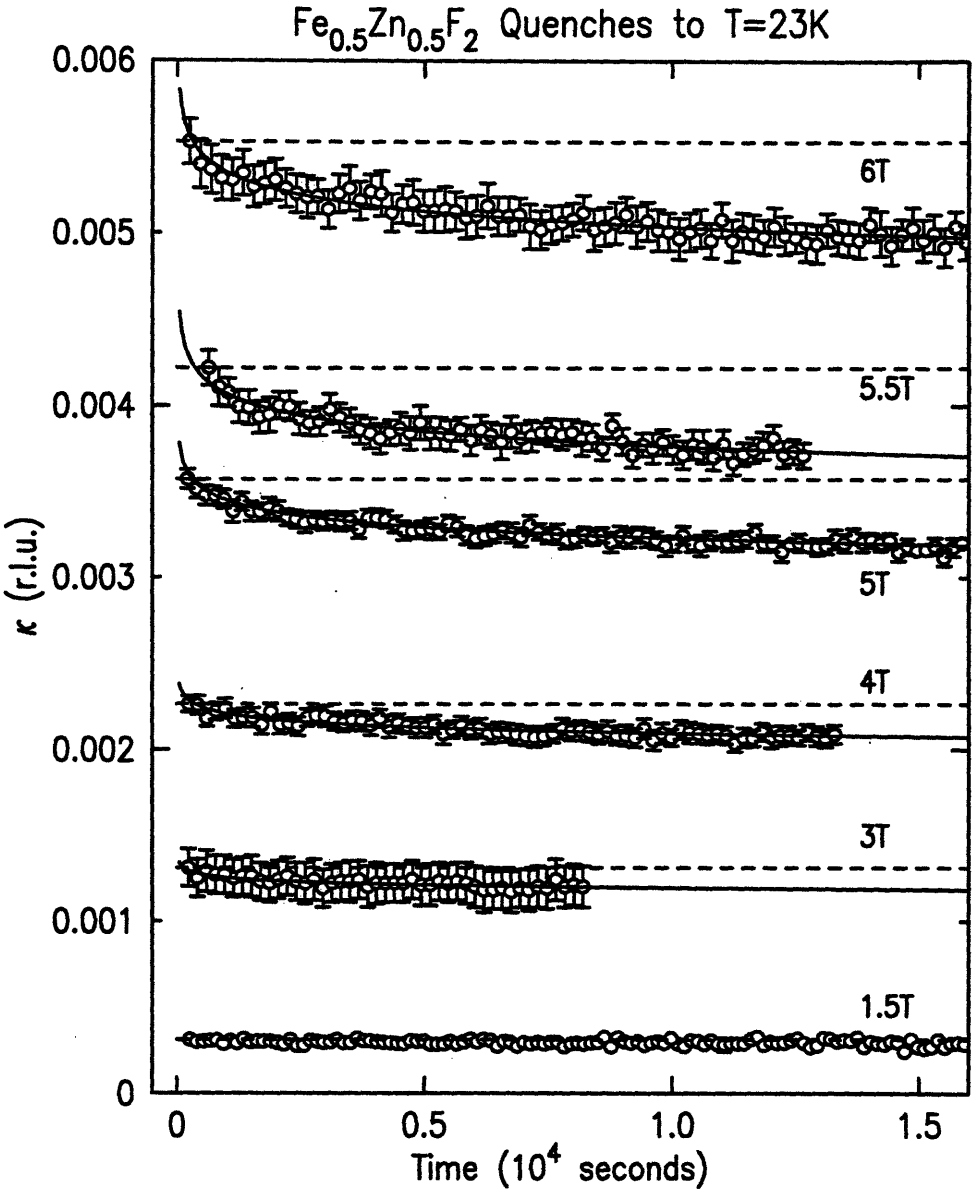

Figure 5-5: Time dependence of the inverse correlation length following FC quenches to 23K at a series of fields. The solid lines are fits to equation 5.4. The dashed lines indicate the value of κ for the first scan at each field, drawn as a reference to show the time dependence more clearly.

taking repeated K scans, except at H=1.5T where H scans were taken to alleviate the mosaic problem. The data points contaminated by this mosaic effect were excluded from the fits whenever necessary. Even though the absolute value of κ may not be completely reliable, the properties of the time and temperature dependences of the fitted parameters are precisely preserved and are consistent in the analysis.

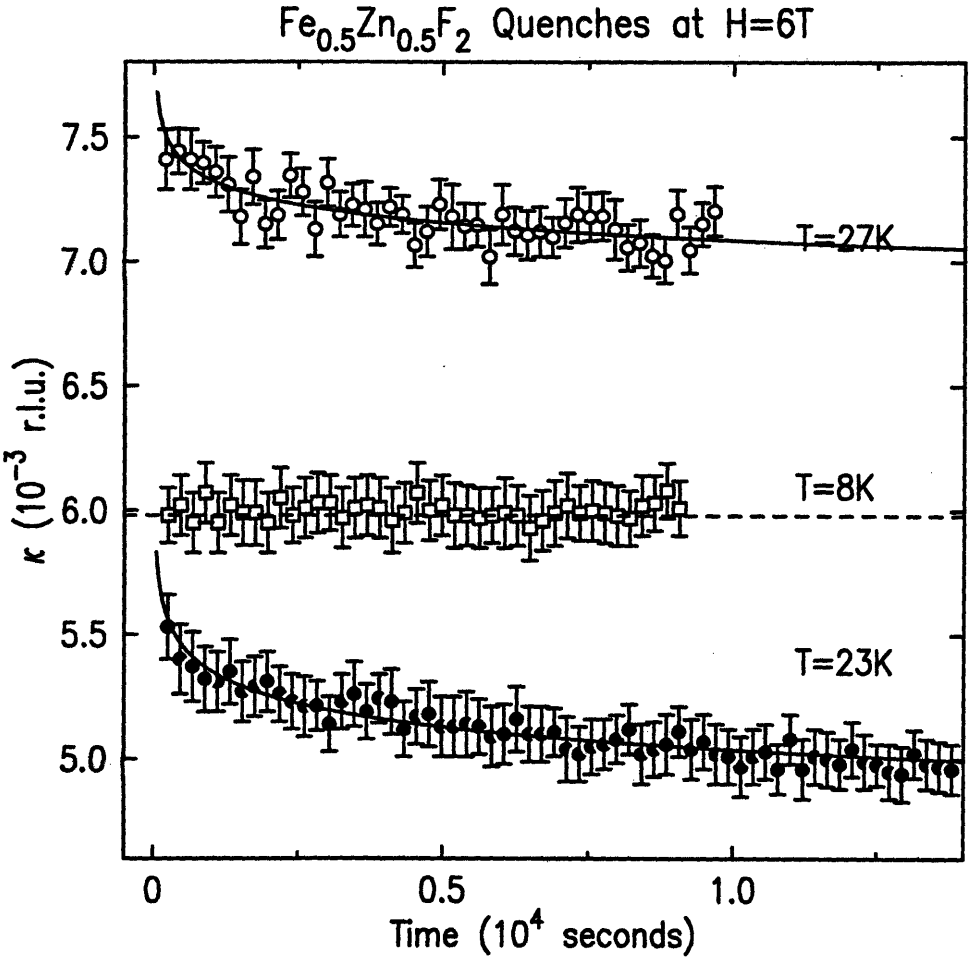

Figure 5-6: Time dependence of the inverse correlation length of FC quenches at H=6T. As seen previously at 5.5T, the decay is most prominent at T=23K, approximately 4.6K below T_C(6T). At 27K, within 0.6K of T_C, there is also observable decay of κ with a smaller change. At T=8K, κ remains unchanged. The solid lines are fits to equation 5.4.

Figure 5-5 summarizes the time dependence of the inverse correlation length κ following FC quenches to T=23K at a series of fields between 1.5T and 6T. It is obvious from this figure that the decay of κ is more pronounced at the higher fields, H=6T, 5.5T, 5T and 4T. AT H=3T, a decaying trend can still be seen but, as the figure

indicates, the magnitude of change is small and in fact the first and the last data point are within errors of each other. At H=1.5T, κ remains a constant over a period of five hours. The time dependence of κ is well described by the logarithmic decay, shown with solid lines in the figure. Least-square fits to equation 5.4 yield the following estimates for the exponent ψ_κ: ψ_κ(6T,23K) =0.95±0.1, ψ_κ(5.5T,23K) =1.2±0.2, ψ_κ(5T,23K) =1.03±0.1, ψ_κ(4T,23K) =0.82±0.15, and ψ_κ(3T,23K) =0.75±0.3. In figure 5-6, we present κ vs. t for three temperature quenches at H=6T, the highest field studied. The behavior of κ at these three temperature is closely similar to that observed earlier at 5.5T. The decay is most prominent at T=23K, approximately 4.6K below T_C(6T). At T=27K, within 0.6K of T_C, the amount of κ decay is smaller and we estimate ψ_κ(6T,27K) =0.52±0.15. At T=8K, κ remains unchanged over time. Therefore, it appears that for fields above H=3T and temperatures away from the transition region but not so low as to inhibit most thermal fluctuations, the value of ψ_κ is consistently in the vicinity of 1, reflecting a purely logarithmic time dependence of domain sizes and in good agreement with the prediction by Villain [152] and Grinstein and Fernandez [26].

Since lowering the field through the AF-PM boundary (FD) produces a domain state that is similar to the one arrived at through field cooling, one would expect to observe similar expansion on these domains over time. As demonstrated in figure 5-7, this is indeed the case. The figure compares time dependences of a field quench from 6T to 4.5T at 28.5K to a temperature quench from 40K (above T_C(4.5T)) to 28.5K at 4.5T. The results from the two quenches are largely similar, with the field quenched κ slightly higher than the thermally quenched ones.

Another interesting feature of the quench data is that there is significant difference between the domain configurations arrived at through a fast quench and a slow field cooling protocol. As shown in the upper panel of figure 5-8, fast quenches generally produce a greater κ, or smaller domains, then slow field cooling. The field dependences of both the quench κ and slow FC κ are compatible with H^2 scaling, shown by the solid lines. The dashed lines are least-square fits to a power law, yielding $H^{2.36\pm0.1}$ for slow FC κ and $H^{2.03\pm0.02}$ for fast quench κ. In the lower panel, the quench κ is shown

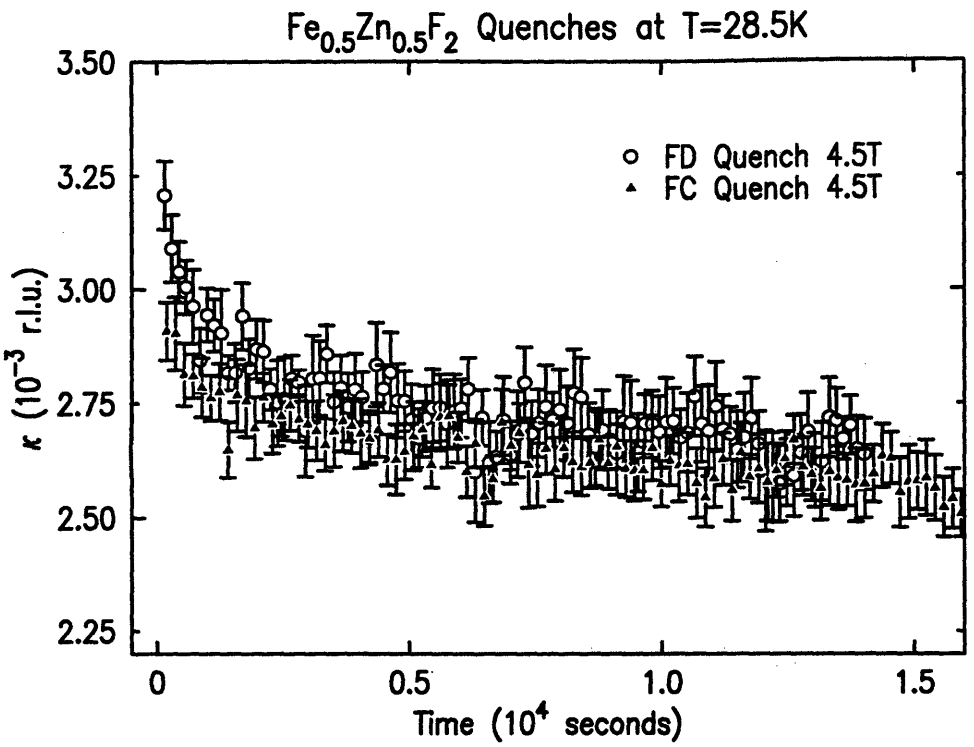

Figure 5-7: Comparison of the inverse correlation length between field quench and temperature quench at T=28.5T. Open circles: field quench from 6T to 4.5T at 28.5K. Closed triangles: field cooling quenches from above T_C to 28.5K at 4.5T.

to exceed the FC κ for three temperatures at 6T that cover a wide temperature range. The difference increases for lower target temperatures. The figure also compares field quenched κ to temperature quenched κ from the first scans at H=4.5T. Note that though the former appears higher, it was taken at 150s while the latter was taken at 190s. The fast decrease of κ in the early seconds of the quench has augmented the difference between the two measurements.

5.4 SQUID Magnetometry Results

Dynamics of 2d and 3d DAFF systems have previously been studied utilizing ac susceptibility[198], optical Faraday rotation [82] and SQUID magnetometry [84, 189]. For 2d RFIM, a logarithmic decay of uniform magnetization was clearly observed by Schins *et al.* [198]. For 3d RFIM, Lederman *et al.* [84, 189] mapped out the dynamic behavior of $Fe_{0.46}Zn_{0.54}F_2$ in the $H-T$ plane and related the decay of the uniform

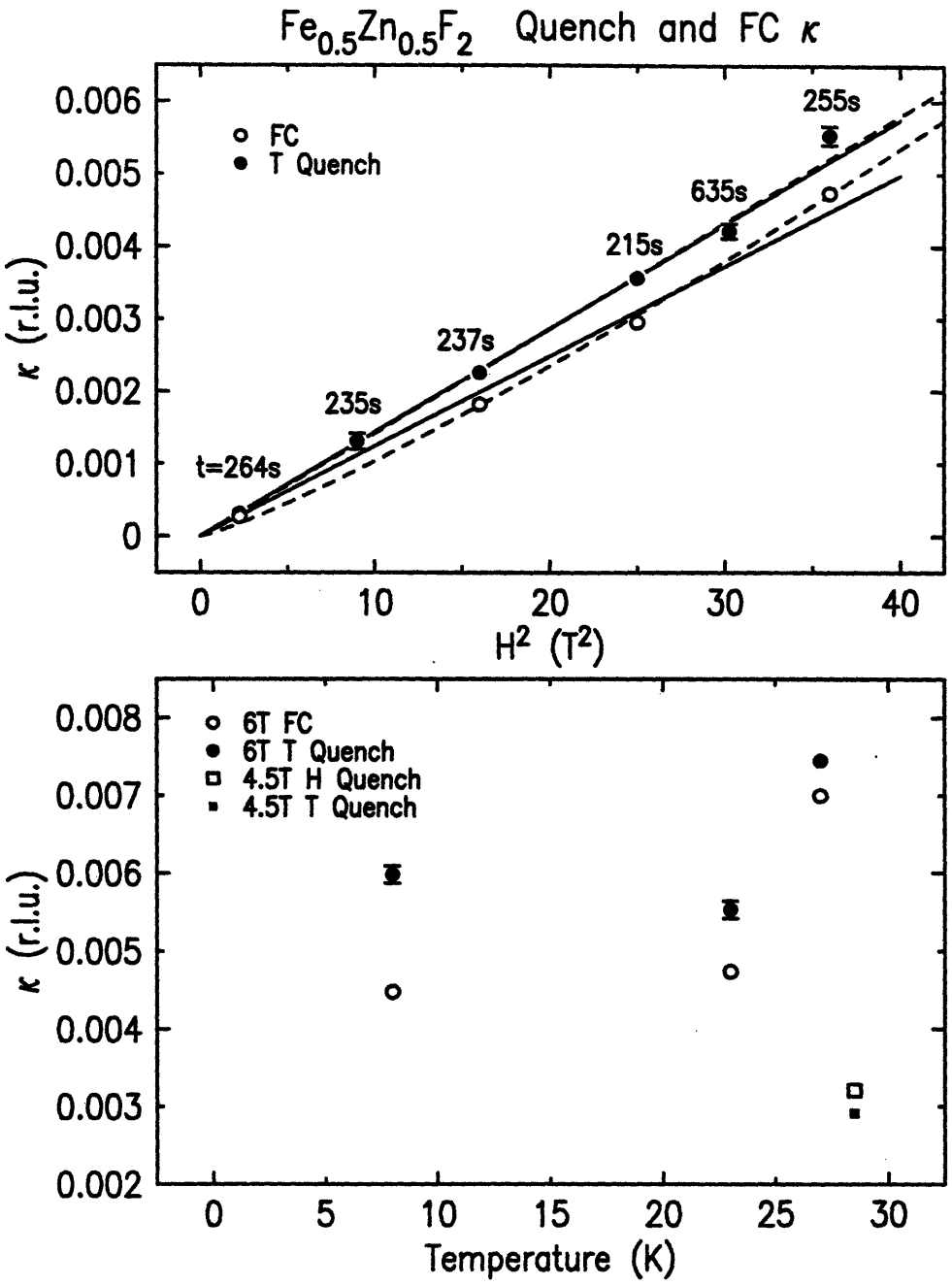

Figure 5-8: Upper panel: comparison of κ obtained from quenching (closed circles) and slow field cooling (open circles). κ is plotted again H^2. Fast quenches generally produce a greater κ, or smaller domains, then slow field cooling. The value of the quench κ is from the first scan taken at each field, with the time of the scan indicated next to each data point. The field dependences of both the quench κ and slow FC κ are compatible with H^2 scaling, shown by the solid lines. The dashed lines are least-square fits to a power law, yielding $H^{2.37\pm0.1}$ for slow FC κ and $H^{2.03\pm0.02}$ for fast quench κ. Lower panel: comparison of quench κ (closed circles) to slow FC κ (open circles) for three temperatures at 6T, and field quench κ (open square) temperature quench κ (closed square) at 4.5T.

magnetization directly to the expansion of domains in the FC state. To complement the neutron work discussed above, we have carried out a similar series of SQUID measurements to study the metastable behavior in $Fe_{0.5}Zn_{0.5}F_2$.

Temperature and field cycles of ZFC followed by FC and FH were performed at several fields between H=0T and H=5.5T to measure the uniform magnetization, M. The hysteresis, reflected in sharp peaks in $\frac{dM}{dT}$ following ZFC procedures but rounded and subdued peaks following FC or FH protocols, has been discussed in Chapter 4. This is in qualitative agreement with other studies on strongly anisotropic DAFFs[82, 84, 83]. The sharp feature in $(\frac{dM}{dT})_{ZFC}$ is now believed to arise from a term that scales like $\frac{dM_s{}^2}{dT}$ [70]. During a ZFC run, the sample has achieved LRO so that the staggered magnetization M_s is non-zero and in a field a volume magnetization M_{ZFC} is also present. In the FC state, one expects an additional contribution to M from the domain walls. Following Lederman *et al.*[84], we subtract M_{ZFC} from the FC magnetization, M_{FC}, at the corresponding temperature and thus obtain the excess magnetization $M_{ex} = M_{FC} - M_{ZFC}$ which is believed to arise primarily from the domain walls. It is M_{ex} that provides information about the size and possibly the fractal properties of the magnetic domains. Quenches were taken at a series of fields and temperatures and M_{ex} was recorded over a period of several hours. Figure 5-9 shows M_{ex} vs. t obtained from quenches to T=22K at H=1.5T, 2.5T, 3.45T, 4T, 5T and 5.5T. The decay of M_{ex} is much more significant at the higher fields. Figure 5-10 shows time dependence of M_{ex} at several temperatures at 5.5T. In all cases, except for quenches to low temperatures ($T \leq 15K$), a significant decrease in M_{ex} is observed. At low temperatures, M_{ex} remains unchanged for at least six hours to within experimental error for all the fields studied, in agreement with the frozen-spin picture.

In some previous reports on measurements of excess magnetization, the formula $M_{ex}(t) \sim (ln\frac{t}{\tau})^{-1}$ has been applied to fit the data[82]. This approach assumes that $M_{ex}(t) \sim R(t)^{-1}$ and $R(t)$ is given by equation 5.3, which is plausible if the domains are compact. However, these fits required unphysical values of τ. Numerous simulation studies [153, 192, 199] have shown that the compact domain assumption is in fact

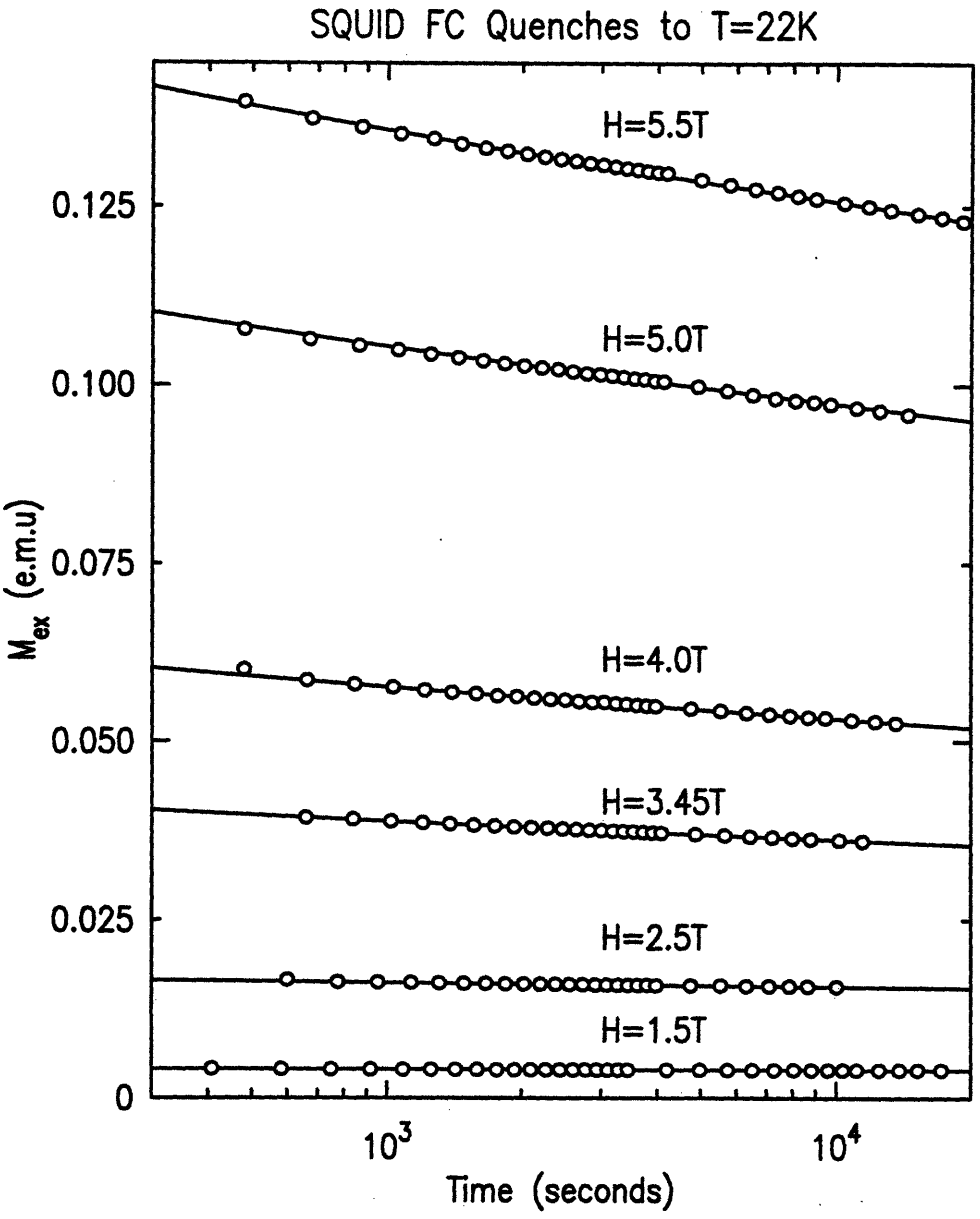

Figure 5-9: Time dependence of quenched excess magnetization, M_{ex}, as measured by a SQUID magnetometer for T=22K, at various fields. The solid lines are fits to equation 5.6 as discussed in the text. For H=1.5T and H=2.5T, the change in M_{ex} occurs within the first few points and the overall change is small compared to that at higher fields.

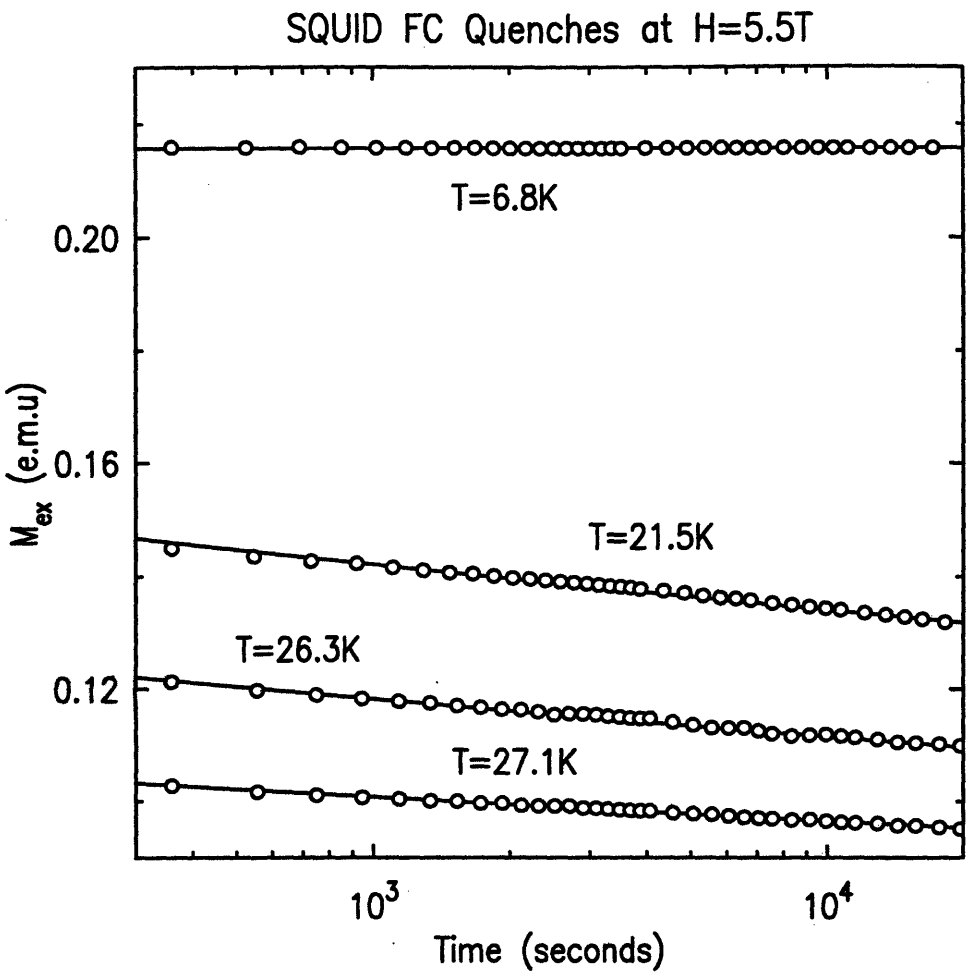

Figure 5-10: Time dependence of the quenched excess magnetization, M_{ex}, as measured by the SQUID at various temperatures at H=5.5T. The solid lines are fits to equation 5.6. M_{ex} is constant over time at T=6.8K due to the finite Ising excitation gap at low temperatures. T_C(5.5T)=27.9K.

unrealistic and domains in a strongly anisotropic DAFF form extremely complicated structures on all length scales. We find that only the M_{ex} decay at H=3.45T agrees with this formula satisfactorily. For the other fields, $M_{ex}(t)$ does not follow a simple inverse logarithmic form.

Nattermann and Vilfan predicted that the time dependence of the magnetization arising from domain surfaces is given by [28]

$$M_s(t) \sim R^{-1}(\frac{T}{J} ln \frac{t}{\tau})^{-\psi_{NV}}. \tag{5.5}$$

The domain radius $R \sim H^{\nu_M}$ and ν_M=2 according to NV. The exponent ψ_{NV} is related to the fractal dimension of the FC domains.

Following equation 5.5, we fit our SQUID quench data to the form,

$$M_{ex} = c(ln\frac{t}{\tau})^{-\psi}. \tag{5.6}$$

By varying the amplitude c and the exponent ψ, with τ held fixed at 7.7×10^{-13}s, excellent fits were obtained and are shown as the solid lines in figure 5-9 and figure 5-10. We find that for a fixed temperature, ψ is field dependent. At T=22K, ψ(1.5T)=0.42±0.14, ψ(2.5T)=0.58±0.06, ψ(3.45T) =1.10±0.03, ψ(4T)=1.26±0.05, ψ(5T)=1.24±0.08 and ψ(5.5T) =1.20±0.05. Note that although ψ is much smaller than 1 at lower fields ($H \leq$2.5T), its value does not vary much for fields above 3.45T, and is again in the vicinity of 1, as the neutron results indicated.

There is also indication that the value of ψ is dependent upon the target temperatures for quenches at a given field. For instance, at H=3.45T for which T_C=32.0K, ψ(22K)=1.10±0.03 and ψ(30K)=0.88±0.11. At H=5.5T from a later experiment on the same sample, ψ(21.5K) =0.91±0.09, ψ(26.3K) =0.91±0.09, while ψ(27.1K) =0.68±0.04. These results indicate that ψ becomes smaller for quenches to temperatures that are closer to T_C. In other words, near the transition temperature, the relative decrease in M_{ex} occurs at a slower rate. This point was also noted in the neutron scattering study discussed above. In all likelihood this is related to the anomalously slow relaxation in the critical region [84] arising from the activated dynamics [151, 187]. Further, the relative decay rate of M_{ex}, and therefore the value of ψ, seems to depend slightly on the rate of cooling during a quench. The smaller value of ψ(21.5K) in the second run (compared to $\psi(22K)$ above) is due to such effect. The value of ψ has been measured previously in other experiments and its field and temperature dependence is consistent with results in the current work [81].

From the SQUID quench data, we can also extract the scaling of the excess magnetization with the strength of the applied field, $M_{ex}(T = 22K) \sim H^{\nu_M}$. Data for the above six fields are summarized in figure 5-11 and a simple power law fit yields

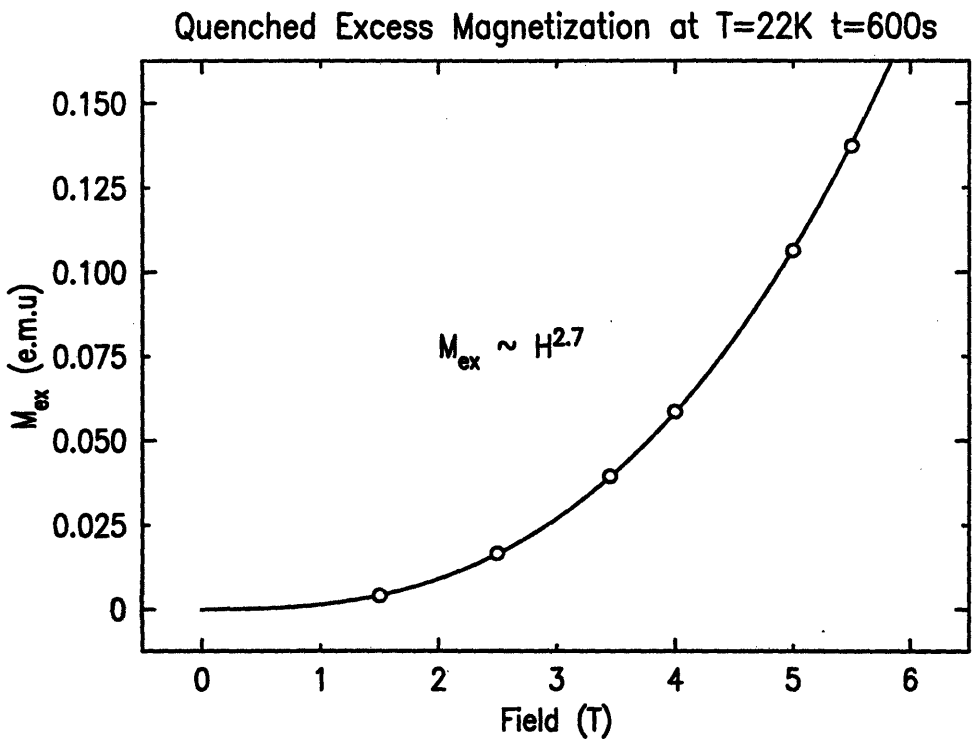

Figure 5-11: The variation of quenched excess magnetization, M_{ex}, with respect to applied field, H, at T=22K, t=600s. This scaling differs from that of the FC inverse correlation length with field, as measured by neutron scattering, suggesting that the domains are fractal in nature.

$\nu_M = 2.70 \pm 0.06$ at t=600s, $\nu_M = 2.69 \pm 0.04$ at t=3000s and $\nu_M = 2.65 \pm 0.06$ at t=10000s. Therefore we estimate $M_{ex} \sim H^{2.7\pm0.1}$ at all times. We discuss the significance of this power law behavior in the next section.

Short quenches to various target temperatures were performed at H=5.5T. The magnetization measured at t=893s is shown in figure 5-12. Clearly, quenches to lower temperatures produce larger excess magnetization. Such temperature dependences agree qualitatively with the NV theory, but the predicted variation $M_{ex} \sim T^{-\psi_{NV}}$ [28] is not seen. This is not surprising in view of the fact that ψ is itself temperature dependent. The temperature dependence of ψ complicates the measurements because in practice quenching to a certain temperature cannot be instantaneous. Cooling through intermediate temperatures and the corresponding finite time interval both allow certain relaxation of the domains before the system reaches the target temperature. Thus one would expect that the observed quenched M_{ex} would deviate

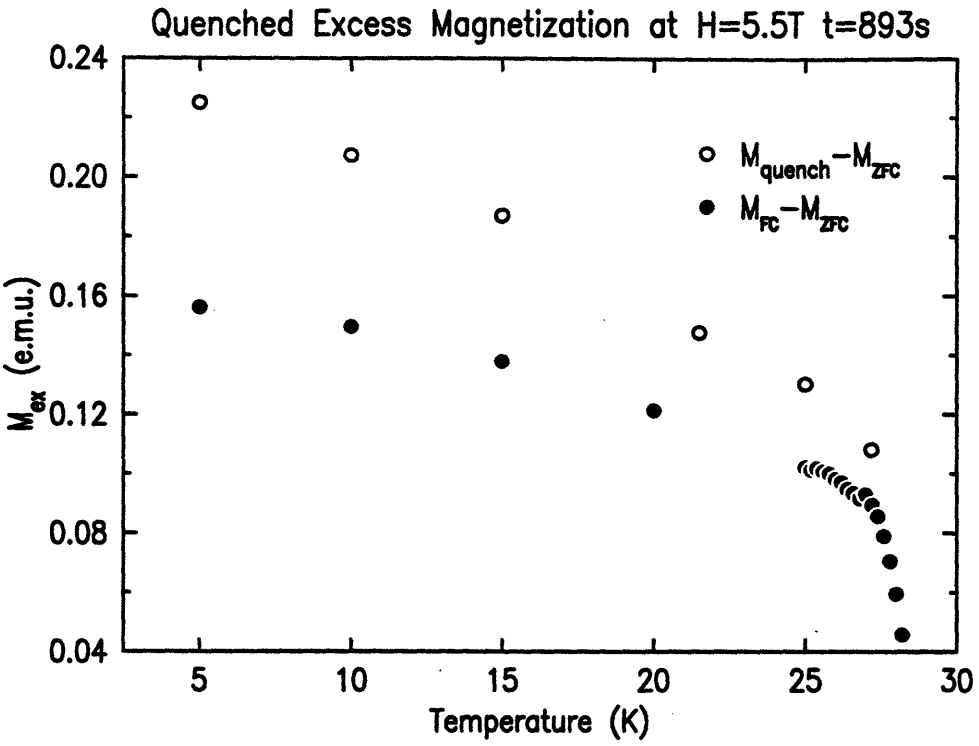

Figure 5-12: The open circles show the excess magnetization, M_{ex}, as measured by SQUID following quenches to various temperatures below the transition at H=5.5T, t=893s. Quenches to lower temperatures produce larger M_{ex}. The results agree qualitatively with DAFF theory. The closed circles are excess magnetization measured in a gradual FC procedure. The difference between the quenched M_{ex} and the slow FC M_{ex} indicates the differing underlying domain structures formed during the two processes.

increasingly from an ideal $T^{-\psi_{NV}}$ form at lower temperatures. This is obvious in figure 5-12. Instead of the $T^{-\psi_{NV}}$ form, which diverges as T tends to zero, M_{ex} approaches a finite value at low temperatures. Compared to the quenched M_{ex}, the FC M_{ex} is substantially smaller in value and shows less dependence on temperature below T_C. The FC measurements are taken at a series of temperatures as the system is gradually cooled. his procedure clearly differs from a rapid quench and hence results in different domain formations. The neutron results have demonstrated that the FC scan profiles are indeed different from those of the quenched ones. Simulation studies have shown that there is no correspondence between the domains created during a quench and those formed during FC to the same temperature at the same field[153]. The gap between the quenched and the FC M_{ex} increases with decreasing temperature, as

shown in figure 5-12. This is consistent with the increase of the difference between the quenched κ and the FC κ for lower temperatures measured by neutron scattering.

5.5 Discussion

In a quenched DAFF system, the metastable domains expand through repositioning of the domain walls. Small, unfavorable domains are eliminated as the larger ones grow. From the parameters τ, J, T and an assumed fractal dimensionality D, we can estimate the length scale L on which energy barriers $\Delta E \sim JL^D$ are overcome at a certain time t. At the time scale of our experiments on $Fe_{0.5}Zn_{0.5}F_2$, $L \sim a(\frac{T}{J} ln \frac{t}{\tau})^{\frac{1}{D}} \sim$ 25Å at T=22K, where $a = 4.7$Å is the lattice constant in the plane perpendicular to the easy axis in $Fe_{0.5}Zn_{0.5}F_2$ and D=2.5 is assumed[199].

A striking result from these studies is the drastically different time dependent behavior observed at low and high applied fields. For a low external field, for example, $H \leq 1.5$T, random bonds appear to play an important role in controlling the domain formation [28]. Domains attain a relatively large size ($R \sim$ 1600Å at H=1.5T) and a great part of the domain walls coincides with the boundary between magnetic and nonmagnetic ions, and is therefore pinned by RBs. Apparently the length scales on which domain surface adjustments occur are much smaller than the domain sizes. Hence a significant increase in the average domain size over time is not expected and the low field situation falls into the regime of the NV theory which assumes a constant domain radius R and attributes any increase in the uniform magnetization to local readjustments in the domain surfaces. This implies that ψ measured at low fields by the SQUID experiment should be close to $\psi_{NV} \approx 0.4$ for 3d systems, and is evinced by our result at H=1.5T.

The smaller values of ψ for $H \leq$2.5T reflect the smaller decrease of M_{ex}, and κ, during quenches at these fields. This result agrees with the observation of Lederman *et al.* [84, 189] who suggested that below a threshold field, the evolution of a DAFF system is controlled by random exchange dynamics, because the random field pinning force is weak and the system relaxes significantly before a measurement can be made

on a typical experimental time scale.

The results at higher fields differ notably from those at lower fields. From the SQUID data, we estimate ψ=1.1±0.3 for fields greater than H=3.45T and temperatures above the region of frozen Ising dynamics. The neutron data yield exactly the same estimate for ψ_κ. In this range of higher fields, the pinning force on the domain walls is derived from both RFs and RBs. Random field dynamics now play a significant role in the evolution of domains. This is evidenced by scattering experiments which show a significant increase in domain radii when the external field is lowered (though the system remains in a SRO state). The length scales, L, on which the domain walls shift are no longer negligible compared to the domain sizes according to our neutron scattering results. The average size of the domains increases notably over time. For example, the change in correlation length $\Delta\xi$ at T=21.5K and H=5.5T is roughly 40Å (for extinction corrected fits, or 20Å if correction is not applied) during the five-hour time span of the neutron scattering measurements. This may be compared with $L \sim 25$Å estimated above. It is interesting to note that $\Delta\xi$ and L are of comparable magnitude.

This is the first study that demonstrates that domain relaxation is indeed at the origin of the previously observed time dependence of the quenched excess uniform magnetization M_{ex} in the presence of strong random fields. In figure 5-13, we compare the inverse correlation length κ obtained from neutron scattering data and the rescaled M_{ex} determined by SQUID measurements, taken at the same temperatures at H=5.5T. At T=6.8K, both techniques show that the magnetic domains are frozen. At T=21.5K and T=27.1K, κ and M_{ex} undergo a similar percentage of decay over the same period of time. The agreement is also reflected in the fact that ψ_κ obtained from neutron scattering and the ψ from the SQUID data are equal to within the combined errors. In this high field regime, our results are compatible with the assumption $M_{ex}(t) \sim \kappa(t)$ made by others[84]. Previously a different depiction of the FC metastability was proposed in which the time dependence seen in M_{ex} arises from both an overall domain growth and local adjustments in domain walls [134]. Assuming neutron scattering is sensitive to the former effect but not the latter, one would

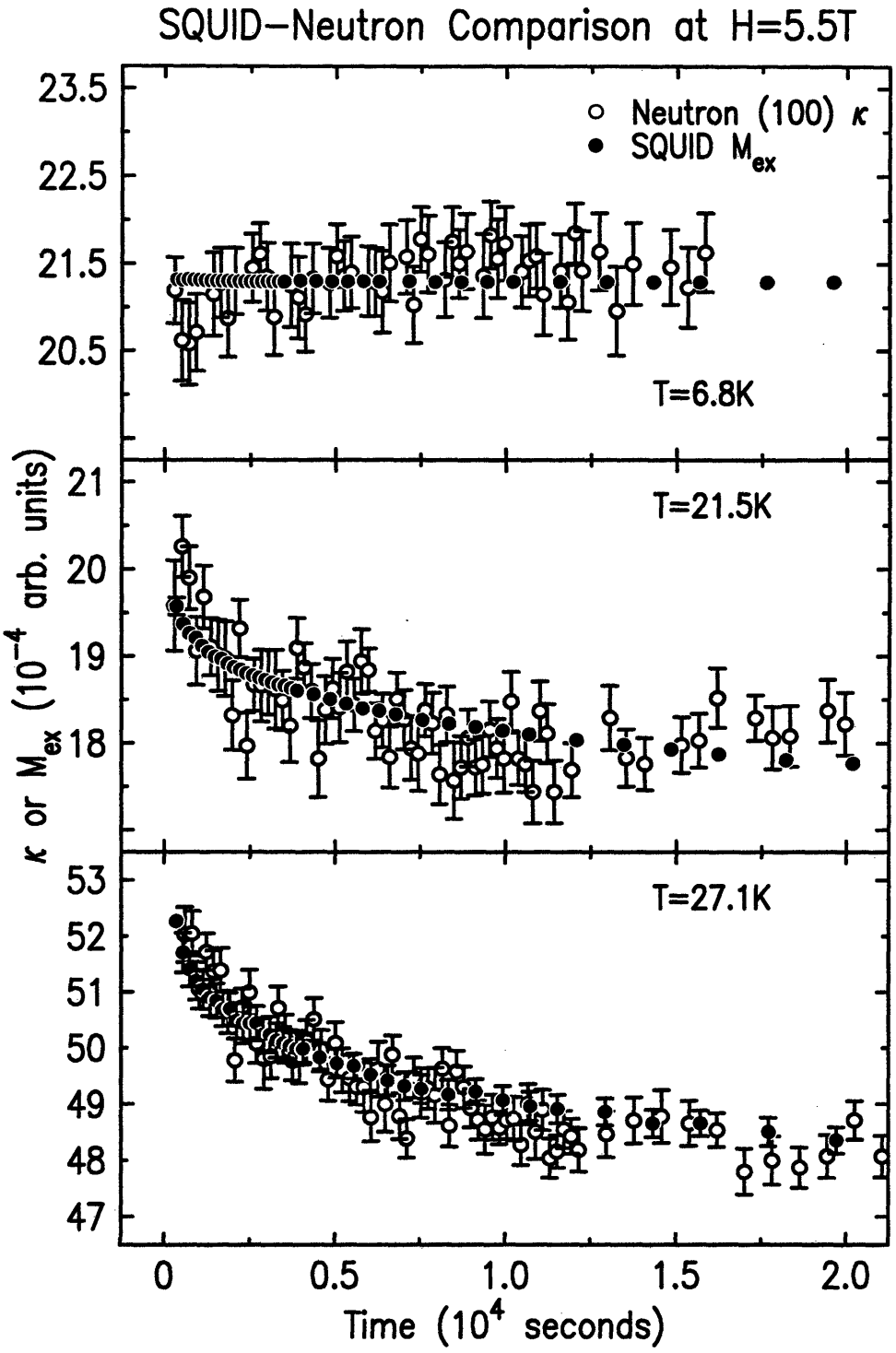

Figure 5-13: Comparison of the time dependence of κ and M_{ex} for three temperatures H=5.5T. The M_{ex} values have been rescaled according to the neutron scattering κ, for which we have used the extinction corrected ones. However, as apparent from the discussion, equally good agreement will remain if κ from fits without extinction correction were used. At higher temperatures, the decay of κ and M_{ex} measured by the two techniques also agree, suggesting that the fractal properties of the domains do not change noticeably while the average size of the domains grow with time.

then expect $\psi = \psi_\kappa + \psi_{NV} \approx \psi_\kappa + 0.4$. In light of the more comprehensive neutron data discussed in the current work, this scenario can be ruled out because of the good agreement between ψ and ψ_κ. This scenario is also likely to be invalid because in deriving equation 5.5, NV assume a well defined domain of time-independent radius R that is compact on large length scales. In fact, simulations have suggested that domain walls are fractal for DAFFs in strong dilution and applied fields [192]. Therefore, the agreement between the time dependence of $\kappa(T)$ and $M_{ex}(T)$ suggests that the neutron scattering and the SQUID magnetometry techniques observe the same time dependent effects in $Fe_{0.5}Zn_{0.5}F_2$. The higher value of ψ at fields $H \geq$3.45T is clearly a random field effect and should therefore be distinguished from the behavior at $H \leq$1.5T. The magnetometry results at H=2.5T lie between these two regimes.

We next turn to a discussion of the field dependence of the excess magnetization. Instead of $M_{ex} \sim H^2$ as predicted by theory[28], we find $M \sim H^{\nu_M}$ with the exponent $\nu_M = 2.7 \pm 0.1$, which is somewhat smaller than the 3.2±0.3 reported by Lederman *et al.* [189]. Because the FC domains are fractal, ν_M need not be the same as the exponent ν_H which describes the scaling of κ with the magnetic field. Our neutron results above yielded ν_H=2.36±0.1 for FC and ν_H=2.03±0.02 for quenches, in good agreement with $\nu_H = 2.2 \pm 0.1$ obtained by Cowley *et al.* [185]. The fact that ν_M is larger than ν_H may be understood by considering the disordered nature of the domain walls. As the external field increases, the local random field increases proportionally and the RF pinning force is stronger, hence the domain interface is generally rougher and more entangled, adding an extra surface magnetization contribution to the simple increase of M_{ex} due to the smaller domain size in higher fields.

Numerical studies of the kinetics of 3d RFIM domain growth show that the early-time expansion follows the Lifshitz-Cahn-Allen law $R(t) \sim t^{\frac{1}{2}}$ which subsequently evolves into an asymptotic logarithmic behavior only after a field-dependent crossover time[18, 200]. This crossover is not seen in either the neutron or the SQUID measurements, presumably because it happens much before the first quench datum point is taken in either case.

This work and others [189] have shown that the metastable state of a FC DAFF

is dependent not only upon the paths in the phase diagram that lead to this state but also the time scales on which it is probed. The evolution of the domains contributes to the hysteresis seen in the various measurements on all metastable RFIM systems. One example of this type of contribution is that the FH domains are generally larger than the FC ones, as evidenced in neutron [67, 71] and x-ray scattering (see Chapter 5) studies. A related effect is that the FH $\frac{dM}{dT}$ peak is generally sharper than the FC peak at the same field (above a certain threshold field in $Fe_xZn_{1-x}F_2$) in bulk measurements [82, 189].

5.6 Results on a Weakly Anisotropic System

The theory by Nattermann and Vilfan predicted no observable time dependence for the metastable domains in weakly anisotropic diluted antiferromagnets placed in a field. The reason is that the domain walls in these systems can be as thick as tens of lattice constant, which is comparable to if not greater than the length scales on which sections of domain surface can move on experimentally accessible observation time. These movements therefore do not contribute to noticeable changes in the typical domain size [28].

The diluted Ising antiferromagnets $Mn_xZn_{1-x}F_2$ have a dipolar anisotropy that is less than 1% of its exchange and are therefore prototypical systems with weak anisotropy and broad domain walls. In order to test the prediction by NV regarding its domain morphology, and also make comparison with $Fe_{0.5}Zn_{0.5}F_2$, we present SQUID magnetometry results from thermal quenches in applied fields taken with a sample of $Mn_{0.45}Zn_{0.55}F_2$. In figure 5-14, we show time dependence of excess magnetization, M_{ex}, measured over a period of nine hours at three temperatures at H=2T. T_C(2T)=15.7K for $Mn_{0.45}Zn_{0.55}F_2$. There is a noticeable step in the data at $t \approx$4000s at all temperatures. This is an artifact caused by a system error in the SQUID that occurred when the frequency of the measurement changed from 70 seconds per data point to 380 seconds per data point. It should therefore be ignored in interpreting the results. At T=5K (open circles), there is no change in M_{ex}. Since $Mn_xZn_{1-x}F_2$ has

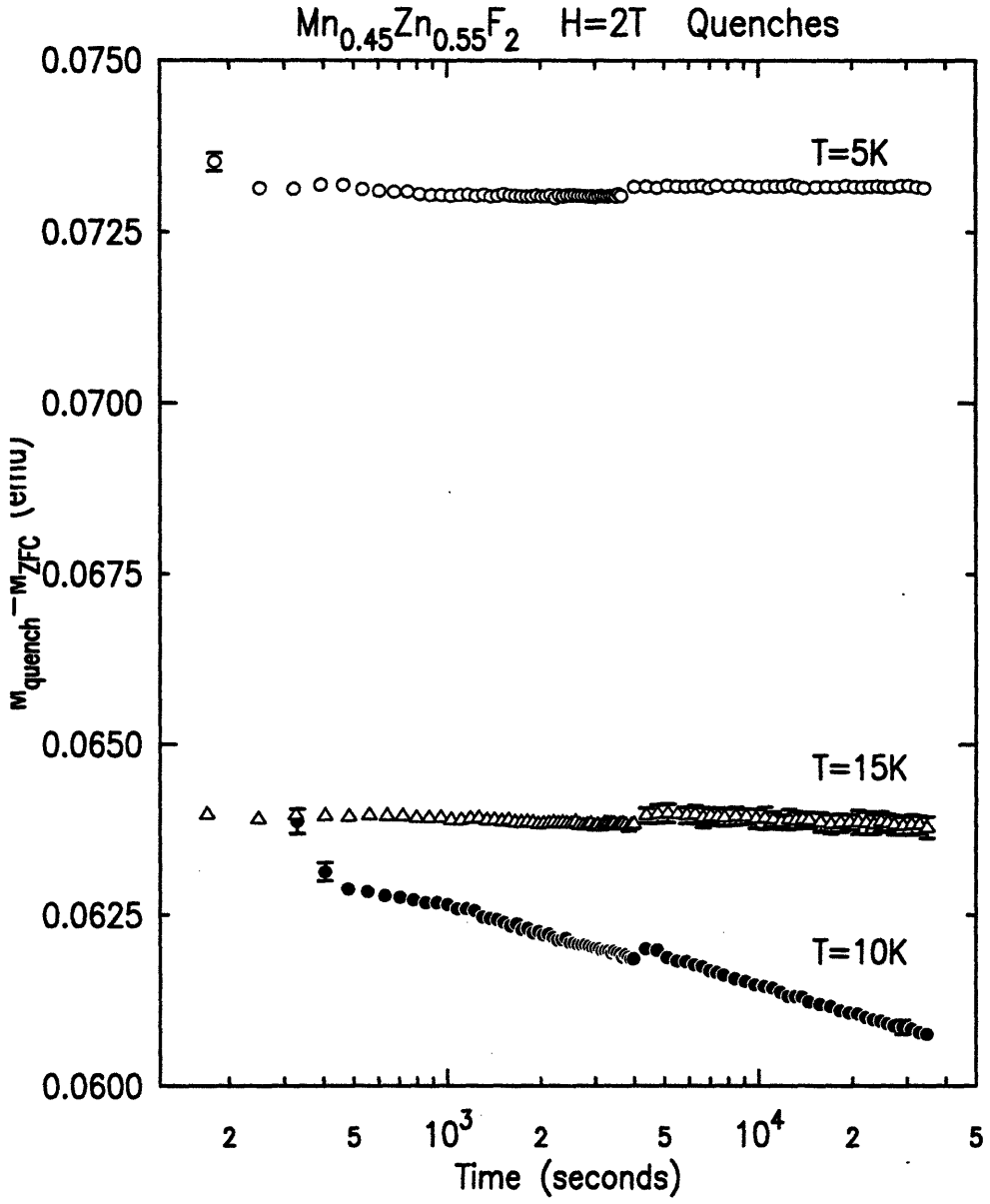

Figure 5-14: Time dependence of M_{ex} at H=2T in $Mn_{0.45}Zn_{0.55}F_2$ measured by SQUID. The data are taken at T=5K (open circles), 10K (closed circles) and 15K (open triangles). T_C(2T)=15.7K. Over a period of nine hours, M_{ex} is constant at 5K but decreases by approximately 4% at 10K and less than 1% at 15K.

a much smaller Ising excitation energy compared to $Fe_xZn_{1-x}F_2$, the freezing of M_{ex} at 5K is probably due to a lack of thermal fluctuations as well as the NV mechanism described above. At T=10K (closed circles), M_{ex} decreases by approximately 4% over the time scope probed and clearly agrees with an inverse logarithm. At T=15K (open triangles), M_{ex} also displays a decay over time but to a much smaller degree (less than 1%). This temperature is 0.7K below T_C(2T) and we expect that random field critical slowing down and broad domain walls both affect the extent to which we can discern changes in the domain radii. In general, the time dependent behavior is very similar to that observed in $Fe_{0.5}Zn_{0.5}F_2$ at higher applied fields, except that the changes measured here are much smaller in magnitude. This can be explained by the NV mechanism that attributes small if not entirely negligible changes in domain sizes to broad domain walls in weakly anisotropic DAFFs.

Studies on the time dependence of FC domains in $Mn_xZn_{1-x}F_2$ have previously been reported by Birgeneau *et al.* and Cowley *et al.* using the neutron scattering technique [104, 71]. The time span probed in these experiments is comparable to the current SQUID work. There appeared to be little indication of domain relaxation. For example, for an x=0.75 sample in a field of 7T and quenched from 0.4K above T_M to 0.4K below, the ratio of the domain sizes at 5.4×10^4 and at 600s was 1.01 ± 0.03. For an x=0.5 sample quenched from 17.4K to 16.2K at 2T, the ratio of the domain sizes for 3.6×10^4 and 480s is 1.03 ± 0.04. And a field quench from the spin-flop phase into the antiferromagnetic domain phase yielded 1.01 ± 0.06 for the ratio of domain sizes at 3.2×10^4 and 600s. These authors therefore concluded there was no significant relaxation of the FC state and ruled out a logarithmic increase in the domain size. Although none of the above ratios is significantly greater than 1, they are all slightly above 1. Clearly, a change of 3% in the domain sizes would be obscured by the error bars (due to counting statistics and fitting errors) in the neutron measurements. On the other hand, SQUID magnetometry, though an indirect technique for studying domains, provides extremely high precision in measuring M. As figure 5-14 shows, a 4% decay in M_{ex} is easily captured in the SQUID data. Therefore, we conclude that the results presented here do not disagree with the earlier neutron results by

Cowley *et al.* Instead, they represent an improvement in the data quality and afford us a better understanding of the FC metastability. In the FC state of a weakly anisotropic DAFF, the domains expand over time. But because of the slow dynamics and broad domain walls, the expansion occurs at a much slower rate compared to a DAFF with strong anisotropy and therefore narrow domain walls.

Chapter 6

Conclusions

Summary

In this thesis, I have presented an experimental study on the three dimensional random field Ising model via the diluted antiferromagnets $Fe_{0.5}Zn_{0.5}F_2$, $Mn_{0.45}Zn_{0.55}F_2$ and $Mn_{0.75}Zn_{0.25}F_2$. These experiments utilized the complementary techniques of magnetic neutron and x-ray scattering, uniform magnetization and direct heat capacity.

The work reported here addressed three important issues concerning the 3d RFIM. First and foremost, we have achieved a consistent phenomenological description for the zero field cooling transition and clearly distinguished it from the underlying equilibrium random field transition. In the superheated ZFC transition from the metastable long range ordered state to the paramagnetic state, the shedding of magnetic order is viewed as the reversal of progressively larger spin blocks the size of which reaches a finite maximum at a transition temperature denoted $T_C(H)$. The non-divergent pseudo-critical behavior is controlled by random field activated dynamics which originates from a complex distribution of free energy minima and causes anomalous critical slowing down. Upon heating or cooling through the transition, the system invariably falls out of equilibrium and effectively freezes into metastable states. This phenomenology gives excellent descriptions for the finite correlation lengths measured by neutron scattering, the rounded order parameter transition measured by magnetic

x-ray scattering and the apparent broadening in the peaks of the thermal derivatives of bulk thermodynamic quantities such as uniform magnetization and linear magnetic birefringence. It is also in complete agreement with the nonequilibrium random field theory. Further, a long awaited reconciliation has been accomplished between the indirect heat capacity measurements, which have previously been interpreted as illustrating logarithmically divergent equilibrium random field heat capacity, and the scattering experiments that demonstrated a non-divergent correlation length signifying a destroyed transition with "trompe l'oeil" critical behavior. A simple, physically motivated conjecture links the apparent peaks in the ZFC indirect heat capacity measurements to the temperature derivative of the order parameter squared which is non-zero in the superheated region. Thus the broadened indirect heat capacity peaks are entirely due to static fluctuations. This interpretation is strongly supported by our direct heat capacity measurements and attributes the hysteresis found in the indirect studies to the underlying hysteresis in the spin configurations. This hypothesis, if correct, will have bridged an important gap towards a consistent understanding of all the experimental results on the 3d RFIM. The random field-induced broadening scales with the applied field as H^2. As discussed in Chapter 3, this may reflect rather than contradict the predicted $h_{RF}^{2/\phi}$ scaling.

A second aspect of the random field Ising problem discussed in this thesis pertains to the equilibrium transition inferred from neutron data above the metastability temperature, $T_M(H)$, and the long range magnetic order formed during field cooling observed by magnetic x-ray scattering. The field cooled neutron measurements show power law dependences for the correlation length, the connected and disconnected susceptibility and suggest an equilibrium Néel temperature $T_N(H)$ that lies below $T_M(H)$. The exponents for these physical quantities were determined to be $\nu = 1.5 \pm 0.3$, $\gamma = 2.6 \pm 0.5$ and $\bar{\gamma} = 5.7 \pm 1.0$, in agreement with current theoretical predictions. Because the data were taken between $T_M(H)$ and $T_N(0)$ at intermediate field strengths, these estimates are the most reliable among experimental reports known to us. A long range order is found in the field cooled state in both $Fe_{0.5}Zn_{0.5}F_2$ and $Mn_{0.45}Zn_{0.55}F_2$ and is shown to coexist with short range order. This unusual be-

havior is therefore not unique to the one $Mn_{0.75}Zn_{0.25}F_2$ crystal on which field cooled long range order was first found. It is shown that the field cooled long range order intensity decreases at higher fields and becomes unobservable above a certain "threshold" field that is less than 3T. The FC LRO begins to grow at a temperature below $T_M(H)$, reminiscent of the T_N determined by neutron scattering at higher fields. The FC order parameter measured by the resolution-limited Bragg peak is not always well described by a simple power law with estimates for β ranging from 0.23 to 0.35. On subsequent field heating, long range order continues to coexist with short range order and its intensity is higher than the field cooled intensity at corresponding temperatures. The FH exponent β is found to be identical to the ZFC β. The origin of this long range order part is not unambiguously determined. A likely cause is the strains and defects in the near-surface region that result from sample preparation. However, the data do not rule out the possible existence of a small yet finite long range ordered backbone of spins at lower fields that is unobservable by neutron scattering.

Combining SQUID magnetometry and neutron scattering techniques for the first time, we have performed a comprehensive study of the time dependence of metastable magnetic domains formed upon temperature or field quenching. Essentially logarithmic expansion of average domain sizes was clearly observed for the strongly anisotropic system $Fe_{0.5}Zn_{0.5}F_2$ at all fields above 3T and temperatures above a spin-frozen temperature $\leq$15K. The good agreement between the decay of the excess uniform magnetization and the inverse correlation length confirms the validity of the previous reports on Faraday rotation and magnetometry measurements. The domain size is found to scale with the field as $\xi \sim H^{-\nu_H}$ where $\nu_H = 2.2 \pm 0.2$. The observed logarithmic domain relaxation is one of the most straightforward illustration of the anomalously slow dynamic effects due to random fields.

Future Directions

It is obvious that much more work is necessary in order to understand fully the random field Ising problem. Further theoretical work needs to converge on a consistent set

of equilibrium critical exponents and the issue regarding the order of the transition. It needs to emphasize linking theoretical predictions to experimentally observable quantities on accessible time scales. Experimentally, efforts should be devoted to understanding the equilibrium behavior of the RFIM. This could conceivably be carried out in the temperature regime above the metastability phase boundary. The most viable approaches may be direct neutron scattering and the promising technique of magnetic x-ray scattering. For neutron scattering, an exact expression for the cross section $I(q)$ and precise measurements covering a wide reciprocal lattice spectrum and temperature range are essential. High resolution neutron scattering, aided by successful treatment of extinction effects, will be useful for investigating the low field behavior. For magnetic x-ray scattering, the high energy and high intensity x-rays produced by the third generation synchrotron source may hold the key to solving the random field mystery. At energies up to 100keV, x-rays can penetrate deeper into the samples at larger momentum transfer, with the cross section loss compensated by the thousand-fold plus increase in photon flux, and probe both near-surface and bulk properties of the DAFFs. The current work has also demonstrated the power of combining various experimental techniques in studying a complex physics problem. It should also be important to extract the random field physics from experimental systems other than the DAFFs in order to avoid possibly small but consequential effects unique to the DAFFs.

Twenty years have passed since the first theoretical construct of the random field Ising model was proposed. Time has witnessed enormous amounts of theoretical and experimental efforts devoted to the ultimate solution of this fundamental physics problem. The journey towards this solution is strewn with controversies, debates and misinterpretations. However, we have learned a tremendous amount from this unusually complex problem. On both theoretical and experimental fronts, pieces of the solution are gradually being combined and congruities are growing. We may finally be standing on the verge of gaining an integrated and unobstructed view of the physics of random fields.

Bibliography

[1] Y. Imry and S. Ma, Phys. Rev. Lett. **35**, 1399 (1975).

[2] T. Nattermann and J. Villain, Phase Transitions **11**, 5 (1988).

[3] K. Huang, *Statistical Mechanics* (John Wiley & Sons, Inc., New York, 1987).

[4] J. Berretti, J. Stat. Phys. **38**, 4831 (1985).

[5] A. Aharony, Y. Imry, and S. Ma, Phys. Rev. Lett. **37**, 1364 (1976).

[6] E. Pytte, Y. Imry, and E. Pytte, Phys. Rev. Lett. **46**, 1173 (1981).

[7] K. Binder, Y. Imry, and E. Pytte, Phys. Rev. B **24**, 6736 (1981).

[8] D. Mukamel and E. Pytte, Phys. Rev. B **25**, 4779 (1982).

[9] J. Villain, Phys. Rev. Lett. **52**, 1543 (1984).

[10] G. Grinstein and S. keng Ma, Phys. Rev. B **28**, 2588 (1983).

[11] J. Chalker, J. Phys. C **16**, 6615 (1983).

[12] D.S. Fisher, J. Frohlich, and T. Spenser, J. Stat. Phys. **34**, 863 (1984).

[13] J. Imbrie, Phys. Rev. Lett. **53**, 1747 (1984).

[14] J. Imbrie, Comm. Math. Phys. **98**, 145 (1985).

[15] A. Aharony and E. Pytte, Phys. Rev. B. **27**, 5872 (1983).

[16] J. G. Y. Imry and S. Kirkpatrick, Phys. Rev. Lett. **51**, 203 (1983).

[17] I. M. Lifshitz, Soviet Physics JETP **15**, 939 (1962).

[18] Z. W. Lai, G. F. Mazenko, and O. T. Valls, Phys. Rev. B **37**, 9481 (1988).

[19] S. Allen and J. Cahn, Acta Metall. **27**, 1085 (1979).

[20] T. Hashimoto, K. Nishihara, and Y. Takeuchi, J. Phys. Soc. Jpn. **45**, 1127 (1978).

[21] S. Nagler, J. R.F. Shannon, C. Harkless, and M. Singh, Phys. Rev. Lett. **61**, 718 (1988).

[22] J. Villain, J. Physique **46**, 1843 (1985).

[23] D. Fisher, Phys. Rev. Lett. **56**, 416 (1986).

[24] A. Bray and M. Moore, J. Phys. C **??**, L927 (1985).

[25] G. Grinstein and S. Ma, Phys. Rev. Lett. **49**, 685 (1982).

[26] G. Grinstein and J. F. Fernandez, Phys. Rev. B **29**, 6389 (1984).

[27] J. Gunton, M. S. Miguel, and P. Sahni, Phase Transitions and Critical Phenomena **8**, C. Domb, J.L. Lebowitz, eds., Academic Press, London (1983).

[28] T. Nattermann and I. Vilfan, Phys. Rev. Lett. **61**, 223 (1988).

[29] A. Aharony, Phys. Rev. B. **18**, 3318 (1978).

[30] A. Khurana, F. Seco, and A. Houghton, Phys. Rev. Lett. **54**, 357 (1985).

[31] A. Houghton, A. Khurana, and F. Seco, Phys. Rev. Lett. **55**, 856 (1986).

[32] A. P. Young and M. Nauenberg, Phys. Rev. Lett. **54**, 2429 (1985).

[33] H. Rieger and A. P. Young, J. Phys. A **26**, 5279 (1993).

[34] A. Ogielski and D. Huse, Phys. Rev. Lett. **56**, 1298 (1986).

[35] A. T. Ogielski and D. A. Huse, Phys. Rev. Lett. **56**, 1298 (1986).

[36] H. Rieger, Phys. Rev. B **52**, 6659 (1995).

[37] M. Nauenberg and B. Nienhuis, Phys. Rev. Lett. **33**, 944 (1974).

[38] S. McCay and A. Berker, J. Appl. Phys. **64**, 5785 (1988).

[39] M. Mézard and A. Young, Europhys. Lett. **18**, 653 (1992).

[40] M. Mézard and R. Monasson, Phys. Rev. B **50**, 7199 (1994).

[41] J. LeGuillon and J. Justin, Phys. Rev. B **21**, 3976 (1980).

[42] K. Newman and E. Riedel, Phys. Rev. B **25**, 264 (1982).

[43] G. Jug, Phys. Rev. B **27**, 609 (1983).

[44] I. Maier and A. Sokolov, Sov. Phys. Solid State **26**, 7076 (1984).

[45] M. Gofman *et al.*, Phys. Rev. Lett. **71**, 1569 (1993).

[46] I. Dayan, M. Schwartz, and A. P. Young, J. Phys. A **26**, 3093 (1993).

[47] M. Schwartz, J. Phys. C **21**, 753 (1988).

[48] S. Fishman and A. Aharony, J. Phys. C **12**, L729 (1979).

[49] P. Z. Wong, S. von Molnar, and P. Dimon, J. Appl. Phys **53**, 7954 (1982).

[50] J. L. Cardy, Phys. Rev. B **29**, 505 (1984).

[51] P. Z. Wong, S. von Molnar, and P. Dimon, Solid State Comm. **48**, 573 (1983).

[52] Y. Shapira and S. Foner, Phys. Rev. B **1**, 3083 (1970).

[53] A. Aharony, Europhys. Lett. **1**, 617 (1986).

[54] I.B. Ferreira, A.R. King, V. Jaccarino, and J.L. Cardy, Phys. Rev. B **28**, 5192 (1983).

[55] M. Hagen, R. A. Cowley, R. Nicklow, and H. Ikeda, Phys. Rev. B **36**, 401 (1987).

[56] H. Ikeda, Y. Endoh, and S. Itoh, Phys. Rev. Lett. **64**, 1266 (1990).

[57] R. Birgeneau, R. Cowley, G. Shirane, and H. Yoshizawa, J. Stat. Phys. **34**, 817 (1984).

[58] P.-Z. Wong, J. Cable, and P. Dimon, J. Appl. Phys. **55**, 2377 (1984).

[59] D. P. Belanger, A. R. King, and V. Jaccarino, J. Appl. Phys. **55**, 2383 (1984).

[60] J. P. Hill, Q. Feng, R. J. Birgeneau, and T. R. Thurston, Z. Phys. B **92**, 285 (1993).

[61] D. P. Belanger, A. R. King, V. Jaccarino, and J. L. Cardy, Phys. Rev. B **28**, 2522 (1983).

[62] D. P. Belanger, A. R. King, and V. Jaccarino, Phys. Rev. Lett. **48**, 1050 (1982).

[63] C.A. Ramos, A.R. King, and V. Jaccarino, Phys. Rev. B **37**, 5483 (1988).

[64] I.B. Ferreira, A.R. King, and V. Jaccarino, Phys. Rev. B **43**, 10797 (1991).

[65] W. Kleemann, A. R. King, and V. Jaccarino, Phys. Rev. B **34**, 479 (1986).

[66] U. Leitão and W. Kleenman, Phys. Rev. B **35**, 8696 (1987).

[67] R.A. Cowley, H. Yoshizawa, G. Shirane, and R.J. Birgeneau, Z. Phys. B **58**, 15 (1984).

[68] H. Ikeda, J. Phys. C **19**, L811 (1986).

[69] P.Z.Wong, Phys. Rev. B **34**, 1864 (1986).

[70] R. J. Birgeneau *et al.*, Phys. Rev. Lett. **75**, 1198 (1995).

[71] R.A. Cowley *et al.*, Z. Phys. B **75**, 303 (1989).

[72] R. Birgeneau *et al.*, Phys. Rev. Lett. **54**, 2147 (1985).

[73] C. Ramos, A. King, V. Jaccarino, and S. Rezende, J. Physique Colloq. **C8**, 1241 (1988).

[74] J.C. Sartorelli, Phys. Rev. B **45**, 10779 (1992).

[75] D.P. Belanger, A.R. King, and V. Jaccarino, Phys. Rev. B **31**, 4538 (1985).

[76] M. Karszewiski *et al.*, J. Phys. C **6**, L75 (1994).

[77] U. Leitão and W. Kleenman, Europhys. Lett. **5**, 529 (1988).

[78] V. Jaccarino and A. King, Physica A **163**, 291 (1990).

[79] D.P. Belanger, V. Jaccarino, A.R. King, and R.M. Nicklow, Phys. Rev. Lett. **59**, 930 (1987).

[80] P. Wong and J. W. Cable, Phys. Rev. B **28**, 5361 (1983).

[81] S.-J. Han, D. P. Belanger, W. Kleemann, and U. Nowak, Phys. Rev. B **45**, 9728 (1992).

[82] P. Pollak, W. Kleemann, and D. P. Belanger, Phys. Rev. B **38**, 4773 (1988).

[83] U. A. Leitão, W. Kleemann, and I. B. Ferreira, Phys. Rev. B **38**, 4765 (1988).

[84] M. Lederman *et al.*, Phys. Rev. B **48**, 3810 (1993).

[85] H. Ikeda and K. Kikuta, J. Phys. C **17**, 1221 (1984).

[86] H. Yoshizawa and D. Belanger, Phys. Rev. B **30**, 5220 (1984).

[87] C.M. Soukoulis, G.S. Grest, C. Ro, and K. Levin, J. Appl. Phys **57**, 3700 (1985).

[88] G. Benedek and T. Kushida, Physical Review **118**, 46 (1960).

[89] O. Dietrich, J. Phys. C **2**, 2022 (1969).

[90] J. W. Stout and E. Catalano, J. Chem. Phys. **23**, 2013 (1955).

[91] G. Low, A. Okazaki, R. Stevenson, and K. Turberfield, J. Appl. Phys. **35**, 998 (1964).

[92] M. T. Hutchings, M. Schulhof, and H. J. Guggenheim, Phys. Rev. B **5**, 154 (1972).

[93] A. King and H. Rohrer, Phys. Rev. B **19**, 5864 (1979).

[94] P. Mitchell *et al.*, Phys. Rev. B **34**, 4719 (1986).

[95] G. Grinstein, S. keng Ma, and G. F. Mazenko, Phys. Rev. B **15**, 258 (1977).

[96] H. Kogon and D. Wallace, J. Phys. A **14**, L527 (1981).

[97] S. Lovesey, J. Phys. C **17**, L213 (1984).

[98] M. Kaufman and M. Kardar, Phys. Rev. B **31**, 2913 (1985).

[99] R. Pelcovits and A. Aharony, Phys. Rev. B **31**, 350 (1985).

[100] H. Yoshizawa *et al.*, Phys. Rev. Lett. **48**, 438 (1982).

[101] M. Hagen *et al.*, Phys. Rev. B **28**, 2602 (1983).

[102] H. Yoshizawa, R. A. Cowley, G. Shirane, and R. J. Birgeneau, Phys. Rev. B **31**, 4548 (1985).

[103] P. Mitchell *et al.*, Phys. Rev. B **34**, 4719 (1986).

[104] R. J. Birgeneau *et al.*, Physica **137B**, 83 (1986).

[105] R.A. Cowley *et al.*, Phys. Rev. B **30**, 6650 (1984).

[106] M. T. Hutchings, M. Schulhof, and H. J. Guggenheim, Phys. Rev. B **5**, 154 (1972).

[107] J. Als-Nielson and G. Materlik, Physics Today **48**, 34 (1995).

[108] J. Hill, *Ph.D. Thesis* (M.I.T., Cambridge,MA, 1992).

[109] B. Warren, *X-Ray Diffraction* (Dover Publications, Inc., New York, 1990).

[110] F. Low, Phys. Rev. **96**, 1428 (1954).

[111] M. Gell-Mann and M. Goldberger, Phys. Rev. **96**, 1433 (1954).

[112] P. Platzman and N. Tzoar, Phys. Rev. B **2**, 3556 (1970).

[113] M. Blume, J. Appl. Phys. **57**, 3615 (1985).

[114] M. Blume and D. Gibbs, Phys. Rev. B **37**, 1779 (1988).

[115] M. Fisher, Philos. Mag. **7**, 1731 (1962).

[116] A. Lidiard, Rep. Progr. Phys. **17**, 201 (1954).

[117] G. Gehring, J. Phys. C **10**, 531 (1977).

[118] J. Clarke, Scientific American August 46 (1994).

[119] S. Foner, Rev. Sci. Instrum. **30**, 548 (1959).

[120] S. Foner, E. McNiff, and Jr., Rev. Sci. Instrum. **39**, 171 (1968).

[121] J. W. Stout and E. Catalano, J. Chem. Phys. **23**, 2013 (1955).

[122] P. Z. Wong, Phys. Rev. B **34**, 1864 (1986).

[123] R.J. Birgeneau *et al.*, Phys. Rev. B **27**, 6747 (1983).

[124] I.B. Ferreira, J.L. Cardy, A.R. King, and V. Jaccarino, J. Appl. Phys. **69**, 5075 (1991).

[125] A.E. Nash, C.A. Ramos, , and V. Jaccarino, Phys. Rev. B **47**, 5805 (1993).

[126] Y. Shapira, N.F. Oliveira, and S. Foner, Phys. Rev. B **30**, 6639 (1984).

[127] R. J. Birgeneau *et al.*, Phys. Rev. Lett. **75**, 1198 (1995).

[128] P.Z. Wong, S. von Molnar, and P. Dimon, Solid State Comm. **48**, 573 (1983).

[129] D. Belanger, Phase Transitions **11**, 53 (1988).

[130] R. Cowley, R. Birgeneau, and G. Shirane, Physica (Amsterdam) **140**, 285 (1986).

[131] R. G. H. Y. Uemura and R.J. Birgeneau, Z. Phys. B **75**, 303 (1989).

[132] D.P. Belanger, A.R. King, V. Jaccarino, and J.L. Cardy, Phys. Rev. B **28**, 2522 (1983).

[133] D. Belanger *et al.*, J. Magn. Magn. Mat. **140-144**, 1549 (1995).

[134] Q. Feng, R. Birgeneau, and J. Hill, Phys. Rev. B **74**, 3840 (1995).

[135] S-J. Han, D.P. Belanger, W. Kleenmann, and U. Nowak, Phys. Rev. B **45**, 9728 (1992).

[136] A.R. King, J.A. Mydosh, and V. Jaccarino, Phys. Rev. Lett. **56**, 2525 (1986).

[137] A.E. Nash, A.R. King, and V. Jaccarino, Phys. Rev. B **43**, 1272 (1991).

[138] M. Lederman *et al.*, Phys. Rev. Lett. **68**, 2086 (1992).

[139] M. Lederman *et al.*, Phys. Rev. B **48**, 3810 (1993).

[140] J.P. Hill *et al.*, Phys. Rev. Lett. **66**, 3281 (1991).

[141] J. P. Hill, Q. Feng, R. J. Birgeneau, and T. R. Thurston, Phys. Rev. Lett. **70**, 3655 (1993).

[142] T. Thurston *et al.*, Phys. Rev. B **37**, 9559 (1988).

[143] P. Pollak, W. Kleemann, and D. P. Belanger, Phys. Rev. B **38**, 4773 (1988).

[144] J. Villain, J. Physique **46**, 1843 (1985).

[145] C. Kittel, *Introduction to Solid State Physics* (J. Wiley and Sons, New York, 1986).

[146] R.A. Cowley, H. Yoshizawa, G. Shirane, and R.J. Birgeneau, Z. Phys. B **58**, 15 (1984).

[147] P. Pollak, W. Kleenman, and D.P. Belanger, Phys Rev. B **38**, 4773 (1988).

[148] C. A. Ramos, A. R. King, and V. Jaccarino, Phys. Rev. B **37**, 5483 (1986).

[149] I. B. Ferreira, A. R. King, and V. Jaccarino, Phys. Rev. B **43**, 10797 (1991).

[150] K. E. Dow and D. P. Belanger, Phys. Rev. B **39**, 4418 (1989).

[151] D. S. Fisher, Phys. Rev. Lett. **56**, 416 (1986).

[152] J. Villain, Phys. Rev. Lett. **52**, 1543 (1984).

[153] G. S. Grest, C. M. Soukoulis, and K. Levin, Phys. Rev. B **33**, 7659 (1986).

[154] I. Ferreira, *Ph.D. Thesis* (U.C.S.B., Santa Barbara, CA, 1992).

[155] M. Fisher and J. Langer, Phys. Rev. Lett. **13**, 665 (1968).

[156] P.Z.Wong, Phys. Rev. B **34**, 1864 (1986).

[157] J. Ferre and G. Gehring, Rep. Prog. Phys. **47**, 513 (1984).

[158] J. Imbrie, Phys. Rev. Lett. **53**, 1747 (1984).

[159] D. P. Belanger, S. M. Rezende, A. R. King, and V. Jaccarino, J. Appl. Phys. **57**, 3294 (1985).

[160] P. Wong and J. Cable, Phys. Rev. B **28**, 5361 (1983).

[161] E. Gawlinski *et al.*, Phys. Rev. Lett. **53**, 2266 (1984).

[162] G.S. Grest, C.M. Soukoulis, and K. Levin, Phys. Rev. B **33**, 7659 (1986).

[163] Y. Kim and A. B. Harris, Phys. Rev. B **32**, 4676 (1985).

[164] U. Nowak and K. D. Usadel, Phys. Rev. B **46**, 8329 (1992).

[165] J. P. Hill, Q. Feng, R. J. Birgeneau, and T. R. Thurston, Z. Phys. B **92**, 285 (1993).

[166] H. Rieger, Phys. Rev. B **52**, 6659 (1995).

[167] H. Ikeda and K. Kikuta, J. Phys. C **17**, 1221 (1984).

[168] F. Montenegro *et al.*, J. Mag. Mag. Mat. **19**, L811 (1986).

[169] H. Ikeda, J. Phys. C **19**, L811 (1986).

[170] M. Blume and D. Gibbs, Phys. Rev. B **37**, 1779 (1988).

[171] J. P. Hill, Q. Feng, Q. J. Harris, R. J. Birgeneau, A.P. Ramirez and A. Cassanho, Phys. Rev. B (submitted).

[172] H. Rieger and A. P. Young, J. Phys. A **26**, 5279 (1993).

[173] A. Bruce and D. Wallace, J. Phys. A **16**, 1721 (1983).

[174] A. Maritan *et al.*, Phys. Rev. Lett. **67**, 1821 (1991).

[175] T. Ryan, R. Nelmes, R. Cowley, and A. Gibaud, Phys. Rev. Lett. **56**, 2704 (1986).

[176] Q. Harris *et al.*, Phys. Rev. B **52**, 15420 (1995).

[177] T. Thurston *et al.*, Phys. Rev. Lett. **70**, 3151 (1993).

[178] T. Thurston *et al.*, Phys. Rev. B **49**, 15730 (1994).

[179] P. Gehring, K. Hirota, C. Majkrzak, and G. Shirane, Phys. Rev. Lett. **71**, 1087 (1993).

[180] K. Hirota, G. Shirane, P. Gehring, and C. Majkrzak, Phys. Rev. B **49**, 11967 (1994).

[181] G. Shirane, R. Cowley, M. Matsuda, and S. Shapiro, Phys. Rev. B **48**, 15595 (1993).

[182] M. Altarelli, M. Núñez-Regueiro, and M. Papoular, Phys. Rev. Lett. **74**, 3840 (1995).

[183] R. J. Birgeneau *et al.*, Physica **137B**, 83 (1986).

[184] T. Nattermann and J. Villain, Phase Transitions **11**, 5 (1988).

[185] R. A. Cowley, H. Yoshizawa, G. Shirane, and R. J. Birgeneau, Z. Phys. B **58**, 15 (1984).

[186] Y. Shapira, N. F. Oliveira, Jr., and S. Foner, Phys. Rev. B **30**, 6639 (1984).

[187] J. Villain, J. Physique **46**, 1843 (1985).

[188] R. A. Cowley *et al.*, Z. Phys. B **75**, 303 (1989).

[189] M. Lederman *et al.*, Phys. Rev. B **48**, 3810 (1993).

[190] J. P. Hill, Q. Feng, R. J. Birgeneau, and T. R. Thurston, Phys. Rev. Lett. **70**, 3655 (1993).

[191] H. Yoshizawa, R. A. Cowley, G. Shirane, and R. J. Birgeneau, Phys. Rev. B **31**, 4548 (1985).

[192] U. Nowak and K. D. Usadel, Phys. Rev. B **46**, 8329 (1992).

[193] *Fundamentals of Crystalograhy*, edited by C. Giagovazzo (Oxford Science Publications, Oxford, 1992).

[194] J. J. Prejean and J. Souletie, J. Physique **41**, 1335 (1980).

[195] M. T. Hutchings, B. D. Rainford, and H. J. Guggenheim, J. Phys. C **3**, 307 (1970).

[196] R.J. Birgeneau *et al.*, Phys. Rev. B **28**, 1438 (1983).

[197] D. A. Huse and C. L. Henley, Phys. Rev. Lett. **54**, 2708 (1985).

[198] A. G. Schins, A. F. M. Arts, and H. W. de Wijn, Phys. Rev. Lett. **70**, 2340 (1993).

[199] J. L. Cambier and M. Nauenberg, Phys. Rev. B **34**, 7998 (1986).

[200] M. Rao and A. Chakrabarti, Phys. Rev. Lett. **71**, 3501 (1993).